



**US Army Corps
of Engineers®**
Engineer Research and
Development Center

Physical Model of Knik Arm and the Port of Anchorage, Alaska

Steven A. Hughes, Julie A. Cohen, and Hugh F. Acuff

May 2010



Physical Model of Knik Arm and the Port of Anchorage, Alaska

Steven A. Hughes, Julie A. Cohen, and Hugh F. Acuff

Coastal and Hydraulics Laboratory
U.S. Army Engineer Research and Development Center
3909 Halls Ferry Road
Vicksburg, MS 39180-6199

Final report

Approved for public release; distribution is unlimited.

Prepared for U.S. Army Engineer District, Alaska
Elmendorf Air Force Base, AK 99506-0898

Abstract: A large physical model replicating approximately 19 miles of Cook Inlet was constructed at ERDC with a horizontal length scale of 800-to-1 and a vertical length scale of 200-to-1. The model included the Knik Arm, a portion of Eagle Bay, and a region south of Point Woronzof. The Port of Anchorage is located in the Knik Arm, and tidal flows at the Port generated by the +30-ft tide range are highly influenced by a large gyre that forms to the south of Cairn Point during ebb tide. The purpose of the physical model was to evaluate changes to tidal flows caused by a large, multi-phased Port expansion that might impact the Alaska District's navigation mission at the Port. Model validation consisted of reasonable reproduction of field-measured tidal velocities collected at three locations near the Port over the spring tide cycle. Velocity measurements over a tide cycle were acquired in the model at strategic locations near the Port berthing areas for each phase of the Port expansion. Comparisons between the different expansion phases quantified expected changes to the flow regime. Potential sedimentation problems were identified using both measurements and flow visualization techniques coupled with time-lapse video.

DISCLAIMER: The contents of this report are not to be used for advertising, publication, or promotional purposes. Citation of trade names does not constitute an official endorsement or approval of the use of such commercial products. All product names and trademarks cited are the property of their respective owners. The findings of this report are not to be construed as an official Department of the Army position unless so designated by other authorized documents.

DESTROY THIS REPORT WHEN NO LONGER NEEDED. DO NOT RETURN IT TO THE ORIGINATOR.

Contents

| | |
|--|------------|
| Figures and Tables | vi |
| Preface | x |
| Unit Conversion Factors | xii |
| 1 Introduction | 1 |
| Background | 1 |
| Overview of the Knik Arm physical models | 4 |
| Physical model objectives and study tasks | 5 |
| Report organization and content | 6 |
| Units of measure | 7 |
| 2 Principles of Physical Modeling | 8 |
| Principles of similitude | 8 |
| Geometrically distorted models | 9 |
| Hydraulic similitude in geometrically distorted physical models | 10 |
| Physical model advantages | 13 |
| Physical model disadvantages | 14 |
| Physical model laboratory effects | 14 |
| Physical model scale effects | 15 |
| Turbulence scale effect in geometrically distorted physical models | 16 |
| Other physical model disadvantages | 18 |
| Physical model appropriateness | 18 |
| 3 Physical Model Design and Construction | 20 |
| Dominant physical processes in the Knik Arm | 20 |
| Model scale selection | 21 |
| Modeled region | 22 |
| Model facility | 25 |
| Model length scales | 26 |
| Hydrodynamics similitude criteria | 27 |
| Tide generation capability | 28 |
| Summary of model scaling | 29 |
| Potential scale and laboratory effects | 31 |
| Scale effects | 31 |
| Laboratory effects | 32 |
| Model design | 33 |
| Model layout | 33 |
| Large-Area Model upstream tidal prism storage surface | 34 |
| Bottom friction | 39 |

| | |
|---|------------|
| Model construction | 41 |
| <i>Bathymetry</i> | 41 |
| <i>Port expansion inserts</i> | 47 |
| 4 Experiment Setup and Operating Procedures | 50 |
| Experiment instrumentation | 50 |
| <i>Water level</i> | 50 |
| <i>Flow velocity</i> | 51 |
| <i>Flow visualization</i> | 53 |
| Operating procedures | 55 |
| <i>Tide generation</i> | 55 |
| <i>Conducting experiments</i> | 56 |
| Data collection and initial analyses | 57 |
| <i>Tides</i> | 57 |
| <i>Velocities</i> | 58 |
| <i>Data synchronization and analyses</i> | 58 |
| 5 Model Calibration and Verification | 60 |
| Field data | 60 |
| <i>Tide</i> | 60 |
| <i>Velocities</i> | 62 |
| Model calibration | 66 |
| <i>Motion of tide outflow gate</i> | 66 |
| <i>Comparison to Knik Arm tide record</i> | 68 |
| <i>Model tide repeatability</i> | 69 |
| Model verification | 73 |
| <i>Initial verification results</i> | 73 |
| <i>Final verification results</i> | 78 |
| 6 Model Test Results | 83 |
| Flow velocity changes due to Port of Anchorage expansion | 83 |
| <i>Model configurations and measurement locations</i> | 83 |
| <i>Flow velocities for each Port expansion phase</i> | 87 |
| <i>Flow velocity comparisons between expansion phases</i> | 96 |
| <i>Summary</i> | 105 |
| Flow velocities at the Port after construction of North Extension | 108 |
| <i>Model configuration and measurement locations</i> | 108 |
| <i>Comparison to Pre-Expansion Port configuration</i> | 110 |
| <i>Effect of South Extension</i> | 111 |
| <i>Velocities along the original dock face</i> | 114 |
| <i>Velocities for the Full Port Expansion</i> | 114 |
| <i>Summary</i> | 123 |
| 7 Summary and Conclusions | 124 |
| Summary of physical model study | 124 |
| <i>Situation</i> | 124 |
| <i>Study objectives</i> | 124 |

| | |
|---|------------|
| Physical model description | 125 |
| Overview of testing program..... | 126 |
| Study observations and conclusions | 127 |
| Physical model utility | 127 |
| Flow velocity changes due to Port of Anchorage expansion..... | 128 |
| Flow velocities at the Port after construction of North Extension | 129 |
| References | 131 |
| Appendix A: Consistency Check Plots | 132 |
| Appendix B: Velocity Plots for Port Expansion Phases | 148 |
| Appendix C: Plots showing South Extension effect..... | 164 |
| Report Documentation Page | |

Figures and Tables

Figures

| | |
|---|----|
| Figure 1. Cook Inlet, Alaska, location map. | 1 |
| Figure 2. Port of Anchorage, Knik Arm, Cook Inlet, Alaska..... | 2 |
| Figure 3. Proposed Port of Anchorage expansions (provided by MARAD)..... | 3 |
| Figure 4. Areal extent of the two physical models. | 23 |
| Figure 5. Downstream boundary flood flow vectors from numerical model..... | 24 |
| Figure 6. Upstream boundary flood flow vectors from numerical model. | 25 |
| Figure 7. ESTEX flume layout and dimensions. | 26 |
| Figure 8. Layout of both models in the ESTEX flume. | 33 |
| Figure 9. Cumulative storage volume vs. tide elevation at Eagle Bay boundary..... | 35 |
| Figure 10. Cross section of prism storage bathymetry. | 36 |
| Figure 11. Newly cast section of the Small-Area Model upstream of the Port of Anchorage..... | 43 |
| Figure 12. Bathymetry contours sketched on the Small-Area Model. | 43 |
| Figure 13. Hand molding bathymetry detail on the Small-Area Model. | 44 |
| Figure 14. Hand molding Cairn Point bathymetry on the Large-Area Model. | 44 |
| Figure 15. Cairn Point bathymetry detail on the Large-Area Model. | 45 |
| Figure 16. Completed Large-Area Model from Point Woronzof. | 46 |
| Figure 17. Large-Area Model from the tidal prism storage area. | 46 |
| Figure 18. Casting of the North Backlands and North Extension insert | 47 |
| Figure 19. Casting of the North Replacement Expansion insert. | 48 |
| Figure 20. Completed Port expansion inserts..... | 48 |
| Figure 21. Acoustic Doppler velocimeter probe head. | 52 |
| Figure 22. Dye injection to visualize flow velocities past the Port of Anchorage..... | 54 |
| Figure 23. Surface tracers used to visualize flow velocities past the Port of Anchorage. | 54 |
| Figure 24. Smoothing of ADV velocity magnitude and direction. | 59 |
| Figure 25. Measured tide in Knik Arm during 5-18 August 2006..... | 61 |
| Figure 26. Selected Knik Arm tide cycle scaled for Large-Area Model. | 62 |
| Figure 27. Locations of ADCP mooring stations near the Port of Anchorage..... | 63 |
| Figure 28. Tides during ADCP velocity data collection. | 64 |
| Figure 29. Station 2 depth- and time-averaged velocity magnitudes and directions..... | 65 |
| Figure 30. Station 4 depth- and time-averaged velocity magnitudes and directions..... | 65 |
| Figure 31. Station 5 depth- and time-averaged velocity magnitudes and directions. | 65 |
| Figure 32. Non-symmetric outflow gate control signal (Equation 49). | 67 |
| Figure 33. Symmetric outflow gate control signal (Equation 51)..... | 68 |
| Figure 34. Unsuccessful early calibration test. | 69 |
| Figure 35. Successful Knik Arm Large-Area Model calibration. | 69 |

| | |
|--|-----|
| Figure 36. Tide cycle repeatability within the same test..... | 70 |
| Figure 37. Tide cycle repeatability at Station 2 between different tests..... | 71 |
| Figure 38. Tide cycle repeatability at Station 5 between different tests. | 72 |
| Figure 39. Modification of Cairn Point bathymetry. | 74 |
| Figure 40. Initial model verification of velocity magnitude and direction at Station 2. | 75 |
| Figure 41. Initial model verification of velocity magnitude and direction at Station 4. | 76 |
| Figure 42. Initial model verification of velocity magnitude and direction at Station 5. | 77 |
| Figure 43. Modification of east Eagle Bay shoreline. | 79 |
| Figure 44. Final model verification of velocity magnitude and direction at Station 2. | 80 |
| Figure 45. Final model verification of velocity magnitude and direction at Station 4. | 81 |
| Figure 46. Final model verification of velocity magnitude and direction at Station 5. | 82 |
| Figure 47. Locations of six ADV current measurement points. | 84 |
| Figure 48. Location of the reference ADV current measurement gauge. | 85 |
| Figure 49. First and Second Port expansion configurations. | 86 |
| Figure 50. Third and Full Port expansion configurations. | 87 |
| Figure 51. Consistency check for Test 48 at location Ref. ADV..... | 89 |
| Figure 52. Consistency check for Test 50 at location Ref. ADV. | 91 |
| Figure 53. Consistency check for Test 55 at location Ref. ADV. | 92 |
| Figure 54. Velocity measurements at Pt. 1 and Pt. 2 (Existing configuration). | 93 |
| Figure 55. Velocity measurements at Pt. 5-2 and Pt. DL (Existing configuration)..... | 94 |
| Figure 56. Velocity measurements at Pt. 17 and Pt. 22 (Existing configuration)..... | 95 |
| Figure 57. Comparison of pre-expansion configuration to Full Port Expansion at Pt. 1. | 97 |
| Figure 58. Comparison of pre-expansion configuration to Full Port Expansion at Pt. 2..... | 98 |
| Figure 59. Comparison of pre-expansion configuration to Full Port Expansion at Pt. 5-2. | 99 |
| Figure 60. Comparison of pre-expansion configuration to Full Port Expansion at Pt. DL. | 101 |
| Figure 61. Comparison of pre-expansion configuration to Full Port Expansion at Pt. 17. | 102 |
| Figure 62. Comparison of pre-expansion configuration to Full Port Expansion at Pt. 22. | 103 |
| Figure 63. Comparison of pre-expansion configuration to Second Port Expansion at Pt. 1..... | 104 |
| Figure 64. Comparison of pre-expansion configuration to Second Port Expansion at Pt. 2..... | 106 |
| Figure 65. Comparison of pre-expansion configuration to Third Port Expansion at Pt. 2. | 107 |
| Figure 66. Measurement locations for North Extension test series. | 109 |
| Figure 67. Effect of North and South Extensions at measurement point 1..... | 112 |
| Figure 68. Effect of North and South Extensions at measurement point 2. | 113 |
| Figure 69. Effect of South Extension at measurement point 6. | 115 |
| Figure 70. Comparison between pts. 1 and 2 with South Extension installed..... | 116 |
| Figure 71. Comparison between pts. 1 and 3 with South Extension installed. | 117 |
| Figure 72. Comparison between pts. 2 and 3 with South Extension installed..... | 118 |
| Figure 73. Comparison between pts. 5 and 9 for completed Port Expansion..... | 119 |
| Figure 74. Comparison between pts. 6 and 10 for completed Port Expansion..... | 120 |
| Figure 75. Comparison between pts. 7 and 11 for completed Port Expansion. | 121 |

| | |
|---|-----|
| Figure 76. Comparison between pts. 8 and 12 for completed Port Expansion..... | 122 |
| Figure A1. Consistency check for Test 46 at location Ref. ADV..... | 133 |
| Figure A2. Consistency check for Test 48 at location Ref. ADV..... | 134 |
| Figure A3. Consistency check for Test 49 at location Ref. ADV..... | 135 |
| Figure A4. Consistency check for Test 50 at location Ref. ADV..... | 136 |
| Figure A5. Consistency check for Test 51 at location Ref. ADV..... | 137 |
| Figure A6. Consistency check for Test 52 at location Ref. ADV..... | 138 |
| Figure A7. Consistency check for Test 53 at location Ref. ADV. | 139 |
| Figure A8. Consistency check for Test 54 at location Ref. ADV..... | 140 |
| Figure A9. Consistency check for Test 55 at location Ref. ADV..... | 141 |
| Figure A10. Consistency check for Test 56 at location Ref. ADV. | 142 |
| Figure A11. Consistency check for Test 57 at location Ref. ADV. | 143 |
| Figure A12. Consistency check for Test 58 at location Ref. ADV. | 144 |
| Figure A13. Consistency check for Test 59 at location Ref. ADV. | 145 |
| Figure A14. Consistency check for Test 61 at location Ref. ADV. | 146 |
| Figure A15. Consistency check for Test 62 at location Ref. ADV. | 147 |
| Figure B1. Velocity measurements at Pt. 1 and Pt. 2 (Existing configuration). | 149 |
| Figure B2. Velocity measurements at Pt. 5.2 and Pt. DL (Existing configuration). | 150 |
| Figure B3. Velocity measurements at Pt. 17 and Pt. 22 (Existing configuration)..... | 151 |
| Figure B4. Velocity measurements at Pt. 1 and Pt. 2 (First Expansion configuration)..... | 152 |
| Figure B5. Velocity measurements at Pt. 5.2 and Pt. DL (First Expansion configuration). | 153 |
| Figure B6. Velocity measurements at Pt. 17 and Pt. 22 (First Expansion configuration). | 154 |
| Figure B7. Velocity measurements at Pt. 1 and Pt. 2 (Second Expansion configuration)..... | 155 |
| Figure B8. Velocity measurements at Pt. 5.2 and Pt. DL (Second Expansion configuration). | 156 |
| Figure B9. Velocity measurements at Pt. 17 and Pt. 22 (Second Expansion configuration). | 157 |
| Figure B10. Velocity measurements at Pt. 1 and Pt. 2 (Third Expansion configuration). | 158 |
| Figure B11. Velocity measurements at Pt. 5.2 and Pt. DL (Third Expansion configuration). | 159 |
| Figure B12. Velocity measurements at Pt. 17 and Pt. 22 (Third Expansion configuration)..... | 160 |
| Figure B13. Velocity measurements at Pt. 1 and Pt. 2 (Full Expansion configuration). | 161 |
| Figure B14. Velocity measurements at Pt. 5.2 and Pt. DL (Full Expansion configuration). | 162 |
| Figure B15. Velocity measurements at Pt. 17 and Pt. 22 (Full Expansion configuration). | 163 |
| Figure C1. Effect of South Extension at measurement point 1. | 165 |
| Figure C2. Effect of South Extension at measurement point 2. | 166 |
| Figure C3. Effect of South Extension at measurement point 3. | 167 |
| Figure C4. Effect of South Extension at measurement point 6. | 168 |
| Figure C5. Effect of South Extension at measurement point 7..... | 169 |
| Figure C6. Effect of South Extension at measurement point 8. | 170 |

Tables

| | |
|--|-----|
| Table 1. Large-Area Model scale ratios and prototype equivalence. | 30 |
| Table 2. Prototype and model parameter values for Large-Area Model. | 30 |
| Table 3. Small-Area Model scale ratios and prototype equivalence. | 30 |
| Table 4. Prototype and model parameter values for Small-Area Model. | 31 |
| Table 5. Field ADCP velocity data collection parameters. | 63 |
| Table 6. Coordinates of ADV current measurement points. | 84 |
| Table 7. Summary of Port expansion tests. | 88 |
| Table 8. Summary of Port North Extension tests. | 110 |

Preface

This technical report describes small-scale physical model experiments simulating the flow patterns around the Port of Anchorage, AK, during the spring tide cycle in the Knik Arm of Cook Inlet. The study was conducted by the U.S. Army Engineer Research and Development Center (ERDC), Coastal and Hydraulics Laboratory (CHL), Vicksburg, MS, for the U.S. Army Engineer District, Alaska (POA). The purpose of the physical model experiments was to evaluate changes to the flow velocities and patterns in the vicinity of the Port of Anchorage that will occur during all phases of the planned Port expansion. Initial funding authority was provided by POA to CHL on 16 March 2007, and a review draft of this report was submitted to POA on 10 June 2009. Review comments from POA, Engineering Division were incorporated into the report on 19-20 November 2009.

Merlin D. Peterson, Hydraulics and Hydrology Section, Civil Works Branch, Engineering Division, POA, was the point of contact for the sponsoring Alaska District, and he provided study oversight and review. Kenneth J. Eisses, Chief, Hydraulics and Hydrology Section, Civil Works Branch, Engineering Division, POA, provided crucial advice and direction throughout the study. John Oliver, Corps of Engineers, retired, provided technical advice and review through a contract with POA.

The physical model study was directed by Dr. Steven A. Hughes, Navigation Division (HN), CHL. Julie A. Cohen of the Harbors, Entrances and Structures Branch (HN-HH), CHL, prepared the model design drawings, managed the day-to-day operation of the physical model, performed data analysis, and assisted in report and figure preparation. Hugh F. Acuff, Jr., HN-HH, provided overall planning and operational guidance throughout the study, and assured all aspects of the study proceeded as planned. The physical model was constructed by craftsmen from the ERDC Department of Public Works under the supervision of Charles Brown, construction leadman, and Frank James, Construction Supervisor. David Daily and Timothy Nisley, Instrumentation Support Division, Information technology Laboratory, supported the instrumentation requirements. Christopher Callegan, Field Data Collection and Analysis Branch, CHL;

and Alex Sanchez, HN-HH, activated the tide generating system in the ESTEX flume.

This study was conducted during the period March 2007 through May 2009 under the direct supervision of Jose E. Sanchez, former Chief, Harbors, Entrances, and Structures Branch; and Jackie S. Pettway, current Chief, Harbors, Entrances, and Structures Branch, Navigation Division, CHL. Administrative supervision was provided by Dr. M. Rose Kress, Chief, Navigation Division, CHL; Thomas W. Richardson, former Director, CHL; and Dr. William D. Martin, Director, CHL.

COL Gary E. Johnston was Commander and Executive Director of ERDC. Dr. Jeffery P. Holland was Director.

Unit Conversion Factors

| Multiply | By | To Obtain |
|-----------------------|----------------|-------------------|
| acres | 4,046.873 | square meters |
| cubic feet | 0.02831685 | cubic meters |
| cubic inches | 1.6387064 E-05 | cubic meters |
| cubic yards | 0.7645549 | cubic meters |
| feet | 0.3048 | meters |
| gallons (U.S. liquid) | 3.785412 E-03 | cubic meters |
| inches | 0.0254 | meters |
| knots | 0.5144444 | meters per second |
| miles (nautical) | 1,852 | meters |
| miles (U.S. statute) | 1,609.347 | meters |
| miles per hour | 0.44704 | meters per second |
| square feet | 0.09290304 | square meters |
| square inches | 6.4516 E-04 | square meters |
| square miles | 2.589998 E+06 | square meters |
| square yards | 0.8361274 | square meters |
| yards | 0.9144 | meters |

1 Introduction

Background

The Port of Anchorage, Alaska, is located on the eastern bank of the Knik Arm of Cook Inlet. Figure 1 shows the approximate location of Anchorage and the Knik Arm.



Figure 1. Cook Inlet, Alaska, location map.

The Port began operations in 1961, and it was reported on the Port's web site that the Port presently serves 80 percent of Alaska's populated area by rail, road, and air connections, and handles over 90 percent of all consumer goods sold in the region. All of the refined petroleum products from Alaska's largest refinery in Fairbanks pass through the Port of Anchorage.

Development, operation, and maintenance of navigation channels and berthing areas at the Port of Anchorage are the responsibility of the Alaska District, U.S. Army Corps of Engineers (USACE). Shoaling at Anchorage Harbor has required annual dredging ranging between 1,500,000 and 2,100,000 yd³ over the last five years. Previously, dredging had been

300,000 - 800,000 yd³ per year. An aerial view of the Port of Anchorage at low tide is shown on Figure 2.



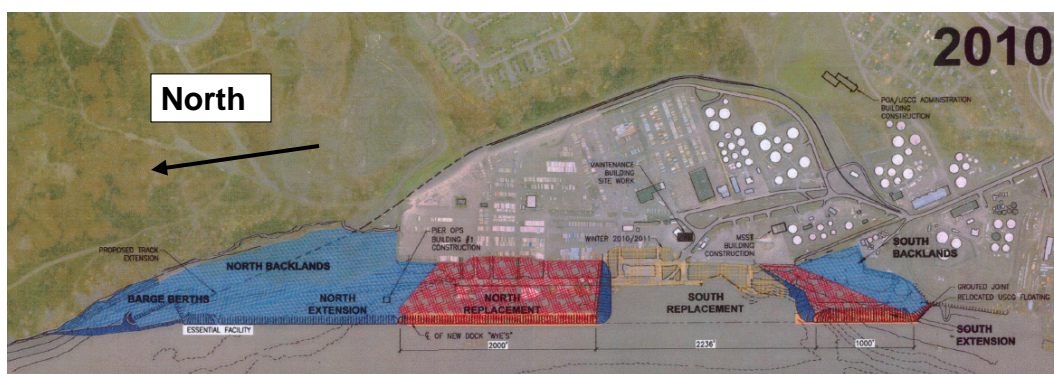
Figure 2. Port of Anchorage, Knik Arm, Cook Inlet, Alaska.

Construction is underway for a significant expansion to the Port of Anchorage with construction to be phased as illustrated in the Figure 3 sketches provided by the U.S. Department of Transportation, Maritime Administration (MARAD). The first Port of Anchorage expansion is shown in Figure 3a. On the north end of the Port (left side of Figure 3a) barge berths have been installed at the seaward edge of the North Backlands fill, and the North Extension has been constructed. At the south end of the Port, a small South Backlands fill has been placed. Port operations will continue at the original berthing areas while new berthing areas are prepared.

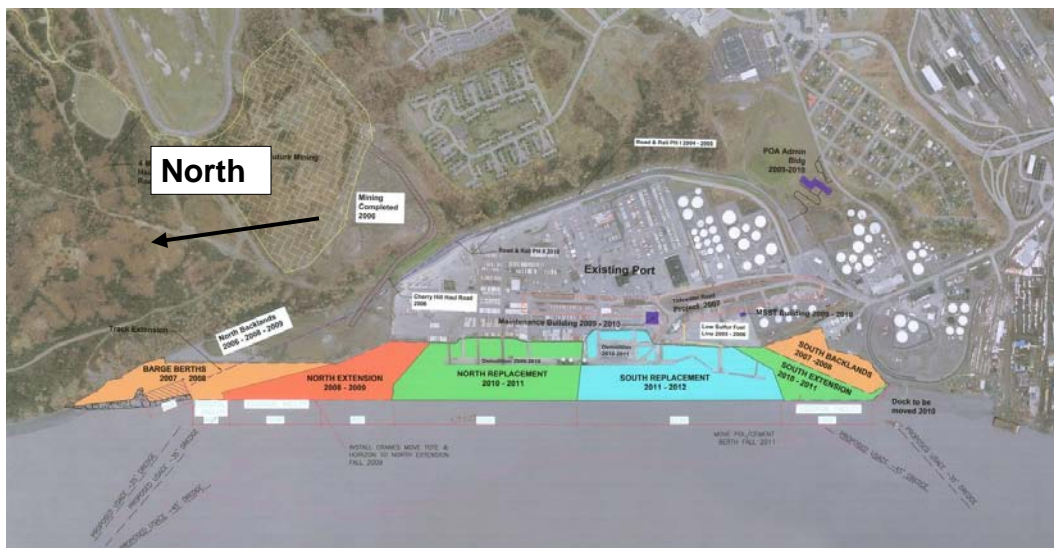
By the end of 2010, the South Extension will be added to the South Backlands as shown in Figure 3b, and a 2,000-ft-long North Replacement expansion will move the dock face about 400 ft seaward from its original location. The final Port expansion will be the addition of the 2,236-ft South Replacement section, as shown on Figure 3c.



a. Port expansion through 2008.



b. Port expansion through 2010.



c. Completed Port expansion.

Figure 3. Proposed Port of Anchorage expansions (provided by MARAD).

In addition to the engineering and construction challenges involved in this port expansion, Port authorities and USACE Alaska District engineers need to understand how the expansion could alter the tidal flow regime in

this highly dynamic region where the tide range varies by as much as 30 feet. Changes to the flow magnitudes and patterns caused by Port expansion and the construction sequence could impact shoaling patterns which, in turn, could affect operations at the Port of Anchorage.

Two critical Alaska District responsibilities related to the Port of Anchorage navigation project are assuring safe navigation conditions and maintaining project depths through annual dredging operations. A key aspect for Alaska District engineers is estimating future dredging requirements to meet navigation needs of the Port so that appropriate funding can be requested in advance. Thus, the changes in the Port of Anchorage footprint must be evaluated by the Alaska District to determine whether the hydrodynamics in the Knik Arm of Cook Inlet will be modified, and how this might affect future Port maintenance operations.

The Alaska District requested technical support from the U.S. Army Engineer Research and Development Center's (ERDC) Coastal and Hydraulics Laboratory (CHL) to help the District evaluate potential impacts to maintenance operations and navigation arising from the Port of Anchorage expansion. Engineers and staff at CHL conducted: (1) field data collection at the Port and in Knik Arm; (2) numerical modeling studies to simulate the tidal hydrodynamics of the Cook Inlet and Knik Arm and to estimate sedimentation at the Port resulting from the expansion; (3) physical modeling to simulate, visualize, and measure the complex flow hydrodynamics at the Port for all phase expansions; and (4) ship navigation simulations of vessels transiting Knik Arm and berthing at the new Port. The three study components were complimentary and coordinated by the Alaska District to assure information exchange and cooperation between the different solution technologies.

Overview of the Knik Arm physical models

The bathymetry of Cook Inlet and Knik Arm surrounding the Port of Anchorage was constructed out of concrete at reduced scale in two physical models. The primary model, termed the "Large-Area Model," covered a reach of Cook Inlet measuring approximately 19 statute miles, replicating the bathymetry of the Knik Arm, portions of Eagle Bay, and part of the upper Cook Inlet south of Point Woronzof. The model was geometrically distorted with a horizontal scale of 800-to-1 (prototype-to-model) and a vertical scale of 200-to-1, giving a geometric distortion (horizontal/vertical) of 4.

The complete time-varying spring tide cycle was reproduced in the Large-Area Model by a calibrated computer system that automatically controlled the water elevation in the model. During the tide cycle, the predominant headlands in the Knik Arm and the variations in the underwater bathymetry off Cairn Point produced large-scale gyres that strongly influence the hydrodynamic conditions at the Port of Anchorage.

Current measurements in the model were used to quantify changes in the tidal flow at the Port of Anchorage that would occur at each stage of the Port expansion. Comparisons between different Port configurations will be used to judge dredging requirements during and after the Port expansion. Dye injections and surface particles were used to visualize the flow patterns, and time-lapse video was recorded to enable better understanding of the complex flow regime in the Knik Arm.

The second Cook Inlet model, termed the “Small-Area Model,” reproduced bathymetry in a 6.5-mile reach of the Knik Arm, centered on the Port of Anchorage. This model had a horizontal scale of 400-to-1 and a vertical scale of 200-to-1, producing less geometric distortion. The purpose of the Small-Area Model was to serve as an alternative if satisfactory results could not be obtained from the Large-Area Model. However, the Large-Area Model produced excellent results, so it was not necessary to activate and calibrate the Small-Area Model.

Physical model objectives and study tasks

The primary objectives of the Knik Arm and Port of Anchorage Physical Model Study were the following:

1. Examine changes to the hydrodynamic flow regime likely to occur after each phase of the planned Port of Anchorage expansion, and quantify differences between the existing Port and the final Port expansion.
2. Assess project impacts to Corps of Engineers navigation, dredging, and port maintenance operations.
3. Provide measurements for improving advanced numerical models of the complex flow and sediment transport regime in the Knik Arm.

The required tasks to achieve the above objectives included: (a) designing the physical model to represent the major physical processes correctly; (b) constructing the physical model with sufficient accuracy to minimize boundary-induced errors; (c) calibrating the tide producing methodology

to reproduce repetitive spring tide cycles; (d) validating the model by reasonable reproduction of field-measured tidal velocities near the Port; and (e) acquiring velocity measurements throughout the tide cycle at numerous locations for all phases of the Port expansion.

Engineers from Alaska's District participated in all phases of the study, particularly the validation and measurements phases. Alaska District understanding of the Knik Arm flow patterns and the Port dredging activities was a crucial contribution to the physical model study and to the decisions that were made regarding the testing program. This active interest, participation, and exchange resulted in a well-considered and meaningful set of model results.

Report organization and content

This report focuses on design and construction of the small-scale tidal physical models of Knik Arm, model calibration and operation, and description and analysis of results. The chapters of this report are organized in chronological order from the initial design of the model through the interpretation of the final results.

Chapter 2 overviews the principles of physical modeling, points out the advantages and disadvantages of the technology, and discusses known scale and laboratory effects and how these two effects might influence model results. Chapter 3 covers design and construction of the Knik Arm - Port of Anchorage physical models in the context of physical facilities available at CHL. Chapter 4 details the experiment setup, instrumentation, tide generation methodology, model operation procedures, data collection, and initial data analyses. Chapter 5 describes the physical model calibration procedure and presents model verification results compared to field measurements acquired near the Port of Anchorage. Chapter 6 overviews the entire testing program, documents measurement locations, and presents results from all the tests conducted in this study. Comparisons are shown that indicate expected changes resulting from each phase of Port expansion. Finally, Chapter 7 presents the summary and conclusions from this study. Appendices A, B, and C contain plots of velocity at selected measurement locations and velocity comparisons for different phases of the Port expansion.

Units of measure

Some dimensional parameters and values cited in this report are given in non-SI units of measurement. Conversion to equivalent SI units can be made using the conversion factors listed on page xiii of this report.

Usually, the values of measured model parameters have been scaled to equivalent prototype values so the reader can better understand the model response. However, there are instances where values are reported in model units without specifically stating whether these are model units. In these cases, the context and/or parameter magnitude will usually reveal whether the value is in model dimensions or equivalent prototype dimensions.

2 Principles of Physical Modeling

This chapter provides a very brief overview of the principles that govern the design and operation of small-scale physical models of free-surface flow phenomena. The purpose of this chapter is to provide readers with a basic understanding of physical model technology. Included is a discussion of the advantages and disadvantages of physical models, along with a description of how the modeling technology can be best applied to investigate complex flow patterns in the Knik Arm and at the Port of Anchorage.

Principles of similitude

The basis of all physical modeling is the idea that the model behaves in a manner similar to the prototype (real world) it is intended to emulate. Thus, a properly validated physical model can be used to predict the prototype under a specified set of conditions. However, there is a possibility that physical model results may not be indicative of prototype behavior due to scale effects or laboratory effects. The role of the physical model engineer is to minimize scale effects by understanding and applying proper similitude relationships and to minimize laboratory effects through careful model operation.

Similarity between the real world (*prototype*) and a small-scale replica (*model*) of a coastal project area is achieved when all major factors influencing reactions are in proportion between prototype and model, while those factors that are not in proportion throughout the modeled domain are so small as to be insignificant to the process. For models of free-surface flow, three general conditions must be met to achieve model similitude:

1. **Geometric similarity** exists between two objects or systems if the ratios of all corresponding linear dimensions are equal. This relationship is independent of motion of any kind and involves only similarity in form (Warnock 1950). Geometrically similar models are also known as *geometrically undistorted models*, because the horizontal and vertical length scales are the same. Departure from geometric similarity is permissible where the free surface flow is restricted to hydrodynamics of long waves and unidirectional flows. The physical models of the Knik Arm were geometrically DISTORTED models.

2. **Kinematic similarity** indicates a similarity of motion between particles in the model and prototype. Kinematic similarity is achieved when the ratio between the components of all vectorial motions for the prototype and model is the same for all particles at all times (Hudson et al. 1979). In a geometrically similar model, kinematic similarity gives particles paths that are geometrically similar to the prototype. Kinematic similarity assures the flow velocities and directions associated with tidal flows and large-scale gyres are correctly replicated in the physical model.
3. **Dynamic similarity** between two geometrically and kinematically similar systems requires that the ratios of all vectorial forces in the two systems be the same (Warnock 1950). This means that there must be constant prototype-to-model ratios of all masses and forces acting on the system. The requirement for dynamic similarity arises from Newton's second law that equates the vector sum of the external forces acting on an element to the element's mass reaction to those forces.

Geometrically distorted models

In the context of free-surface hydrodynamic physical models, a “*geometrically distorted*” model is a physical model having a vertical length scale that differs from the horizontal length scale. Geometric distortion, in general, invalidates the necessary scaling criteria; but under very specific conditions, the impact of geometric distortion is minimized to the point that model results can be reliably scaled to prototype dimensions. Specifically, geometrically distorted models can be used in situations where the vertical components of flow velocities and accelerations are very small in comparison to the horizontal components (Hughes 1993). This implies that water pressure is hydrostatic throughout the inviscid flow region. Flow conditions that meet this specific criterion include “*long-wave models*” (tidal flows) and unidirectional flow models. However, there are certain restrictions that must be observed.

The main advantage of geometrically distorted physical models is the flexibility in choosing the horizontal scale so that large horizontal areas can be modeled in existing model facilities. Without geometrical distortion, model water depths may be very small, and model results could be severely affected by surface tension effects and bottom friction. Distorted models allow greater water depths, require less horizontal area, exhibit less frictional losses, and facilitate more accurate vertical measurements (water surface elevations).

The main drawback to using geometrically distorted models is the inability to simulate short waves (wind waves) in addition to long waves. Also, boundary slopes are steeper in distorted models so model engineers must consider how this might influence the particular flow situation being modeled.

In geometrically **undistorted** models, macro-scale features of turbulence are in similitude with the prototype, so overall characteristics of hydrodynamic processes like breaking waves, hydraulic jumps, and regions of flow separation are faithfully reproduced by the model. Conversely, in geometrically **distorted** models, turbulent processes are not in strict theoretical similitude. For most distorted physical models, this is generally not a problem either because the modeled flow situation does not have significant large-scale turbulence, or because the turbulent processes that do occur have little impact on the flow features being simulated. However, if flow patterns in the main region of interest are strongly influenced by turbulence, a *scale effect*¹ will be present in a distorted model. The Knik Arm physical models were geometrically distorted, and large-scale turbulent gyres and eddies are prominent flow features, so the scale effect related to turbulence in geometrically distorted physical flow models must be examined. This is done in the following section.

Hydraulic similitude in geometrically distorted physical models

Perfect similitude requires that the prototype-to-model ratios of the inertial, gravitational, viscous, surface tension, elastic, and pressure forces be identical. In practice, perfect similitude is impossible at reduced model scale. Fortunately, many coastal problems and flow regimes are adequately modeled by an imperfect similitude where inertia and gravity forces dominate while all other forces are small in comparison. This is the case for free-surface tidal flows.

For convenience, physical modeling similitude requirements are expressed in terms of *scale ratios*, defined as the ratio of a parameter in the prototype to the value of the same parameter in the model. The scale ratio is represented by the notation

¹ Scale effects are differences between the prototype and model response that arise from the inability to simulate all relevant forces in the model at the proper scale dictated by the scaling criteria.

$$N_x = \frac{X_p}{X_m} = \frac{\text{value of } X \text{ in prototype}}{\text{value of } X \text{ in model}} \quad (1)$$

where N_x is the prototype-to-model scale ratio of the parameter X . For example, the horizontal length scale is usually denoted as N_x ; the vertical length scale is N_z ; and the velocity scale is N_v .

Hydraulic similitude requirements for coastal hydrodynamic long-wave and tidal models can be derived (e.g., Hughes 1993) from the continuity and Navier-Stokes equations governing incompressible free-surface flows. The resulting similitude conditions are listed below. In Equations 2–4, the expressions on the left side give the similitude criteria, which are also given in terms of scale ratios on the right side (Hughes 2003).

1. The model may be geometrically distorted, i.e., horizontal and vertical length scales are different provided (a) the vertical pressure distribution is well approximated as hydrostatic, and (b) the vertical velocities and accelerations are small compared to the horizontal velocities and accelerations.
2. The Froude number (ratio of inertia force to gravity force) based on representative horizontal velocity and vertical length must be the same in the model as in the prototype, i.e.,

$$\left(\frac{V}{\sqrt{gZ}} \right)_p = \left(\frac{V}{\sqrt{gZ}} \right)_m \quad \text{or} \quad \frac{N_v}{\sqrt{N_g N_z}} = 1 \quad (2)$$

3. The Strouhal number (ratio of temporal to convective inertial forces) based on representative horizontal velocity and length must be the same in the model as in the prototype, i.e.,

$$\left(\frac{X}{V \cdot t} \right)_p = \left(\frac{X}{V \cdot t} \right)_m \quad \text{or} \quad \frac{N_x}{N_v N_t} = 1 \quad (3)$$

4. The Reynolds number, which is the ratio of inertia to viscous forces, must be the same in the model as in the prototype, i.e.,

$$\left(\frac{\rho X V}{\mu} \right)_p = \left(\frac{\rho X V}{\mu} \right)_m \quad \text{or} \quad \frac{N_p N_x N_v}{N_\mu} = 1 \quad (4)$$

where:

- V = characteristic velocity
- g = gravitational acceleration
- Z = characteristic vertical length
- X = characteristic horizontal length
- t = time
- ρ = fluid density
- μ = fluid dynamic viscosity.

and the subscripts p and m represent *prototype* and *model*, respectively.

The geometric similarity criterion (condition 1) coupled with the Froude Criterion (condition 2) assure that all terms in the governing long-wave flow equations are in similitude with the exception of the viscous and turbulence terms.

Viscous effects can only be modeled if the Reynolds Criterion (condition 3) is met along with the Froude criterion in a geometrically similar model. In general, this is practical only at prototype scale (full-size scale). Consequently, tidally-driven long-wave models with geometric distortion cannot truly simulate viscous shear stresses. At the slower flow speeds in the physical model, laminar boundary layers are more likely to occur at locations where turbulent boundary layers occur in the prototype. This situation is alleviated by adding artificial roughness elements in the model to assure fully rough boundary layers in the model. The resulting turbulent boundary layers will not be in exact similitude, but they will be more similar than laminar boundary layers.

The hydrodynamic time scale for Froude-scaled hydrodynamic models is obtained by solving Equation 2 for N_V and substituting into Equation 3 and then rearranging to give

$$N_t = \frac{N_X}{N_g N_Z} \quad (5)$$

Because the gravitational force will be the same in the model as in the prototype, the ratio N_g will be unity, and it is usually not included in the scaling criteria. Other scale ratios derived from Froude and Reynolds scaling are given in most similitude texts (e.g., Hughes 1993). Scale ratios

of particular interest for the Knik Arm physical model include the velocity scale

$$N_V = \sqrt{N_g N_Z} \quad (6)$$

the horizontal area scale

$$N_{AX} = N_X^2 \quad (7)$$

the cross-section area scale

$$N_{AZ} = N_X N_Z \quad (8)$$

and the volumetric discharge scale

$$N_Q = N_V N_{AZ} = (N_g)^{1/2} N_X (N_Z)^{3/2} \quad (9)$$

Physical model advantages

Small-scale physical models are essentially analog computers of all the physical processes being simulated with the model. Nonlinearities and complex physical interactions between fluid and solid boundaries are faithfully reproduced without compromise provided the model has been scaled correctly and laboratory effects are controlled. For this reason, small-scale physical models offer an opportunity to examine those processes that are beyond our theoretical understanding or are too complicated to represent adequately with simplified analytical or numerical modeling tools. The following is a list of advantages associated with physical models (Hughes 1993).

- a. Physical models incorporate and integrate the fully nonlinear governing equations of the modeled process without simplifying assumptions.
- b. Complex boundaries and bathymetry can be included without difficulty.
- c. The small size of the model permits easy data collection.
- d. Model forcing conditions can be easily simulated and controlled.
- e. Similitude requirements for many problems are well understood and easily implemented.
- f. Visual feedback from a physical model often reveals aspects of the physical process that had not been considered previously. Observations also help us

- to understand the differences that arise from changing the forcing conditions, and they often stimulate new ideas or alternative solutions.
- g. Engineering solutions can be optimized in a physical model to achieve project functionality at minimum expense.
 - h. Often, physical models are a cost-effective option relative to alternate study methods.

The benefits arising from physical model studies depend largely on the careful operation of the model coupled with a full understanding of the potential problems and shortcomings that may exist because of scale or laboratory effects.

Physical model disadvantages

The major disadvantages associated with small-scale physical models relate to either scale effects or laboratory effects.

Physical model laboratory effects

Laboratory effects in geometrically distorted long-wave physical models are primarily related to the following:

- a. Physical constraints on flow in the model are caused by the need of representing a portion of the prototype in a finite amount of space. Model boundaries will exist where there is no such boundary in the prototype. At the model boundaries flow must be introduced or removed as the tidal cycle is simulated. This assumes that the flow rates at these locations in the prototype are known, and that an adequate means is available to regulate the boundary flows.
- b. Ideally, mechanical generation of tidal currents at the boundary would recreate not only the time variation of total discharge at that boundary, but also simulate the cross-channel discharge distribution (that might vary in time). This is a most difficult task, and even the most careful model engineer will probably not be able to achieve the ideal. However, if the model inflow boundary is far enough upstream of the main area of interest, and the total discharge is accurate, the flow should naturally adjust to a correct cross-channel distribution downstream.
- c. Prototype forcing conditions are simplified and only a subset of all possible conditions can be selected for testing. This could mean representing the tide cycle by a sinusoidal wave, and not reproducing all aspects of the spring-neap tidal variations.

- d. Slopes in a geometrically distorted physical model are steeper than the prototype. For the mean flow condition steeper slopes do not cause any problems. Hughes and Pizzo (2003) analyzed the Navier Stokes equations in cylindrical coordinates for flow around a bend, and they concluded that all the primary convective acceleration terms maintained similitude while those convective acceleration terms not in similitude are considered inconsequential by most researchers. However, steeper slopes will impact the three-dimensional structure of large eddies and gyres.
- e. Including the discharge from a number of smaller streams and rivers feeding the Cook Inlet within the boundaries of the physical model adds complexity to model operation, and decisions were made on the relative importance of the river flow input.

Laboratory effects in physical models are analogous to problems in numerical models caused by numerical approximation to the equations, roundoff and truncation errors, and computer speed, memory, and availability (Kamphuis 1991).

Physical model scale effects

Scale effects in coastal hydrodynamic models result primarily from the Froude scaling assumption that gravity is the dominant physical force balancing the inertial forces. The other physical forces of viscosity, elasticity, and surface tension are incorrectly scaled with the belief that these forces contribute little to the physical processes. Scale effects in physical models are analogous to decreased accuracy that occurs in numerical models when complex physical processes are represented by simplified mathematical formulations (Kamphuis 1991).

In geometrically distorted long-wave models, the primary scale effect arises whenever vertical flow velocities and accelerations cannot be considered negligible compared to horizontal velocities and accelerations. For a tidally-driven model such as the Knik Arm model, this scale effect may occur if large gyres and eddies formed by flow separation at the headlands have significant three-dimensional structure. The turbulence scale effect is discussed in more detail in the following section.

In fixed-bed models, a scale effect occurs wherever flows in the model become so slow that the flow regime might transition from turbulent to laminar flow conditions, whereas such a transition would not occur in the prototype. In this case, the bottom friction is dominated by viscous forces

in the model that would not be in similitude. The solution is to try and replicate the bottom friction to scale, and then add roughness elements if necessary to help maintain a turbulent bottom boundary layer.

Turbulence scale effect in geometrically distorted physical models

Hughes and Pizzo (2003) analyzed the turbulence “Reynolds stress” terms in the Navier-Stokes equations for conservation of mass and momentum to determine potential scale effects that could arise when three-dimensional, large-scale turbulence is generated in geometrically distorted physical models. Their analysis showed that the theoretical turbulence terms formed as the product or squares of horizontal turbulent fluctuations or vertical fluctuations (5 of the 9 terms) would be in similitude in a geometrically distorted model. However, turbulence terms formed as the product of horizontal and vertical turbulent fluctuations (4 of the 9 terms) would produce a scale effect. Laboratory measurements were conducted to assess this potential scale effect.

The impact of the turbulence scale effect depends on the relative magnitudes of the turbulence in the horizontal and vertical planes. The smallest turbulence scale effect will occur in situations where the turbulence is manifested primarily in either the horizontal or vertical plane. Conversely, the maximum scale effect occurs when the turbulence strength is the same in both horizontal and vertical planes. The magnitude of the turbulence scale effect in distorted models will vary with each situation and the amount of model distortion. For some studies, the effect may be negligible so long as the major flow features are reasonably reproduced. For example, if there is a region of flow separation in the lee of a headland, we expect the distorted model to reproduce the geometry of the flow separation downstream of the headland (particularly on the surface). The maximum velocity magnitudes and directions caused by flow accelerations along the line of separation should scale reasonably correct. Within the area of reduced flow adjacent to the line of flow separation, velocity vectors may not be in similitude with the prototype, but this might not be as important so long as it is recognized that this might be an area where sedimentation could take place. Any observed vertical velocities are likely to be more pronounced in the distorted model; but on the other hand, the steeper slopes in the distorted model will produce smaller vertical velocities so this could help balance the disparity.

Hughes and Pizzo (2003) concluded:

Based on: (a) performance of the 3-D flow table model with horizontal-to-vertical distortion of 15; (b) theoretical analyses of potential scale effects; and (c) flow table experiments, it is the opinion of the report authors that turbulent scale effects in the proposed distorted physical model of Cook Inlet would not significantly influence model results. In other words, hydrodynamic flow patterns, regions of flow separation, generation of large-scale gyres, and results of sediment tracer and dye injection experiments from the distorted model would closely resemble those of an undistorted model. Differences will occur in the immediate vicinity of flow separation boundaries closer to the bottom, but these differences are expected to be localized and should not influence overall flow patterns. Three-dimensional flow structures will also have a scale effect with vertical velocity components being stronger than they should be. However, this is partially offset by the steepening of slopes in the distorted model that will decrease the vertical turbulent fluctuations. An important consideration in large distorted physical models is providing sufficient bottom and boundary roughness to assure a fully turbulent boundary layer.

Geometrically distorted physical models retain all of the nonlinearities inherent in complex flow situations, including turbulence generation. Even though known scale effects will alter the value of some turbulence terms, the overall turbulence flow field will still exhibit most of the behavior expected from an undistorted physical model. For cases where turbulence and 3-D flow patterns dominate, the distorted physical model provides more reality than depth-averaged numerical models or even 3-D numerical flow models that discard or linearize the convective accelerations and/or simplify terms related to turbulence. Consequently, where space limitations prohibit construction of an undistorted model, a geometrically distorted physical model may be the best tool for examining engineering problems related to flow turbulence and 3-D flow fields.

Other physical model disadvantages

Cost of physical model construction and operation is an important factor to consider. Construction costs increase directly with the model area, so the reduction in potential scale effects that arise from larger models will come at higher cost. Operation of a physical model requires skilled engineers and technicians, and significant time and effort is spent minimizing laboratory effects and assuring quality measurements. Also, time scales in physical models are determined by the similitude relationships so some time-dependent simulations may take a long time to complete (when compared to numerical modeling).

Even though data acquisition in a physical model is much easier than field data collection, there are inherent limitations. The number of measurement locations in the model is limited by available instrumentation and data channels. Therefore, careful consideration must be given about what to measure and where to place the instruments.

Physical model appropriateness

In many cases, a coastal problem can be examined by several different methods including numerical models, physical models, analytical techniques, statistical analyses, and desktop studies such as literature review and examination of past studies. Selecting which techniques are most suited to a particular problem requires (a) knowledge of the primary forcing and responses that shape the coastal processes in the problem area, and (b) an understanding of how well the forcing and responses are replicated by the alternative technologies. Often multiple methodologies are employed with each providing part of the answer.

Physical models are appropriate where the hydrodynamic physical processes are complex (wave nonlinearities, wave/current interactions, complex bathymetry, numerous boundaries), and where the response to the hydrodynamics is not well understood or quantified. In addition, the similitude relationships for the dominant processes must be known, and the potential scale and laboratory effects must be thought to be surmountable.

Complex flow patterns dominated by turbulent, large-scale, tidally-generated gyres and smaller-scale eddies qualifies as a complicated hydrodynamic physical process. Tidal flows sweeping past predominant

headlands and over complex bottom variations result in flow separation, regions of nearly quiescent water with little motion, regions where adjacent water is entrained into faster flows, and even detachment and down-stream propagation of rotating flow structures.

3 Physical Model Design and Construction

This chapter describes the design of the Knik Arm and Port of Anchorage physical models. Included in the chapter are descriptions of the modeling facility; the rationale for scale selection; details of design and construction of the physical model; and a summary of potential scale effects and how they might influence model results.

Dominant physical processes in the Knik Arm

Tides in the Knik Arm of Cook Inlet are semidiurnal (two high and two low tides each tidal day) with a mean range of 26.2 ft and a diurnal range (difference in height between mean higher high water [mhhw] and mean lower low water [mllw]) of 29.2 ft. The maximum water level of 34.6 ft above mllw was recorded in 1980. Because of relatively rapid uplift in Alaska, National Oceanic and Atmospheric Administration's (NOAA) tide estimates are based on 5-year records rather than the usual 19-year tidal epoch.

The physical boundaries of the upper Cook Inlet, combined with a tide range exceeding 30 ft, generate complex flow conditions in the Knik Arm. Large-scale turbulent gyres and smaller-scale eddies formed by both flood and ebb tidal flow past prominent headlands in the Knik Arm influence hydrodynamic conditions near the Port of Anchorage. These large rotating flows may have substantial variation in depth as well as in the horizontal plane, making the flow hydrodynamics fully three dimensional. The hydrodynamics, in turn, contribute to sedimentation at the Port by transporting suspended sediment and depositing it where the flow weakens.

Over a tidal cycle, large mud flats are alternately inundated and exposed, further complicating the problem of representing the hydrodynamics correctly during modeling. Proposed modifications to the Port of Anchorage will change the flow boundary and could alter the flow regime, causing a change in sediment deposition patterns and rates.

The physical models were required to capture as many aspects as possible of the three-dimensional turbulent flow in the large gyres over a relatively small region centered on the Port of Anchorage. Results from the companion numerical model study that covered a much larger area of Cook

Inlet supplied the time-varying flow boundary conditions for the physical model.

Wind generated water waves are not considered important to the hydrodynamic processes that govern flow patterns in and around the Port of Anchorage. Seasonal phenomena in the Knik Arm that were also considered less important include: (a) formation of ice during winter months that can cover the mud flats and effectively bind the sediment; (b) ice floes that hinder navigation but do not affect the flow patterns significantly; and (c) spring fresh water run-off into Cook Inlet from streams and rivers.

In summary, the main physical processes and features that need to be recreated in the fixed-bed physical models of the Knik Arm were the following:

1. Time-varying water levels associated with the spring tide.
2. Accurate bathymetry of the modeled region.
3. Accurate topography to an elevation above the spring tide maximum.
4. Tidal prism storage beyond the upstream model boundary.

Absent from the physical models were wave effects (thought to be small), wind-driven current (unknown influence), ice effects (could be substantial and should be considered in the navigation process), fresh water run-off, and other physical processes that may have some minor sway on the complex flow patterns, but are thought to be orders of magnitude less influential than the dominant tidal hydraulics.

Model scale selection

Selecting physical model scale ratios requires consideration and assessment of multiple requirements and limitations. The model must include as much of the project site area as needed to simulate the physical forcing, but this area is constrained by the size of the available space in the model facility. Those physical processes identified as being the dominant forcing in the project area must be scaled according to established similitude criteria at a scale as large as can be accommodated in the model facility to minimize potential scale effects. Existing flow pumps and controls must be able to reproduce the maximum time-varying tides to be used in testing at the selected scale. If existing equipment is insufficient in this regard, either new equipment must be sought, or the model scale must be reduced to meet the requirement. Known scale effects, laboratory effects, and other

limitations must be assessed to determine possible impacts on model results. The following sections detail the scale section processes for the physical models of Knik Arm and the Port of Anchorage.

Modeled region

The first step in designing a tidal flow physical model is determining the areal extent of the model. Consideration must be given to the problems to be addressed, the locations of interest within the modeled domain, and location of the upstream and downstream boundaries relative to the main area of interest.

The main goal of conducting the physical model study was to evaluate and quantify changes to flow patterns that are likely to occur during construction and after completion of the Port of Anchorage expansion. To achieve this goal, it was necessary to replicate the physical bathymetry and topography of Knik Arm sufficiently far upstream and downstream of the Port of Anchorage to avoid any adverse flow conditions that might occur at the model boundaries. However, if the optimum model boundary locations are too distant, the horizontal scale of the model might be reduced to the point that either scale effects become excessive, or quantifying measurements become difficult.

ERDC and Alaska District engineers were concerned that the required scale for a physical model with distant flow boundaries might be too small to acquire high-quality flow measurements. Conversely, a larger model of a smaller region would facilitate accurate flow measurement, but this model might contain errors due to having the tidal inflow and outflow boundaries too close to the area of interest.

The decision was made to reduce the risk of unsuccessful physical modeling by designing and constructing two physical models at different scales. The “Large-Area Model” replicated the bathymetry of the Knik Arm, portions of Eagle Bay, and part of the upper Cook Inlet south of Point Woronzof, as shown by the larger box in Figure 4. This model represented a length of nearly 19 statute miles. The “Small-Area Model” comprised the area shown by the smaller box in Figure 4, and it represented a region having a length of about 6.5 statute miles.

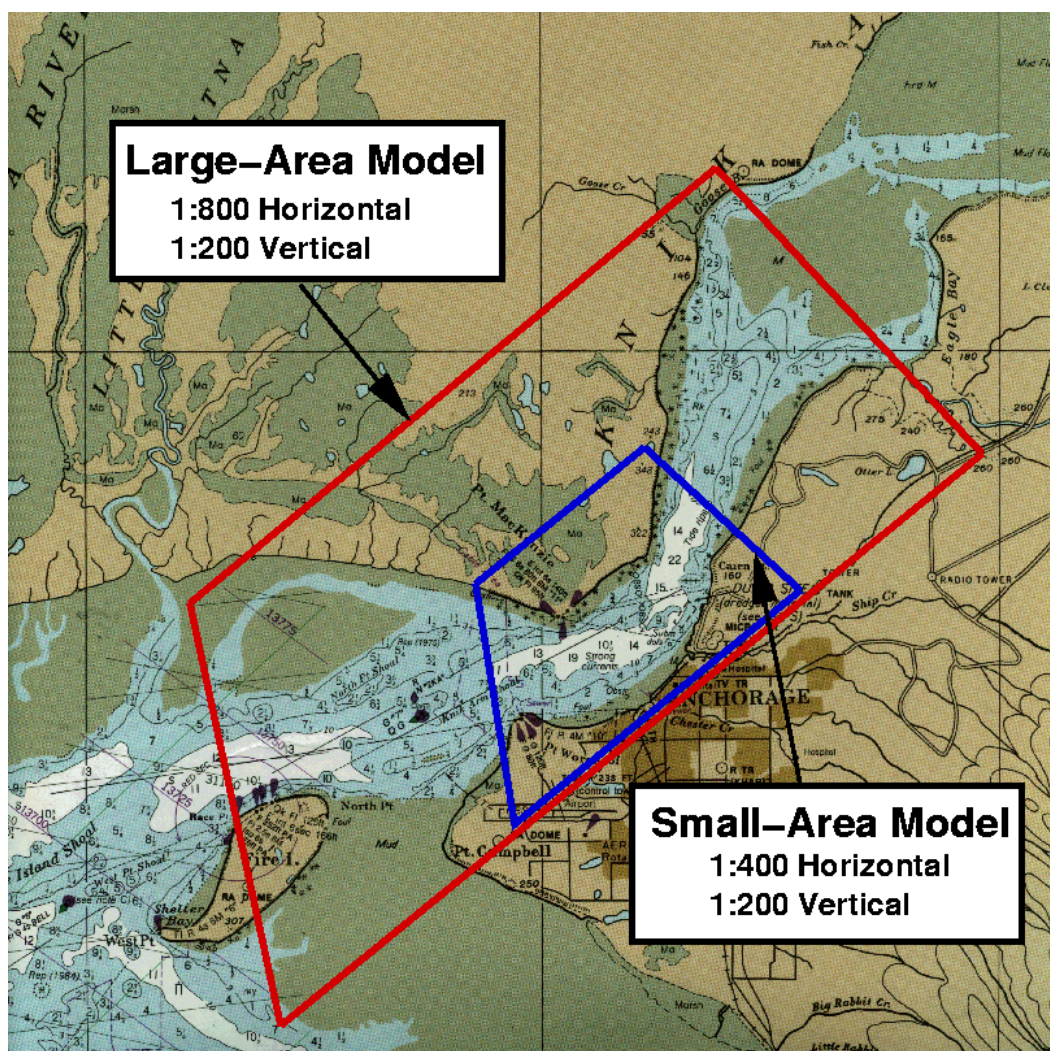


Figure 4. Areal extent of the two physical models.

The idea behind having two models was that the Large-Area model could be calibrated and tested first to make certain the flow regime was being reproduced with reasonable accuracy. If high-quality measurements of flow velocity around the Port of Anchorage could be obtained in this model, there would be no need to activate the Small-Area Model. In the event that more refinement and detail was needed in the velocity measurements around the Port, then the Small-Area Model could be calibrated and operated using measured boundary forcing conditions obtained during runs of the Large-Area Model. This would partially alleviate the problem of the flow boundaries being too close to the area of interest in the Small-Area Model.

Time varying flow input at the model boundaries will reproduce the complete tidal cycle (water elevations and corresponding currents) in the Knik Arm and at the Port of Anchorage. Therefore, it is best to position flow boundaries where flow conditions are not expected to be too complex. The upstream and downstream boundaries shown in Figure 4 were selected by examining depth-averaged velocity magnitudes and directions across several proposed boundaries. These velocity transects were generated by the sophisticated numerical tidal circulation model of Cook Inlet and Knik Arm used in the companion study. Figure 5 illustrates the numerically generated velocity vectors at the downstream boundary of the Large-Area Model near maximum flood tide. Placing the boundary at this location meant including the northern portion of Fire Island in the model. On the far right side of Figure 5 just off the northern tip of Fire Island is an entrance to the Turnagain Arm. The numerical model indicated very little tidal exchange between Turnagain Arm and Knik Arm, so the decision was made to not include the Turnagain Arm in the Large-Area Model.

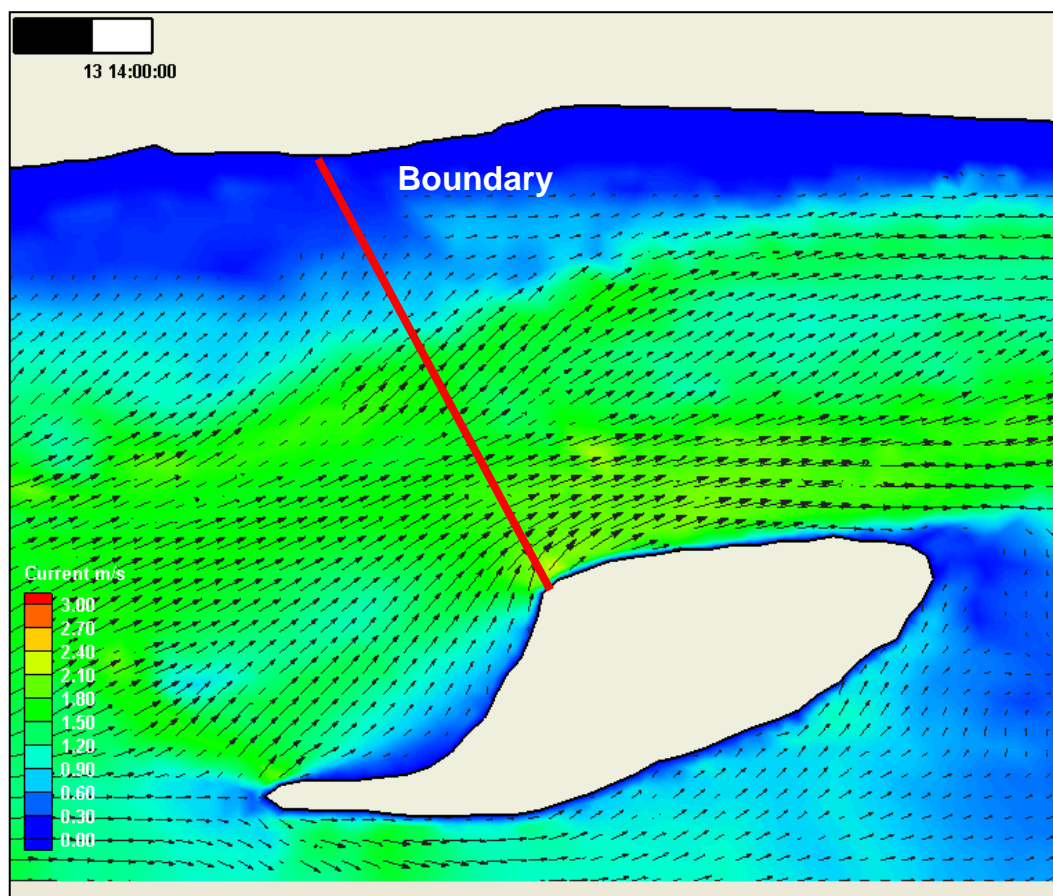


Figure 5. Downstream boundary flood flow vectors from numerical model.

A similar plot of numerically generated ebb flow velocity vectors is given in Figure 6 for the upstream boundary of the Large-Area Model. This boundary is located at about the widest portion of Eagle Bay to the north of the Port of Anchorage. The velocities represent the nearly maximum ebb flow. At both boundaries, the flow vectors remained reasonably uniform throughout the tidal cycle, making these good boundary locations.

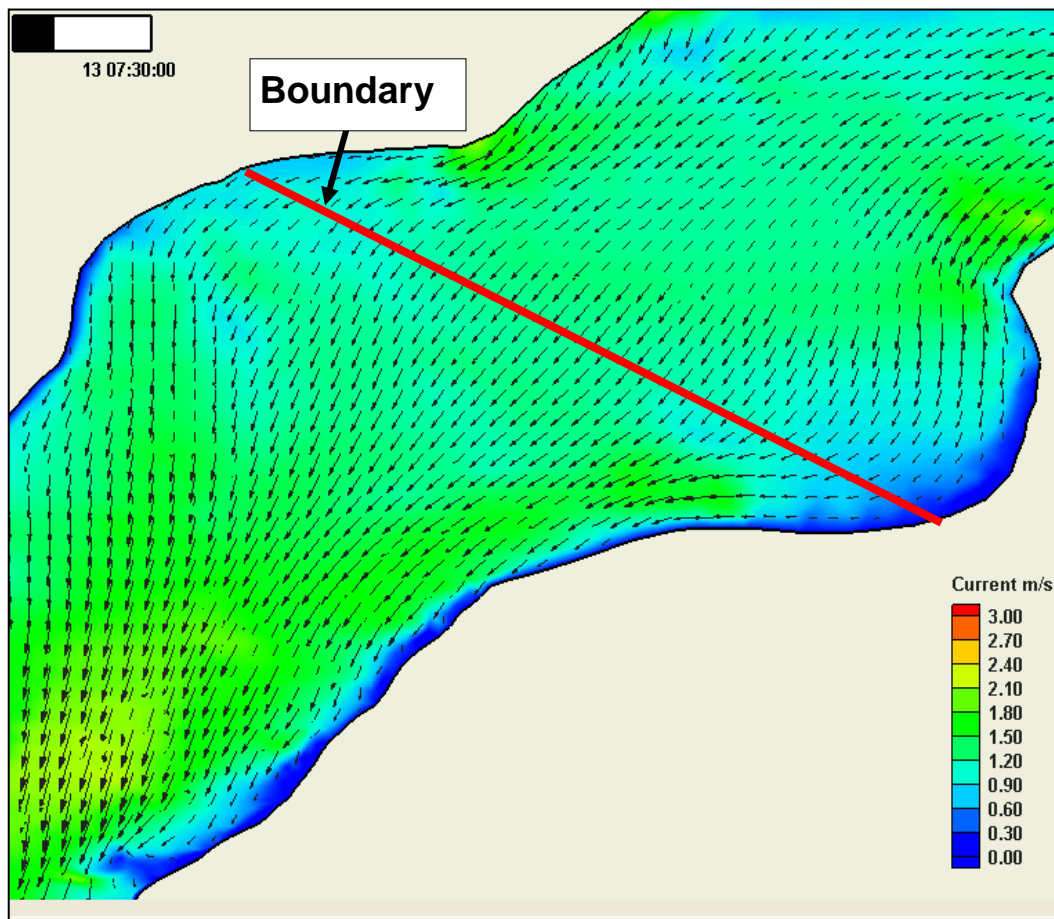


Figure 6. Upstream boundary flood flow vectors from numerical model.

Model facility

An existing modeling facility named the ESTEX flume was the best available facility at the ERDC for construction of the Knik Arm physical models. The ESTEX flume features a channel that is 60 ft wide and 420 ft long, as shown in Figure 7. The flume has substantial flow capacity, and a system of pumps, gates, and controlling software capable of producing tides was already installed. The flume length allowed construction of bathymetry for two different-scale physical models within the same facility. All other model areas considered for potential use for this study would have cost

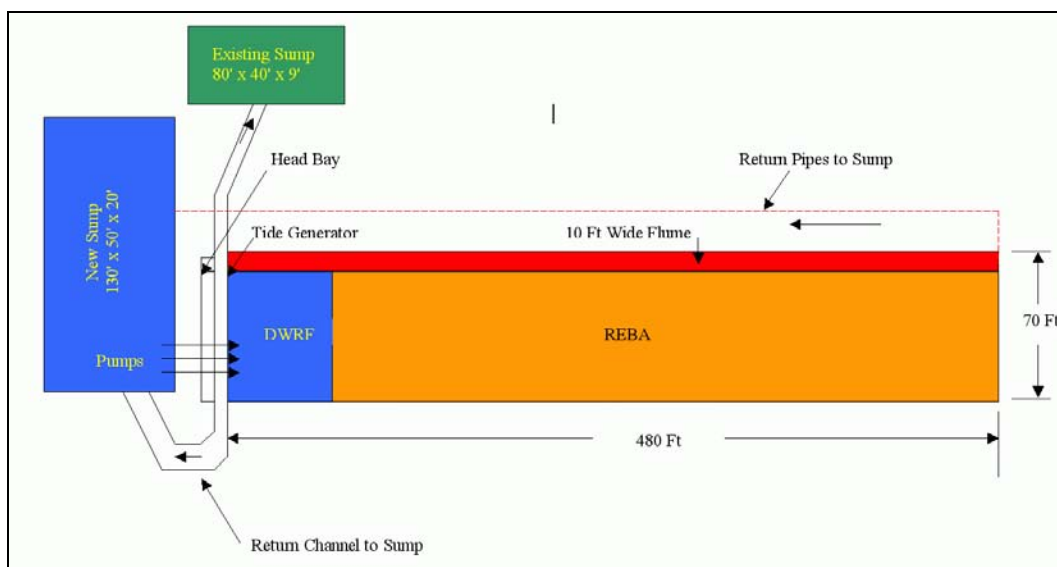


Figure 7. ESTEX flume layout and dimensions.

significantly more because of the need to install necessary systems to simulate the tidal cycle accurately. The main drawback to the ESTEX flume was the 60-ft width that constrained the horizontal length scale of the models.

Model length scales

The physical models of the Knik Arm of Cook Inlet were geometrically distorted, meaning the vertical length scale was different from the horizontal length scale. Geometric distortion is accepted practice for tidally-driven flow models, as explained in Chapter 2.

Once the ESTEX flume was identified as a suitable model facility, the next step in model design was selecting a horizontal length scale for the models. Horizontal length scale selection is a compromise between economics, the need to build the model at the largest possible size to minimize scale effects, and available space for constructing the model. The horizontal length scale was determined as the ratio needed to fit the modeled region width (see Figure 4) into the 60-ft width of the ESTEX flume. For the Large-Area Model a suitable prototype-to-model horizontal length scale was determined to be

$$N_X = \frac{X_p}{X_m} = 800 \quad (10)$$

The appropriate horizontal length scale for the Small-Area Model was established as

$$N_X = \frac{X_p}{X_m} = 400 \quad (11)$$

Both Knik Arm physical models had prototype-to-model vertical length scales of

$$N_Z = \frac{Z_p}{Z_m} = 200 \quad (12)$$

This vertical scale allowed sufficient water depth in the models to avoid surface tension scale effects over most of the modeled area. At this vertical scale, the 33-ft tide spring range at the Port of Anchorage will be 0.165 ft (2.0 in.) in the model.

Model geometric distortion is defined as the horizontal length scale divided by the vertical length scale, or

$$\Omega = \frac{N_X}{N_Z} \quad (13)$$

Therefore, the Large-Area Model distortion is 4, and the Small-Area Model distortion is 2. These distortions are within acceptable ranges.

Hydrodynamics similitude criteria

Once the horizontal and vertical length scales are selected, all other scale ratios related to geometry and hydrodynamics can be calculated. Below are the scale ratios for important model parameters determined using the formulas based on Froude similitude that are given in Chapter 2.

Large-Area Model scales

From Equation 5 the Large-Area Model time scale is given as

$$\text{Time scale: } N_t = \frac{N_X}{\sqrt{N_g N_Z}} = \frac{800}{\sqrt{(1)(200)}} = 56.6 \quad (14)$$

The velocity scale is found using Equation 6, i.e.,

$$\text{Velocity scale: } N_V = \sqrt{N_g N_Z} = \sqrt{(1)(200)} = 14.14 \quad (15)$$

The horizontal area and vertical cross-section area scales are determined using Equations 7 and 8, respectively

$$\text{Horizontal area scale: } N_{AX} = N_X^2 = (800)^2 = 640,000 \quad (16)$$

$$\text{Cross-section area scale: } N_{AZ} = N_X N_Z = (800)(200) = 160,000 \quad (17)$$

Finally, the volumetric discharge scale for the Large-Area Model is determined from Equation 9 as

$$\text{Discharge scale: } N_Q = N_V N_{AZ} = (14.14)(160,000) = 2,262,742 \quad (18)$$

Small-Area Model scales

Similarly, the scales for the Small-Area Model are derived using the same equations as above with the horizontal length scale of $N_Z = 400$ substituted. These scales are summarized below.

$$\text{Time scale: } N_t = \frac{N_X}{\sqrt{N_g N_Z}} = \frac{400}{\sqrt{(1)(200)}} = 28.3 \quad (19)$$

$$\text{Velocity scale: } N_V = \sqrt{N_g N_Z} = \sqrt{(1)(200)} = 14.14 \quad (20)$$

$$\text{Horizontal area scale: } N_{AX} = N_X^2 = (400)^2 = 160,000 \quad (21)$$

$$\text{Cross-section area scale: } N_{AZ} = N_X N_Z = (400)(200) = 80,000 \quad (22)$$

$$\text{Discharge scale: } N_Q = N_V N_{AZ} = (14.14)(80,000) = 1,131,370 \quad (23)$$

Tide generation capability

The tidal prism was calculated for the Knik Arm using an estimate of the maximum flow discharge based on field measurements. Assuming a

sinusoidal tide variation, the time-varying total discharge, $Q(t)$, can be approximated by the expression

$$Q(t) = \frac{\pi P}{T} \cos\left(\frac{2\pi t}{T}\right) \quad (24)$$

where:

P = tidal prism

T = tidal period

t = time.

The maximum discharge occurs at mid-tide ($t = 0, T/2, T, \dots$), which yields the relationship

$$Q_{\max} = \frac{\pi P}{T} \quad \text{or} \quad P = \frac{Q_{\max} T}{\pi} \quad (25)$$

Substituting Equation 25 into Equation 24 gives the time-varying total discharge in terms of the maximum total discharge, i.e.,

$$Q(t) = Q_{\max} \cos\left(\frac{2\pi t}{T}\right) \quad (26)$$

Summary of model scaling

Large-Area Model

The important model scale ratios (value in the prototype divided by the equivalent value in the model) are listed in Table 1 for the Large-Area Model. The fundamental scaling parameters are the horizontal length scale, N_x , and the vertical length scale, N_z . Also shown in the table is the model equivalence for prototype values of lengths, areas, time, velocity, and discharge.

Values of several parameters related to tidal flow and water depth were estimated to serve as guidelines for determining model construction and operation costs. Table 2 gives the prototype (full size) and model equivalent values for these parameters for the Large-Area Model.

Table 1. Large-Area Model scale ratios and prototype equivalence.

| Scale | Scale Ratio | Model Equivalence |
|----------------------------|--------------------|---|
| Horizontal length scale | $N_X = 800$ | 1 ft = 800 ft |
| Vertical length scale | $N_Z = 200$ | 1 ft = 200 ft |
| Time scale | $N_t = 56.6$ | 1 s = 56.6 s |
| Velocity scale | $N_V = 14.14$ | 1 ft/s = 14.14 ft/s |
| Horizontal area scale | $N_{AX} = 640,000$ | 1 ft ² = 14.7 acres |
| Vertical area scale | $N_{AZ} = 160,000$ | 1 in ² = 1,111 ft ² |
| Volumetric discharge scale | $N_Q = 2,262,742$ | 1 gal/s = 301,485 ft ³ /s |

Table 2. Prototype and model parameter values for Large-Area Model.

| Parameter | Prototype Value | Model Value |
|----------------------------|---|---|
| Maximum flow velocity | 10 ft/s (6 kts) | 0.71 ft/s |
| Maximum discharge | 7,170,000 ft ³ /s | 3.17 ft ³ /s (1,422 gal/min) |
| Tide cycle period | 12.42 hr | 0.22 hr (13.17 min) |
| Total tidal prism | 1.03 (10) ¹¹ ft ³ | 800 ft ³ (6,000 gal) |
| Maximum water elevation | +33 ft mllw | +0.165 ft (+2.0 in) mllw |
| Minimum water elevation | -2.0 ft mllw | -0.01 ft (-0.12 in) mllw |
| Elevation of deepest point | -170 ft mllw | -0.85 ft (-10.2 in) mllw |

Small-Area Model

Table 3 gives the important model scale ratios and model equivalence for the Small-Area Model. Velocity scale is the same for both models because it is a function of only the vertical length scale, which is the same.

Table 3. Small-Area Model scale ratios and prototype equivalence.

| Scale | Scale Ratio | Model Equivalence |
|----------------------------|--------------------|---|
| Horizontal length scale | $N_X = 400$ | 1 ft = 400 ft |
| Vertical length scale | $N_Z = 200$ | 1 ft = 200 ft |
| Time scale | $N_t = 28.3$ | 1 s = 28.3 s |
| Velocity scale | $N_V = 14.14$ | 1 ft/s = 14.14 ft/s |
| Horizontal area scale | $N_{AX} = 160,000$ | 1 ft ² = 3.7 acres |
| Vertical area scale | $N_{AZ} = 80,000$ | 1 in ² = 555 ft ² |
| Volumetric discharge scale | $N_Q = 1,131,370$ | 1 gal/s = 151,252 ft ³ /s |

Table 4 presents the Small-Area Model prototype (full size) and model equivalent values for several of the parameters related to the tide, flow, and bathymetry.

Table 4. Prototype and model parameter values for Small-Area Model.

| Parameter | Prototype Value | Model Value |
|----------------------------|---|---|
| Maximum flow velocity | 10 ft/s (6 kts) | 0.71 ft/s |
| Maximum discharge | 7,170,000 ft ³ /s | 6.34 ft ³ /s (2,846 gal/min) |
| Tide cycle period | 12.42 hr | 0.22 hr (26.33 min) |
| Total tidal prism | 1.03 (10) ¹¹ ft ³ | 3,219 ft ³ (24,080 gal) |
| Maximum water elevation | +33 ft mllw | +0.165 ft (+2.0 in) mllw |
| Minimum water elevation | -2.0 ft mllw | -0.01 ft (-0.12 in) mllw |
| Elevation of deepest point | -170 ft mllw | -0.85 ft (-10.2 in) mllw |

Potential scale and laboratory effects

Scale effects and laboratory effects were summarized in general terms in Chapter 2. An assessment of how these scale and laboratory effects might influence results obtained from the Knik Arm and Port of Anchorage physical models is given in the following paragraphs.

Scale effects

Even though the Large-Area Model was scaled to a smaller size than typical tidal flow models, the hydrodynamics were still in similitude according to the Froude criterion, so there were no appreciable scale effects related to the hydrodynamics. The current magnitudes and directions should be correctly reproduced, and the horizontal flow patterns and large gyres created by tidal flow past the various headlands should be similar to what occurs in the Knik Arm.

The major consideration for geometrically distorted physical models is the validity of the assumption that vertical components of velocities and accelerations are small compared to the horizontal components. Because the model is driven by a long-period tide signal, this assumption is reasonable for the time-averaged mean values of velocity. There will be some vertical flow components in the large-scale turbulent gyres, and there is a scale effect associated with the turbulent flow as discussed in Chapter 2.

The physical model will produce stronger vertical mixing than might be expected in the prototype. However, the main focus of the measurement program is documenting the changes in the horizontal velocities and the horizontal flow patterns in the large-scale gyres, and these aspects are expected to be reasonably reproduced in a geometrically distorted physical

model. Therefore, all the important hydrodynamic processes that occur in the Knik Arm and around the Port of Anchorage were correctly simulated in the physical model.

Because of the small scale of the two models, there was a possibility that bottom friction in the model might reduce flow velocity, particularly in portions of the model with very shallow depths or during slack water when the flow is very slow and laminar boundary layers can occur. This scale effect was alleviated somewhat by finishing the model bathymetry with a roughness representative of the correctly scaled bottom roughness assumed for the prototype. Also, the primary areas of interest are in deeper water depths where flows are sufficiently fast to avoid laminar flow conditions. The scaling of bottom roughness is given in the model design and construction section below.

The Knik Arm physical model was conducted using fresh water to simulate the slightly brackish salt water environment in the Knik Arm. This is a practical compromise to avoid corrosion of laboratory facilities and delicate instrumentation. The slight difference in water density between model and prototype has virtually no impact on hydrodynamics as proven by many studies over the past 50 years (Hughes 1993).

Laboratory effects

The primary laboratory effects in the Knik Arm physical models were related to the model boundaries and the tide simulation. As mentioned, considerable thought went into establishing the model boundaries in the Large-Area Model that were sufficiently far away from the Port of Anchorage and also had reasonably well-behaved flows across the boundary. The region in the model beyond the upstream boundary did not reproduce the rest of the Eagle Bay bathymetry, so it was necessary to manage the flow volume passing through that boundary during the entire tide cycle. Failure to do this properly would result in a distorted tide signal and incorrect flow patterns. The design of the tidal prism storage area upstream of the Large-Area Model boundary is presented in the following section.

The physical model shoreline slopes are steeper in the model because of the model geometric distortion. The main laboratory effect of the steeper shoreline in a tidal model is actually beneficial because it helps to reduce

vertical mixing in the turbulent gyres (which is greater than it should be because of model distortion).

The tide cycle in the physical model was simulated using a constant amplitude sinusoidal tide as an approximation to the actual tide in which the amplitude varies with each cycle between spring and neap tide. The sinusoidal signal was selected to best represent the amplitude and period of the maximum spring tide cycle.

Model design

Model layout

Both models were positioned and constructed in the ESTEX flume as illustrated in Figure 8. Water enters and exits the flume at the north end (left side of sketch in Figure 8). The models could not both be operated at the same time because of the differing discharge and time scales. The Large-Area model required a smaller tidal prism volume, so it was located at the far end (right side of sketch) of the flume.

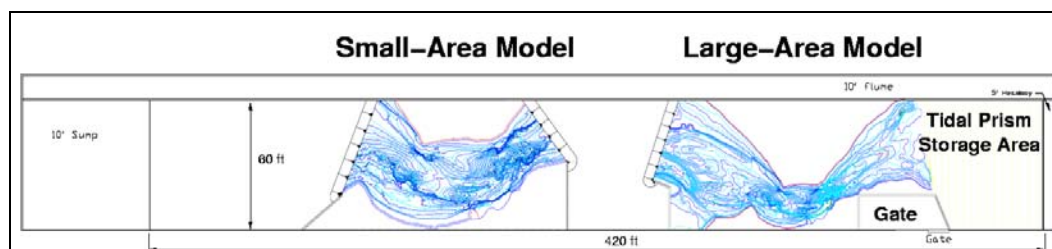


Figure 8. Layout of both models in the ESTEX flume.

The Small-Area Model had an area of 5,930 ft² molded in concrete. This corresponded to an area of approximately 34 mi² in the prototype. The modeled bathymetry portion of the Large-Area Model was 5,450 ft² representing an area of 125 mi² in the prototype. The area of the Large-Area Model tidal prism storage surface was 2,288 ft².

While the Large-Area Model was operated, water flowed through the Small-Area Model during flood tide to reach the downstream boundary of the Large-Area Model. Water flowing past the upstream boundary of the Large-Area Model was contained in the tidal prism storage area shown to the far right side of the Figure 8 sketch. The design of the tidal prism storage area is given below.

The Small-Area Model was positioned as shown in Figure 8 so there was more area that could serve as storage for the larger tidal prism associated with this model. Water flowing past the upstream boundary of the Small-Area Model would pass into the Large-Area Model as necessary.

Ideally, the Small-Area Model would not have been constructed until it was determined that the model was needed to better resolve velocities and flow patterns at the Port and in the Knik Arm. Unfortunately, the flume gate (lower right side of Figure 8 sketch) provided the only flume access for equipment, and it would be impossible to construct the Small-Area Model if the Large-Area Model had already been constructed. Equipment transporting concrete would have severely damaged any constructed bathymetry if it had to traverse the Large-Area Model. Consequently, the decision was made to construct the Small-Area Model first, even though there was a possibility the model would never be used in the study. This strategy is similar having a spare tire in your car. If you need it, you are glad you have it along.

Large-Area Model upstream tidal prism storage surface

The Large-Area and Small-Area physical models of the Knik Arm reach of Cook Inlet have upstream boundaries beyond which the actual bathymetry is not reproduced. To simulate tidal flow correctly, it was necessary to provide an upstream storage surface to contain the flood tide volume that passed the upstream boundary. Furthermore, the water head in this storage volume was the sole driving force for the ebb portion of the tide cycle. So, an additional requirement was that the shape of the storage surface must be such that the cumulative tidal prism volume must have the correct water surface elevation throughout the flood tide. The following analysis was performed only for the Large-Area Model. If it had been necessary to activate the Small-Area Model, an alternative means for storing and releasing the stored tidal prism would have been required for that model.

Eagle Bay boundary

Numerical model simulations from the companion study using the model ADCIRC were conducted over several maximum spring tide cycles, and the cumulative total flood flow volume passing through the upstream boundary selected for the physical model was determined as a function of tidal elevation at the boundary. The resulting numerical calculations are

summarized by the data points on Figure 9. The data points (originally provided in prototype-scale units at 0.5-m water elevation intervals) have been scaled to model scale units for the Large-Area Model using a horizontal length scale of $N_X = 800$ and a vertical length scale of $N_Z = 200$. This plot represents the flux of water volume across the upstream Eagle Bay physical model boundary while the tide was in the flood stage.

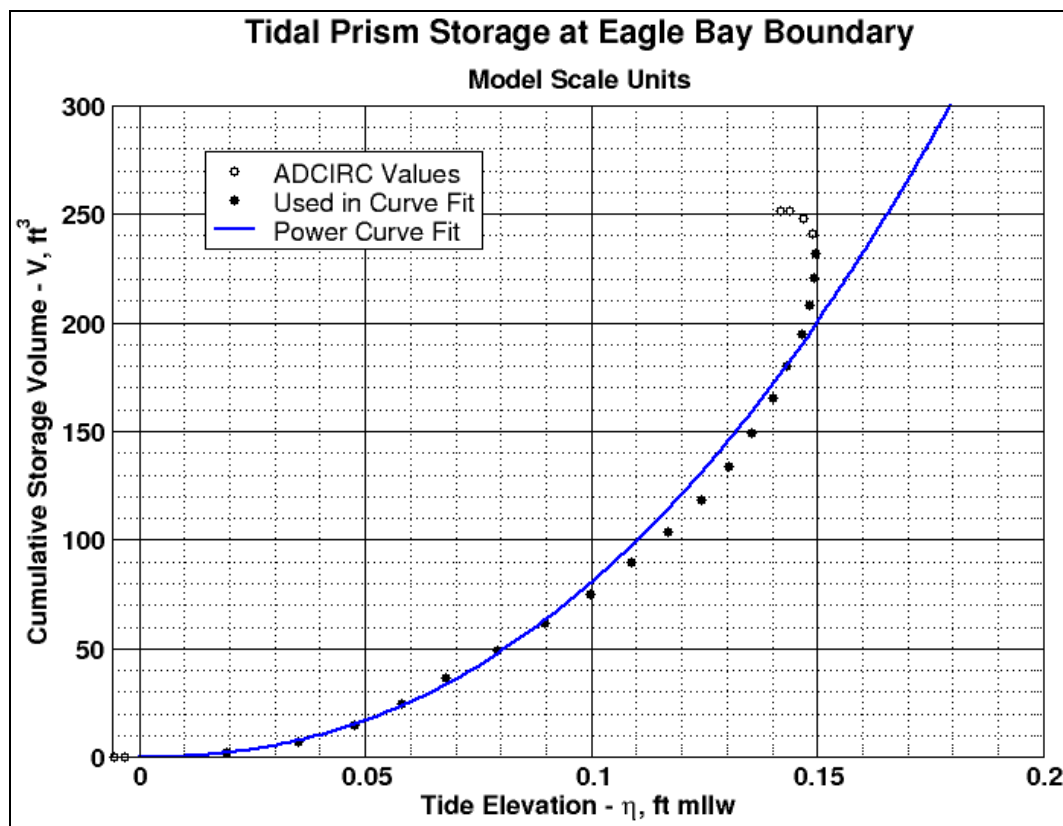


Figure 9. Cumulative storage volume vs. tide elevation at Eagle Bay boundary.

Notice that the cumulative storage volume continues to rise after the highest water elevation is reached. This is thought to be continuing water flux across the boundary as the surface elevation begins to fall. This behavior has been observed in the field. Currents change to ebb first over the shallower mudflats, while the deeper portions of the cross-section are still flooding. Similar behavior was observed in the physical model.

As a first step toward designing an appropriate bathymetry that will replicate the volume versus tide elevation shown by the data points in Figure 9, several different mathematical curves were fitted to the data points. The four unshaded data points in the plot at the maximum storage volume

were not used in the curve fits. A simple power curve, shown by the solid line in Figure 9, and given by the expression

$$V(\eta) = 14,463 \eta^{2.26} \quad (27)$$

provided one of the best curve fits with a correlation coefficient of 0.998.

Storage bathymetry cross section

It was assumed that a satisfactory tidal prism storage bathymetry could be constructed as a geometric volume having cross-flume width, B , and a constant cross-sectional area specified by a two-parameter power curve of the form

$$\eta = ax^m \quad (28)$$

as illustrated in Figure 10.

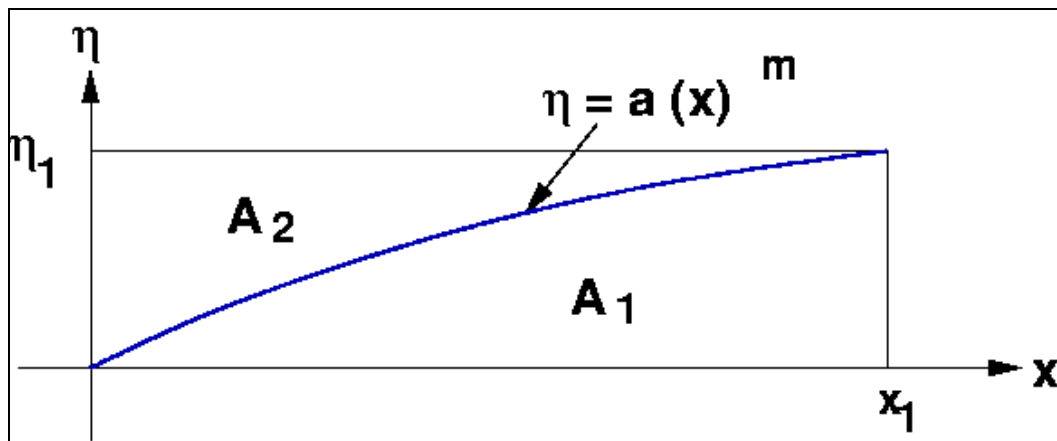


Figure 10. Cross section of prism storage bathymetry.

The area designated as A_2 is the tidal prism storage area at elevation η_1 , and the volume is simply

$$V(\eta_1) = A_2(\eta_1) \cdot B \quad (29)$$

To find an expression for the area A_2 , first determine area A_1 by integrating the power curve given by Equation 28, i.e.,

$$A_1(x_1) = \int_0^{x_1} ax^m dx = \frac{a}{(m+1)} (x_1)^{m+1} \quad (30)$$

The area A_2 is then

$$\begin{aligned}
 A_2(x_1, \eta_1) &= x_1 \eta_1 - \frac{a}{(m+1)} (x_1)^{m+1} \\
 A_2(x_1, \eta_1) &= x_1 \left(\frac{m}{m+1} \right)
 \end{aligned} \tag{31}$$

where Equation 28 was used to make the substitution $\eta_1 = a (x_1)^m$. (As a check, note that area $A_2 = (x_1 \eta_1)/2$ when $m=1$.)

The final step is to determine area A_2 as a function of only η_1 . Solving Equation 28 for x_1 , i.e.,

$$x_1 = \left(\frac{\eta_1}{a} \right)^{1/m} \tag{32}$$

and substituting into Equation 31 yields

$$\begin{aligned}
 A_2(\eta_1) &= \left(\frac{\eta_1}{a} \right)^{1/m} \eta_1 \left(\frac{m}{m+1} \right) \\
 &= \left(\frac{m}{m+1} \right) \left(\frac{1}{a} \right)^{1/m} \eta_1^{\left(\frac{m+1}{m} \right)}
 \end{aligned} \tag{33}$$

The correctness of the derivation can be shown by differentiating A_2 with respect to η_1 to recover the original power curve representing the bathymetry, i.e.,

$$\begin{aligned}
 x_1 &= \frac{d}{d\eta_1} [A_2(\eta_1)] = \left(\frac{m}{m+1} \right) \left(\frac{1}{a} \right)^{1/m} \frac{d}{d\eta_1} \left[\eta_1^{\left(\frac{m+1}{m} \right)} \right] \\
 &= \left(\frac{m}{m+1} \right) \left(\frac{1}{a} \right)^{1/m} \left(\frac{m+1}{m} \right) \eta_1^{1/m} \\
 x_1 &= \left(\frac{\eta_1}{a} \right)^{1/m}
 \end{aligned} \tag{34}$$

which is the same as Equation 32 (rearranged version of Equation 28).

From Equation 29 the cumulative prism storage at any tide elevation η is now given as

$$V(\eta) = B \cdot \left(\frac{m}{m+1} \right) \left(\frac{1}{a} \right)^{1/m} \eta^{\left(\frac{m+1}{m} \right)} \quad (35)$$

(Note that the subscript on η has been dropped.) This is a most fortuitous result because Equation 35 is a power curve having the same form as the curve fit to the data points given by Equation 27!

Determination of bathymetry cross-section parameters

Comparing Equations 27 and 35, we first equate the exponents of the two equations to get

$$2.26 = \left(\frac{m+1}{m} \right) \quad \text{or} \quad m = 0.794 \quad (36)$$

Little accuracy is lost by rounding the exponent up to $m = 0.8$.

Next, equate the coefficients of Equations 27 and 35 and substitute in the value of $m = 0.8$, i.e.,

$$14,463 = B \cdot \left(\frac{0.8}{0.8+1} \right) \left(\frac{1}{a} \right)^{1/0.8} = B \cdot \left(\frac{0.8}{1.8} \right) \left(\frac{1}{a} \right)^{1.25} \quad (37)$$

With the tidal prism storage bathymetry cross section extending for the entire width of the ESTEX flume, $B = 60$ ft (units must be in feet). Making this substitution into Equation 37 and solving for the parameter a yields

$$\begin{aligned} \frac{14,463}{60} \left(\frac{1.8}{0.8} \right) &= \left(\frac{1}{a} \right)^{1.25} \\ \left(\frac{1}{a} \right) &= (542.36)^{0.8} = 153.97 \\ a &= 0.0065 \end{aligned} \quad (38)$$

Therefore, the final bathymetry cross-section equation for the tidal prism storage volume associated with the Large-Area Model is given by

$$\eta = 0.0065 x^{0.8} \quad (39)$$

over the entire flume width of 60 ft. The overall length of the cross section is found by substituting the maximum tide elevation of $\eta = 0.15$ ft into Equation 39 and solving for x , i.e.,

$$\begin{aligned} 0.15 &= 0.0065 (x_{\max})^{0.8} \\ x_{\max} &= \left(\frac{0.15}{0.0065} \right)^{1/0.8} \\ x_{\max} &= 50.58 \text{ ft} \end{aligned} \quad (40)$$

This calculated tidal prism storage surface was added to the Large-Area Model at the upstream boundary in Eagle Bay.

Bottom friction

The initial adjustment to replicate the bottom friction of the Knik Arm in the physical models was to determine an appropriate concrete finish roughness that gave the properly scaled value of Manning's n . If calibration and verification testing indicated that this initial adjustment was insufficient, there was the option of adding additional roughness elements on the bathymetry to promote fully turbulent boundary layers in certain portions of the model.

Hudson et al. (1979) derived scaling relationships for bottom friction in geometrically distorted estuarine models. They started with the Chezy equation (a version of the momentum equation for quasi-steady flow) given by

$$v = C_Z (R \cdot S_f)^{1/2} \quad (41)$$

where:

- v = velocity
- C_Z = Chezy friction coefficient
- R = hydraulic radius
- S_f = friction slope.

Hudson et al. assumed the Chezy equation needed to be the same in the model as in the prototype. This resulted in the following similitude relationship

$$N_v = N_{CZ} N_R^{1/2} N_{Sf}^{1/2} \quad (42)$$

Substituting Equation 6 for the velocity scale into Equation 42, and noting for wide channels that the hydraulic radius scale is simply the vertical length scale and the friction slope scale is vertical length scale over horizontal length scale yields

$$N_Z^{1/2} = N_{CZ} N_Z^{1/2} \left(\frac{N_Z}{N_X} \right)^{1/2} \quad \text{or} \quad N_{CZ} = \left(\frac{N_X}{N_Z} \right)^{1/2} \quad (43)$$

The Chezy coefficient can be expressed in terms of Manning's n by the equation (Henderson 1966)

$$C_Z = \frac{R^{1/6}}{n} \quad (44)$$

which produces the corresponding scale relationship of

$$N_{CZ} = \frac{N_R^{1/6}}{N_n} = \frac{N_Z^{1/6}}{N_n} \quad (45)$$

Equating Equations 43 and 45 and rearranging provides the appropriate scaling relationship for Manning's n , i.e.,

$$N_n = \frac{N_Z^{2/3}}{N_X^{1/2}} \quad (46)$$

The Knik Arm has bottom roughness varying from smooth mudflats to gravel and small boulders in the fast-flowing deeper portions of the channel. Where the flow is rapid, bottom friction will have less effect, but the slower flows over the mudflats would be influenced more by bottom friction. Henderson (1966) lists the following typical values of Manning's n for relatively smooth channels without vegetation: Smooth earth with no weeds $n = 0.02$; clean and straight natural channel $n = 0.025 - 0.030$. For model design, the lower value was targeted because additional roughness

could be added later if needed, but roughness is difficult to remove once it is installed in the model.

Manning's n for Large-Area Model

Substituting the Large-Area Model horizontal and vertical length scales in Equation 46 yields

$$\frac{n_p}{n_m} = N_n = \frac{N_Z^{2/3}}{N_X^{1/2}} = \frac{(200)^{2/3}}{(800)^{1/2}} = 1.21 \quad \text{or} \quad n_m = \frac{n_p}{1.21} \quad (47)$$

For a prototype-scale Manning's $n_p = 0.02$, the required model Manning's $n_m = 0.017$. This model value was reasonably well simulated by brush-finished concrete that has a Manning's n of about 0.014 (Henderson 1966).

Manning's n for Small-Area Model

Substituting the Small-Area Model horizontal and vertical length scales in Equation 46 yields

$$\frac{n_p}{n_m} = N_n = \frac{N_Z^{2/3}}{N_X^{1/2}} = \frac{(200)^{2/3}}{(400)^{1/2}} = 1.71 \quad \text{or} \quad n_m = \frac{n_p}{1.71} \quad (48)$$

For a prototype-scale Manning's $n_p = 0.02$, the required model Manning's $n_m = 0.012$. This model value was almost exactly simulated by smooth trowel-finished concrete that has a Manning's n of about 0.012 (Henderson 1966).

Model construction

Bathymetry

Once the region to be modeled was scaled to fit within the available space, plan view drawings were prepared and correspondence between prototype and model coordinate systems was established. This was followed by construction of the fixed-bed bathymetry and topography.

The procedure for constructing fixed-bed models is to begin with a flat, horizontal floor, place compacted sand on the floor up to about 2 in. from the required elevation, then fill in the remaining elevation with mortar that sets into a hard surface. The construction technique is guided by tem-

plates that are normally spaced throughout the model at approximately 4-ft spacing. However, the Knik Arm model bathymetry was sufficiently complex that this spacing between templates had to be reduced in many places to capture the details.

Prototype-scale bathymetry and topography for the fixed-bed portion of the models between elevations +35 ft and -170 ft mllw were scaled to model dimensions and contoured on a plan view drawing in AutoCAD software. Template lines were selected based on the contours. When possible, the template lines were kept parallel and evenly spaced; but in some locations variation was needed to assure accurate molding of the bathymetry. Experience by the model designer helped establish a useful set of templates. The software produced profiles for each template along with the information necessary to position the template spatially in the model. Full-sized drawings of the templates were produced, and the model shop at ERDC cut the templates out of medium gauge sheet metal.

Fixed-bed bathymetry construction of the Small-Area Model started at the northern end of the ESTEX flume (left side of Figure 8) at the downstream flow boundary. Construction proceeded through to completion of the upstream boundary. Each template was positioned, and the elevation was precisely adjusted. After several templates had been placed, the space between adjacent templates was filled with construction-grade sand that was then wetted and compacted. Finally, ready-mixed concrete mortar was placed, and the surface was floated to a smooth finish level with the top of the templates. It was also necessary to hand-finish the bathymetry to capture local variations between templates that had been noted on the drawings. This was especially the case for the bathymetry through the narrowest part of Knik Arm and in the vicinity of Cairn Point.

Next, the Large-Area Model bathymetry was constructed starting at the downstream boundary at Fire Island and proceeding upstream through the Port of Anchorage area and halfway into Eagle Bay. Lastly, the tidal prism storage area was constructed beyond the upstream boundary, as shown in Figure 8.

The construction technique is illustrated by the photographs in Figures 11-15. Figure 11 shows a freshly poured section of the Small-Area Model. In the summer time, the heat in the flume shelter was so intense that sometimes only one section could be poured in a day because of time needed to

hand mold the detailed bathymetry before the concrete set up. Figures 12, 13, and 14 show the hand molding technique needed for complex sections.



Figure 11. Newly cast section of the Small-Area Model upstream of the Port of Anchorage.



Figure 12. Bathymetry contours sketched on the Small-Area Model.



Figure 13. Hand molding bathymetry detail on the Small-Area Model.



Figure 14. Hand molding Cairn Point bathymetry on the Large-Area Model.

Figure 15 shows the just-completed section of the Large-Area Model that includes Cairn Point and the deepest portion of the Knik Arm. The Port of Anchorage is on the left side of the photograph about mid-height. Some of the slopes off Cairn Point are steep in nature, but in the Large-Area Model the slopes are 4 times as steep because of the geometric distortion.



Figure 15. Cairn Point bathymetry detail on the Large-Area Model.

As the concrete was curing, the models were constantly kept wet to reduce cracking caused by rapid heat loss. This was particularly crucial during the hot summer months. The Small-Area Model bathymetry was completed by the end of August, 2007; and the Large-Area Model and tidal prism storage area were completed by the end of November, 2007.

Figures 16 and 17 show the Large-Area Model completed bathymetry. The model has been painted to better delineate the shoreline. The change in colors was located at the approximate mean higher high water level (mhhw). The view in Figure 16 is from Point Woronzof looking toward Anchorage. The men in the photograph are standing in the vicinity of the Port of Anchorage. At the upper portion of the photograph is the tidal prism storage area. The Figure 17 photograph was taken from the tidal prism storage area looking down Eagle Bay. Anchorage is on the left side of the photograph about where the man is standing.



Figure 16. Completed Large-Area Model from Point Woronzof.



Figure 17. Large-Area Model from the tidal prism storage area.

Port expansion inserts

Simulation of the various phases of the Port of Anchorage expansion required construction of model inserts to represent the change to the Port's footprint during expansion. These expansion inserts needed to be removable to give flexibility to the testing program. In other words, it was possible to place or remove Port expansion inserts to test the original Port configuration or any sequence of expansion.

The Port expansion inserts were cast out of concrete as shown in Figure 18. A plastic sheet was laid down and a special concrete made with light-weight aggregate was placed inside a form for the particular expansion phase. Eye-bolts were cast into the inserts to facilitate lifting the insert.



Figure 18. Casting of the North Backlands and North Extension insert .

After the first expansion casting had set, the abutting insert was formed and cast in a similar manner as seen in Figure 19. The completed Port expansion is shown in Figure 20. Initially, both the South Backlands and the South Extension were cast as a single piece, but during testing it was determined by Alaska District engineers that these two expansion phases should be separated to test specific Port configurations. Consequently, two new inserts were cast to replace the single insert.



Figure 19. Casting of the North Replacement Expansion insert.



Figure 20. Completed Port expansion inserts.

During construction of the original bathymetry, a similar technique was used to represent the deeper dredging depths (maximum -50 ft mllw) to be maintained after completion of the Port expansion. The concrete bathymetry was placed at the -50 ft mllw depth. After the concrete had cured, a plastic sheet was placed on top of the concrete, and an additional thin layer of concrete was placed to bring the depths up to the current authorized dredging depth of -35 ft mllw. This depth reduction insert can be seen on Figure 20 in the region seaward of the Port. However, the concrete for this insert was so thin that it was not practical for the dredging insert to be removed and then replaced again. Thus, replacement of the insert after removal required casting a new insert.

4 Experiment Setup and Operating Procedures

A physical model is similar in ways to an analog computer because reactions in the model are governed by the physical forces generated by waves and flowing water. If the model is not properly configured, or if the model is not properly operated, model results can be negatively influenced or even incorrect. Thus, care is needed in setting up the experiments and assuring that correct operating procedures are followed.

This chapter describes the instrumentation used to record model response, discusses the procedures followed when operating the physical model, and describes the data collection and initial data analyses.

Experiment instrumentation

Physical parameters measured during testing of the Large-Area physical model included water level and flow velocity. Throughout the experiments, flow visualization techniques were used to gain insight into the complex flow patterns and their evolution during the tide cycle. The following sections briefly describe the instrumentation and techniques used to acquire measurements in the physical model.

Water level

Each experiment began with a period of up to one hour during which time the water level in the ESTEX flume was adjusted to the level associated with mllw at the Port of Anchorage. Monitoring of the water level during this adjustment was done using a standard point gauge referenced to the model vertical datum.

Four capacitance-type wave gauges were placed in the ESTEX flume to record the variations in water level elevation during the tide cycle. The gauges work by sensing the change in capacitance in a thin insulated vertical wire as the water elevation varies on the wire. Each gauge captures a time series of information that can be converted into water surface elevations at that location.

The most important water level gauge was positioned in the Large-Area Model at a location corresponding to the coordinates of the NOAA tide gauge near the Port of Anchorage. Two additional water level gauges were located in the center of the main flow channel at the downstream and upstream model boundaries. A fourth water level gauge was positioned at the far end of the ESTEX flume where water inflow and outflow occurs (left side of Figure 8). This gauge was needed to help guide the model calibration described in Chapter 5.

All water level gauges were mounted on precision mechanisms that permitted the gauges to be raised and lowered manually precise vertical distances for calibration. Water level gauges were calibrated daily with the water motionless and at a depth equal to the model mllw datum. The gauges were calibrated using the two end points of the 2-in. tide range to establish the linear relationship between water elevation and gauge frequency output. After the calibration was applied, the gauges were checked for accuracy by verifying two to three additional check elevations within the tide range. This methodology was justified based on observations that these gauges have proven to be very linear in many previous model studies. Provided all gauges exhibited the expected calibration, the calibration relationships were saved in a file for later application to the measured raw water elevation data collected the same day as the calibration.

For all experiments, time series of water surface elevation were collected at a 20-Hz rate. Water level data were transmitted into the main control room and recorded on a computer for post-experiment processing.

Flow velocity

Water velocity measurements in the model were used to quantify changes in the tidal flow at the Port of Anchorage that would occur under various construction sequence scenarios. These comparisons will be used to judge dredging requirements during and after the Port expansion.

Horizontal flow velocities in the Large-Area Model were measured and quantified using three Sontek MicroADV acoustic Doppler velocimeters (ADV) with sideward-looking probe heads, as shown in Figure 21. The ADVs were oriented to measure two orthogonal horizontal components of flow velocity with one component aligned with true north in the Knik Arm. Water velocities were obtained at a point located horizontally approximately 2 in. from the probe vertical support rod. For example, the ADV

pictured in Figure 21 measured the velocity above the center of the 2-in.-diameter circle drawn on the concrete (see figure).



Figure 21. Acoustic Doppler velocimeter probe head.

At each measurement location, the ADV measurement head was positioned at about mid-depth when the water level was at mllw. Therefore, the vertical position of the velocity measurements relative to the total water depth varied during a tide cycle. For example, had the probe been placed in a location having a 30-ft depth at mllw (prototype-scale units), the probe would be positioned 15 ft above the bottom. At the peak of a 30-ft tide, the probe will be located at a point corresponding to the lower 1/4 of the water column.

All three ADV current meters were connected to a collector unit that synchronized data and transferred it to a computer. The computer software controlled the data collection, displayed data recording in real time, and saved the data to files for post-processing. Velocity data were collected at a 10-Hz rate for all experiments.

The ADV current meter system required no calibration because equations are available to relate the sensed Doppler shift frequency directly to velocity as a function of acoustic sound wave velocity. However, it was necessary to input the water temperature for accurate calculation of the speed of sound during each experiment.

The ADV system required that water passing through the sensing volume flume be seeded with small particles to reflect the sound waves. A fluid mixture of water and tiny glass beads was seeped into the flume water in the vicinity of each ADV gauge to assure a sufficient supply of seed particles was available at each measurement location. Computer software continuously monitors the signal-to-noise ratio to assure quality data are obtained.

Flow visualization

An important aspect of understanding the complex flow patterns in the Knik Arm was being able to visualize the large-scale gyres in motion and to be able to gauge the relative flow velocities in different parts of the model. Two flow visualization techniques were used. Dye was placed in the model using squirt bottles for injecting long dye lines, and a hypodermic syringe to inject smaller dye amounts at precise locations. Figure 22 shows a portion of a dye line injected off of Ship Creek (lower right corner of photograph) as it passes by the unexpanded Port of Anchorage during flood tide. The current out in the Knik Arm main channel is clearly moving at a faster pace.

The second flow visualization technique was to sprinkle baby powder on the surface of the flow water. The powder floated, and in some respects mimicked ice floes seen in the Knik Arm during the winter months. This type of Lagrangian tracer was very effective in showing the large-scale gyres and how the gyres influence the hydrodynamics at the Port during most phases of the tide. Figures 22 and 23 show the powder tracer. Of course, still photography does not convey the movements of the gyres that can be seen when watching the model in operation. Time-lapse video taping of the flow tracers and dye injections was done for all Port of Anchorage expansion configurations, and this provided a means for conducting side-by-side visual comparisons of the differences in flow patterns for various expansion phases. The filming rate was 1 frame per sec. which is about 1 frame per min. at full scale. When shown at the normal video rate of 30 frames per second, the entire tide cycle is completed in 26 sec.

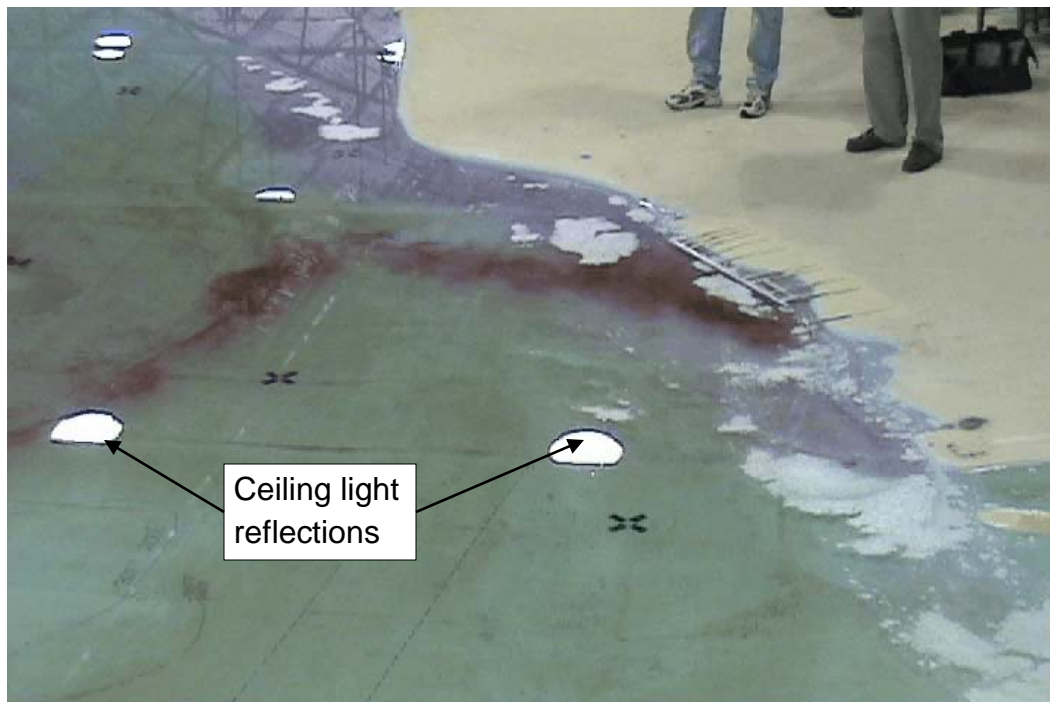


Figure 22. Dye injection to visualize flow velocities past the Port of Anchorage.

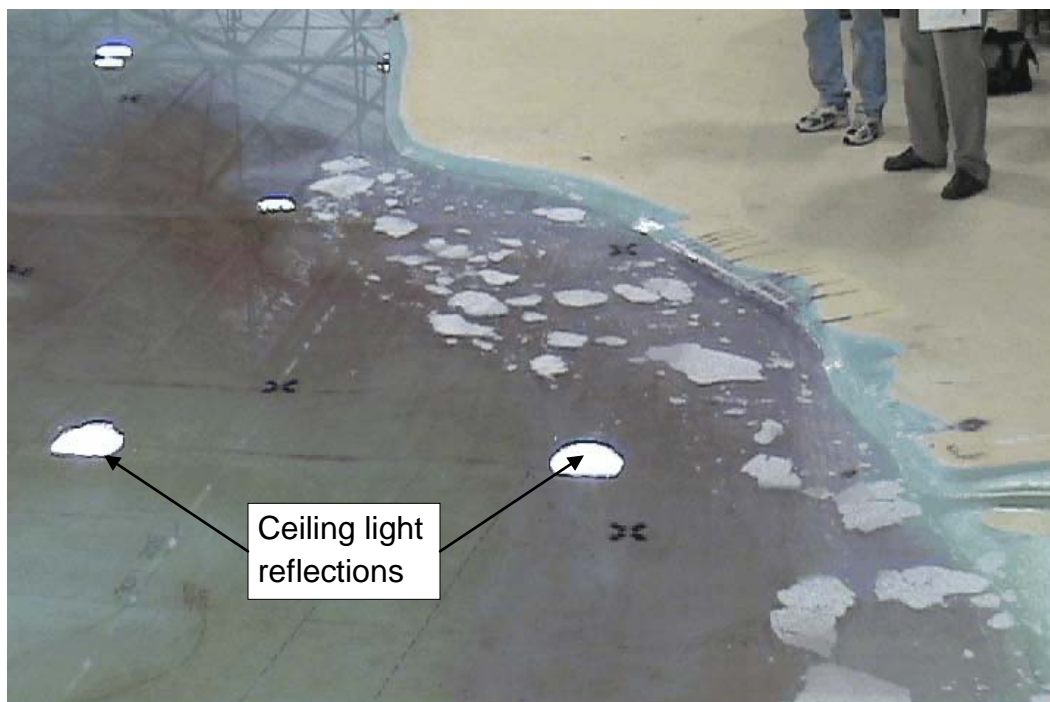


Figure 23. Surface tracers used to visualize flow velocities past the Port of Anchorage.

One interesting phenomenon observed using the powder tracers was the movement of water through the modeled regime over the course of the tide cycle. Powder placed at the Port of Anchorage during flood tide would travel through Eagle Bay into the tidal prism storage area, and eventually arrive back into the vicinity of the Port during ebb flow. The powder would then continue south past Fire Island, and finally reappear at the Port during the following flood cycle.

Operating procedures

Tide generation

Tides are generated in the ESTEX flume by controlled filling and draining of water at the north end of the flume (left side of sketch in Figure 8). For the Knik Arm physical model experiments, only a small portion of the tide producing capability was required due to the relatively small model tidal prism and maximum flow rate as seen in Table 2.

To generate tides, water was introduced into the flume using one of the constant flow pumps. Water was taken from a sump having a set initial water level. At the same time an underflow gate was opened that allowed water to drain out of the flume and return to the sump. The gate elevation was adjusted until the amount of water leaving the flume was the same as the water being pumped into the flume, and this created a constant water level throughout the flume.

The tide cycle was simulated by lowering and raising the outflow control gate in a prescribed manner to replicate the scaled period of the tide signal. As the gate was lowered, more water flowed into the flume than was flowing out, and the water surface rose. After the gate reached the lowest position corresponding to the maximum flow rate (mid-flood tide), the gate began to open and the inflow rate decreased. The gate continued to rise past its starting position to cause the net inflow rate to be negative. At this point the water elevation began to decrease. When the gate was in the maximum open position, the outflow rate was at maximum (mid-ebb tide). Finally, the gate returned to its original position just as the water elevation reached the starting point at mllw. The cycle then repeated itself.

The actual maximum spring tide cycle measured at the Port of Anchorage between 1200 hr on August 11 and 0500 hr on August 12, 2006 was approximated as a sinusoidal curve having the same peak amplitudes and

period. A time series of tide elevations was mathematically created and scaled to model dimensions for use in the Large-Area Model. Each experiment consisted of four consecutive, identical tide cycles, whereas in nature there is variation from one cycle to the next. A comparison between the actual and theoretical spring tide used for these experiments is presented in Chapter 5.

Conducting experiments

Prior to each experiment, the three ADV current meters were positioned in the model at the locations where velocity data were to be collected. This involved positioning the instrument, rotating the probe head to align one component of horizontal velocity with the model coordinate system true north, and adjusting the probe head elevation to approximately mid-depth at mllw.

The next step was to bring the water level in the model up to the elevation of mllw and hold it at that elevation while long-period oscillations in the basin stopped. This took between one and two hours. The long-period oscillations were created by the initial flooding of the model. Water elevation variations were monitored at a point gauge and by viewing real time output from the water elevation gauges. At the end of this settling period, seeding of the water in the vicinity of the ADV gauges was begun.

Once the water in the flume was established at mllw without any motion, the operator started the experiment by hitting a key on the control computer. This activated the closing motion of the outflow gate and started computer recording of data from the three water elevation gauges situated in the Large-Area Model. At exactly one minute after starting the tide, the operator initiated data collection for the three current meters using a different computer system.

Approximately two and a half minutes after starting the tide, water began to move in the Large-Area Model. This time lag in the flume was a function of the distance between the tide control system and the Large-Area Model located at the opposite end of the ESTEX flume. The flood flow raised the water elevation in the Knik Arm as it passed through the model and into the tidal prism storage area upstream. The tide then reversed, and the ebb flow was driven by the head of the water contained in the tidal prism storage area.

Four identical tide cycles were simulated without interruption for each experiment. For calibration runs data were collected at the water level gauges and ADVs during all four tide cycles. After calibration was completed, most runs were ended after two complete tide cycles with the data obtained from the second tide cycle used in subsequent analyses.

Flow visualization experiments were conducted without ADV gauges in the model so the oblique view from the time-lapse video camera was not obstructed. These tests were repeats of previous tests in which velocities were measured. The purpose of filming the flow visualization was to provide qualitative assessment of differences between flow patterns in the vicinity of the Port due to expansion phases. This objective was achieved by synchronizing video footage between different experiments and viewing the two videos side-by-side. Dye injection and introduction of powder into the model was done according to a specific schedule tied into the start of the experiment. This provided consistency between experiments with dye injection and powder placement occurring at the same time in each video.

During the experiments, the record of water elevation variation was examined to determine that successive tide cycles had the same high and low water elevations. If the control gate opening was off by just a little, there might be a slow linear increase or decrease in the mean water level due to a net mean increase or decrease in flume water. For example, if there was a net increase in mean flume water volume, each successive high tide would be higher than the previous. Eventually, the tide would overflow the banks of the model. Test runs were terminated immediately when it became obvious that the tide cycles were not repeating correctly.

Data collection and initial analyses

Tides

For all experiments, water level data collection started at the same instant the tide generation was activated, and continued until the tide system was halted. Time series sea surface elevation data were collected at a 20-Hz rate. At the completion of each experiment, the collected data were immediately converted into engineering units of model feet by applying the calibration factors determined at the start of testing for that day and stored in a computer file containing the necessary identifying information.

Data collection at a 20-Hz rate for two completed tide cycles in the Large-Area Model lasted about 30 min. giving a water surface elevation time series of about 36,000 points for each data channel. Runs including all four tide cycles lasted about 57 min.

Velocities

Horizontal velocity magnitudes and directions were collected at a 10-Hz rate using a separate computer system. For two completed tide cycles lasting a total of about 30 min., the ADVs collected 29 min. of data so each ADV time series had about 17,400 data points. The computer saved the data to files in units of model cm/s along with information identifying the test and the model configuration.

Data synchronization and analyses

Post-processing of the tidal water elevation and velocity time series was accomplished using two custom MatLab® scripts on a standard PC workstation running the Linux® operating system. One script compared model measurements with field data, and the other script compared results from different model runs. Both scripts read in the model data and converted the time-series data into consistent units scaled up to prototype (full scale). Water elevations and flow velocities were converted to SI metric units of meters and cm/s, respectively. This allowed engineers to have a better understanding of the measurements, and to give a sense of data correctness based on the engineers' experience with full-scale tidal flows.

Time series data from the ADV current gauges contained some high frequency variation that probably was a combination of turbulence and random noise. A smoothing filter was applied to make the velocity plots easier to interpret. Figure 24 shows a typical time series plot of velocity magnitude and direction. The smoothed signals are shown as the heavy black lines with the original measured data distributed around the smoothed result.

The model water elevation and velocity time series for each test were synchronized in the script by applying a 60-sec time lag to account for the fact that velocity data collection was initiated 1 min. after tide data collection started. An error of ± 1 sec. in starting the velocity data collection would translate into an error of ± 1 min. in the prototype. This is equivalent to a phasing error of less than 0.1 percent.

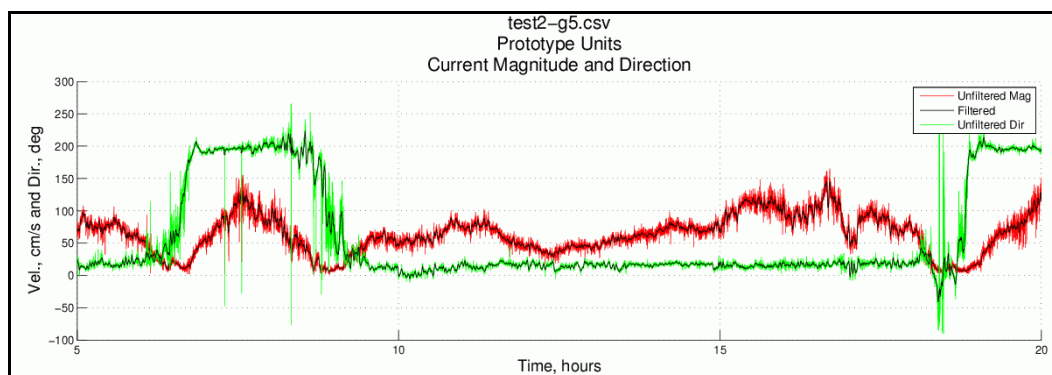


Figure 24. Smoothing of ADV velocity magnitude and direction.

Measured field time series of tide elevation and velocity in the Knik Arm were referenced to the same time, so these field measurements were already synchronized. However, synchronization of the model time series to the field data required shifting the model tide time series relative to the field-measured tide until the time series had a close match at the mid-tide elevation. The model tide was four identical sinusoidal waves, and the corresponding field record was created by repeating and splicing the measured highest spring tide signal for four tide cycles.

Once all of the time series were synchronized in time, the MatLab® scripts plotted comparisons between model and field measurements or between various model tests. For most comparisons, the second tide cycle of the model run was used to assure that no start-up transient waves were adversely influencing the flow patterns, and to confirm the tide cycle simulation was exactly repeating.

The videos of different experiments were synchronized according to the movie frame showing the start of the first dye insertion. The first dye insertion occurred exactly 3 min. from the start of the tide simulation for every video-taped experiment. All the movies were then edited to the same total number of frames so they could be viewed side-by-side using a special viewer written by Jarrell Smith, CHL.

5 Model Calibration and Verification

The primary function of the Knik Arm physical model was to examine how the Port of Anchorage expansion might affect the dredging and navigation missions of the Alaska District. However, before the model can be used for this purpose, the model had to be calibrated and verified. Calibration of a tidal hydraulics physical model means establishing the proper (and repeatable) procedures to reproduce the entire tide cycle in the model. The resulting model tide measurements must closely replicate the actual tide when scaled to prototype size.

Once the model was calibrated to produce the correct tidal variations, it was then verified by demonstrating that velocity magnitudes and directions measured in the model and scaled to prototype were similar to the velocities magnitudes and directions measured in the Knik Arm.

This chapter reviews the subset of available field data used for calibrating and verifying the physical model, describes the model calibration, and presents model verification results. The verification was performed at three locations just seaward of the existing Port of Anchorage dock face.

Field data

Field measurements used to calibrate and verify the Knik Arm Large-Area physical model were collected by Jarrell Smith, CHL, during August 2006. The measurement campaign included numerous vessel transects in Cook Inlet and Knik Arm over extended periods using an acoustic Doppler current profiler (ADCP) along with real-time vessel positioning equipment. The ADCPs were also used to record velocities at stationary mooring locations over a complete tide cycle.

Tide

Tide elevation is continuously recorded by the NOAA at a tide station located adjacent to the Port of Anchorage. Time series of water surface elevations at 6 min. intervals, spanning the period of the August 2006 field data collection project, were obtained from NOAA. Figure 25 is a plot of the Knik Arm tide for the period 5-18 August 2006. The tick marks on the abscissa represent the time of hours GMT (Greenwich Mean Time) on the

given day. The maximum spring tide occurred around 11-12 August. During the summer months, Alaska uses daylight savings time; and the local Anchorage time is 8 hr behind GMT, i.e., GMT-8.

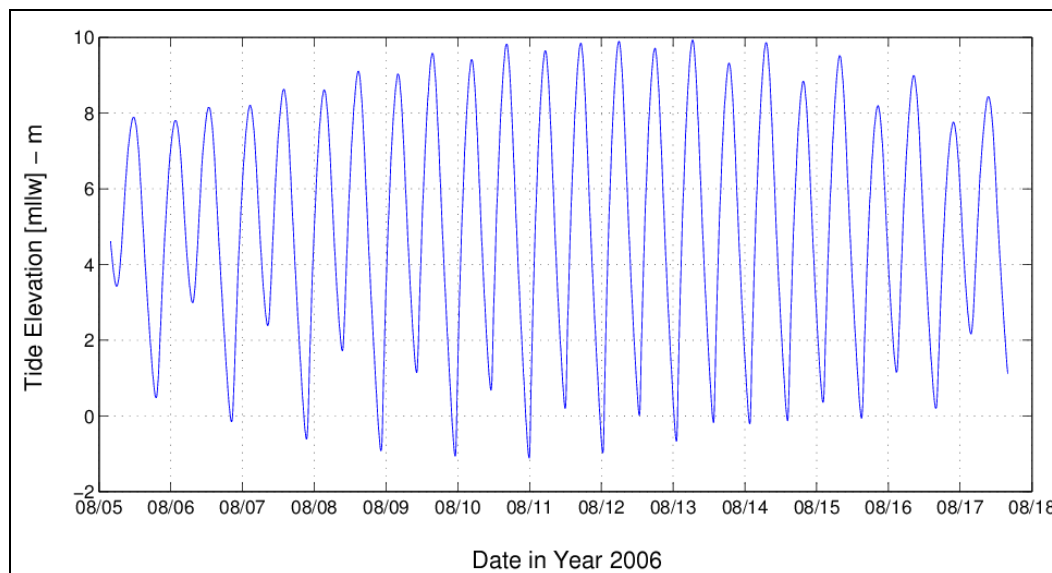


Figure 25. Measured tide in Knik Arm during 5-18 August 2006.

In theory, the tide generation methodology used in the ESTEX flume could be programmed and calibrated to produce a tide signal that matched several successive tide cycles in the spring tide range. But in practice, this would have been extraordinarily difficult and time consuming. A workable compromise was to select an actual 12-hr spring tide cycle and then synthesize a four-cycle tide by repeating the selected tide cycle.

The selected spring tide cycle had a low tide of +0.72 ft mllw at about 1200 hr GMT (0400 hr Anchorage time) on 11 August, a high tide of 32.25 ft mllw at about 1700 hr GMT, and a low tide of -2.05 ft about 0000 hr GMT on 12 August. Thus, the tide range on the flood tide was 31.53 ft, and the range was 34.20 ft on the ebb tide. The average of the two tide ranges is 32.9 ft, and this was used as the initial target tide range for the model calibration.

Figure 26 shows a 20-hr section of the measured tide record bracketing the selected spring tide cycle. The field data are plotted in 1-hour increments, and the data have been scaled to model units using the Large-Area Model vertical scale and time scale (given in Table 1). The upper plot abscissa is given in model minutes, and the lower plot is model seconds.

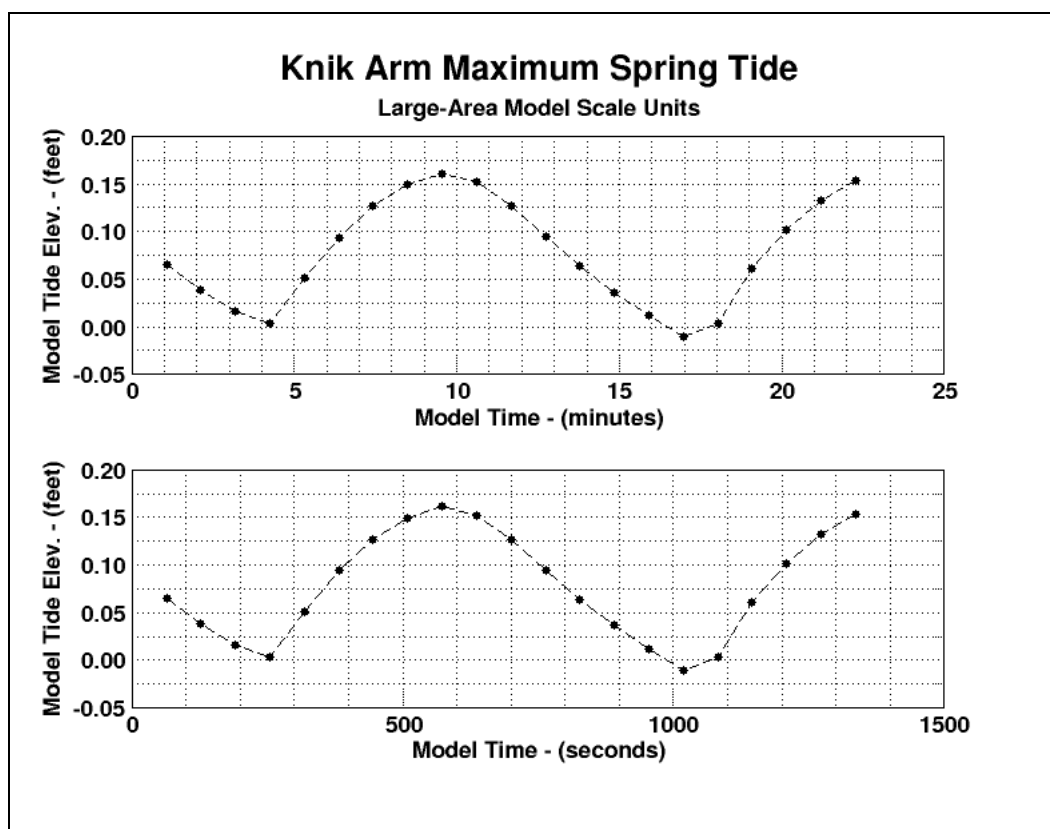


Figure 26. Selected Knik Arm tide cycle scaled for Large-Area Model.

Velocities

Velocity data were collected over a complete 12-hr spring tide cycle at four mooring locations near the Port of Anchorage during the period 9-13 August 2006. The mooring locations are shown on Figure 27. The irregular tracks at each station indicate the vessel's movement about its mooring line during the tide cycle.

Stations 2, 4, and 5, shown on Figure 27, were selected for physical model verification using the three available laboratory ADV current meters. Table 5 contains the latitude and longitude of the three selected mooring locations (approximate center of the mooring track) along with the approximate starting and ending times of the data collection. The times are given in GMT, so the actual starting and ending times in local Anchorage daylight savings time are found by subtracting 8 hr from the times given in Table 5.

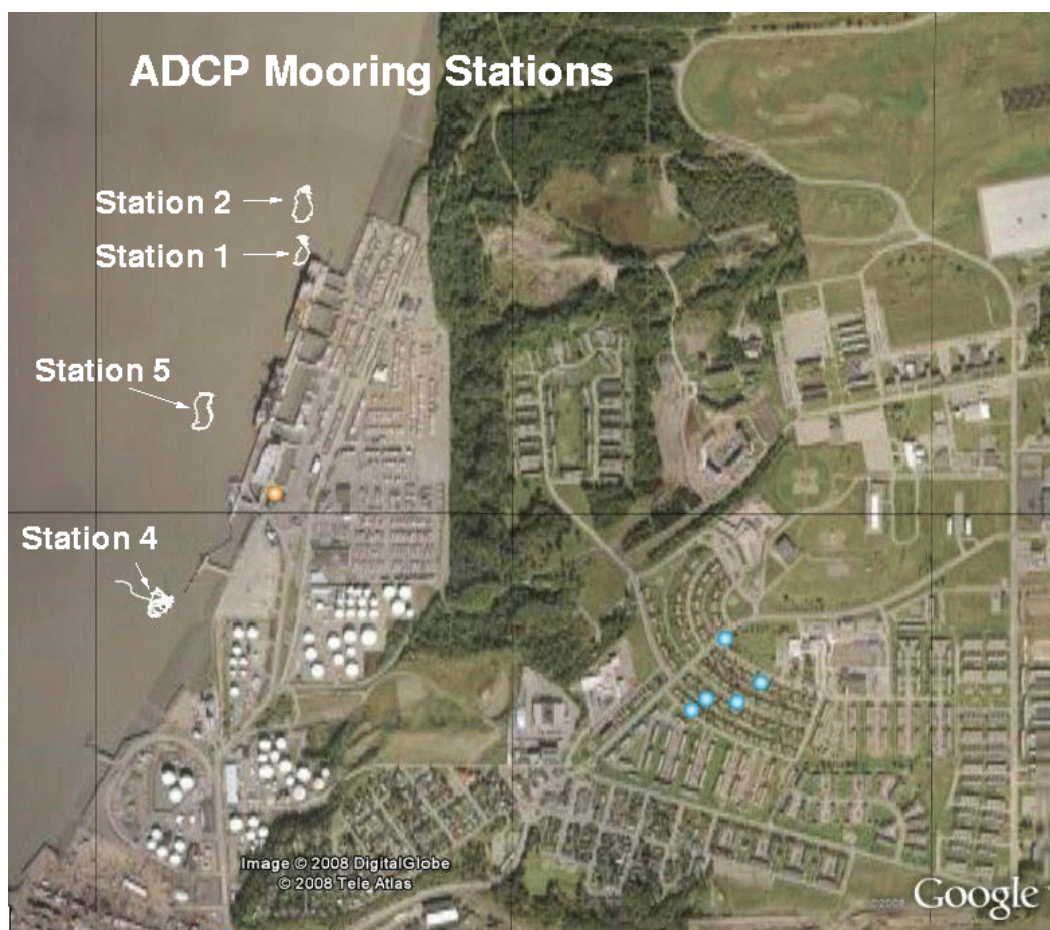


Figure 27. Locations of ADCP mooring stations near the Port of Anchorage.

Table 5. Field ADCP velocity data collection parameters.

| Station | Latitude | Longitude | Approx. Start Time | Approx. End Time |
|-----------|-----------------|------------------|--------------------|------------------|
| Station 2 | 61° 14' 44.21"N | 149° 53' 11.56"W | 8/10 - 1600 GMT | 8/11 - 0400 GMT |
| Station 4 | 61° 14' 07.47"N | 149° 53' 38.61"W | 8/11 - 1800 GMT | 8/12 - 0300 GMT |
| Station 5 | 61° 14' 25.26"N | 149° 53' 30.31"W | 8/12 - 1600 GMT | 8/13 - 0400 GMT |

Tides associated with the three velocity data collection periods are shown by the dashed boxes in Figure 28. The tide cycles are a little different for each data collection period. The tide period chosen for model calibration began on 11 August at 1200 and ended around 0000 on August 12, 2006, and it included a portion of the Station 4 data collection.

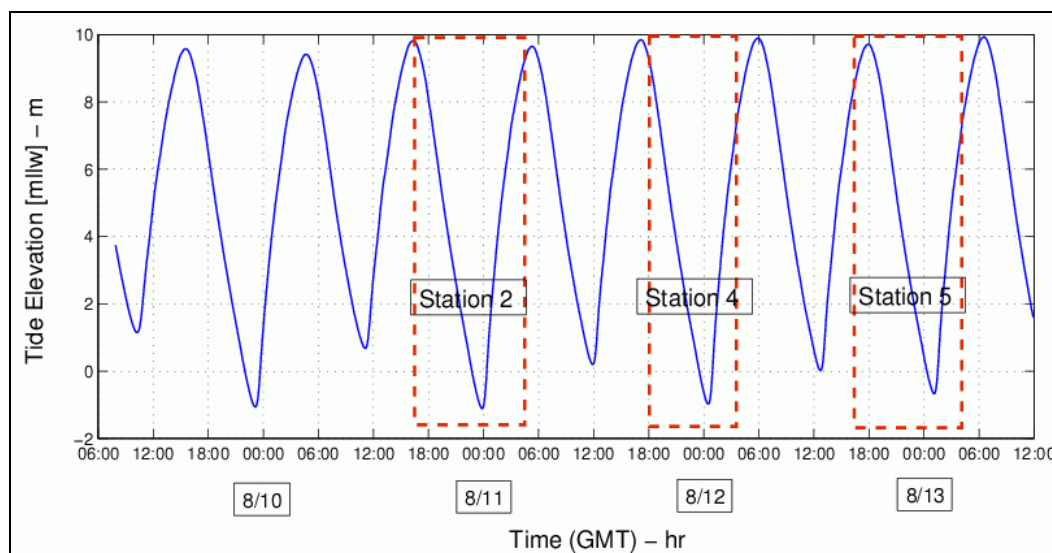


Figure 28. Tides during ADCP velocity data collection.

Acoustic Doppler current profilers simultaneously measure three velocity components at multiple water depths. The water column is divided into discrete bins, and the velocity vector reported for that bin represents the average over the water volume defined by the discrete bin vertical dimension and the horizontal circle corresponding to the acoustic beam width at that depth. Tidal flow velocities were sampled every 2.5 sec over the nearly 12-hour period spent at each location.

The laboratory ADV current meters provide only two components of horizontal velocity at one depth. Therefore, it was necessary to decimate the field data to provide velocity values that could be compared to model measurements. Jarrell Smith, CHL, processed the original ADCP data and provided time series of depth-averaged horizontal velocities that had been time averaged at 1 min. intervals.

Figures 29, 30, and 31 present the time series of velocity magnitude (solid line) and velocity direction (dashed line) for Stations 2, 4, and 5, respectively. Maximum velocity magnitudes approached 135 cm/s (4.4 ft/s or 2.6 kts) during both flood and ebb tide. Flow directions around 0 deg correspond to flow moving north (flood), and flow directions around 180 deg are flows moving south (ebb). The velocity measurements confirm the common knowledge that tidal flows near the Port of Anchorage move in a northerly direction between 60 and 80 percent of the time.

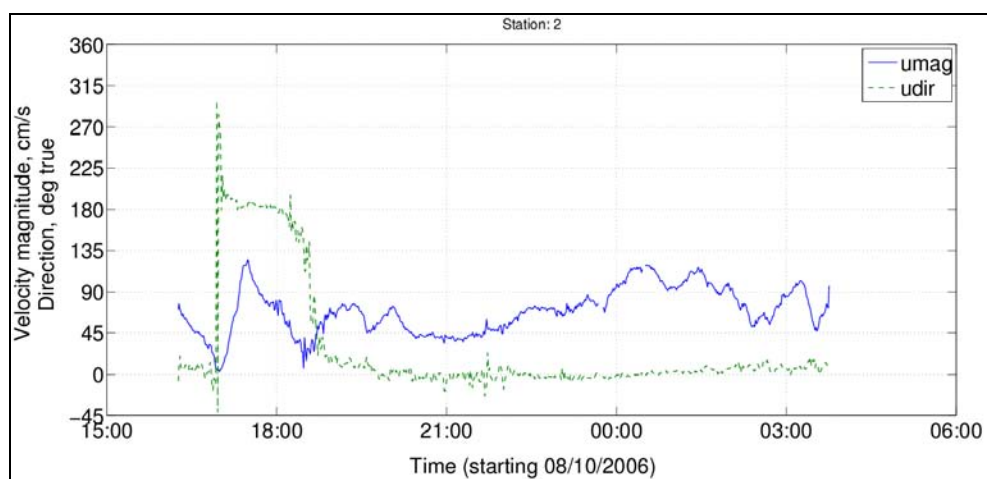


Figure 29. Station 2 depth- and time-averaged velocity magnitudes and directions.

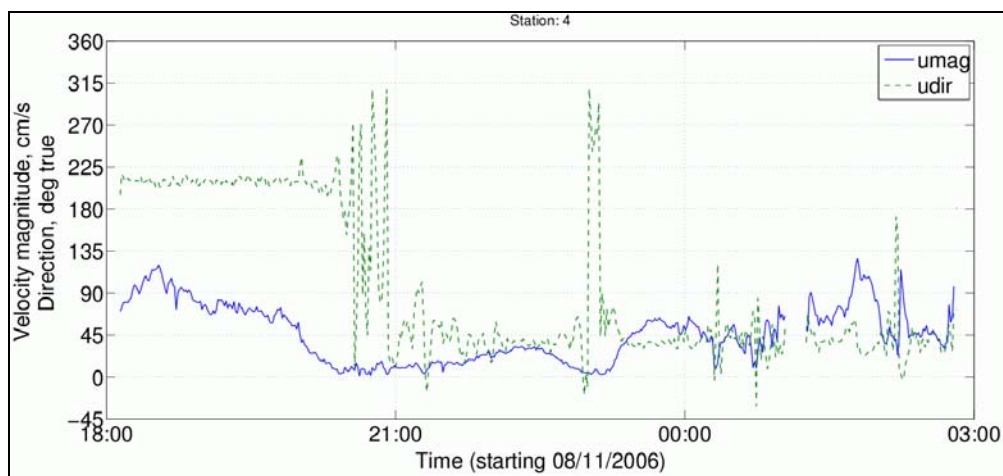


Figure 30. Station 4 depth- and time-averaged velocity magnitudes and directions.

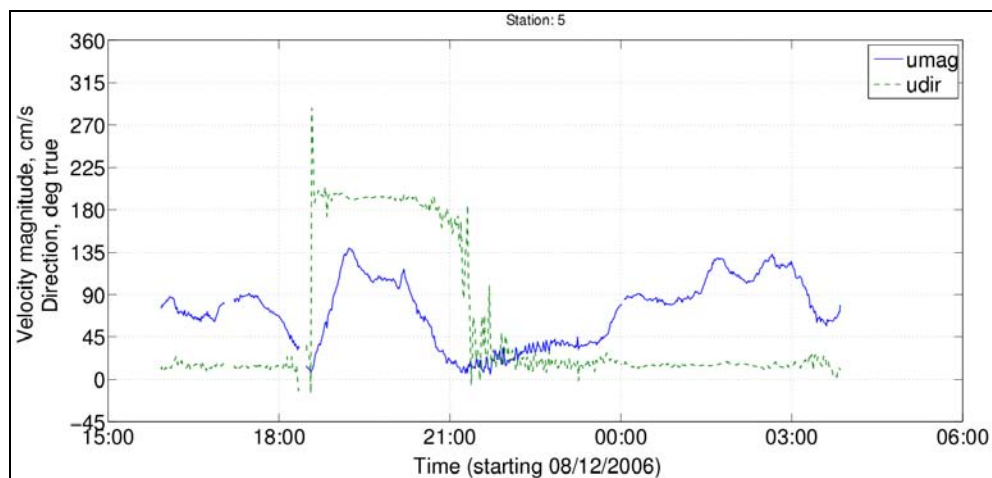


Figure 31. Station 5 depth- and time-averaged velocity magnitudes and directions.

The disparity between flood and ebb flow direction is caused by the large gyre formed in the lee of Cairn Point during ebb tide. At full development, the gyre can extend the entire length of the Port, and the flow close to the dock face moves upstream (north) while the flow farther offshore in the main channel is moving downstream (south).

Model calibration

Calibration of the Large-Area Model of Knik Arm began in December, 2007, and proceeded through February, 2008. The following sections describe the calibration procedure, present calibration results, and demonstrate repeatability of the model tide cycle.

Motion of tide outflow gate

As discussed previously, tides are generated in the ESTEX flume by opening and closing one of the flume's outflow gates which changes the net rate of water entering (or exiting) the flume. The flume water level adjusts accordingly. Adjustable gate parameters are the initial gate opening, range of gate motion, and shape of the oscillatory gate signal as described below. It was planned that any adjustments to the tidal prism storage area would be made by adding sand bags at different elevations to displace water volume and raise the prism head. Fortunately, this step was unnecessary.

There was no theoretical or empirical formulation available to guide the model engineers, so the calibration procedure was strictly one of trial and error with previous experience being the only guide. After viewing results, small changes were made to the tide program, and another test was conducted.

The outflow gate was controlled by a Matlab[®] script that could either operate the gate according to a specified cosine function, or read in a file containing a time series of gate elevations. To give greater flexibility during the calibration, another script was written to generate more complex periodic signals specified by the following formulation

$$Z_{gate}(t) = \left[\frac{A \cos \left(\frac{\pi t}{T} + \theta \right)}{1 + B \sin \left(\frac{\pi t}{T} + \theta \right)} \right] - \frac{A}{2} \quad (49)$$

where Z_{gate} is the vertical elevation of the gate about its initial open position ($Z_{gate} = 0$), t is time, A is the total vertical range of gate motion, T is model tide period, B is a signal shape factor, and θ is a phase lag given as

$$\theta = \cos^{-1} \left[\left(\frac{1+B}{2+B} \right)^{1/2} \right] \quad (50)$$

This more complicated equation was thought to be necessary because of the hydraulics associated with the underflow gate. Figure 32 shows an example of an early non-symmetric gate control signal that featured a longer time for net inflow and a shorter period for net outflow. The range for this signal was $A = 7.3$ in., and the shape factor was $B = 2.0$. The phase lag given by Equation 50 shifted the signal to the starting point shown on Figure 32.

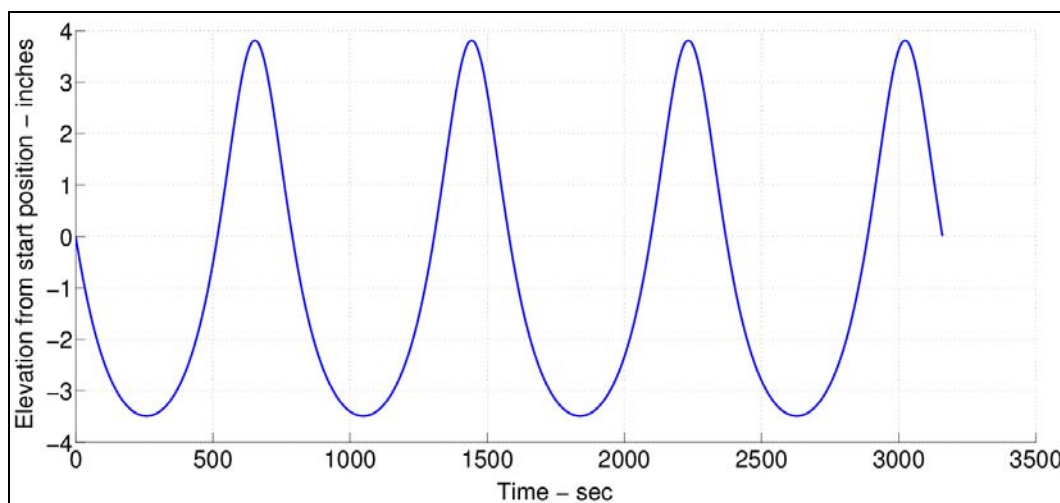


Figure 32. Non-symmetric outflow gate control signal (Equation 49).

It was eventually discovered that the best oscillatory gate motion was produced when the shape factor was set to $B = 0$. This value of shape factor reduced Equation 49 to a simple cosine-squared function given by

$$Z_{gate}(t) = A \cos^2 \left(\frac{\pi t}{T} + \frac{\pi}{4} \right) - \frac{A}{2} \quad (51)$$

Figure 33 shows a symmetric outflow gate signal having a range of $A = 7.3$ in.

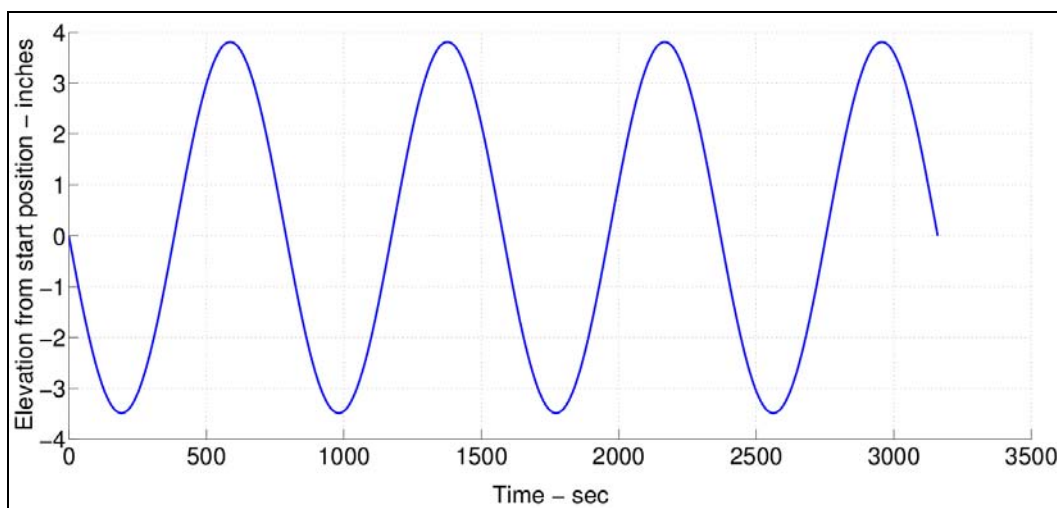


Figure 33. Symmetric outflow gate control signal (Equation 51).

Comparison to Knik Arm tide record

During the model calibration phase, actual tide elevations for the selected period measured at the Knik Arm NOAA tide gauge were scaled to model dimensions and compared to measurements made in the physical model. The model water level gauge was located in the model at the same coordinates as the NOAA tide gauge.

Figure 34 shows an early unsuccessful model calibration attempt. The tide signal shape is incorrect, and there was an obvious net increase to the total flume water over the course of the simulation. Each successive low and high tide was at a higher elevation, and the test was terminated after the water overflowed the model banks. The dashed line in Figure 34 is the scaled-down prototype tide signal patched together to form a four-cycle tide signal.

After a difficult and time consuming iterative process of making slight variations to the tide program parameters, successful replication of the time-varying water elevation was accomplished. Figure 35 presents a successful example of a calibration experiment in the Large-Area Model. The model tide matched the scale-down target tide extremely well for four complete tide cycles. The gate initial opening was 0.304 ft (3.65 in.), and a range of $A = 0.608$ ft (7.3 in.) was used in Equation 51.

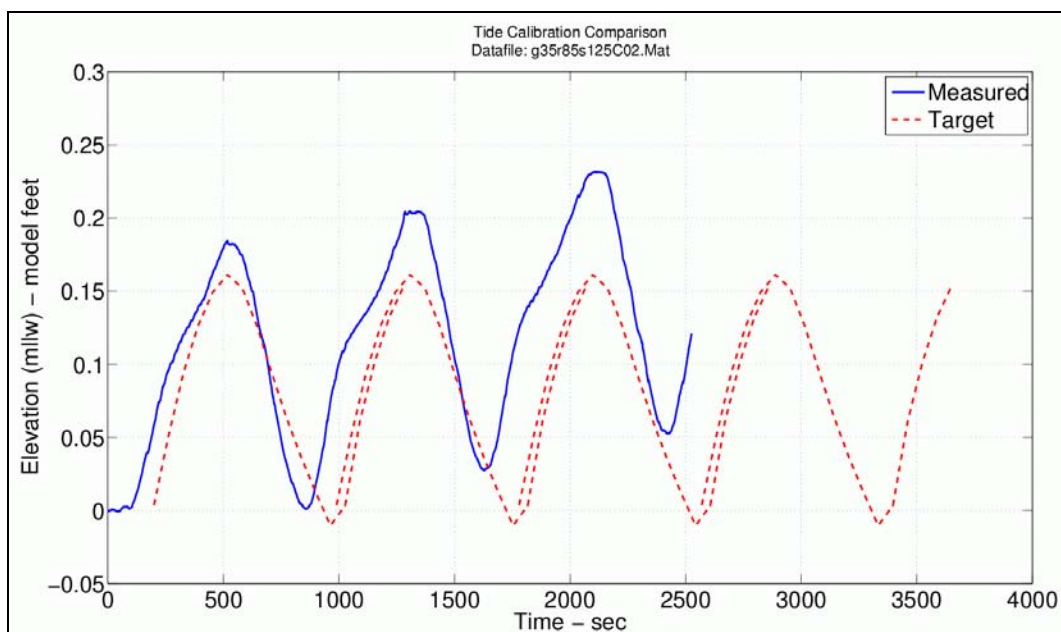


Figure 34. Unsuccessful early calibration test.

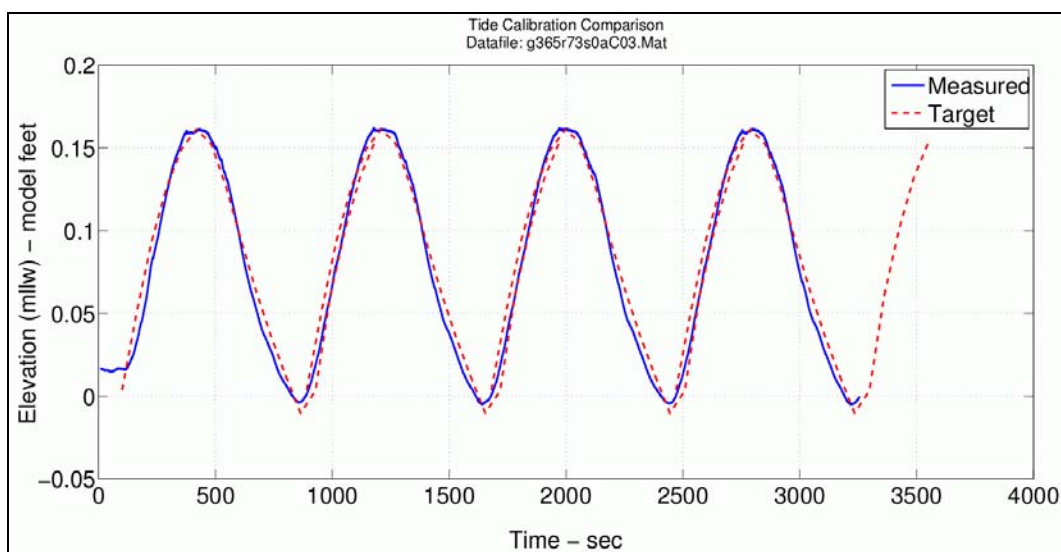


Figure 35. Successful Knik Arm Large-Area Model calibration.

Model tide repeatability

An overriding issue of importance for the Knik Arm Large-Area physical model was demonstrated repeatability of the calibrated tide cycle. This means that any observed differences in measured tide elevation and velocity at specific locations must be small to the point of insignificance. Model simulation repeatability is necessary for obtaining velocity measurements at numerous locations in the model using a limited number of ADV current meters. Current meters that recorded measurements during

one test can be moved to new locations for the next test. If all tests are identical (for a specific Port configuration), the combined results from several tests with a limited number of current meters are assumed to be equivalent to a single test with enough current meters to occupy every measurement position.

Figure 36 gives an example of the tide cycle repeatability during a single test consisting of four tide cycles. Velocity magnitude and time have been scaled up to prototype units. The solid line is velocity magnitude and the dashed line is velocity direction. Visually, the magnitudes and directions (relative to true north) at Station 5 appear similar between all the tide cycles. During each cycle the flow direction changes at the same time, and the durations of flood and ebb flow directions are the same.

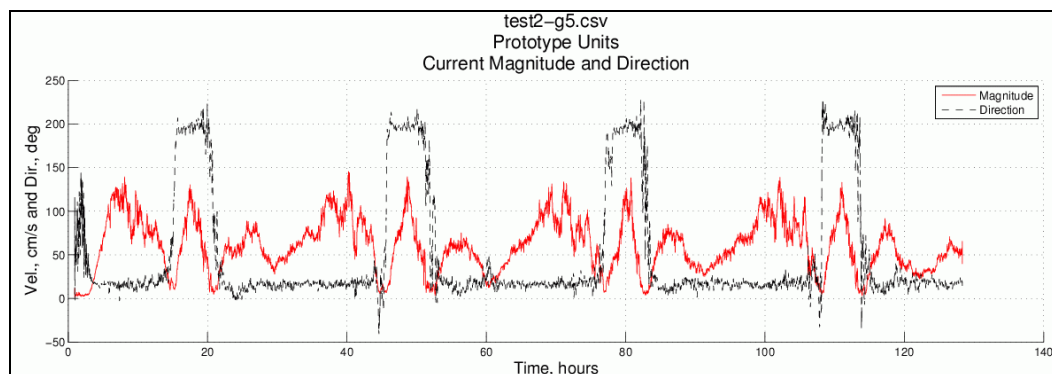


Figure 36. Tide cycle repeatability within the same test.

Repeatability between different tests is demonstrated by the plots shown for Station 2 and Station 5 in Figures 37 and 38, respectively. (Results have been scaled to prototype values.) Even with the tide signal for test 4 being a little higher, the velocity magnitudes and directions show remarkable agreement. This was a satisfying result because both of these measurement stations were within the large Cairn Point gyre during most of the ebb tide where the flow can be classified as large-scale turbulence.

Numerous other test comparisons exhibited similar repeatability. Test repeatability is also evident on some comparisons presented in Chapter 6.

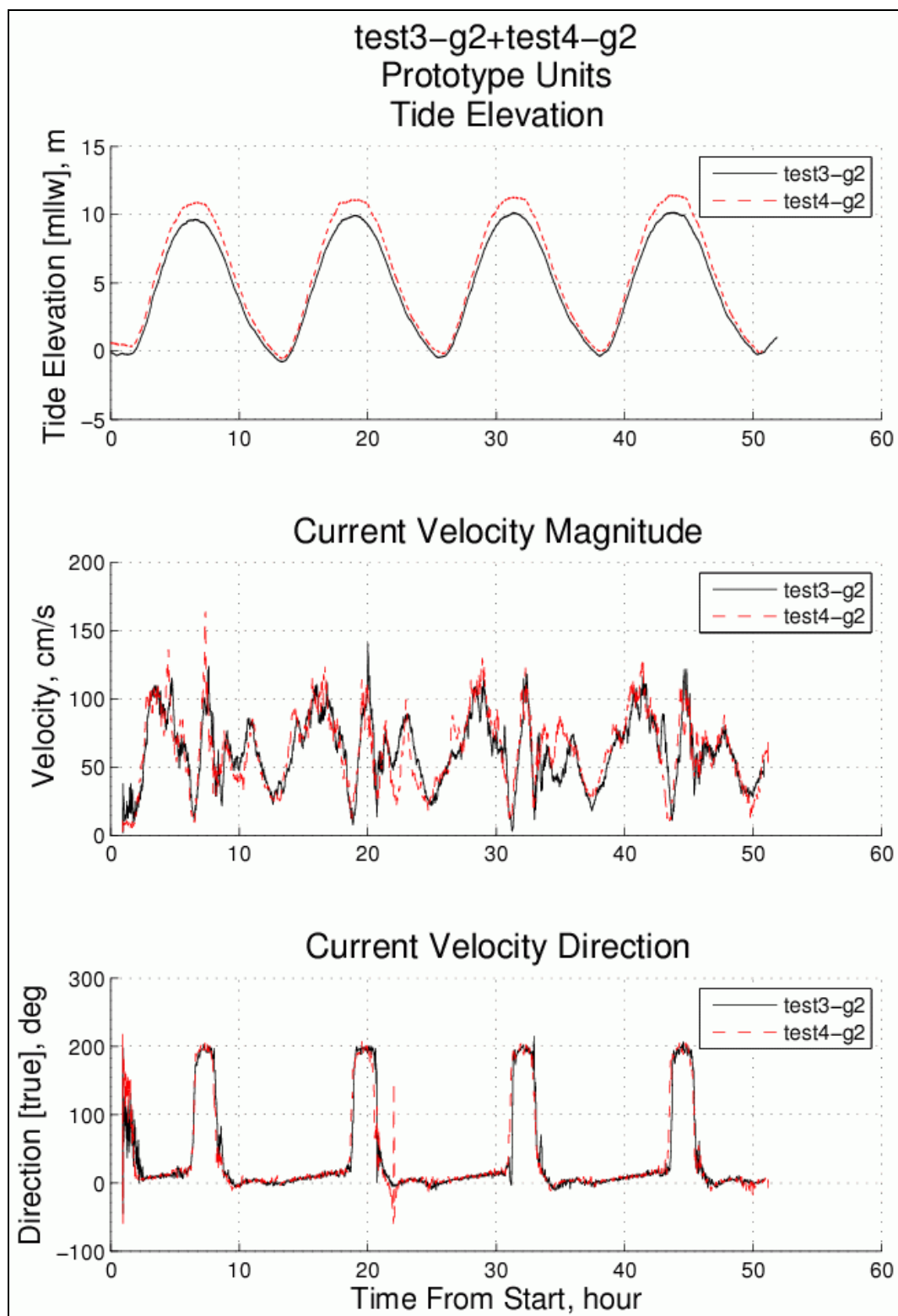


Figure 37. Tide cycle repeatability at Station 2 between different tests.

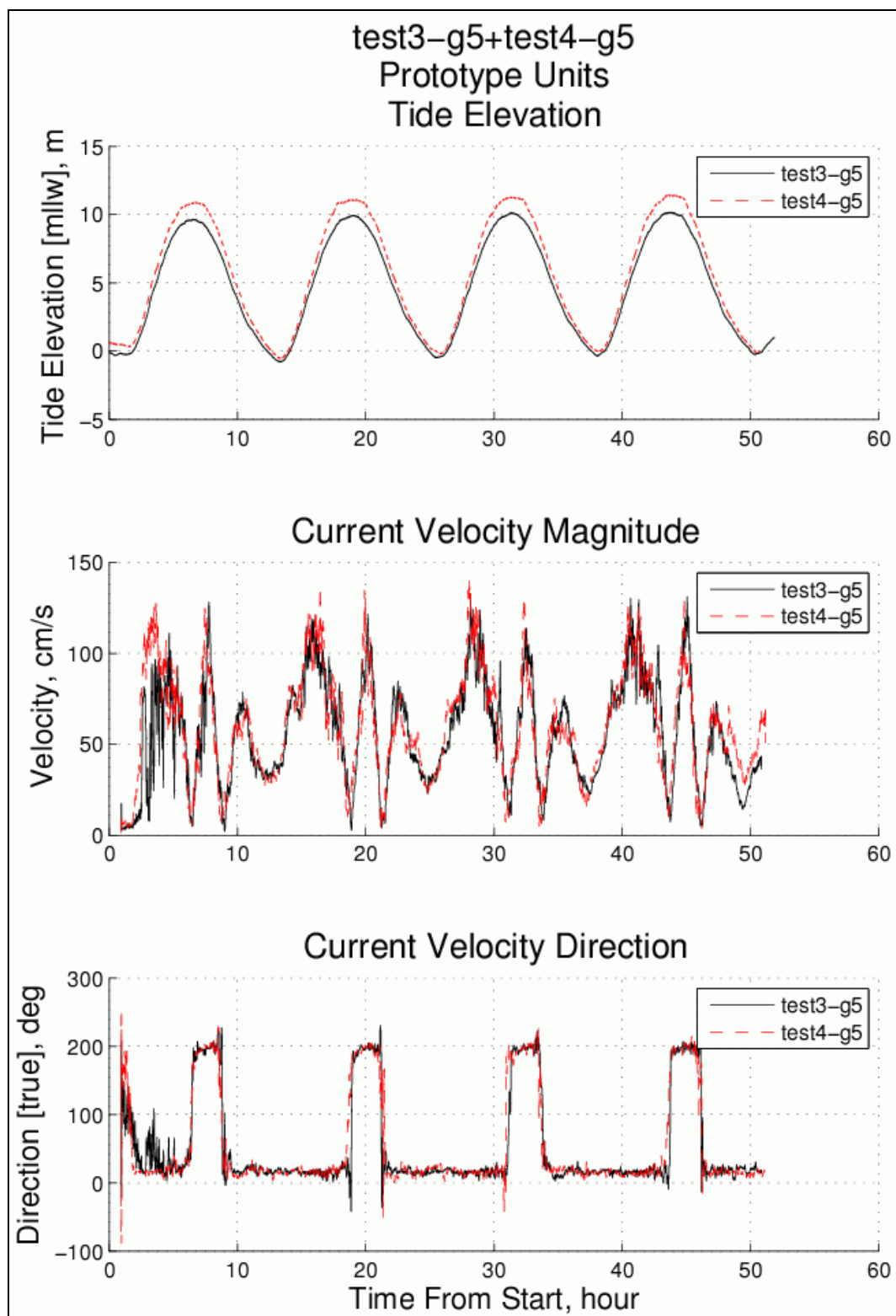


Figure 38. Tide cycle repeatability at Station 5 between different tests.

Model verification

Initial verification results

Verification of the Large-Area Knik Arm model was the most important step in the study. Before verification started, model engineers harbored much uncertainty as to whether the model measurements would even be close to the field measurements described earlier in this chapter. Once the model was able to reproduce the correct time variation in water level, the hydrodynamic response of the model was completely determined by the model boundaries and the bottom friction. In other words, opportunities to adjust the model to better replicate the field-measured velocities were very limited, and any improvement through slight adjustment of bathymetry would be relatively minor. If the initial comparison between the model and field measurements was poor, little could be done to improve the comparison to the point where the model could be considered verified.

Verification testing began in May, 2008, and the very first test provided model velocity measurements at the locations of the three stationary ADCP moorings (denoted Stations 2, 4, and 5) that exhibited remarkable similarity to the field measurement in both velocity magnitude and flow direction during all phases of the tide. For the remainder of May, small adjustments were made to the ADV current meter locations and orientations, and numerous tests were run to better understand the physical model behavior. Small adjustments in the bathymetry upstream of the Port of Anchorage were made to see if the comparisons between field and physical model could be improved. During this period, engineers from the Alaska District traveled to Vicksburg and participated in the model testing.

ERDC engineers working on numerical modeling of Cook Inlet and the Knik Arm discovered that the original bathymetry used for both the numerical and physical models had lower elevations for the shallow portions of the Cairn Point underwater bathymetry. This meant the elevations in this region needed to be increased the equivalent of about 10 ft in the prototype (0.6 in. in the model) to represent the prototype more accurately. Model engineers surmised that this bathymetry change would improve the model-to-prototype comparisons because of the expected response of the Cairn Point gyre to decreased depths. Before modifying the model bathymetry, a layer of sand was added to represent the needed decrease in model depth at Cairn Point, and tests were conducted.

During the month of June, 2009, the bathymetry at Cairn Point was modified. Figure 39 shows the portion of modified model bathymetry at Cairn Point (near center of the photograph). The bathymetry closer to shore above mllw was also modified based on aerial photography that was scaled and superimposed on the AutoCAD drawing of model contours. Up to this juncture in the testing, a total of 35 calibration tests had been completed.



Figure 39. Modification of Cairn Point bathymetry.

This correction was made in the model, and the calibration showed a slight improvement. Although the comparison was not perfect, it was deemed to be very satisfactory and as good as can be expected from a physical model.

Figures 40, 41, and 42 compare the model velocity measurements to field measurements at Stations 2, 4, and 5 respectively. (See Figure 27 for station locations). Field measurements are indicated by the dashed lines and the model measurements are shown with solid lines. Model measurements are plotted for almost two tide cycles whereas the field measurements cover only 12-hr time spans. Model velocities have been scaled to prototype-scale units of cm/s and the tide elevations have been scaled to prototype-scale meters. The field tide record is for the actual time during which velocity measurements were made at the mooring station.

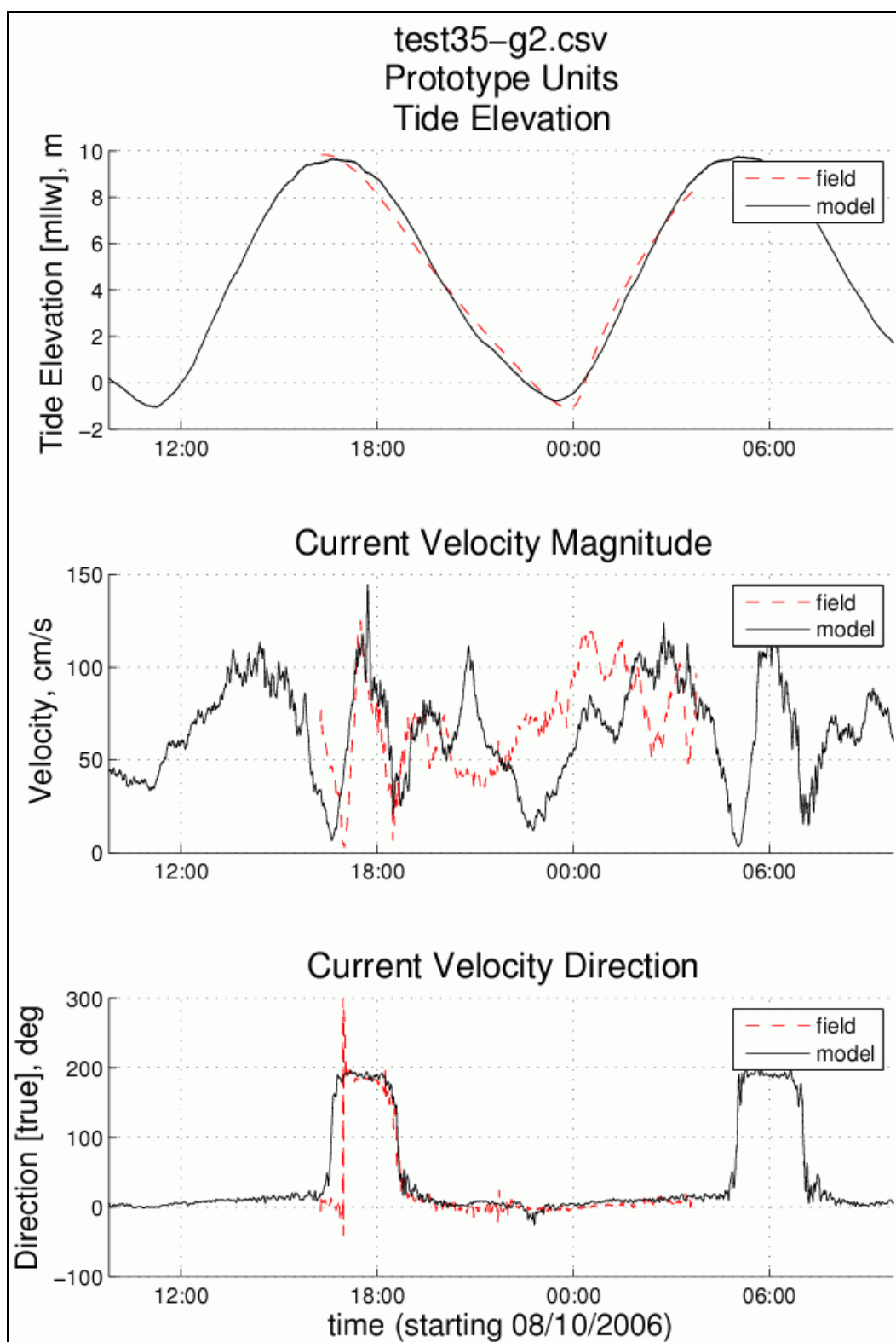


Figure 40. Initial model verification of velocity magnitude and direction at Station 2.

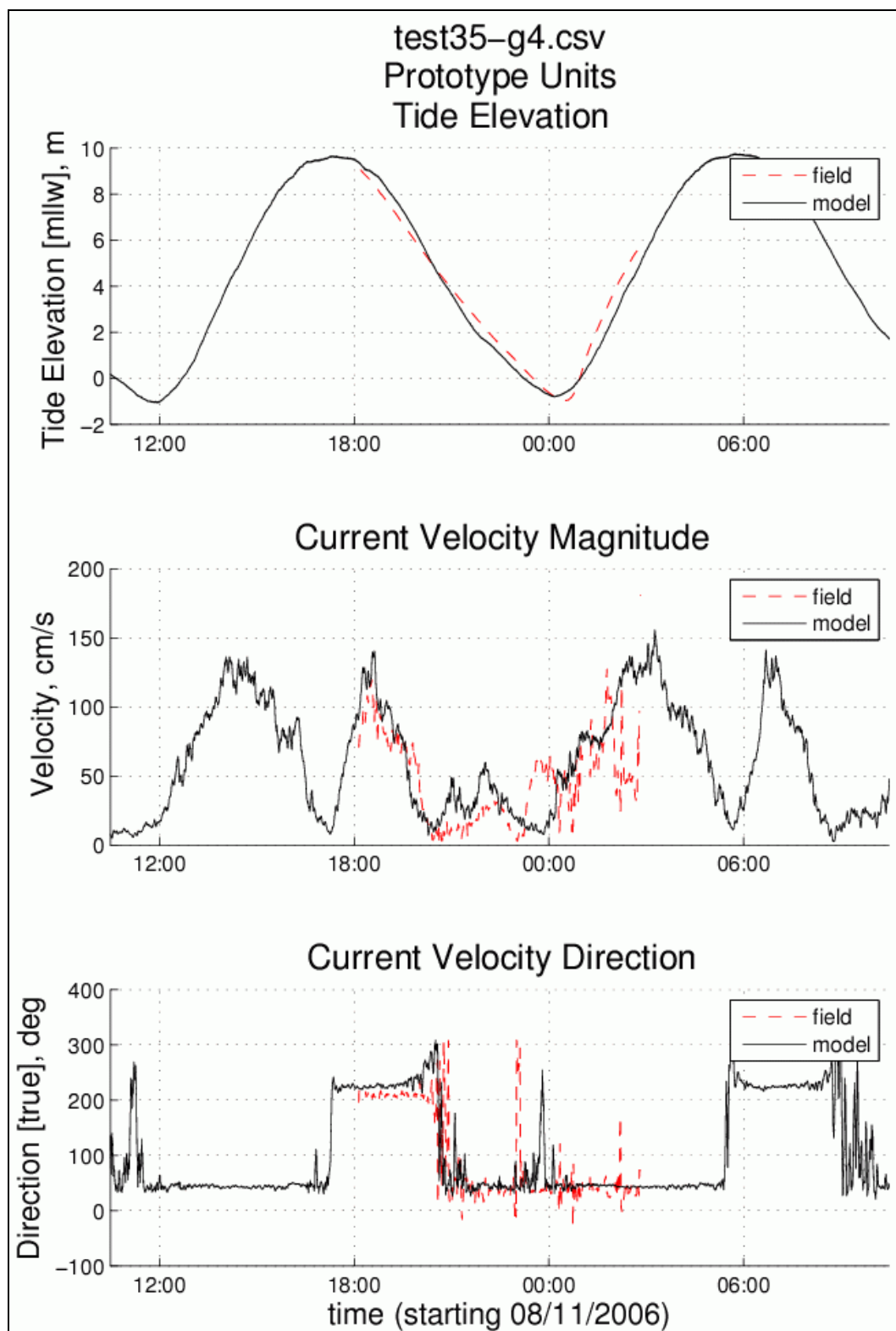


Figure 41. Initial model verification of velocity magnitude and direction at Station 4.

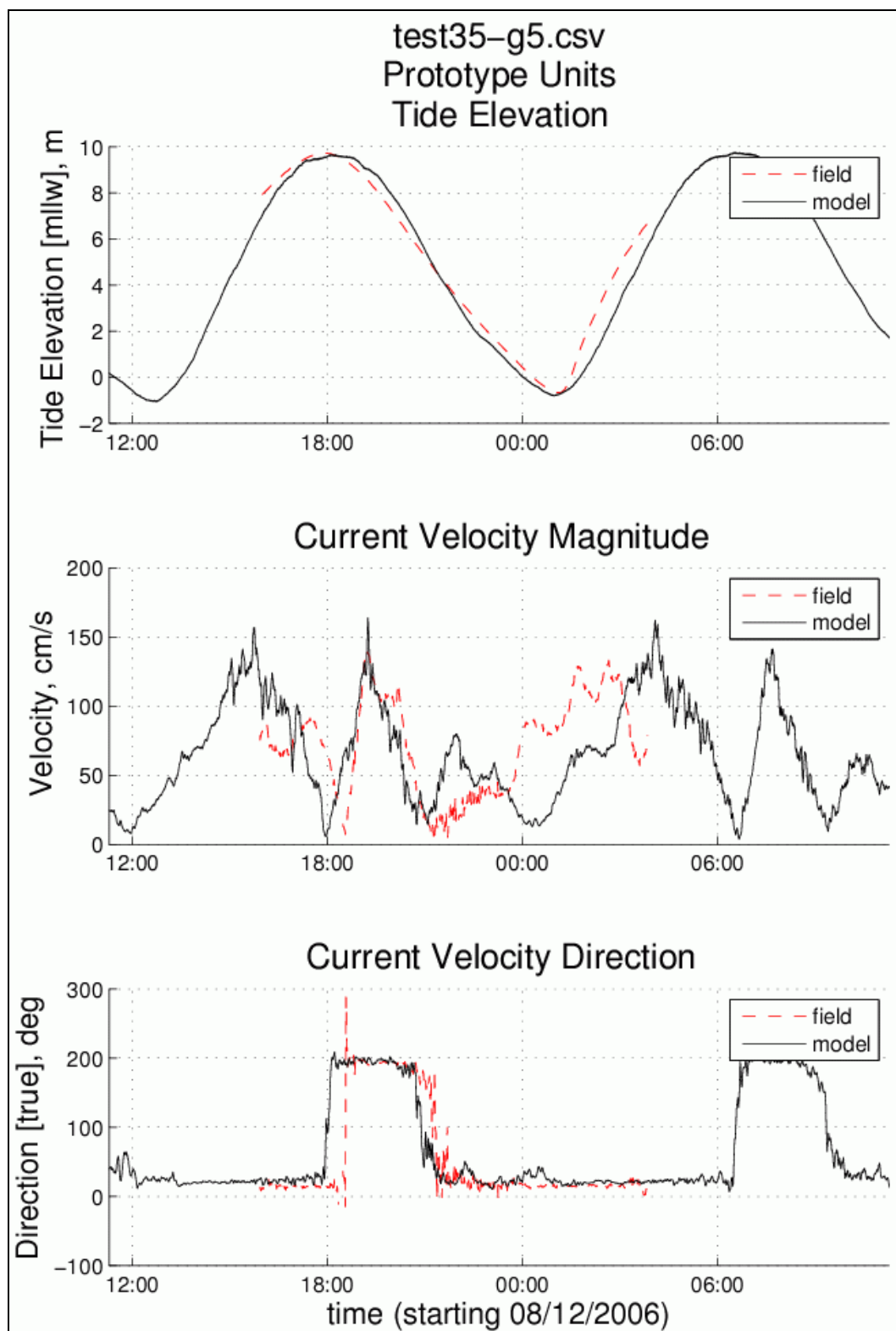


Figure 42. Initial model verification of velocity magnitude and direction at Station 5.

In all three comparisons, the tide was well reproduced by the model. At Station 2, which is closest to Cairn Point, Figure 40 indicates the velocity magnitude of the ebb flow is matched throughout the relatively short time that the flow is in a southerly direction past the Port. The magnitudes do not match as closely during the remainder of the ebb tide during development of the Cairn Point gyre. However, when the tide starts to flood, the velocity magnitude has a peak flood value similar to the field data. The velocity directions at Station 2 match very well.

The comparisons shown in Figure 41 for Station 4, toward the south end of the Port, exhibit very good correspondence between model and field measurements for both velocity magnitude and direction. At this location, the flow reversal during ebb tide is delayed while the gyre builds, so the duration of southerly-directed flow during ebb tide is longer than at Station 2.

Comparisons between field and model measurements at Station 5 (see Figure 42) are also deemed quite reasonable in both velocity magnitude and direction. The main difference is that the field velocity magnitudes moving upstream during the ebb tide are higher than measured in the model. This variance is related to the large-scale gyre structure, and further attempts to improve the verification were focused on trying to improve that portion of the comparison associated with the Cairn Point gyre.

During the month of September, 2008, the shoreline bathymetry upstream of Cairn Point on the east side Eagle Bay was modified to better match aerial photography. The shoreline was not accurately depicted by the original digital bathymetry used to construct the model. Figure 43 shows the section of Eagle Bay shoreline that was cut out of the model so that new bathymetry could be cast in its place. The Port of Anchorage is in the upper right side of the photograph. A similar shoreline adjustment was made to the western Eagle Bay shoreline in early October, 2008, also based on aerial photography overlain on the physical model contours.

Final verification results

After modification of the Eagle Bay shoreline in the Large-Area physical model, a handful of additional verification tests were completed. Comparison of model velocity measurements to velocity field measurements at Stations 2, 4, and 5 for test number 41 were slightly improved as shown by Figures 44, 45, and 46, respectively.



Figure 43. Modification of east Eagle Bay shoreline.

As in earlier verification tests, the model maximum tidal velocities matched the field measurements very well. The velocity directions were consistent between the field and model measurements, and the total duration of southerly- and northerly-directed flows was well reproduced in the physical model.

The main discrepancy between the model and the field data remained in the magnitude of velocity while the Cairn Point gyre was growing during the ebb tide. This gyre is essentially large-scale, chaotic turbulence that depends to a great extent on the Cairn Point bathymetry and shoreline. The differences between model and field velocity magnitudes could be the combination of errors introduced into the model by the following: (a) errors in the bathymetry values used in the model; (b) the aforementioned turbulence scale effect associated with model geometric distortion; and (c) field velocity magnitudes that were averaged over the depth whereas the model measurements were obtained at a fixed depth above the bottom.

Despite the differences between model and field data, the comparisons were judged to be good (much better than originally anticipated), and the model was considered to be both calibrated and verified to the extent

possible. Visiting Port pilots confirmed the flow patterns resembled those of Knik Arm during all phases of the tide.

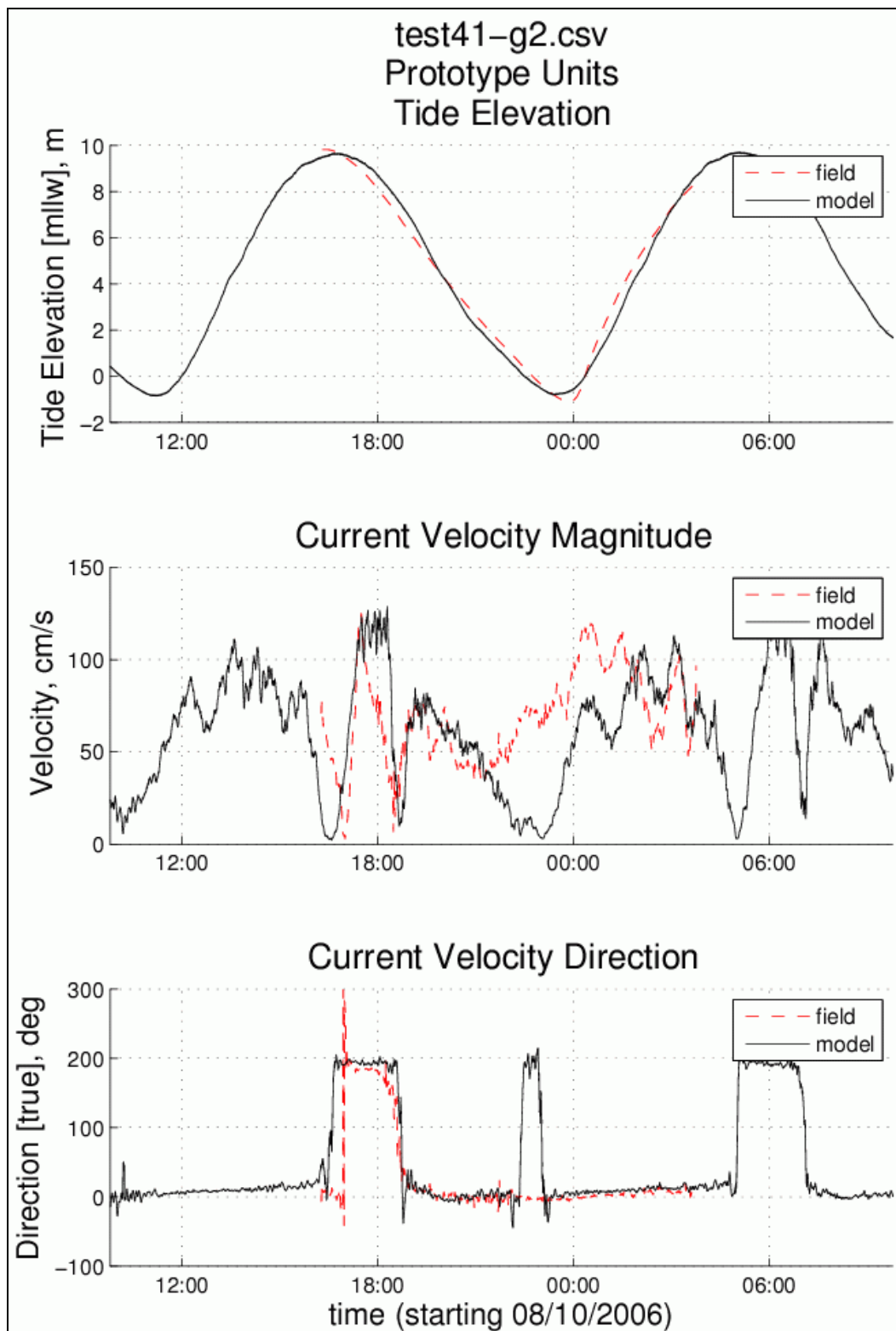


Figure 44. Final model verification of velocity magnitude and direction at Station 2.

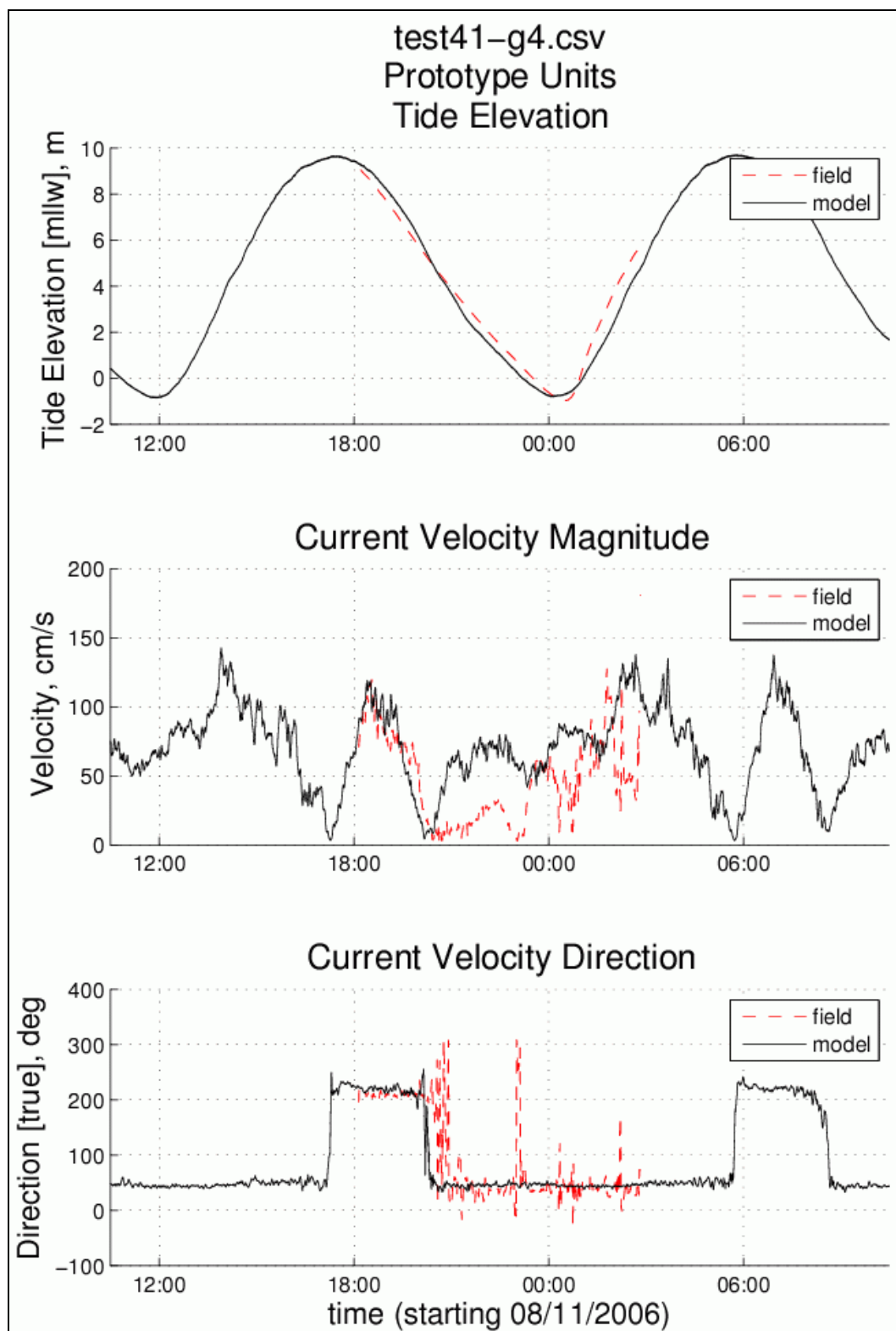


Figure 45. Final model verification of velocity magnitude and direction at Station 4.

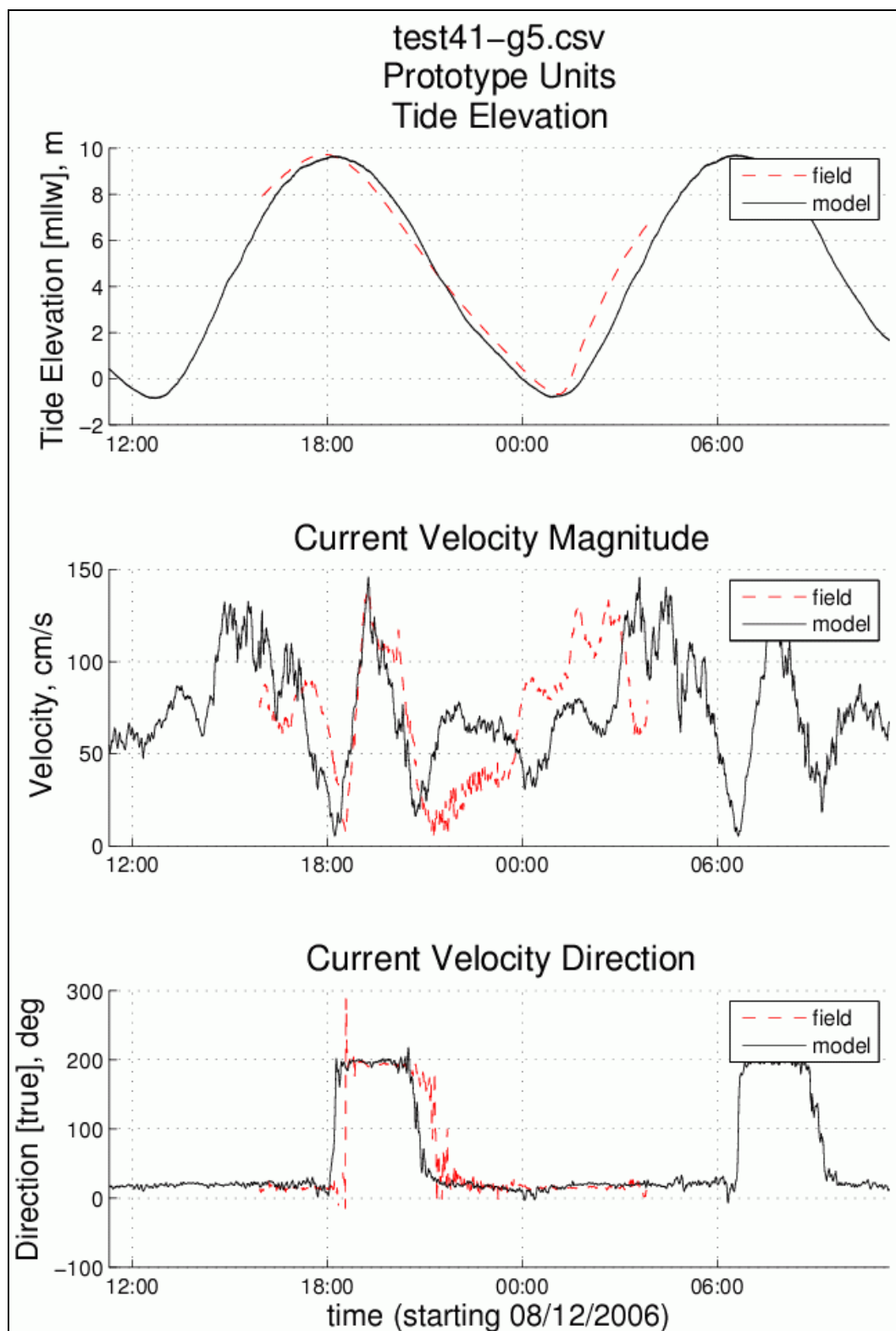


Figure 46. Final model verification of velocity magnitude and direction at Station 5.

6 Model Test Results

This chapter describes and presents tidal hydraulic results measured in 26 tests conducted in the Large-Area physical model of Knik Arm and the Port of Anchorage. Two different test series were conducted. The first test series measured tidal flow velocities at six fixed locations in the vicinity of the Port of Anchorage. Velocity comparisons were plotted showing the differences due to different phases of the Port expansion. The second test series examined in more detail flow velocities for the expansion phase that included the North Extension, South Backlands, and South Extension (see Figure 3).

Flow velocity changes due to Port of Anchorage expansion

This section includes an overview of the model configuration and measurement locations for this test series, plots of tidal velocity at each location for each Port expansion phase, selected comparisons of velocity between different phases, and a summary of observations from this test series.

Model configurations and measurement locations

A total of six locations near the Port of Anchorage in the Large-Area Model were selected for flow velocity measurements during a visit by POA engineers to Vicksburg. The purpose of these measurements was to compare differences in velocity at these six locations for the existing pre-expansion Port configuration and for all phases of the Port expansion plan. All locations were seaward of the completed Port expansion dock face.

Figure 47 shows the location of the ADV current measurement points superimposed on an aerial image obtained from Google Earth. All of the points, with the exception of Pt. DL, were selected from the original list provided by POA. The location designated as Pt. DL was a measurement position representing the dredge limits for the new Port expansion. This location was situated on the -50 ft contour, centered on the existing Port. The coordinates of the selected six ADV current measurement locations are listed in Table 6. Also listed in the table are the coordinates of a reference gauge location designated as Ref. ADV.

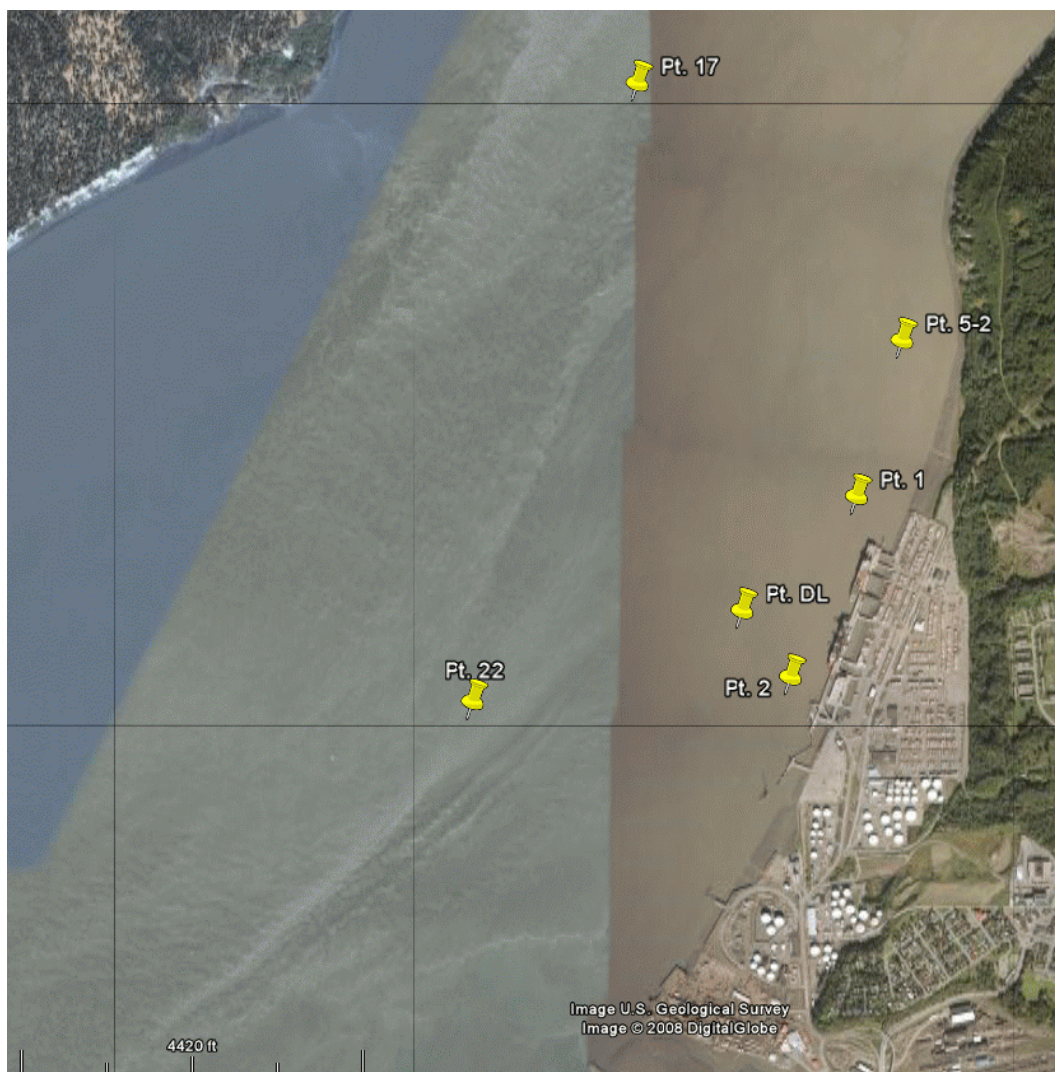


Figure 47. Locations of six ADV current measurement points.

Table 6. Coordinates of ADV current measurement points.

| ADV Pt. | Northing | Easting | Latitude | Longitude |
|-----------|------------|------------|------------------|-------------------|
| Pt. 1 | 2647087.41 | 1660250.67 | 61° 14' 43.01" N | 149° 53' 14.60" W |
| Pt. 2 | 2644757.25 | 1659401.71 | 61° 14' 20.07" N | 149° 53' 32.03" W |
| Pt. 5-2 | 2649102.74 | 1660836.02 | 61° 15' 02.84" N | 149° 53' 02.57" W |
| Pt. 17 | 2652418.71 | 1657408.12 | 61° 15' 35.56" N | 149° 54' 12.54" W |
| Pt. 22 | 2644429.31 | 1655293.53 | 61° 14' 16.90" N | 149° 54' 55.99" W |
| Pt. DL | 2645612.31 | 1658775.48 | 61° 14' 28.51" N | 149° 53' 44.80" W |
| Ref. ADV. | 2637014.83 | 1635359.01 | 61° 13' 03.97" N | 150° 01' 43.29" W |

Figure 48 shows an expanded view of the Knik Arm that includes the ADV reference gauge location. This location is in the middle of the channel well away from Point Woronzof and Point MacKenzie, and it was anticipated that the tidal flow magnitude and direction at this location would not be affected by the Port expansion.

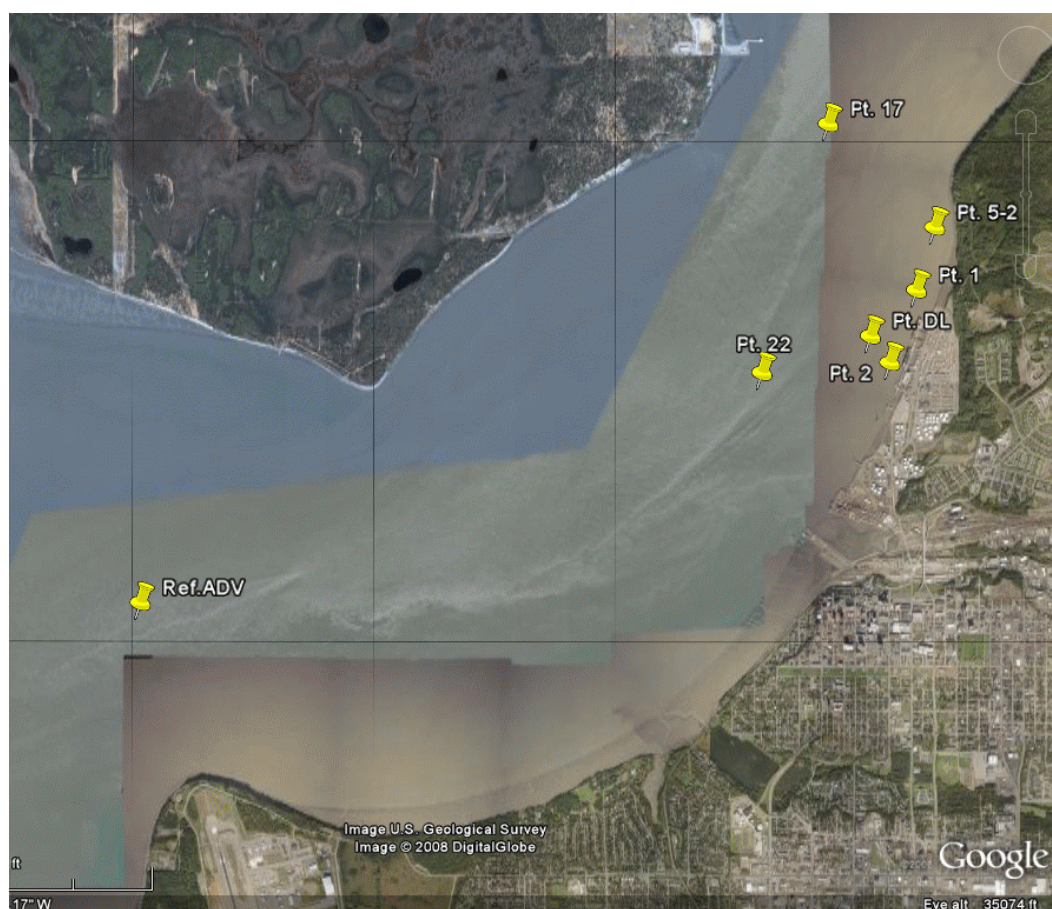


Figure 48. Location of the reference ADV current measurement gauge.

The reason for establishing a reference location where velocity is not expected to change was to provide a consistency check between tests in this series. There were more measurement points (6) than available current meters (3). Therefore, one of the ADV current meters was permanently stationed at the Ref. ADV position for all tests in the series, and the other two ADV gauges were moved to different locations for each repeat test. The initial reference velocity signal over a tide cycle with the ADV reference gauge positioned at Ref. ADV was obtained with the other two gauges in their original calibration locations. Good comparison of the calibration gauges to the previous calibration run was an indication that the new reference velocity signal was valid.

For each Port expansion phase it took three repeat tests to measure velocities at the six locations using the two available gauges. Comparisons of the reference velocity at the Ref. ADV gauge to the velocities measured for the three tests assured the model engineers that all runs were very similar because the runs reproduced the same velocity record at the Ref. ADV gauge.

Port configurations installed in the Large-Area Model for this test series included: (a) the pre-expansion condition, termed *Existing*; (b) addition of the North Backlands and North Extension, termed *First Port Expansion*; (c) addition of the South Backlands and South Extension, termed *Second Port Expansion*; (d) addition of the North Replacement, termed *Third Port Expansion*; and (e) addition of the South Replacement, termed *Full Expansion*. These expansion configurations are shown on Figures 49 and 50, along with the four ADV measurement locations close to the Port.

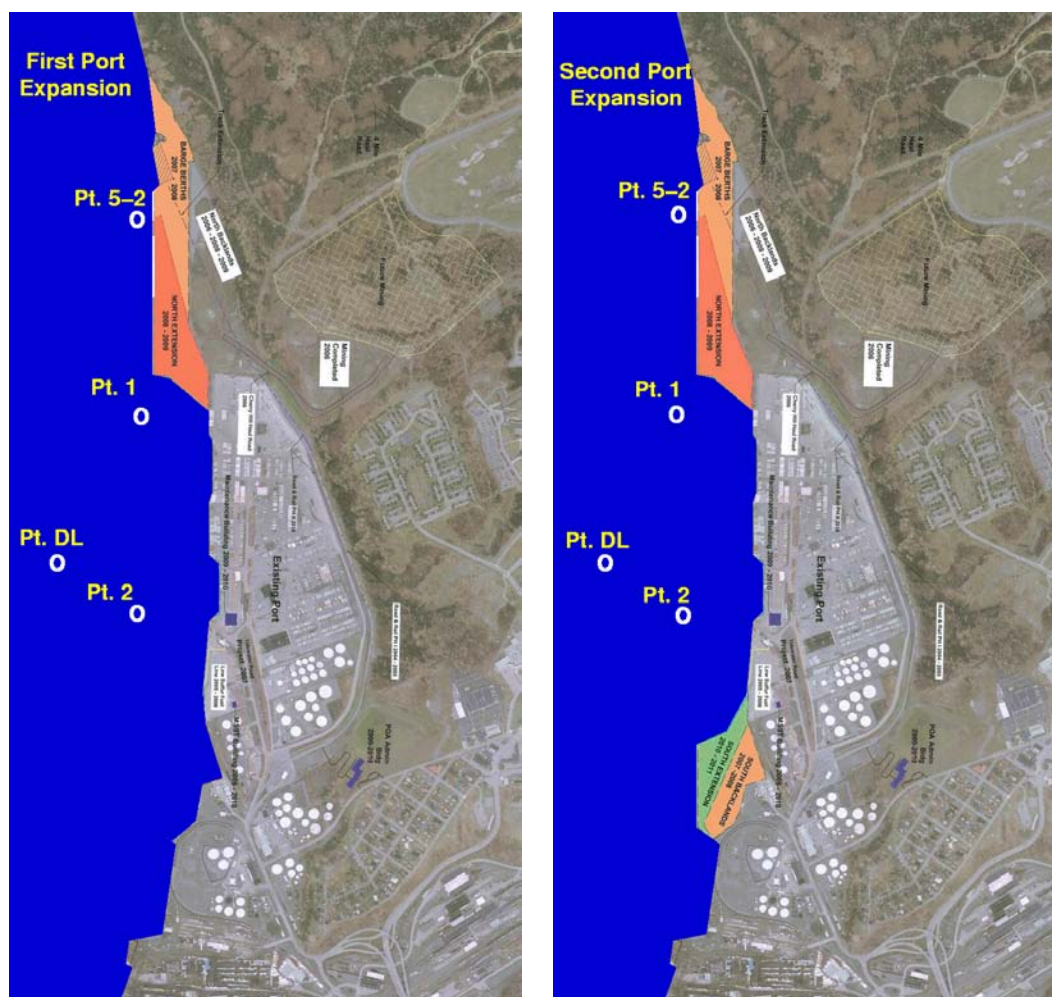


Figure 49. First and Second Port expansion configurations.

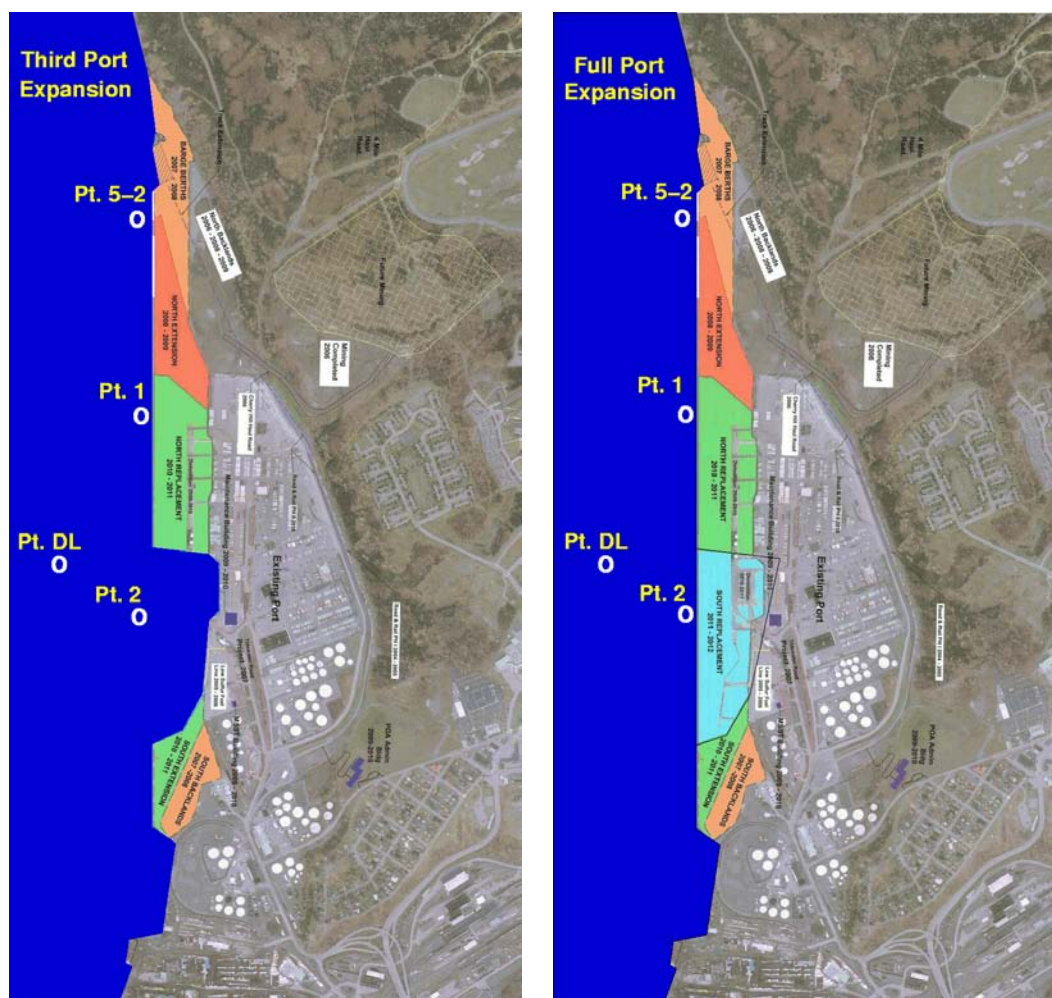


Figure 50. Third and Full Port expansion configurations.

Flow velocities for each Port expansion phase

Summary of tests

Flow velocity measurements at the six selected ADV locations for the existing condition and the four Port expansion configurations began during the last few days of October, 2008. The test series ran through mid-November, 2008, and it included a total of 19 individual tests. Sixteen of the tests met the criteria for success, and three tests failed because of inconsistent tide cycles (non-repeating).

The test series is summarized in Table 7. Current meter locations given in columns 3 and 4 of the table refer to the stationary points indicated on Figures 47-50. Columns 5 and 6 describe the Port configuration for each test as defined by Figures 49 and 50. As many as three tests could be completed during a full work day. It took an hour or more to establish a still

water level at mllw before each test, and each test of four tide cycles lasted nearly an hour. Sometimes the tests were terminated after three tide cycles if it appeared that data collection was successful and the tide cycle was repeating.

Table 7. Summary of Port expansion tests.

| Test ID | Date | Current Meter Locations | | Expan. Phase | Comments |
|---------|----------|-------------------------|---------|--------------|---------------------------|
| | | ADV 4 | ADV 5 | | |
| Test 44 | 10/29/08 | St. 4 | St. 5 | Existing | Reference velocity test |
| Test 46 | 10/30/08 | Pt. 2 | Pt. 1 | Existing | Pre-expansion condition |
| Test 48 | 10/30/08 | Pt. DL | Pt. 5-2 | Existing | Pre-expansion condition |
| Test 49 | 10/31/08 | Pt. 22 | Pt. 17 | Existing | Pre-expansion condition |
| Test 50 | 11/12/08 | Pt. 22 | Pt. 17 | Full | Expansion complete |
| Test 51 | 11/12/08 | Pt. DL | Pt. 5-2 | Full | Expansion complete |
| Test 52 | 11/12/08 | Pt. 2 | Pt. 1 | Full | Expansion complete |
| Test 53 | 11/17/08 | Pt. 2 | Pt. 1 | Third | All but South Replacement |
| Test 54 | 11/17/08 | Pt. DL | Pt. 5-2 | Third | All but South Replacement |
| Test 55 | 11/17/08 | Pt. 22 | Pt. 17 | Third | All but South Replacement |
| Test 56 | 11/18/08 | Pt. 22 | Pt. 17 | Second | North and south expansion |
| Test 57 | 11/18/08 | Pt. DL | Pt. 5-2 | Second | North and south expansion |
| Test 58 | 11/18/08 | Pt. 2 | Pt. 1 | Second | North and south expansion |
| Test 59 | 11/19/08 | Pt. 2 | Pt. 1 | First | North expansion only |
| Test 61 | 11/19/08 | Pt. DL | Pt. 5-2 | First | North expansion only |
| Test 62 | 11/19/08 | Pt. 22 | Pt. 17 | First | North expansion only |

Consistency checks

Test 44 established the reference velocity at location Ref. ADV, shown in Figure 48. Velocities at that same location gathered in subsequent tests were compared to the Test 44 reference velocity to assure consistency between model simulations. Figure 51 gives an example of a consistency check between Test 48 and the reference Test 44. The velocities above about 200 cm/s (prototype scale) are not real because the current meter range was not adjusted properly for higher velocities. This was corrected for Test 50 and all subsequent tests. For the velocity range below 200 cm/s the two records show good correspondence.

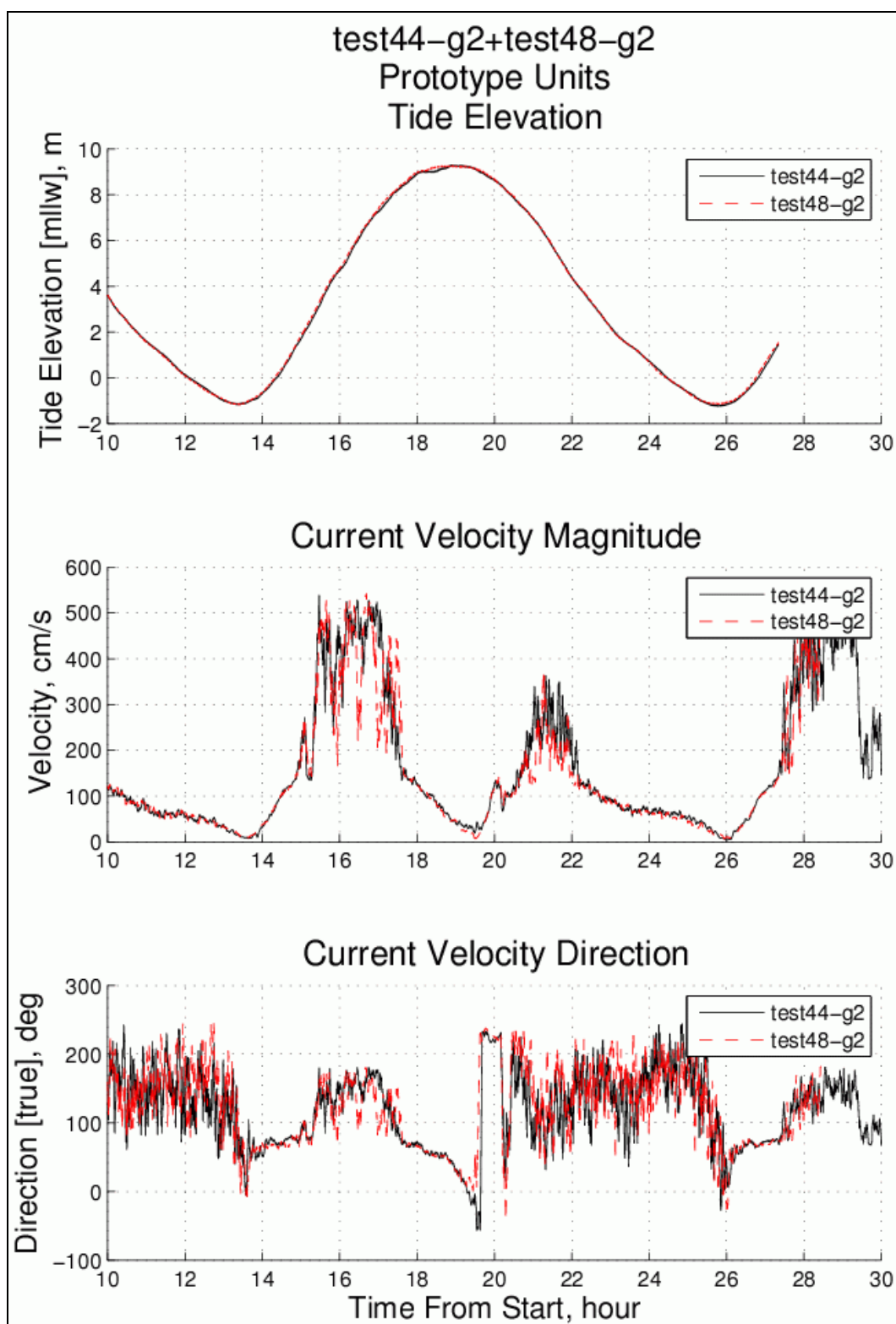


Figure 51. Consistency check for Test 48 at location Ref. ADV.

Figure 52 shows the consistency check for Test 50 after the reference current meter ranges had been corrected. Maximum velocities are now correct and indicate a maximum tidal velocity of about 200 cm/s (6.6 ft/s or 3.9 kts). Test 50 became the consistency check reference velocity for the remaining tests in the series.

An example of a consistency check using Test 50 as the reference velocity is shown in Figure 53. All 15 of the consistency check plots are given in Appendix A.

Velocity plots

Five different Port configurations were tested (Existing, First Expansion, Second Expansion, Third Expansion, and Full Expansion) with velocity measurements recorded at six locations. Appendix B contains plots of all of the velocity measurements for each Port configuration. The plots of measurements for the pre-expansion Port configuration (Existing) are presented in Figures 54-56 as an example. Comparisons between different Port configurations are presented in the next section.

Figure 54 shows the measured velocities at Pt. 1 (solid line) on the north end of the existing dock face and at Pt. 2 (dashed line) on the south end of the Port (see Figure 47). Similar velocity magnitudes are seen at both locations with maximum values of about 125 cm/s (4.1 ft/s or 2.4 kts). The difference in flow direction is mainly due to the shoreline orientation at those two locations. Pt. 1 (north end of Port) is aligned in a more northerly direction. During ebb tide the flow reversal starts earlier at the north side of the Port, as indicated by the direction plot for Pt. 1. As the gyre grows in the downstream direction, the ebb flow reverses at Pt. 2.

Figure 55 plots velocities for Pt. 5-2, farther north of the Port (solid line), and the velocities at Pt. DL (dashed line), representing the Port dredging limit (see Figure 47). The maximum flow velocities at the Pt. DL dredge limit during flood tide reach about 180 cm/s (5.9 ft/s or 3.5 kts), but the ebb velocities are reduced. Also note that the duration of southerly-directed flow during ebb tide is longer than at Pt. 5-2, and the eventual flow reversal at Pt. DL doesn't happen until about mid-tide of the ebb cycle.

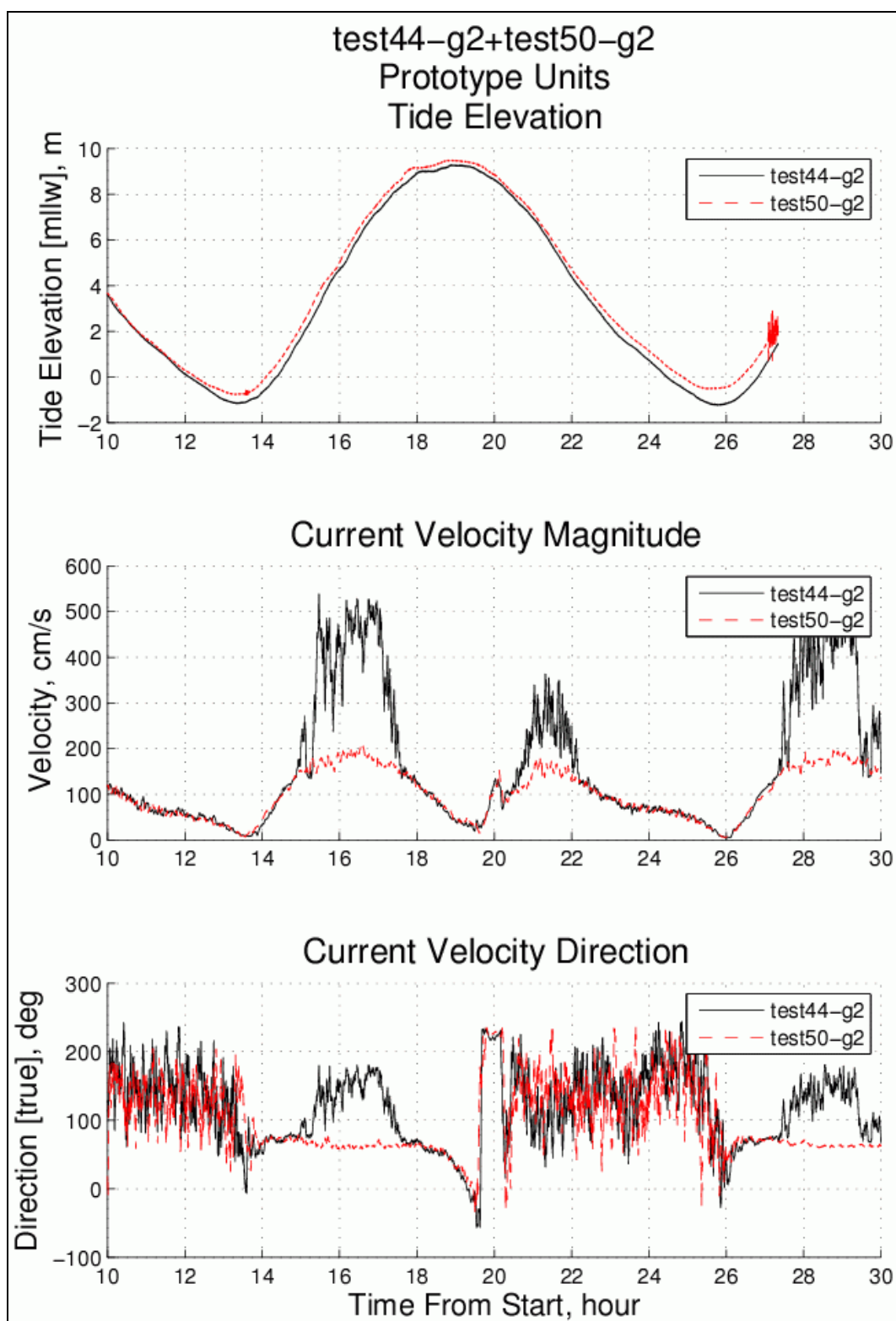


Figure 52. Consistency check for Test 50 at location Ref. ADV.

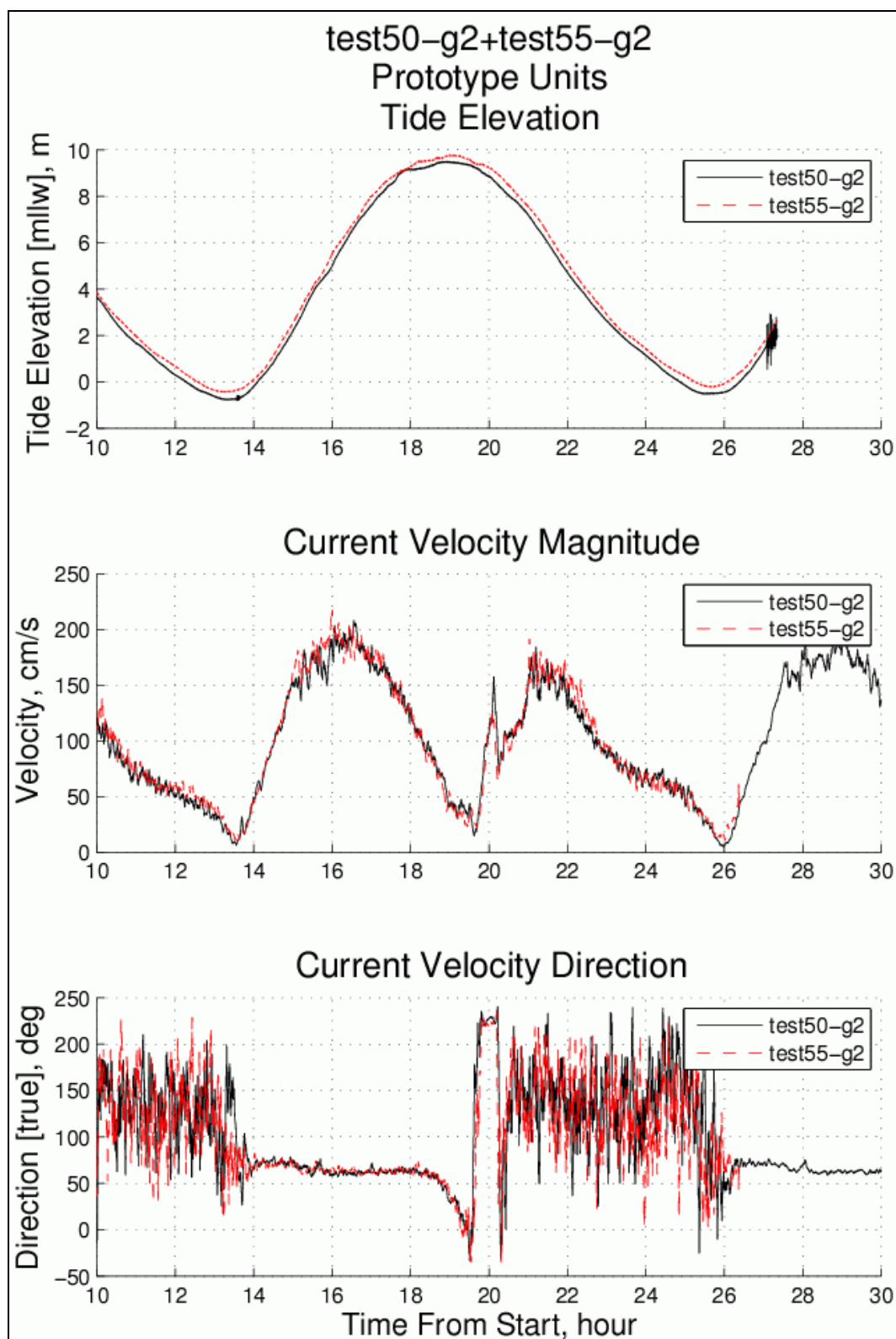


Figure 53. Consistency check for Test 55 at location Ref. ADV.

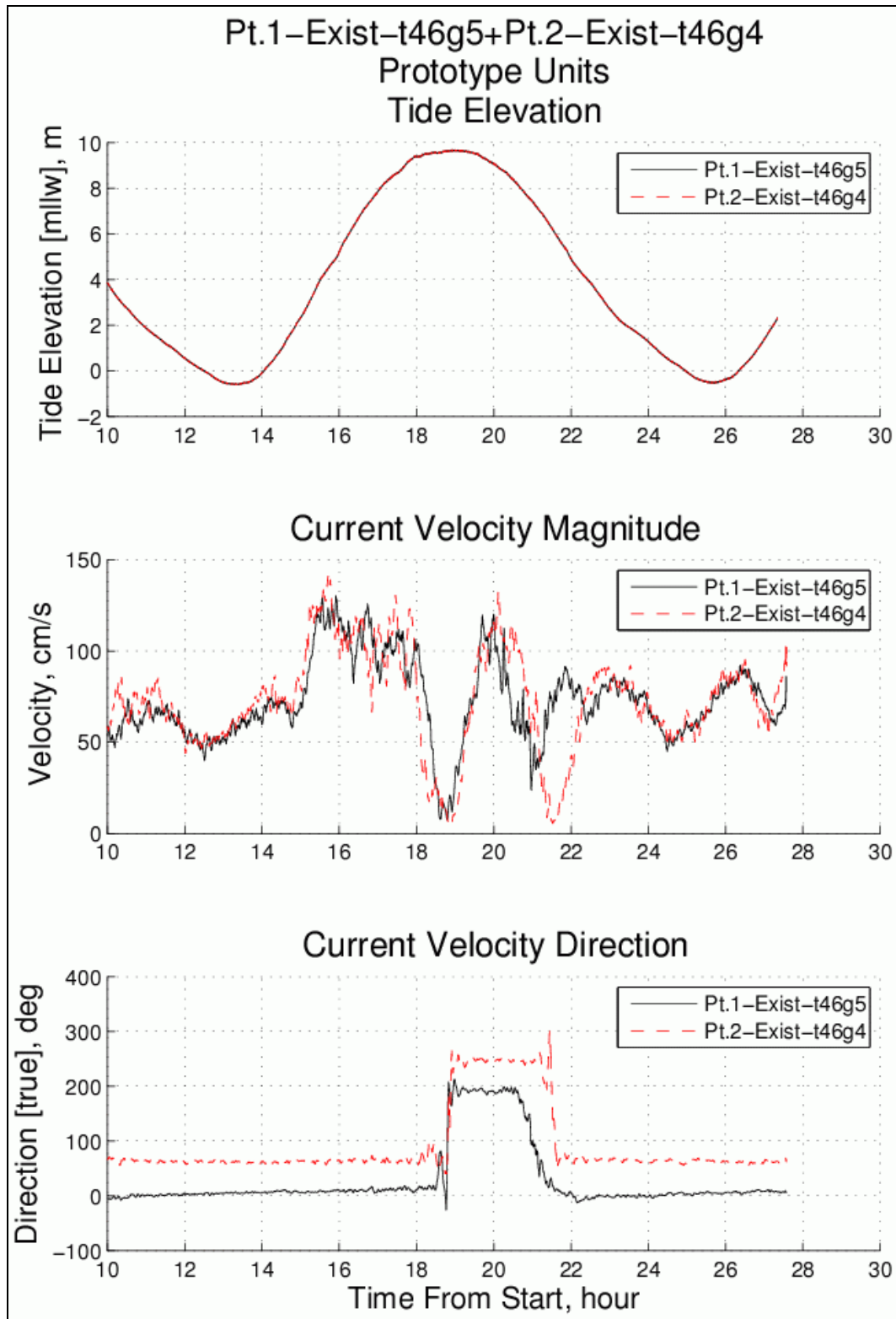


Figure 54. Velocity measurements at Pt. 1 and Pt. 2 (Existing configuration).

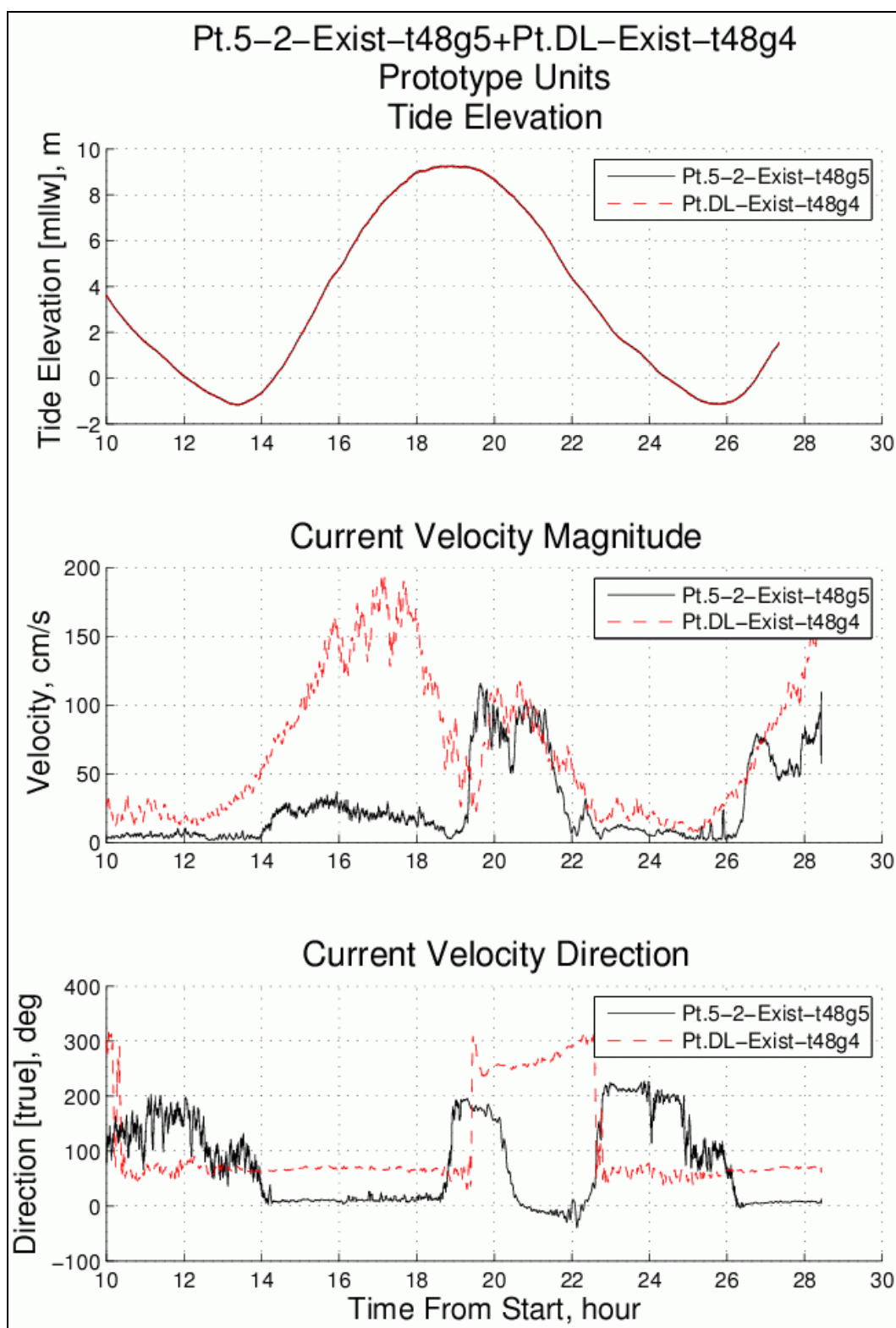


Figure 55. Velocity measurements at Pt. 5-2 and Pt. DL (Existing configuration).

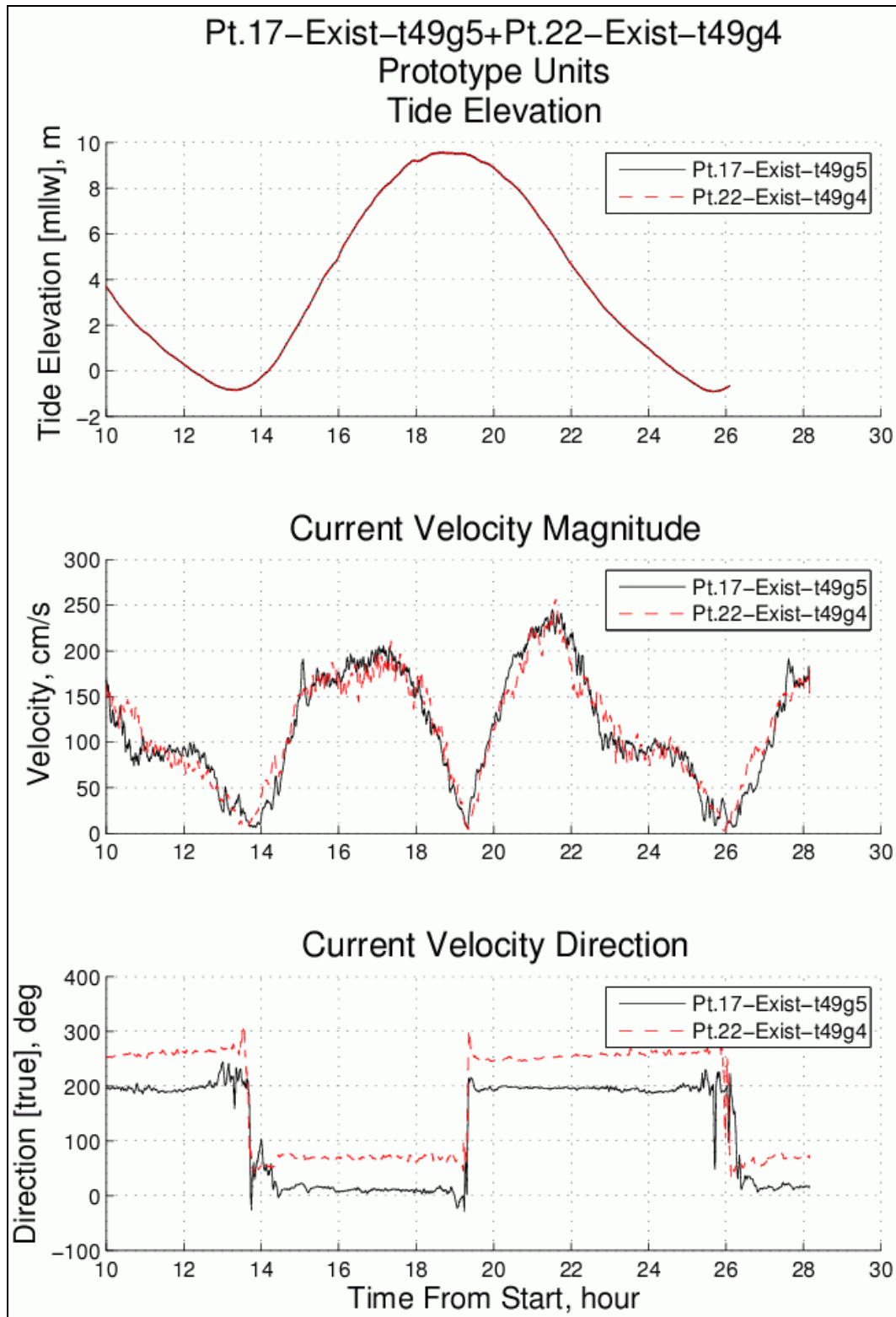


Figure 56. Velocity measurements at Pt. 17 and Pt. 22 (Existing configuration).

Figure 56 presents an interesting comparison between measurements at gauge locations Pt. 17 (solid line) and Pt. 22 (dashed line). The magnitudes are nearly identical, and the velocity records are nearly in phase throughout the complete tide cycle. There is no appreciable lag apparent between the two locations. Observations of floating tracers on the water surface during subsequent tests indicated points Pt. 17 and Pt. 22 were more or less on a flow pathline. In other words, tracers passing over Pt. 22 also passed over Pt. 17 to the north during flood with the reverse happening during ebb tide. The only difference between the two velocity records was the change of flow direction due to the main channel orientation. The maximum ebb velocity was approximately 240 cm/s (7.9 ft/s or 4.7 kts).

Flow velocity comparisons between expansion phases

The purpose of collecting velocity measurements at the same locations for the different phases of Port expansion was to predict changes to the flow condition that would occur at each location. The most interesting comparison was between the pre-expansion Port (Existing) and the completed Port expansion (Full). Figures 57-62 present comparisons for all six measurement locations. Pre-expansion velocity magnitudes and directions are shown by the solid line and the completed Port expansion is given by dashed lines.

Figure 57 shows the comparison at Pt. 1, located north of the pre-expansion dock face. The only difference seen at this location was an increase in the southerly-directed ebb tide maximum from about 110 cm/s to about 140 cm/s for the completed Port expansion. This increase was equivalent to about 0.6 kts or about a 27 percent increase in maximum current speed. Maximum velocities during flood tide were similar for both Port configurations. Farther south at Pt. 2, a similar increase in maximum ebb flow speed was seen, as shown in Figure 58. Also, the duration of the southerly-directed ebb flow was a bit longer for the completed Port expansion.

Installation of the North Replacement changed the nature of the gyre formation at Pt. 5-2 (see Figure 59). The current magnitudes were not large, and the maximum magnitudes did not increase. However, the changes in flow direction during ebb tide were substantially different for the completed Port expansion. In other words, the new boundary altered the gyre development in this region.

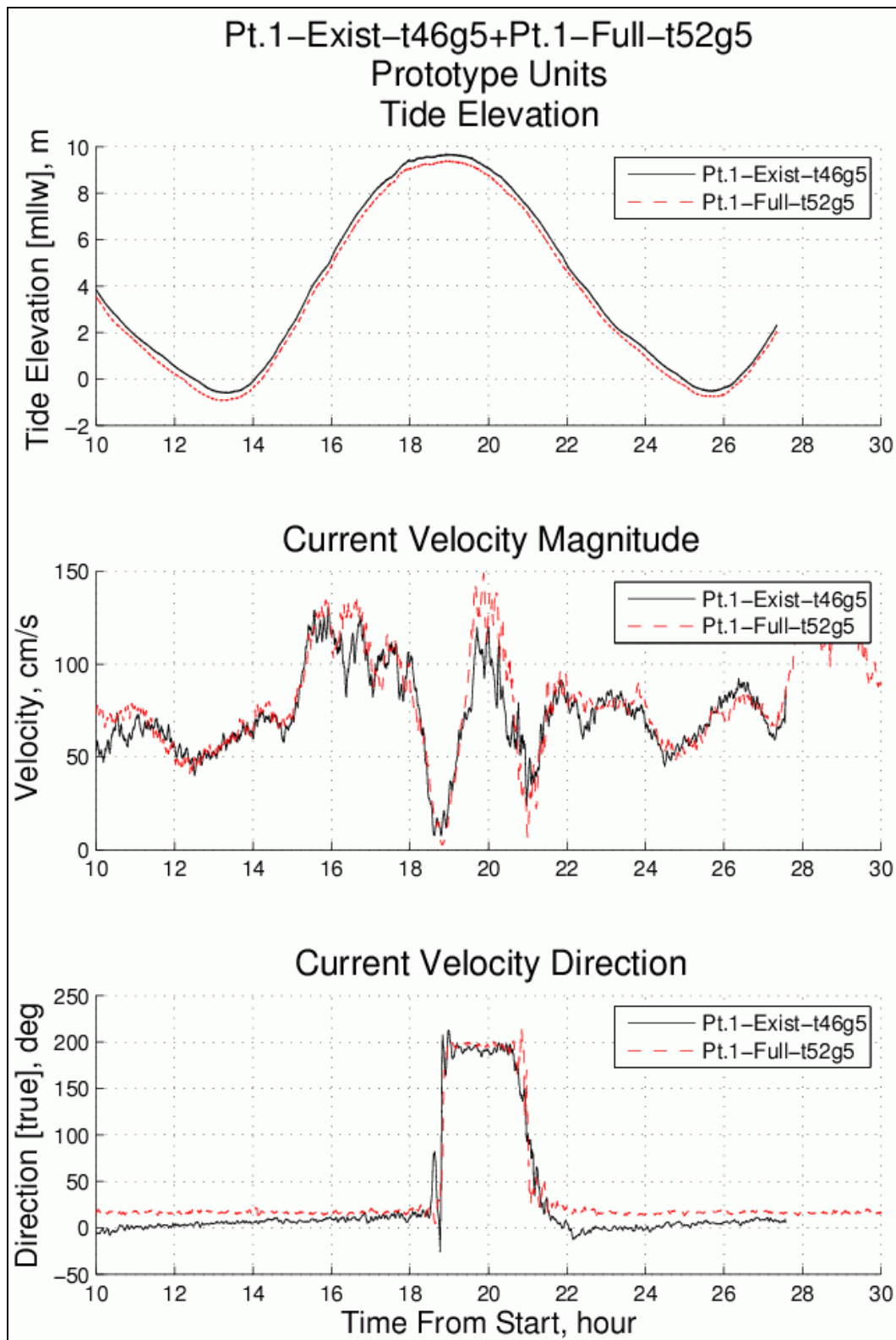


Figure 57. Comparison of pre-expansion configuration to Full Port Expansion at Pt. 1.

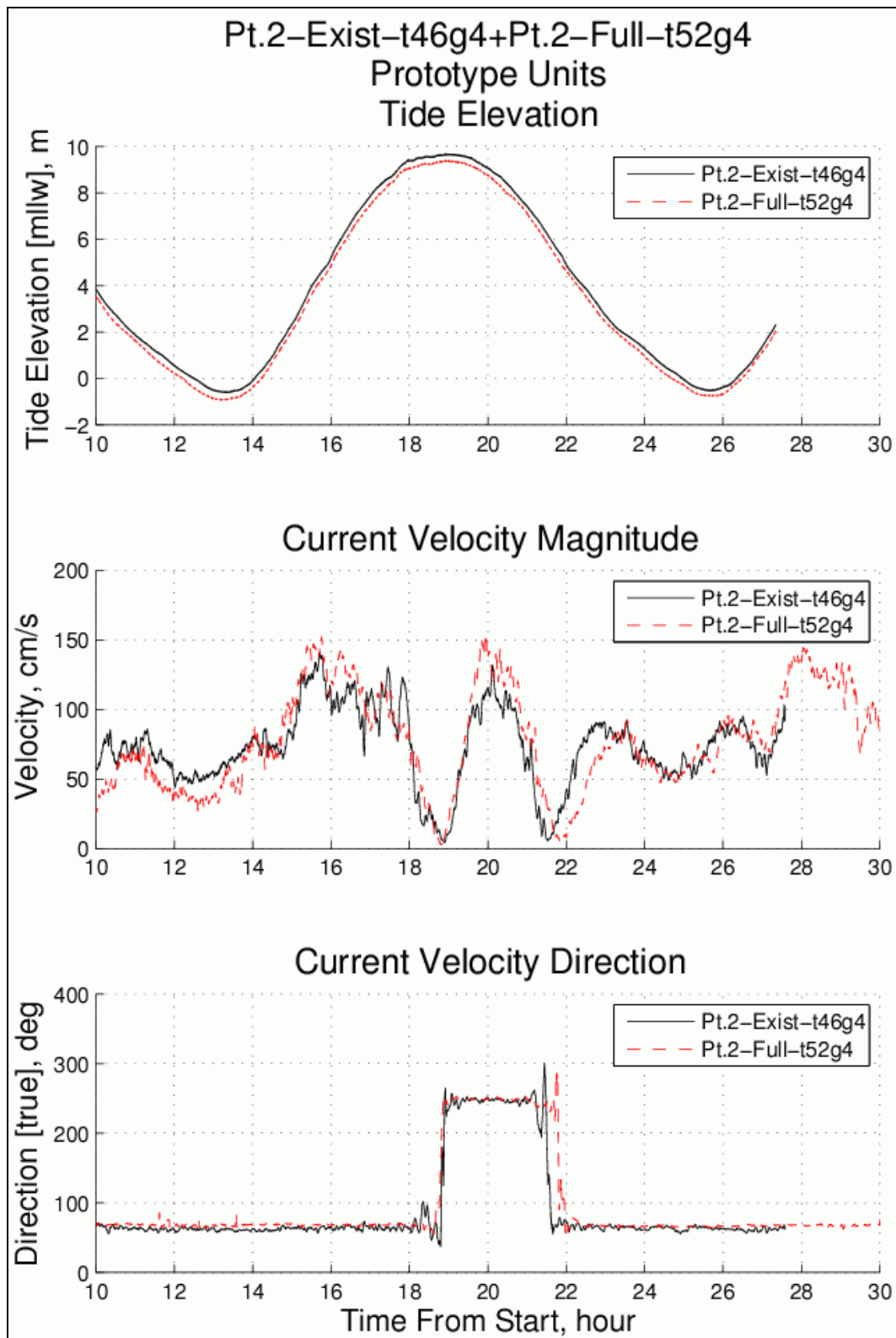


Figure 58. Comparison of pre-expansion configuration to Full Port Expansion at Pt. 2.

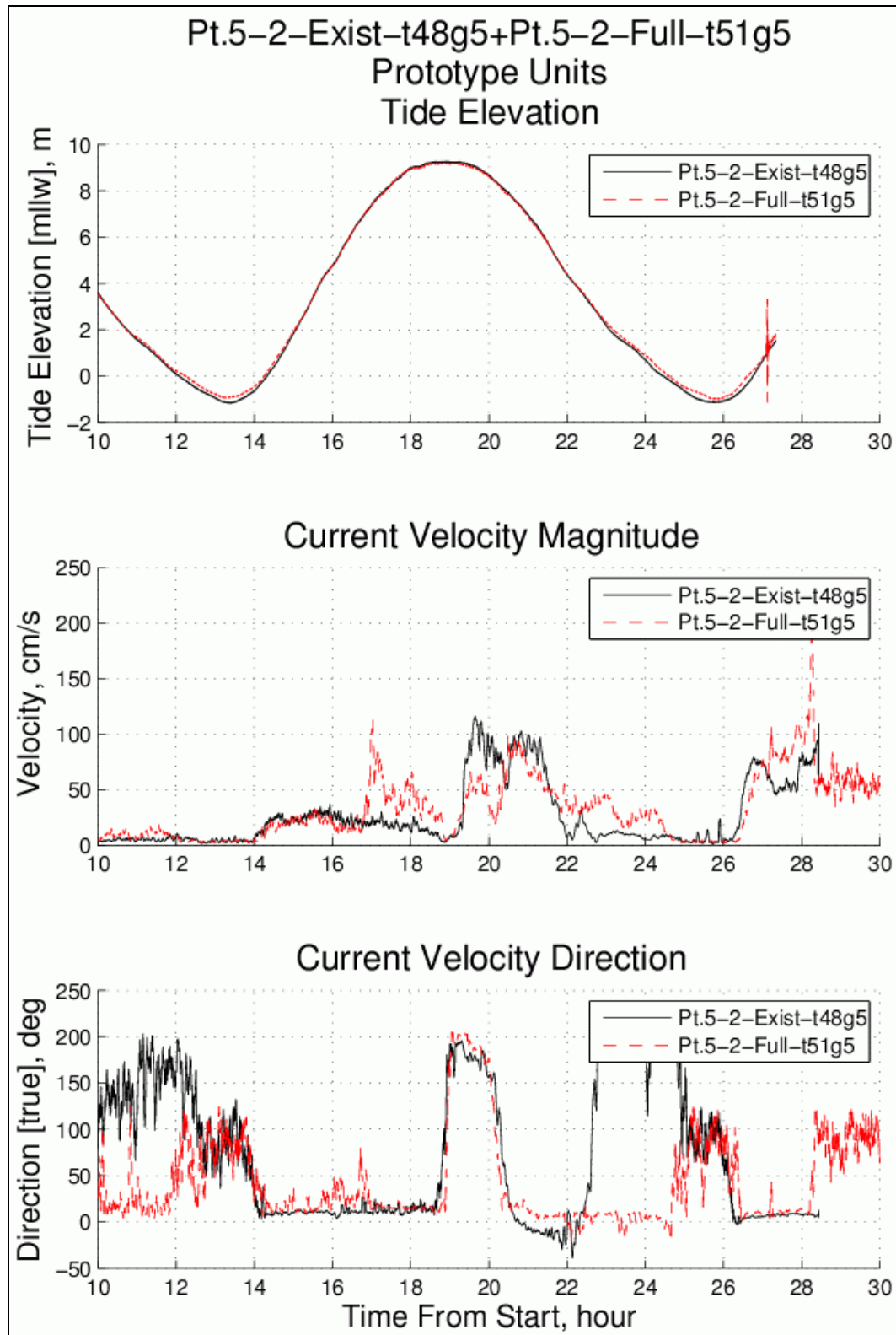


Figure 59. Comparison of pre-expansion configuration to Full Port Expansion at Pt. 5-2.

Comparisons between the pre-expansion configuration and the completed Port expansion at Pt. DL, Pt. 17, and Pt. 22 are shown on Figures 60, 61, and 62, respectively. The flow magnitudes were basically unchanged for these three locations, indicating that Port expansion does not alter the flow patterns farther out in the channel. The one exception was some variation in flow direction at Pt. DL toward the end of the ebb cycle when the flow magnitudes were small.

The measurement locations discussed in this section were located outside the completed Port expansion footprint. The differences were not significant, and the velocity magnitudes can be used to access mooring requirements at the dock face of the new Port when it is completed.

During testing in early December, 2008, engineers and planners from the Alaska District visited ERDC to observe operation of the Large-Area physical model with various Port expansion configurations in place. No measurements were recorded, but flow visualization techniques were used to indicate flow patterns and current speed. The Alaska District observers were particularly interested in areas of reduced flow velocity within the boundaries of authorized maintenance dredging for the Port of Anchorage.

Decreased flow magnitudes allow suspended sediment to settle out of the water column, and mobilization of deposited sediment is less likely to occur if the flow speed is slow. At locations with reduced tidal flow, dredging requirements will increase and the District must plan accordingly to maintain the navigation project at authorized depths.

The Port expansion phase showing the most obvious potential shoaling problem was the configuration after completion of the North and South Extensions. This configuration was denoted as the Second Expansion, as shown on the right-hand side of Figure 49. The two measurement points of interest were Pt. 1 and Pt. 2.

Figure 63 compares velocities between the Existing and Second Expansion configurations at Pt. 1, located near the southern end of the North Extension. With the Second Expansion in place, the flow magnitudes were significantly decreased during the latter portion of ebb tide and the beginning of flood tide. This decrease corresponded to a slow-moving stationary eddy that set up in the region just south of the North Extension. During the peak of the flood tide, the flow comparison was similar; but during the

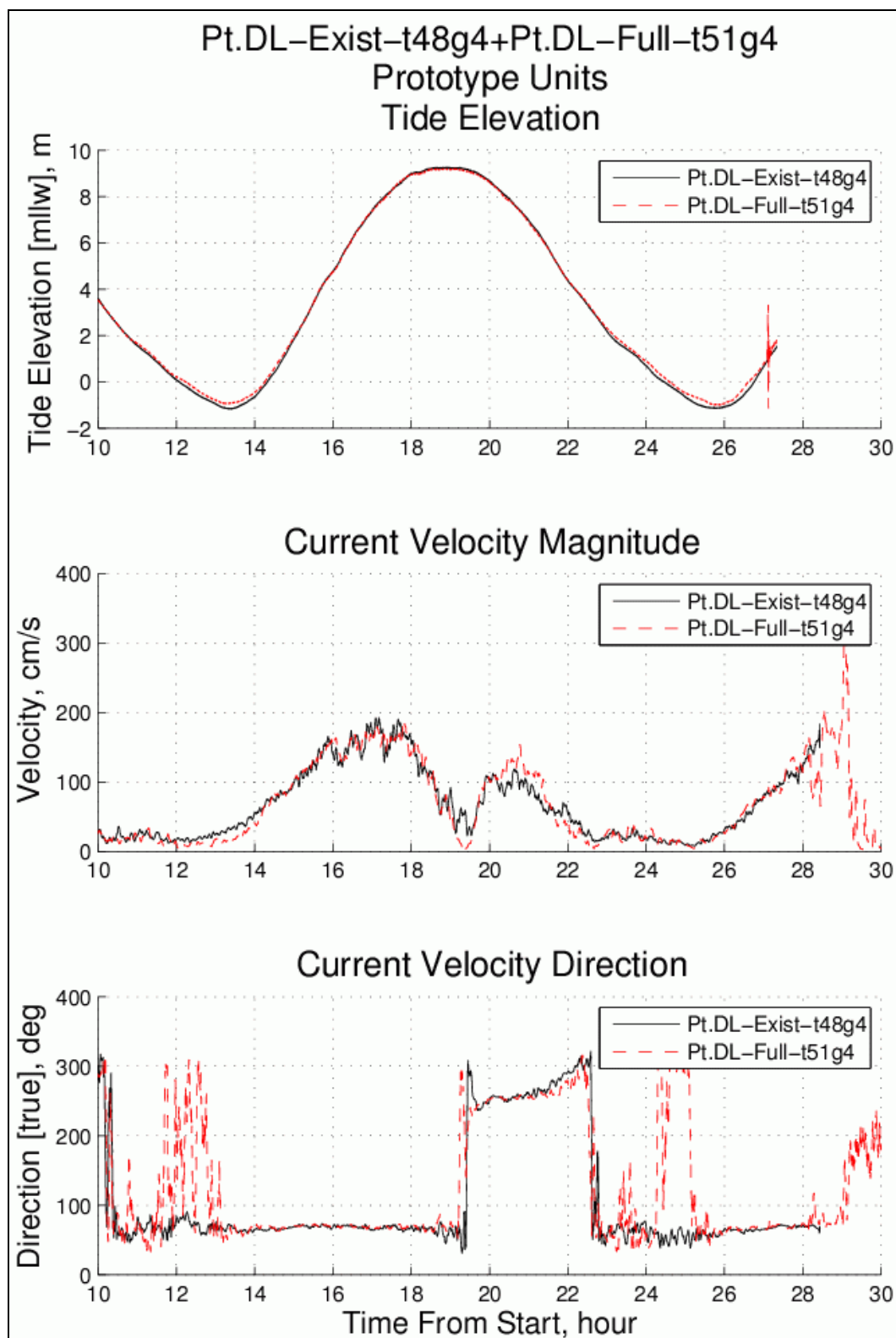


Figure 60. Comparison of pre-expansion configuration to Full Port Expansion at Pt. DL.

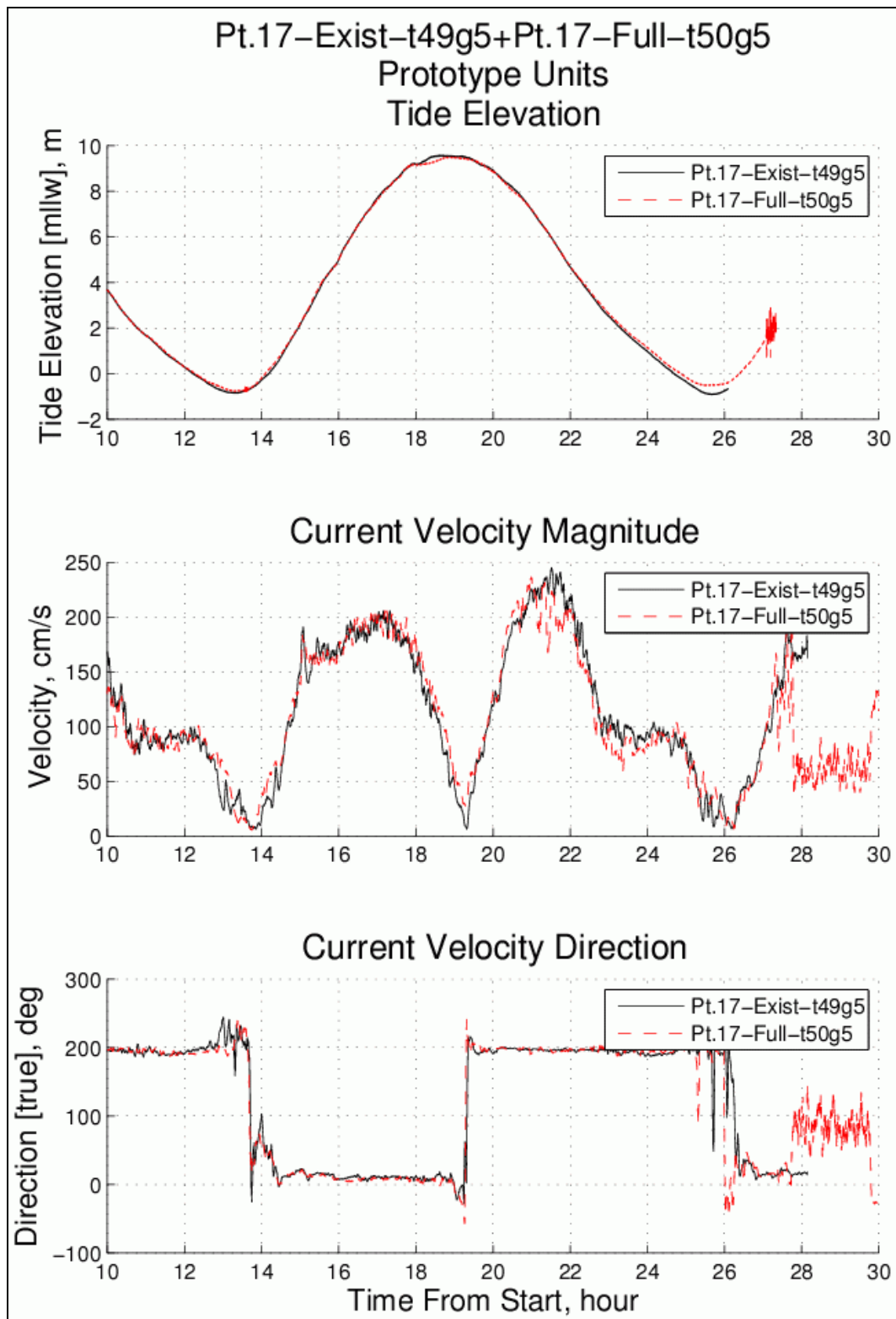


Figure 61. Comparison of pre-expansion configuration to Full Port Expansion at Pt. 17.

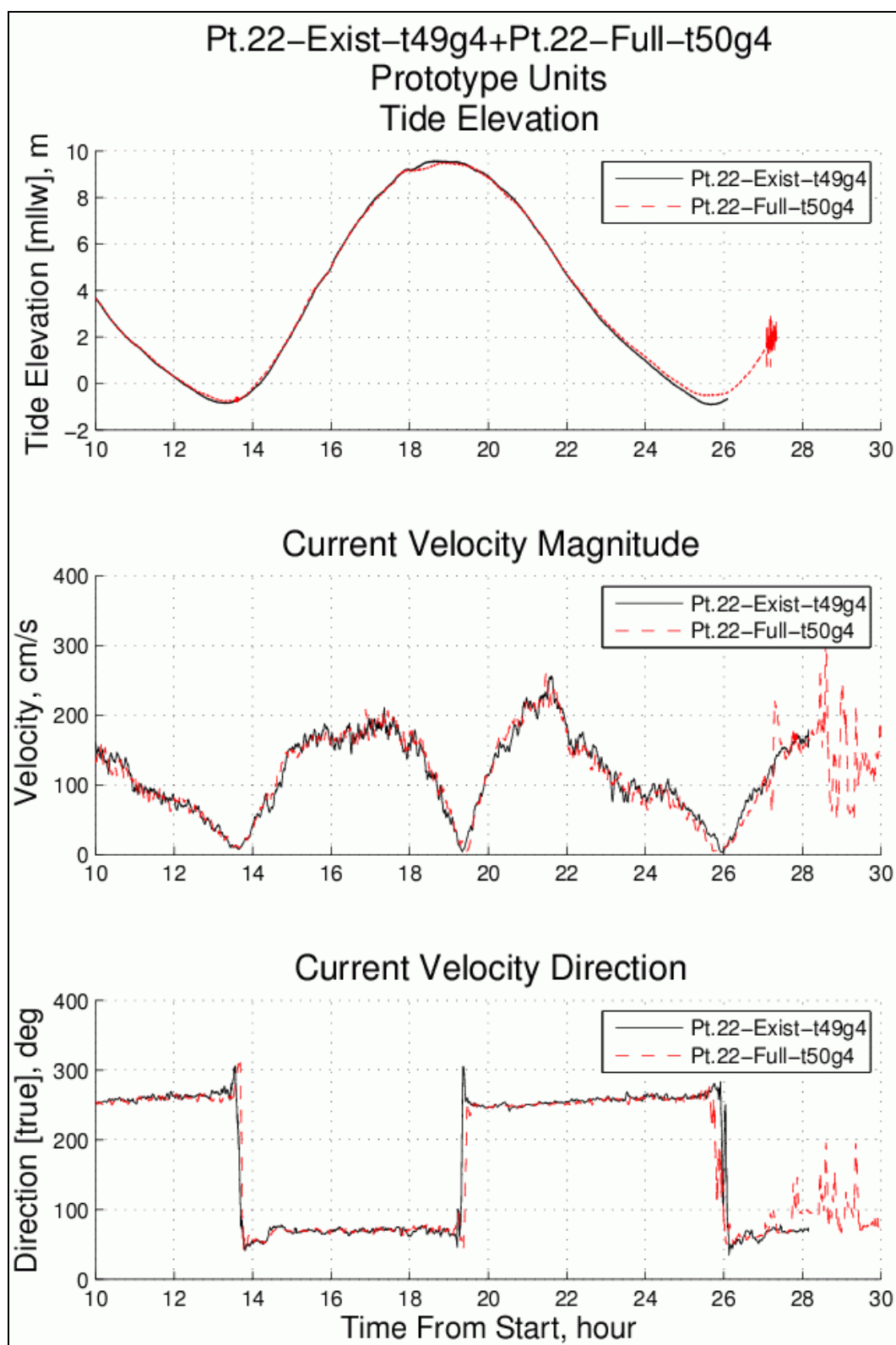


Figure 62. Comparison of pre-expansion configuration to Full Port Expansion at Pt. 22.

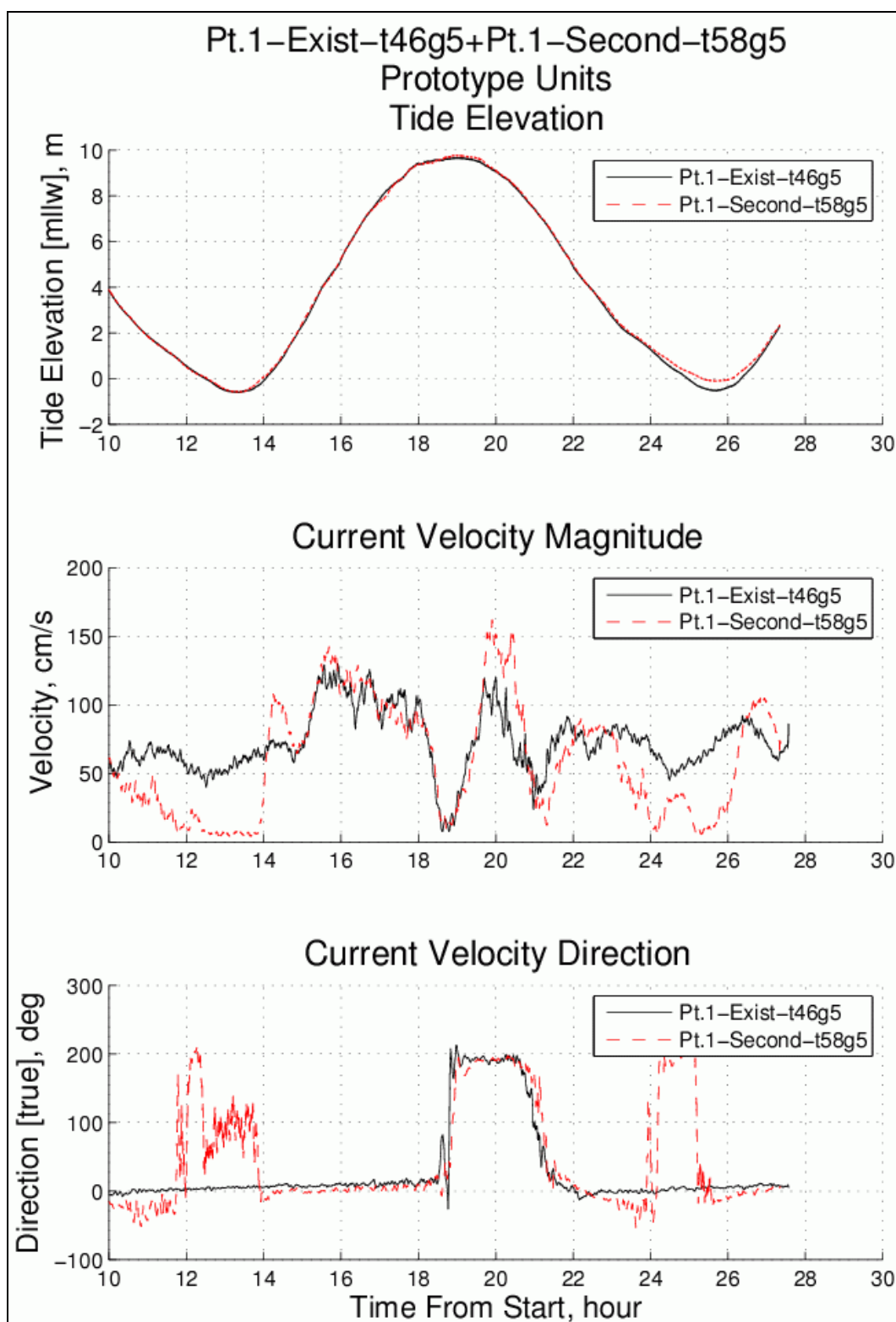


Figure 63. Comparison of pre-expansion configuration to Second Port Expansion at Pt. 1.

southerly-directed portion of the ebb tide, the flow magnitudes were higher due to narrowing of the Cairn Point gyre by the North Extension.

The decrease in flow magnitudes (see Figure 64) measured at Pt. 2, located in the gap between the North and South Extensions, was less pronounced due to the fact that this location was farther away from the Port expansion influence. However, addition of the North Replacement (Third Port Expansion shown in Figure 50) resulted in a significant decrease in flow magnitude at Pt. 2, as shown in Figure 65. Keep in mind that all of these measurement locations are outside the Port expansion footprint, and flow velocities inside the footprint will be less.

Summary

Flow velocity measurements were acquired in the Large-Area physical model at four selected locations adjacent to the seaward extent of the Port of Anchorage expansion and at two location farther out in the Knik Arm. The measurements revealed the complex nature of the spring tide range around the Port with much of the flow pattern during ebb tide being a consequence of a large-scale gyre formed by Cairn Point.

Comparisons of velocities made between the pre-expansion Port and the completed Port expansion revealed only a slight increase in maximum velocity magnitudes at locations along the future dock face. Farther seaward of the Port, little difference was seen between the before- and after-expansion configurations.

Flow measurements and visualization corresponding to the Port expansion phase after completion of the North and South Extensions suggested the potential for increased shoaling in the area between the two extensions. During portions of the ebb tide, flow magnitudes decreased substantially, and this decrease will be even more pronounced during neap tides when less tidal prism is moving through the Knik Arm.

In the time before completion of the North Replacement section, the original Port mooring facilities will continue to serve the Port of Anchorage until such time that new facilities can be provided along the North Extension. Therefore, the Alaska District's maintenance dredging of the mooring areas between the North and South Extensions will continue to be a priority with the possibility that more material will need to be excavated to maintain navigation depths.

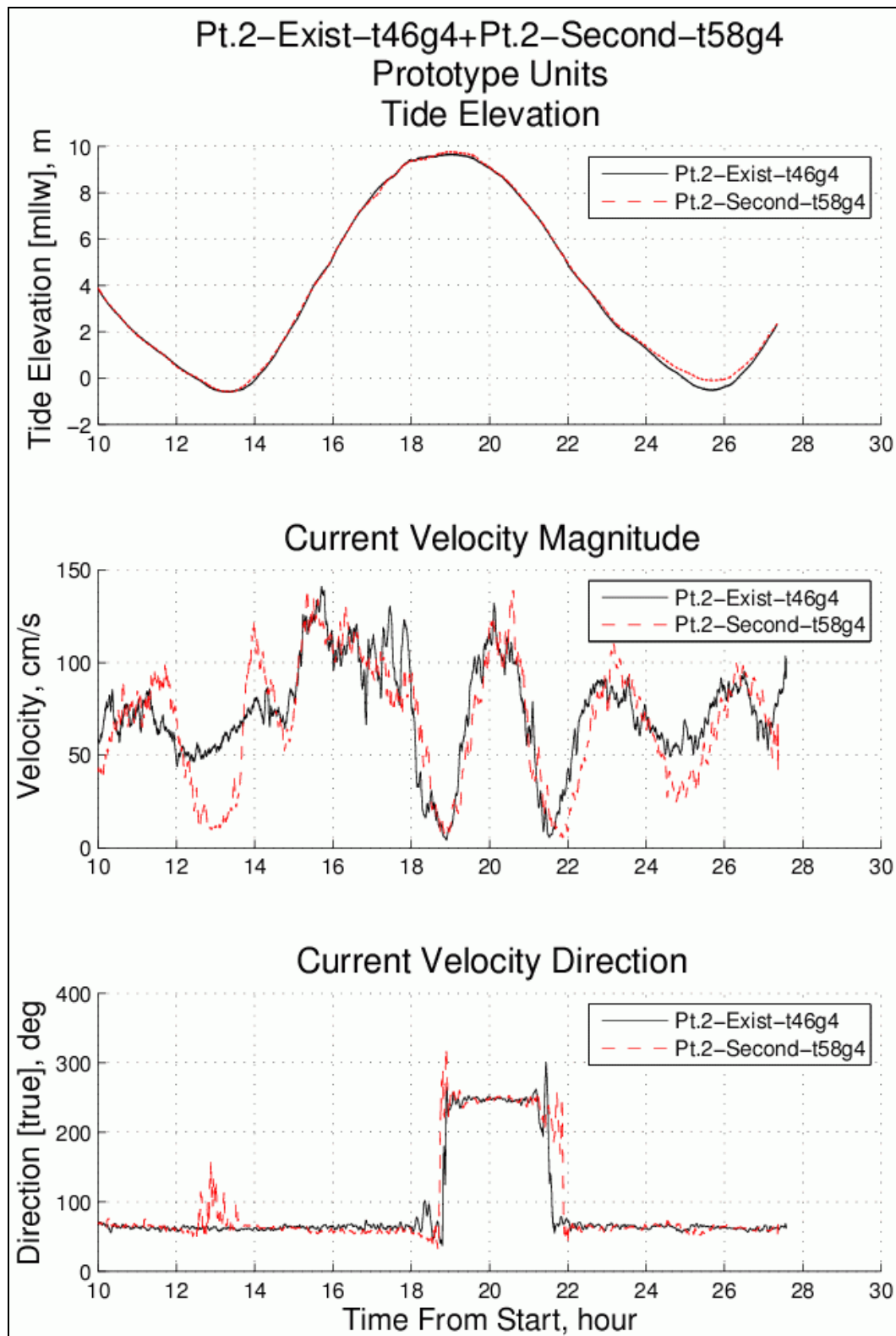


Figure 64. Comparison of pre-expansion configuration to Second Port Expansion at Pt. 2.

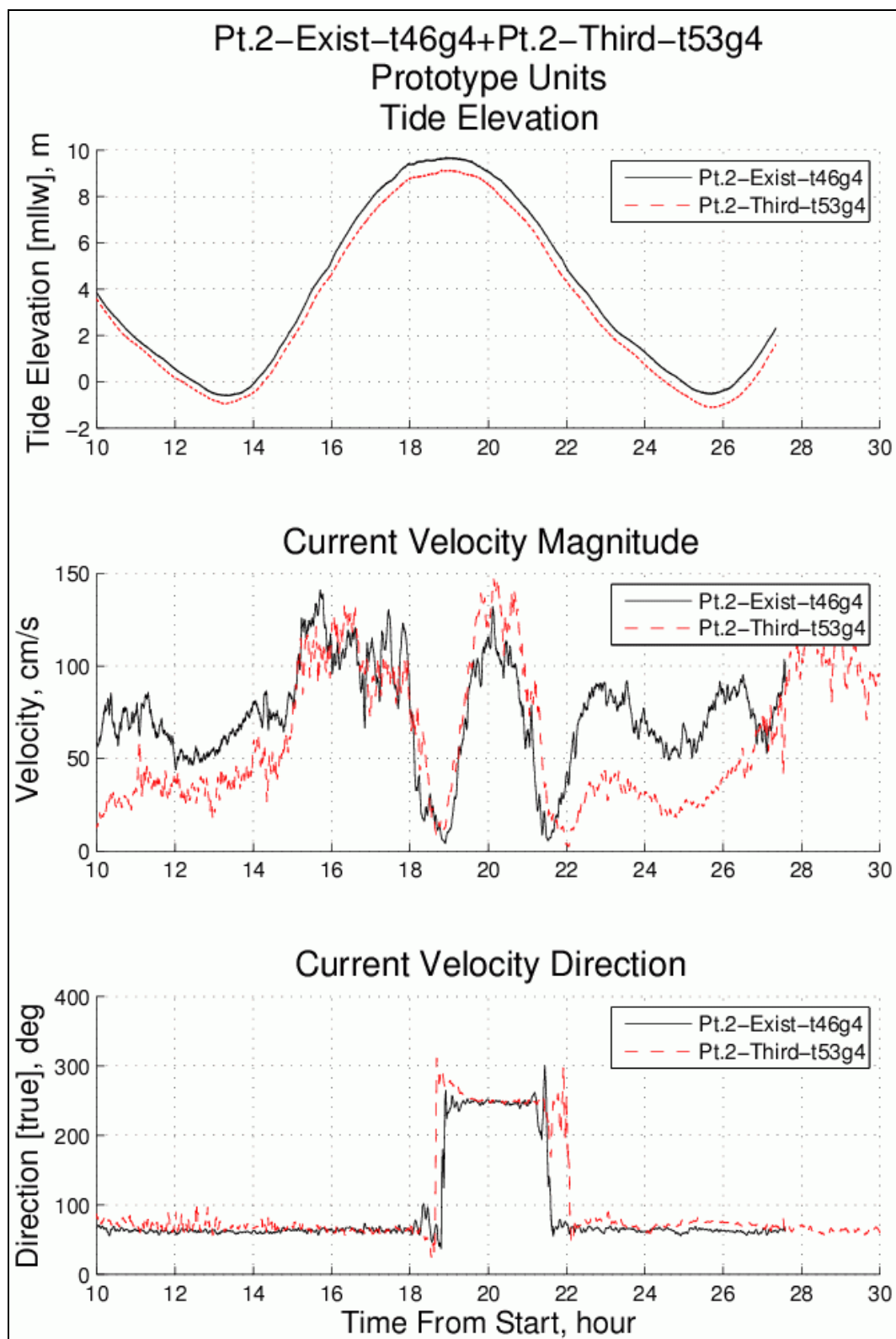


Figure 65. Comparison of pre-expansion configuration to Third Port Expansion at Pt. 2.

Flow velocities at the Port after construction of North Extension

Concern about increased shoaling potential after construction of the North and South Extensions prompted a second series of tests in the Large-Area Model that focused on tidal flows between the North and South Extensions. This section overviews the measurement locations, plots the measured velocities, and presents selected comparisons between measurements to better illustrate potential shoaling problems.

Model configuration and measurement locations

During a visit to ERDC in December, 2008, by Alaska District engineers, a total of twelve measurement locations were selected for flow measurements in the Large-Area Model adjacent to the Port of Anchorage. The purpose of these measurements was to examine the flow magnitudes between the North and South Extensions before the addition of the North Replacement. Observations during earlier tests of this partial expansion phase revealed slower flow magnitudes due to modification of the Cairn Point gyre by the North and South Extensions.

Figure 66 shows the locations of the measurement points for this test series. The twelve points were positioned in a nearly rectangular grid aligned with the completed Port expansion dock face shown by the dashed line on Figure 66. Four lines perpendicular to the dock face were spaced at 880-ft centers (prototype scale units) with the line containing points 4, 8, and 12 being 880 ft from the southerly end of the North Extension. Points 1, 2, and 3 were located landward of the future dock face by distances of 344 ft, 392 ft, and 352 ft, respectively. (No measurements were made at Pt. 4.) Points 5, 6, 7, and 8 were positioned 80 ft seaward of the future dock face. Point 9 was 304 ft seaward of the future dock face, whereas points 10, 11, and 12 were 384 ft seaward. Also shown on Figure 66 are the locations of Points Pt. 1, Pt. 2, Pt. 5-2, and Pt. DL used in the previous test series. The new point 1 was near the field data collection Station 4, and the new point 2 was in the vicinity of Station 5.

Table 8 details the ten tests in this test series. Measurements were made at two ADV locations during each test, as denoted by columns 3 and 4 in the table. Tests 63-70 (conducted in January 2009) measured flow velocity at ADV locations 1, 2, 3, 6, 7, and 8. Three of the tests were run without the South Extension in place, and three were run with the South Extension in the model, as noted by the last column in Table 8. Tests 71-74 (conducted

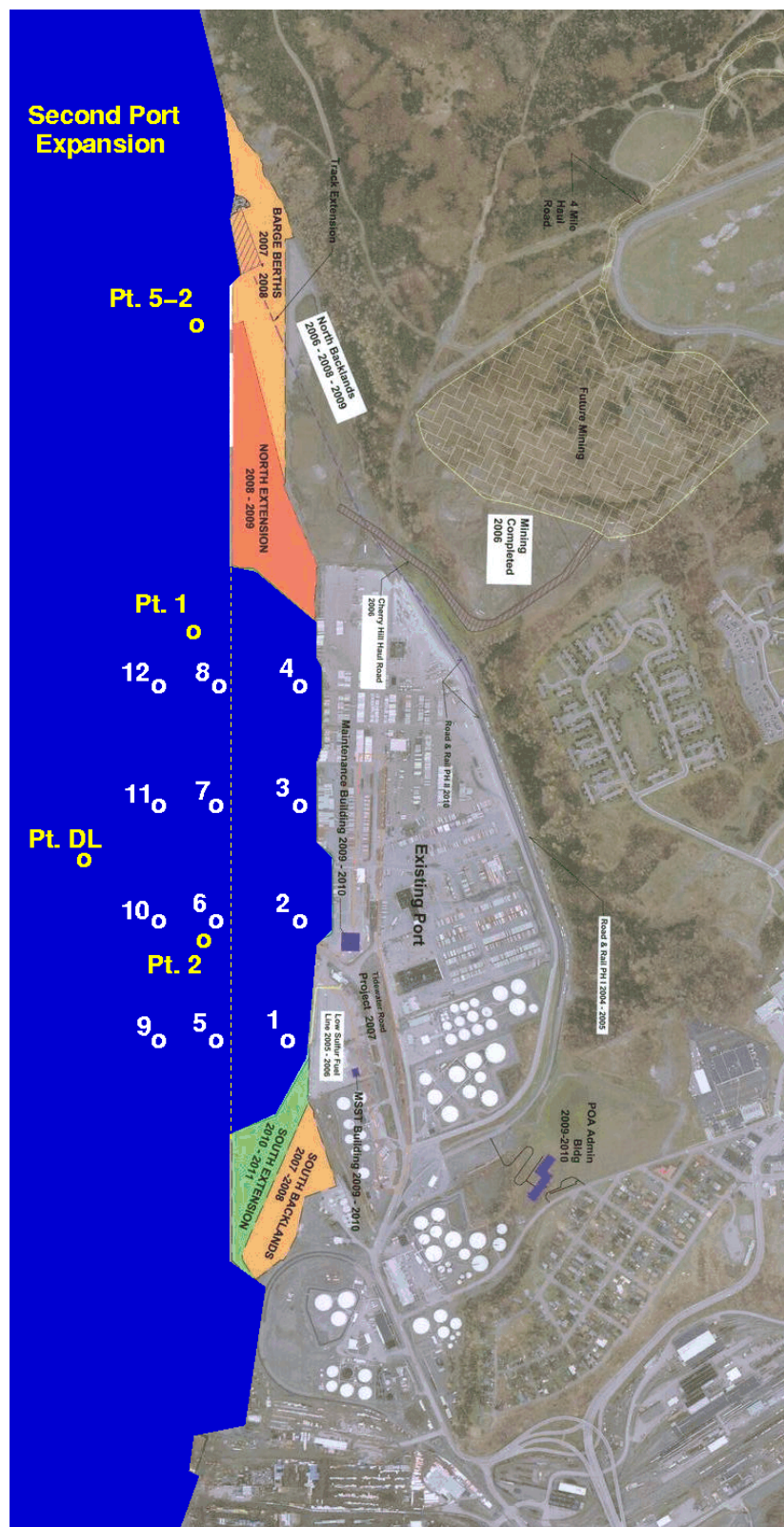


Figure 66. Measurement locations for North Extension test series.

Table 8. Summary of Port North Extension tests.

| Test ID | Date | Current Meter Locations | | Expan. Phase | Comments |
|---------|---------|-------------------------|-------|--------------|---------------------|
| | | ADV 4 | ADV 5 | | |
| Test 63 | 1/07/09 | Pt. 1 | Pt. 8 | Second | South Extension OUT |
| Test 64 | 1/07/09 | Pt. 1 | Pt. 8 | Second | South Extension IN |
| Test 65 | 1/08/09 | Pt. 2 | Pt. 7 | Second | South Extension OUT |
| Test 66 | 1/09/09 | Pt. 2 | Pt. 7 | Second | South Extension IN |
| Test 67 | 1/09/09 | Pt. 6 | Pt. 3 | Second | South Extension OUT |
| Test 70 | 1/13/09 | Pt. 6 | Pt. 3 | Second | South Extension IN |
| Test 71 | 4/02/09 | Pt. 12 | Pt. 5 | Full | |
| Test 72 | 4/02/09 | Pt. 11 | Pt. 6 | Full | |
| Test 73 | 4/03/09 | Pt. 10 | Pt. 7 | Full | |
| Test 74 | 4/03/09 | Pt. 9 | Pt. 8 | Full | |

in April 2009) measured flow velocity at the eight locations seaward of the future dock face (points 5, 6, 7, 8, 9, 10, 11, and 12) with the full Port expansion placed in the physical model.

The velocity reference gauge used in the previous test series to confirm consistency between tests was not available due to instrument failure. However, good test repeatability was shown in all previous tests in which the tide cycle was well reproduced; and this was taken to be an indicator of a valid test in lieu of having velocity comparisons at the Ref. ADV point.

Comparison to pre-expansion Port configuration

No flow velocity measurements were made at ADV current meter locations 1, 2, and 3 with the pre-expansion Port configuration. However, measurement point 1 was in the vicinity of the stationary calibration location designated at Station 4, and point 2 was near calibration Station 5. Therefore, meaningful comparisons could be made to judge the effect on dredging activities brought about by constructing the North and South Extensions.

Figure 67 compares the pre-expansion velocities at Station 4 (solid line), from Test 41, to the velocities at point 1 (dashed line) after installation of the North and South Extensions (Test 64). Measured flow magnitudes after the addition of the two Port extensions were dramatically decreased throughout most of the tide cycle when the flow was in the flood direction (northerly). This was a direct consequence of gyres forming at the northern end of the South Extension. During a four-hour ebb-flow period beginning at high water, the effect of the South Extension was minimized. The significant decrease in flow velocity over much of the tide cycle is expected to promote deposition of suspended sediment, resulting in increased dredging requirements during this phase of Port expansion. Figure 68 shows a similar comparison of the Station 5 pre-expansion velocities (Test 41) with the velocities at point 2 after the North and South Expansion (Test 66). A decrease in flow magnitude is evident, but the decrease was not as significant as seen at point 1 because of greater distance from the South Extension.

The comparisons shown in Figures 67 and 68, along with visual documentation in the form of time-lapse video of dye and tracer injections, provide compelling evidence that the time period between the installation of the North and South Extensions and the completion of the entire Port expansion will require increased dredging activity because of the likelihood of increased sedimentation.

Visual observations of the flow at point 4 (see location on Figure 66) indicate a similar region of slowly moving eddies just south of the North Extension end, and significant shoaling should be anticipated in this region until construction of the North Replacement section. However, no measurements were made to quantify these visual observations other than time-lapse video recordings.

Effect of South Extension

Flow velocities measured at points 1, 2, 3, 6, 7, and 8 with the North Extension installed, but only the South Backlands in place (Tests 63, 65, and 67) were compared to measurements obtained at the same locations with addition of the South Extension (Tests 64, 66, and 70). The purpose of these comparisons was to evaluate whether the addition of the South Extension would increase shoaling potential at the original dock face.

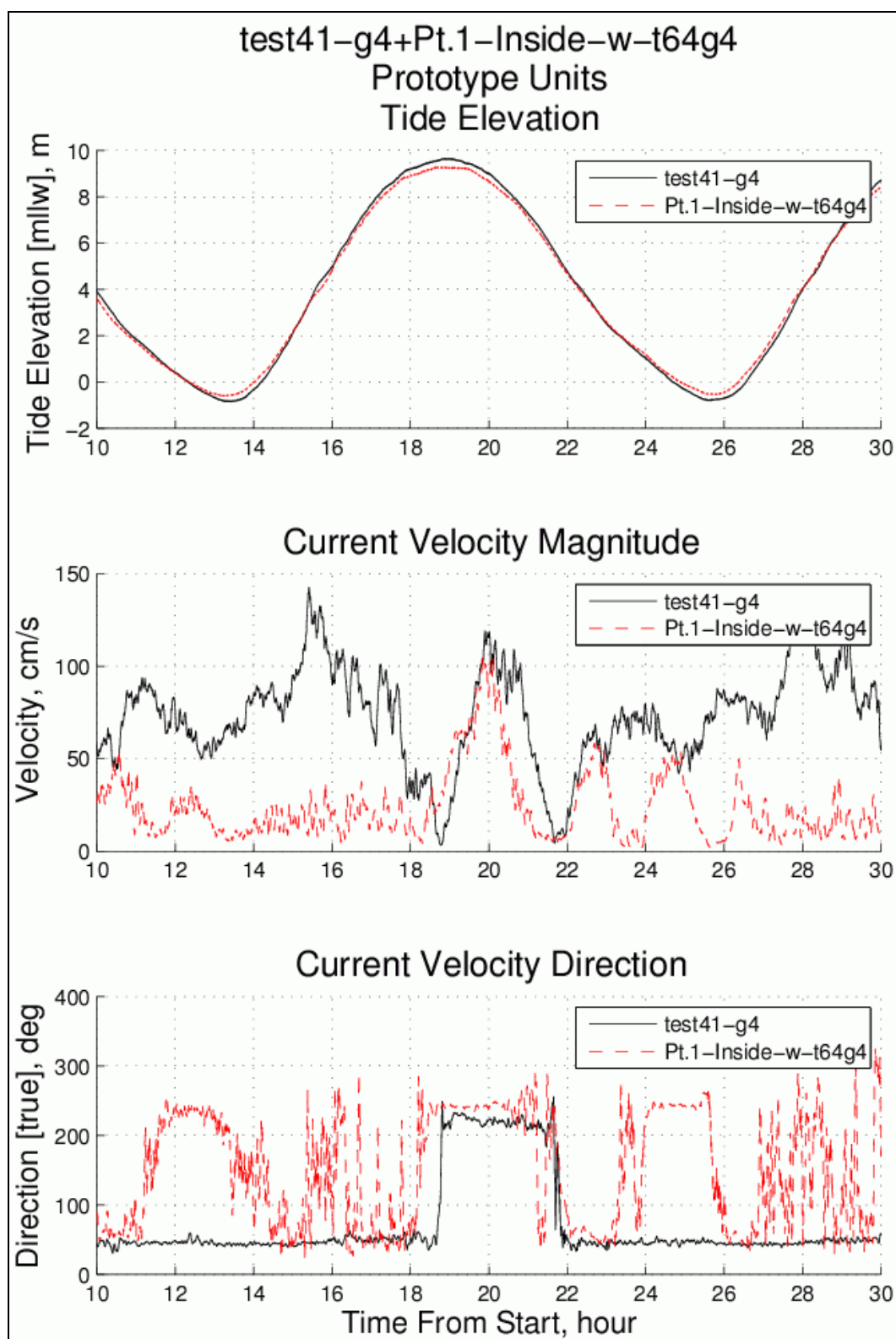


Figure 67. Effect of North and South Extensions at measurement point 1.

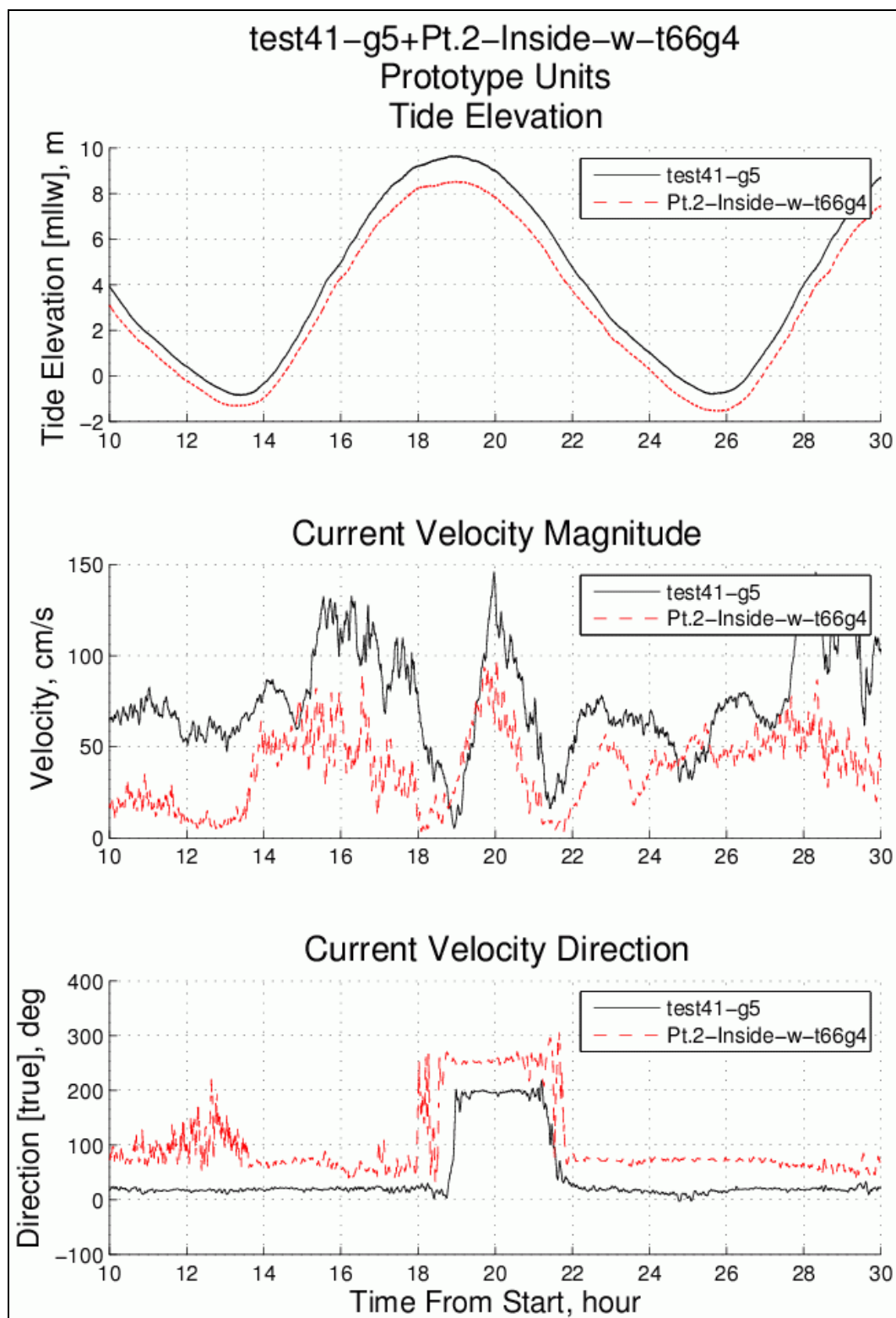


Figure 68. Effect of North and South Extensions at measurement point 2.

Generally, there was little difference with or without the South Extension installed. The largest difference was seen at point 6 during the latter part of ebb tide and at low water, as seen in Figure 69. This decrease, with the addition of the South Extension, was due to growth of the Cairn Point gyre to the full length of the Port toward the end of the ebb cycle. The low velocities noted for point 1, in Figure 67, were similar with only the South Backlands expansion. All six comparisons are given in Appendix C.

Velocities along the original dock face

The velocities adjacent to the original Port of Anchorage dock face were smaller near the ends of the North and South Extensions and increased away from the abrupt changes in planform geometry. Figure 70 compares the velocities at point 1 (solid line) with the somewhat larger point 2 velocities (dashed line). Similarly, Figure 71 indicates that the velocities at point 3 were larger than at point 1, and Figure 72 shows that point 3 velocities were also larger than point 2 velocities. A similar trend was seen for points 6, 7, and 8 with the South Extension included; but the change in magnitude was not as great, and the comparison plots have not been included here.

Velocities for the Full Port Expansion

The final set of tests in the Large-Area physical model of Knik Arm measured velocities with the completed Full Port Expansion placed in the model (see Figure 50). Tests 71-74 measured flow velocities at points separated by 880 ft (prototype units) along a line 80 ft seaward of the future dock face (points 5, 6, 7, and 8 on Figure 66) and along a line about 384 ft seaward of the dock face (points 9, 10, 11, and 12). (Point 9 was 304 ft seaward of the dock face).

Figures 73-76 show measurement plots for each pair of ADV locations close to the future dock face and farther seaward. Generally, the velocity magnitudes were similar for all 8 measurement points throughout the tide cycle, indicating consistent flow magnitudes along most of the new dock face. The maximum flood and ebb flow magnitude was about 150 cm/s (4.9 ft/s or 2.9 kts). As noted previously, the maximum for the completed Port expansion was an increase of about 0.6 kts over what was measured at similar locations without any Port expansion in place. The slightly increased velocities seen for the completed Port expansion should help reduce sedimentation of suspended sediment, and help mobilize sediment deposited during times of slow flows and slack water.

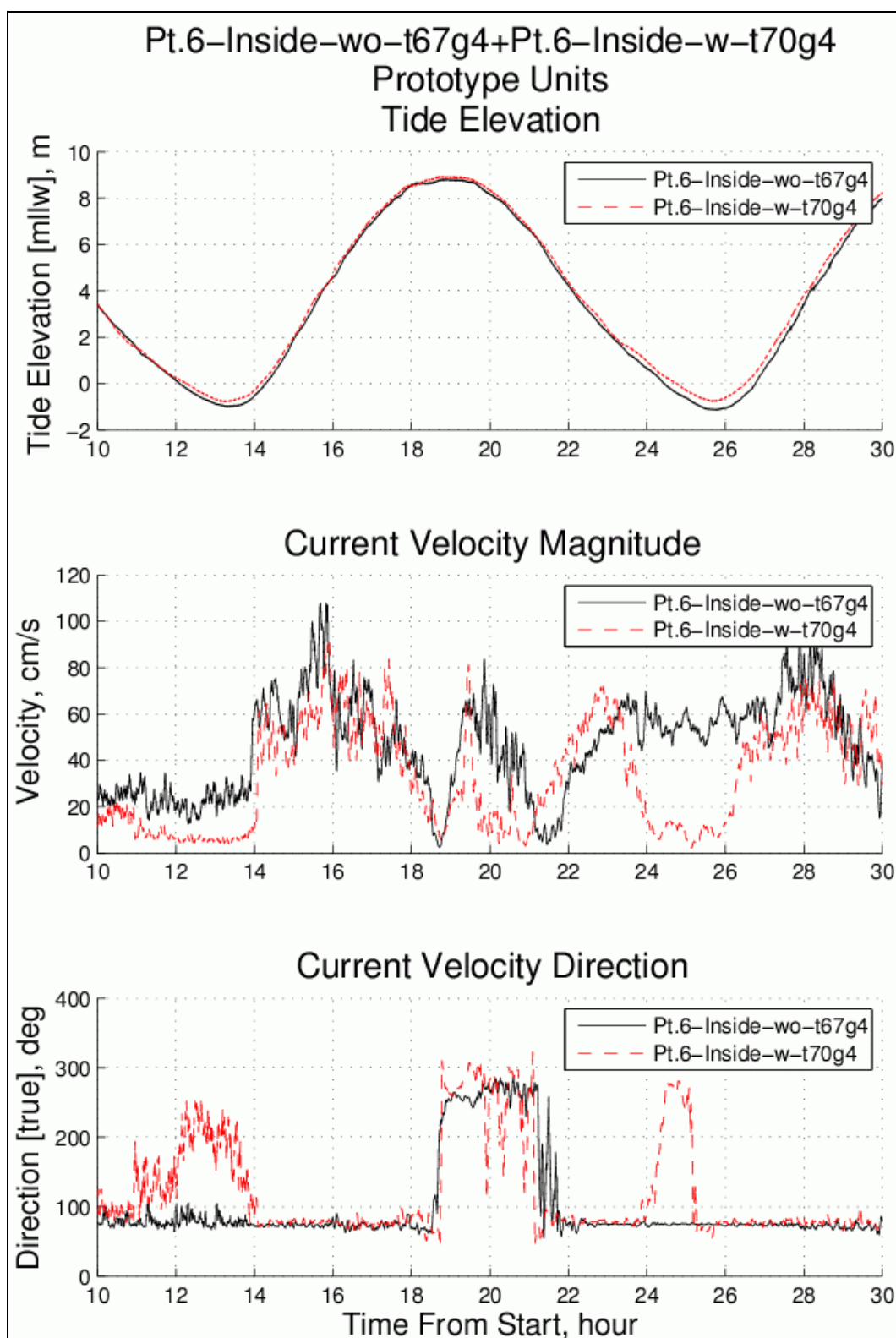


Figure 69. Effect of South Extension at measurement point 6.

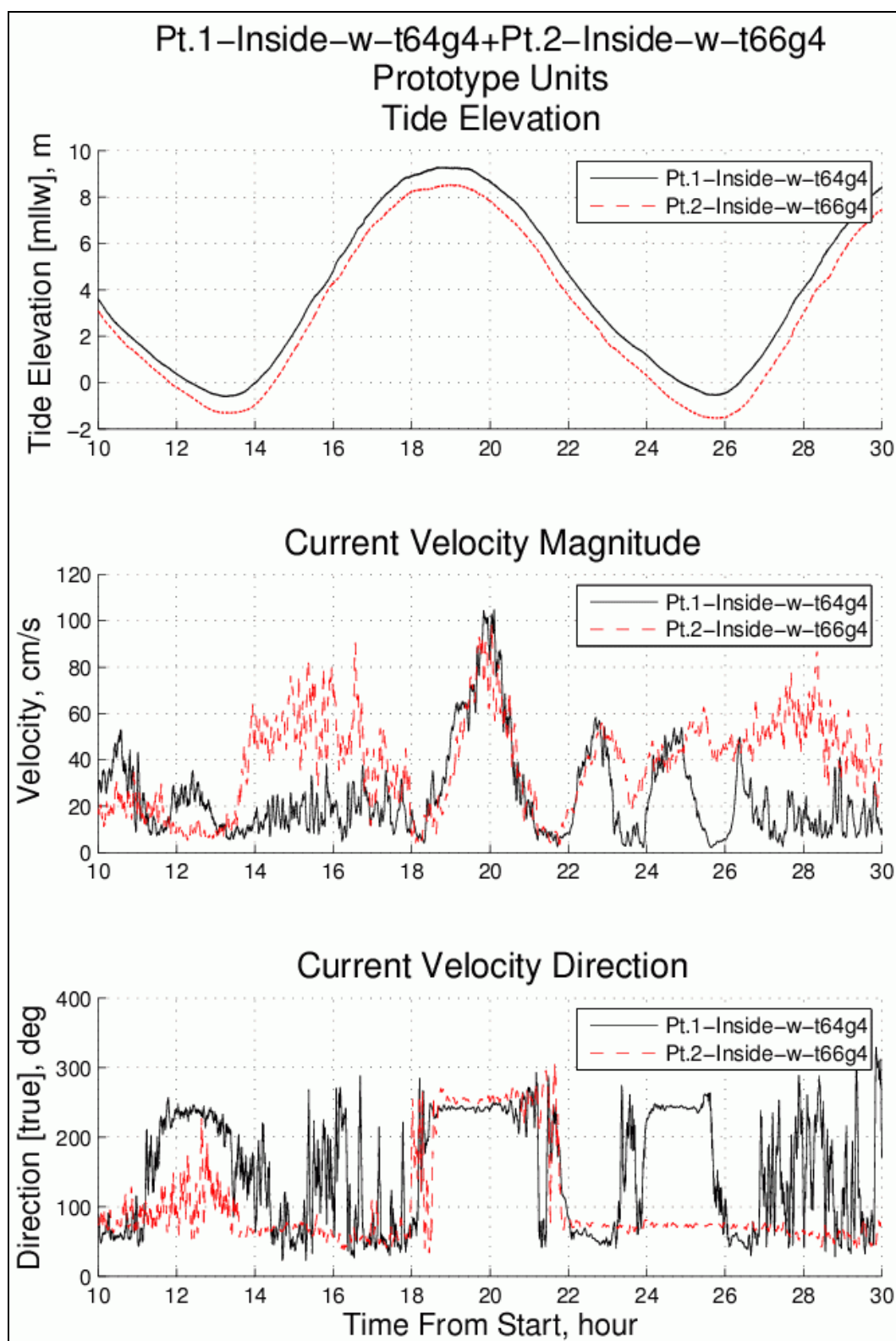


Figure 70. Comparison between pts. 1 and 2 with South Extension installed.

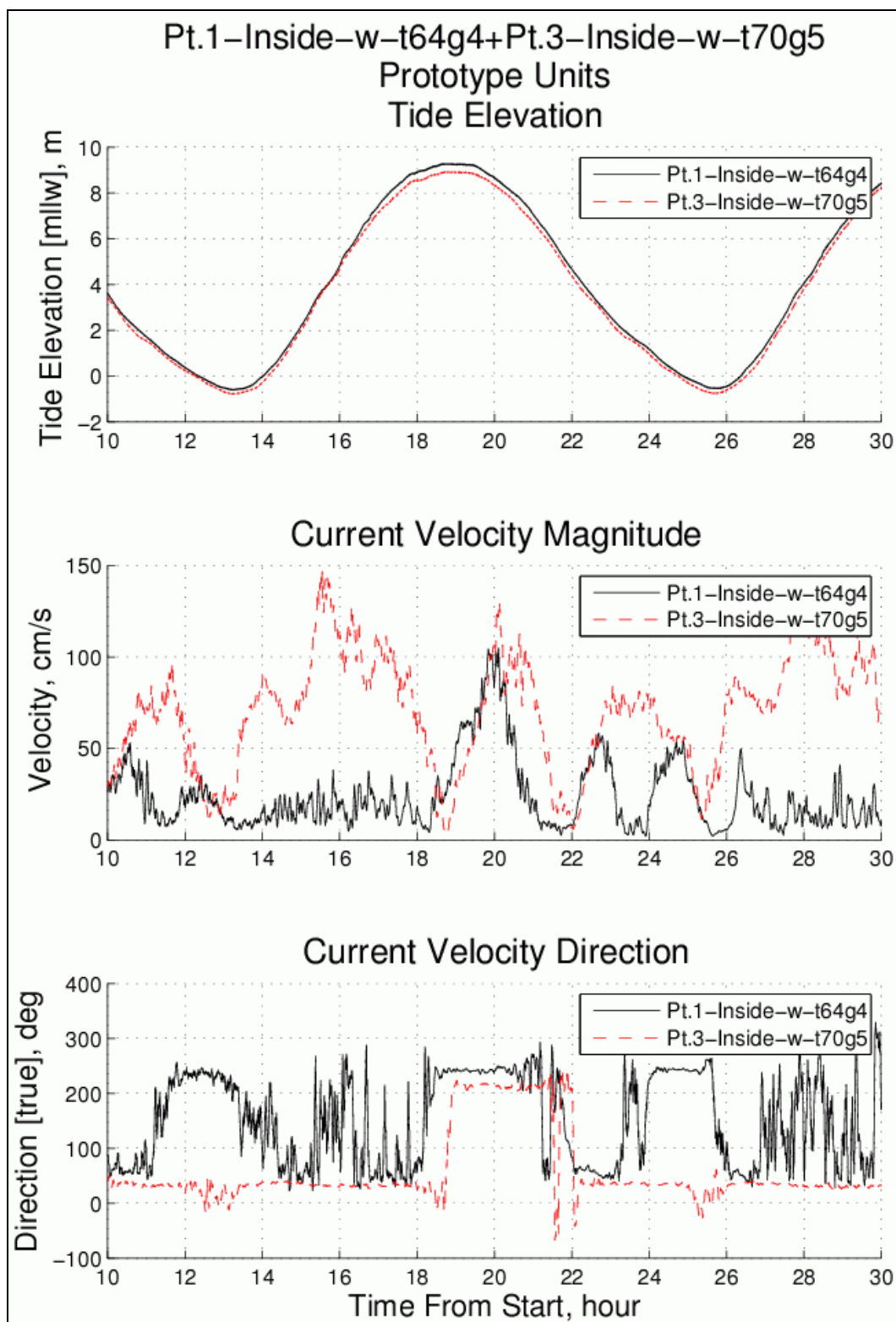


Figure 71. Comparison between pts. 1 and 3 with South Extension installed.

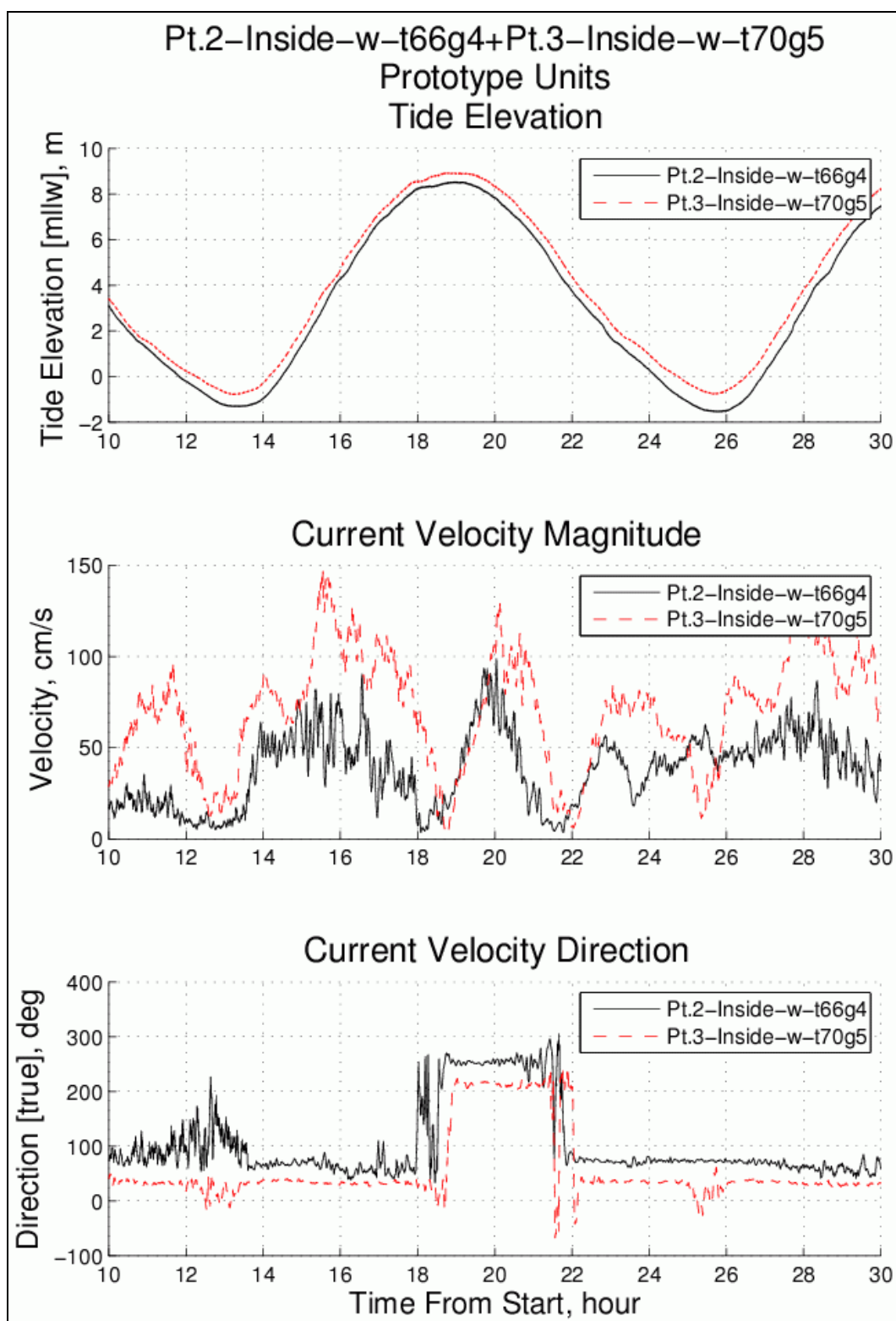


Figure 72. Comparison between pts. 2 and 3 with South Extension installed.

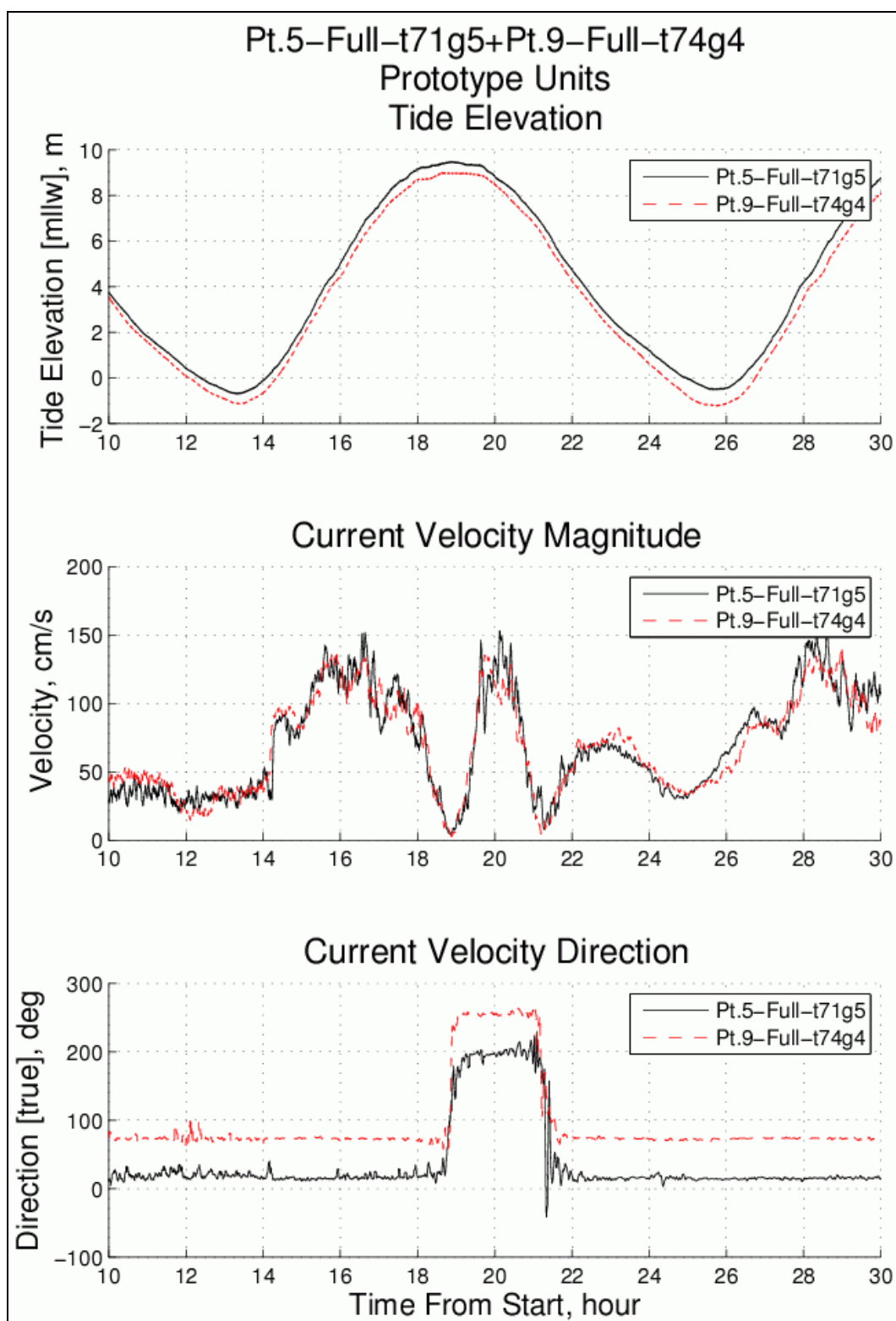


Figure 73. Comparison between pts. 5 and 9 for completed Port Expansion.

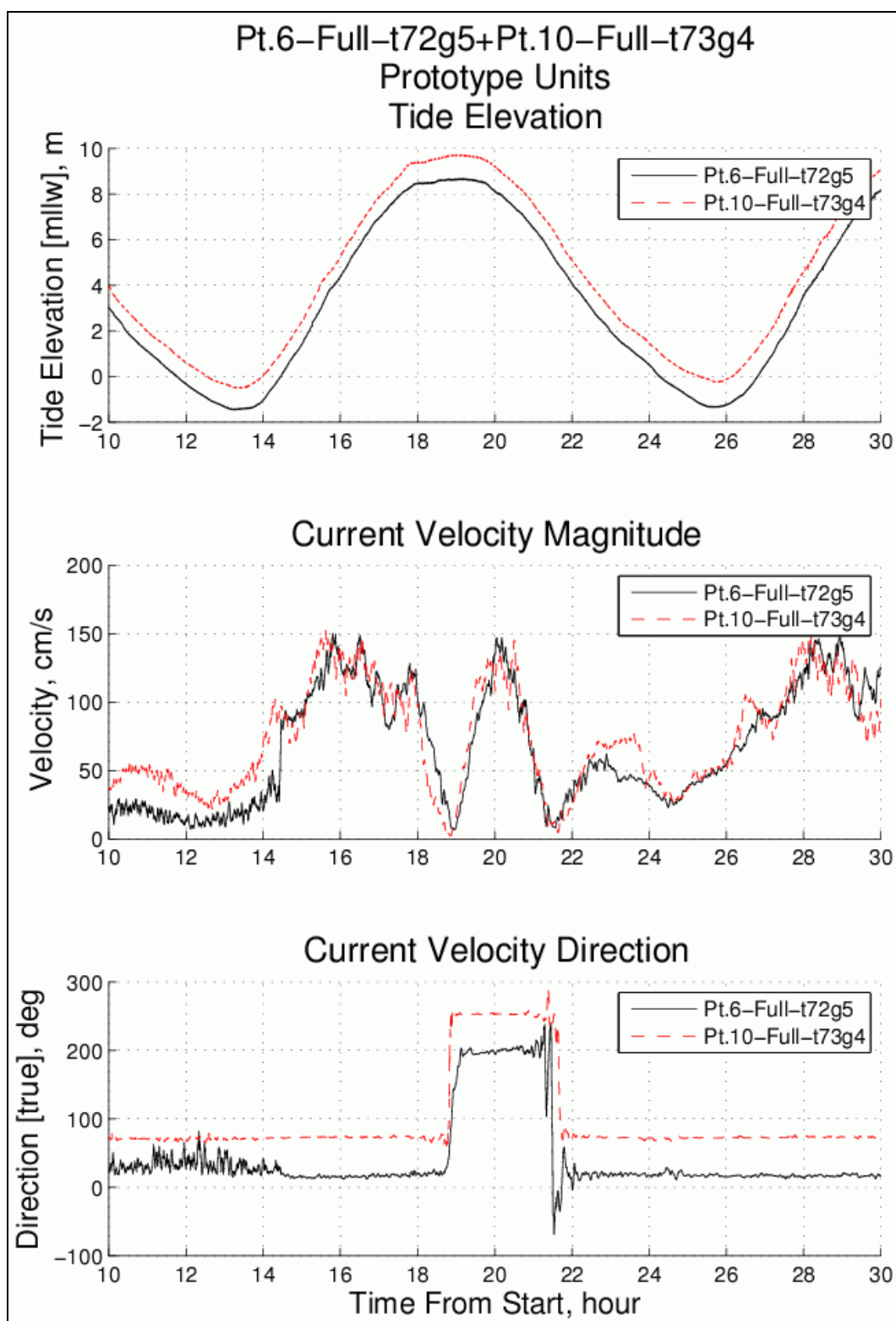


Figure 74. Comparison between pts. 6 and 10 for completed Port Expansion.

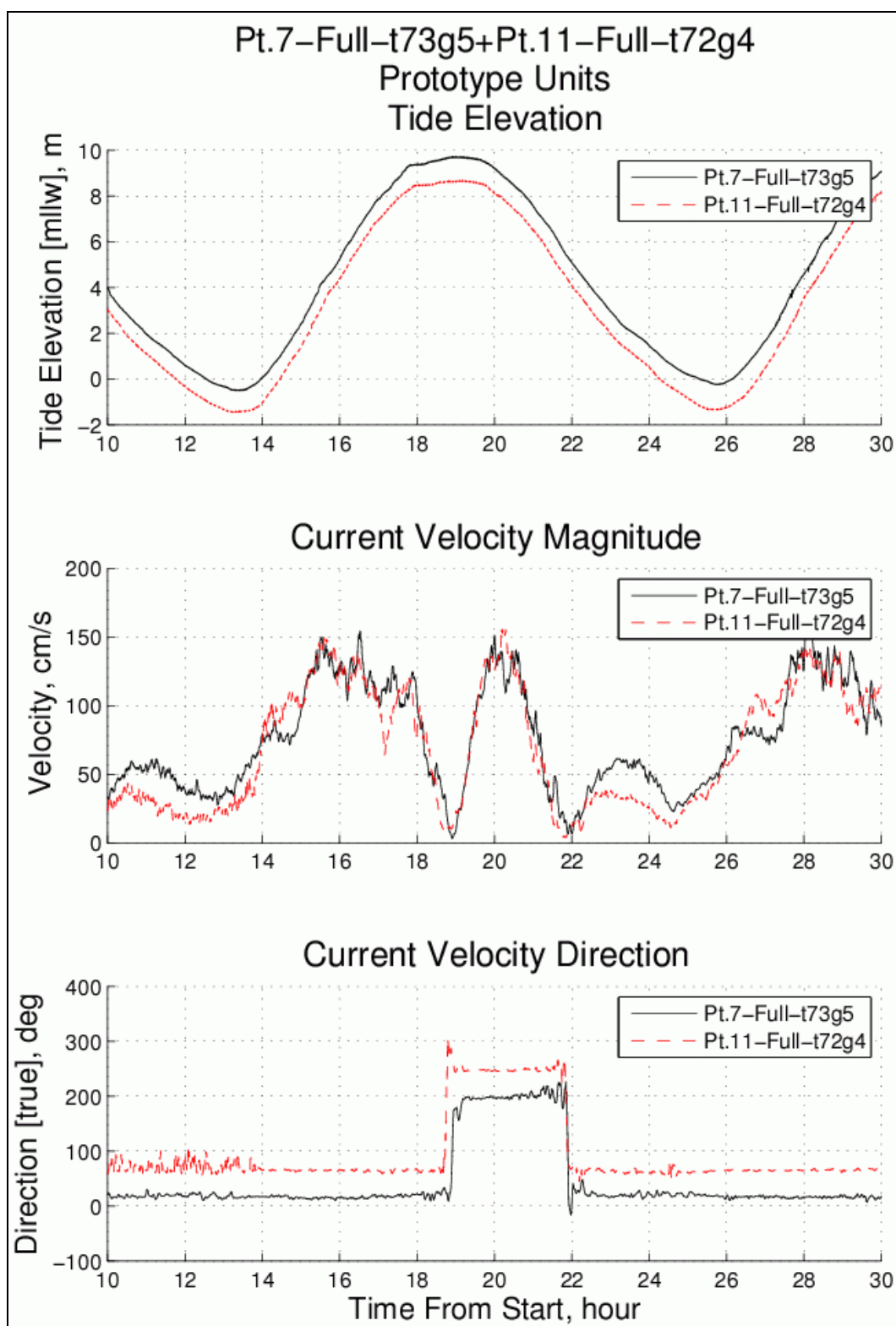


Figure 75. Comparison between pts. 7 and 11 for completed Port Expansion.

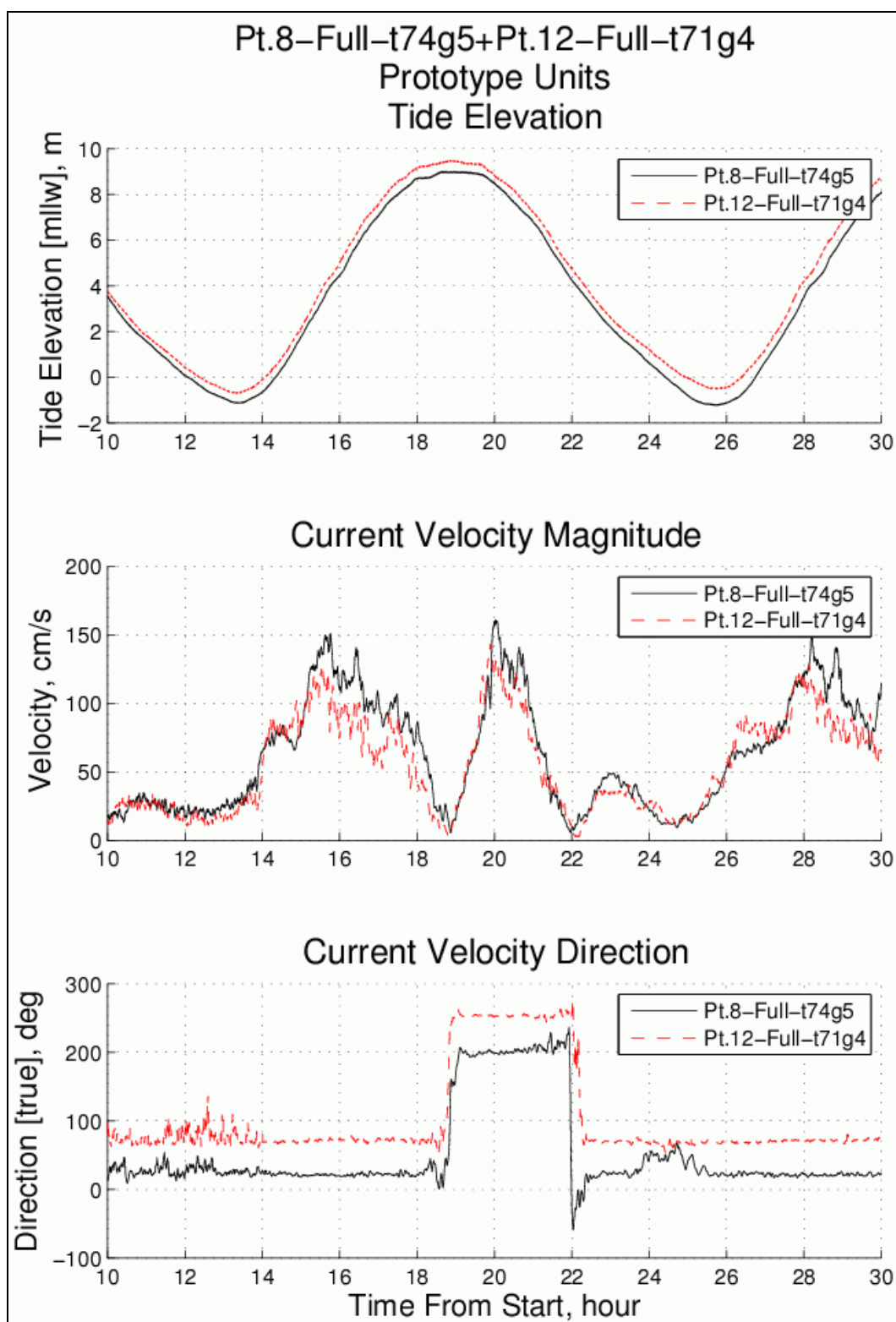


Figure 76. Comparison between pts. 8 and 12 for completed Port Expansion.

Summary

Flow velocity measurements were acquired at 11 locations in the Large-Area physical model inside and outside the footprint of the complete Port expansion. The purpose for these measurements was to assess whether decreased flow circulation in the region of the original Port dock face may require additional maintenance dredging during the time after installation of the North and South Extensions and before completion of the North Replacement expansion phase.

Velocities were significantly reduced near the original dock face, particularly on the north and south ends of the gap between the extensions. At these locations, slow rotating gyres form, and little water is exchanged between the gyres and the faster moving tidal flow farther out in the channel.

Flow velocities at the future dock face, once the entire Port expansion is completed, were uniform along the dock face with maximum magnitudes of around 150 cm/s (2.9 kts). Maintenance dredging requirements are expected be on par with, or less than, dredging before commencement of Port expansion, assuming that all other non-hydraulic physical processes remain unchanged.

7 Summary and Conclusions

This chapter provides a summary of the physical model study of the Knik Arm of Cook Inlet, Alaska, and the Port of Anchorage; and it gives conclusions based on measured velocities at specific locations near the Port for different phases of the Port expansion.

Summary of physical model study

Situation

The flow regime in the upper Knik Arm of Cook Inlet is dominated by a 30-ft tide range and by large gyres formed in the lee of prominent headlands. The Port of Anchorage is situated south of Cairn Point, and the flow patterns at the Port are heavily influenced by a large gyre formed in the lee of Cairn Point during the ebb tide cycle. Development, operation, and maintenance of navigation channels and berthing areas at the Port of Anchorage are the responsibility of the Alaska District, U.S. Army Corps of Engineers (USACE).

Presently, a reported \$700M expansion to the Port of Anchorage is underway. Changes to the flow magnitudes and patterns caused by Port expansion and the construction sequence could modify shoaling and sediment deposition rates and thus affect operations at the Port of Anchorage. Evaluation of navigation safety and potential berthing problems are also of paramount concern.

Study objectives

The primary objectives of the Knik Arm and Port of Anchorage physical model study were the following: (1) examine changes to the hydrodynamic flow regime likely to occur after each phase of the planned Port of Anchorage expansion; (2) assess Port expansion impacts to Corps of Engineers navigation, dredging, and port maintenance operations; and (3) provide measurements for improving advanced numerical models of the complex flow and sediment transport regime in the Knik Arm.

Physical model description

The required tasks to achieve the above objectives included: (a) designing the physical model to represent the major physical processes correctly; (b) constructing the physical model with sufficient accuracy to minimize boundary-induced errors; (c) calibrating the tide producing methodology to reproduce repetitive spring tide cycles; (d) validating the model by reasonable reproduction of field-measured tidal velocities near the Port; and (e) acquiring velocity measurements throughout the tide cycle at numerous locations for all phases of the Port expansion.

The bathymetry of Cook Inlet and Knik Arm surrounding the Port of Anchorage was constructed out of concrete at reduced scale in two physical models. Only the primary model, termed the “Large-Area Model,” was tested during this study. The Large-Area Model covered a reach of Cook Inlet measuring approximately 19 statute miles; and it replicated the bathymetry of the Knik Arm, portions of Eagle Bay, and part of the upper Cook Inlet south of Point Woronzof. The model was geometrically distorted with a horizontal length scale of 800-to-1 (prototype-to-model) and a vertical length scale of 200-to-1, giving a geometric distortion (horizontal/vertical) of 4.

A tidal prism storage area was designed and constructed in the model beyond the Eagle Bay upstream model boundary. The storage was designed to hold the proper water volume with the correct water surface elevation during all stages of the spring tide. Ebb tide in the model was driven by the head of water contained in the tidal prism storage area of the model.

The complete time-varying spring tide cycle was reproduced in the Large-Area Model by a calibrated computer system that automatically controlled the water elevation in the model. During the tide cycle, the predominant headlands in the Knik Arm and the variations in the underwater bathymetry off Cairn Point reproduced the known large-scale gyres that strongly influence the hydrodynamic conditions at the Port of Anchorage.

Time varying water elevations in the model were measured using three capacitance water level gauges. Tidal flow velocity magnitudes and directions were quantified using three acoustic Doppler velocimeters (ADV) that measured two components of horizontal velocity at a fixed elevation above the bottom. Complex flow patterns were visualized using dye

injection and surface Lagrangian tracers, and time-lapse video was used to document the dye and tracer movements.

The Large-Area model was calibrated by successful reproduction of the scaled water surface elevation variation over a complete 12-hr tide spring tide cycle recorded at the NOAA tide gauge near the Port of Anchorage. Physical model validation was then achieved by reasonable reproduction of field-measured velocity time series collected at three mooring locations in the vicinity of the pre-expansion dock face. The field data spanned the entire 12-hr tide cycle at each location.

Simulation of the spring tide cycle in the Large-Area physical model was shown to be repeatable with a good degree of accuracy, both within a single test and across multiple tests. Repeatability was essential to enable velocity measurements at numerous locations with a limited number of ADV current meters. Essentially, measurements collected from repeat tests were treated as if all measurements had been collected during a single test.

Overview of testing program

Flow velocity measurements in the model were used to quantify changes in the tidal flow at the Port of Anchorage that would occur at each stage of the Port expansion. A total of 26 successful tests were completed in the Large-Area physical model of Knik Arm and the Port of Anchorage. Two different test series were conducted.

The first test series (16 tests) measured tidal flow velocities at six fixed locations in the vicinity of the Port of Anchorage. The purpose of these measurements was to compare differences in velocity at these six locations for the pre-expansion Port configuration and for all phases of the Port expansion plan. All velocity measurement locations were seaward of the completed Port expansion dock face.

At the end of the first test series, the ADV current meters were removed and 11 time-lapse video recordings were made, showing the different Port expansion phases. The flow patterns were visualized using dye injection and baby powder sprinkled on the water surface.

The second test series (10 tests) examined in more detail flow velocities for the expansion phase that included only the North Extension, South

Backlands, and South Extension. A total of eleven measurement locations were selected for flow measurements in the Large-Area Model adjacent to the Port of Anchorage, with three of the locations being inside the completed Port expansion footprint. The purpose of these measurements was to examine the flow magnitudes between the North and South Extensions before the addition of the North Replacement. Observations during earlier tests of this phase of the expansion revealed slower flow magnitudes due to modification of the Cairn Point gyre by the North and South Extensions. Slower velocities would lead to increased shoaling during this phase of Port expansion. Also included in this test series were measurements along the future dock face after the completion of the entire Port expansion plan.

Study observations and conclusions

This section summarizes observations made based on analysis of measured flow velocity magnitudes and directions at selected locations in the Large-Area physical model for various Port expansion phases. Conclusions based on the measurements and observations are offered.

Physical model utility

The Large-Area physical model of Knik Arm and the Port of Anchorage was a difficult challenge for the ERDC engineers and technicians. The model was constructed at length scales smaller than typical, and simulation of four identical tide cycles had not been attempted at ERDC in recent history. Once the model calibration was achieved by replicating the tidal water level variations, the engineers had few options available for “tweaking” the model to achieve a reasonable validation. The fact that the model was satisfactorily verified is a tribute to accurate model construction and careful operation by the laboratory staff.

The flow regime in the Knik Arm is dominated by large-scale turbulent gyres and smaller-scale eddies that can change dramatically when the flow boundaries are altered. The physical model was able to simulate these complex processes because all of the associated physics are inherently included in a properly-scaled physical model, provided that scale and laboratory effects are kept to a minimum.

The various Port expansion phases were easily placed in the model and removed at will, and the flow visualization techniques graphically illustrated what was happening at the Port (and other locations) during any

phase of the tide. The physical reproduction of the complete Knik Arm at small scale, and the ability to see the variations in tidal flow as it occurs is perhaps the most important attribute of the physical model. Visitors to the Knik Arm physical model with little to no prior knowledge of the area quickly understood the issues and potential problems because the human mind can gather and assimilate large quantities of visual data very rapidly.

Alaska District engineers and consultants were eager participants in the testing because they knew from past model experiences that watching the model in action would provide greater understanding of both present problems and potential future problems. Most physical models provide one or more surprises and cause observers to re-think pre-conceived notions about the subject being modeled. The Large-Area model of Knik Arm was no exception.

Flow velocity changes due to Port of Anchorage expansion

Flow velocity measurements were acquired in the Large-Area physical model at four selected locations adjacent to the seaward extent of the Port of Anchorage expansion and at two locations farther out in the Knik Arm. The measurements, coupled with flow visualization, revealed the complex nature of the spring tide range around the Port with much of the flow pattern during ebb tide being a consequence of a large-scale gyre formed by Cairn Point, just north of the Port.

Comparisons of velocities between the pre-expansion Port and the completed Port expansion revealed only a slight increase in prototype-scale maximum ebb tide velocity magnitudes, from about 110 cm/s to 140 cm/s (2.1 kts to 2.7 kts) at locations along the future dock face. Farther seaward of the Port, little difference was seen between the before- and after-expansion Port configurations.

Construction of the Port expansion phases, beginning with the North Extension, will alter the characteristics of the large-scale gyre formed to the south of Cairn Point during ebb tide. Ship simulator studies will examine navigation issues related to the Port expansion during construction and with new dock face in place. The physical model did not indicate any changes to the flow pattern that would make approaching the new dock face more difficult than at present, with the exception of faster maximum flow velocities along the dock face.

Flow measurements and visualization, corresponding to the Port expansion phase after completion of the North and South Extensions, suggested the possibility for increased shoaling in the area between the two extensions. During portions of the ebb tide, flow magnitudes decreased substantially, and this decrease will be even more pronounced during neap tides when less tidal prism is moving through the Knik Arm. The original mooring area will continue to service the Port of Anchorage until such time that new facilities can be provided along the North Extension. The prospect for increased dredging requirements prompted a second test series to examine this issue in more detail.

Flow velocities at the Port after construction of North Extension

Flow velocity measurements were acquired at 11 locations in the Large-Area physical model inside and outside the footprint of the complete Port expansion. The purpose for these measurements was to assess whether decreased flow circulation in the region of the original Port dock face may require additional maintenance dredging during the time after the installation of the North and South Extensions and before the completion of the North Replacement expansion phase.

Velocities were significantly reduced near the original dock face, particularly on the north and south ends of the gap between the extensions. At these locations, slow rotating gyres formed, and little water was exchanged between the gyres and the faster moving tidal flow farther out in the channel. At the measurement point located closest to the South Extension, the prototype-scale velocity magnitudes decreased to values of around 20 cm/s (0.4 kts) for nearly the entire 6-hr duration of the flood tide (see Figure 67). Conversely, similar measurements acquired at the nearby Station 4 location for the pre-expansion Port configuration showed prototype-scale flood-tide velocities ranging between 50 and 130 cm/s (1.0 to 2.5 kts). Flow visualization indicated that the area just south of the North Extension will experience similar significant reduction in flow velocity magnitude during ebb tide. Flow velocity decreases were also measured at other locations in the gap between the North and South Extensions, but the decreases were not as dramatic as those closest to the ends of the North and South Port Extensions.

Based on the measured and observed substantial reduction in flow velocity magnitude during lengthy periods of the tidal cycle, sedimentation is expected to increase substantially along the original dock face after the

construction of the North and South Extensions. Consequently, dredging requirements are expected to increase for longer periods of time if present authorized depths are to be maintained. This assumes that there are no significant changes in the suspended sediment concentrations typically experienced in the Knik Arm. The increased rate of sediment deposition cannot be estimated using measurements from the Large-Area physical model.

Flow velocities at the future dock face, once the entire Port expansion is completed, were uniform along the dock face with maximum magnitudes approaching 150 cm/s (2.9 kts) in prototype-scale units. Maintenance dredging requirements should be on par with dredging before commencement of Port expansion, assuming that all other non-hydraulic physical processes in the Knik Arm remain unchanged. In other words, concentrations of suspended sediment, fresh water run-off, ice break-up, etc., continue to fluctuate about the long-term averages.

The Large-Area physical model simulations of Knik Arm has illustrated the value of a well-designed and verified laboratory model to investigate potential impacts related to Port expansion in a highly-complex flow regime. Information and estimates obtained from the physical model will allow Alaska District to anticipate potential problems associated with the Port expansion and to respond with the most efficient and appropriate actions.

References

- Henderson, F. M. 1966. *Open Channel Flow*. New York, NY: MacMillian Publishing Co., Inc.
- Hudson, R. Y., F. A. Herrmann, R. A. Sager, R. W. Whalin, G. H. Keulegan, C. E. Chatham, and L. Z. Hales. 1979. Coastal hydraulic models. Special Report No. 5. Vicksburg, MS: U.S. Army Engineer Waterways Experiment Station.
- Hughes, S. A. 2003. Physical modeling considerations for coastal structures. In *Advances in coastal structure design*, ed. R. Mohan, 97–115. ASCE.
- Hughes, S. A. 1993. Physical models and laboratory techniques in coastal engineering. In *Advanced series on ocean engineering 7*. Singapore: World Scientific.
- Hughes, S. A. and Pizzo, G.-M. 2003. *Flow table study of Cook Inlet, Alaska*. ERDC/CHL TR-03-6. Vicksburg, MS: U.S. Army Engineer Research and Development Center.
- Kamphuis, J. W. 1991. Physical modeling. In *Handbook of coastal and ocean engineering 2*, ed. J. B. Herbich. Houston, TX: Gulf Publishing Company.
- Warnock, J. E. 1950. Hydraulic similitude. In *Engineering hydraulics*, ed. H. Rouse, 136–176. New York: John Wiley & Sons.

Appendix A: Consistency Check Plots

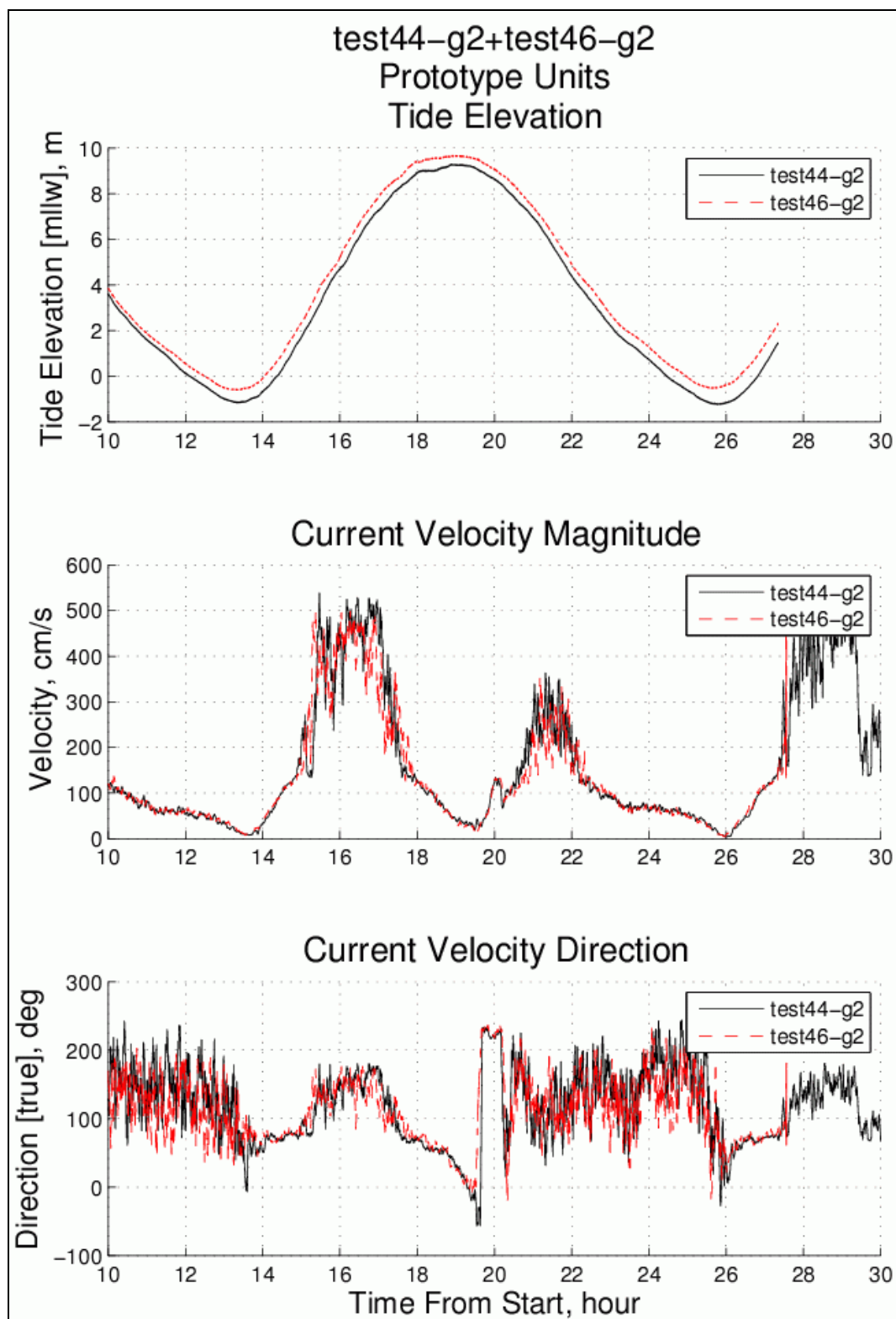


Figure A1. Consistency check for Test 46 at location Ref. ADV.

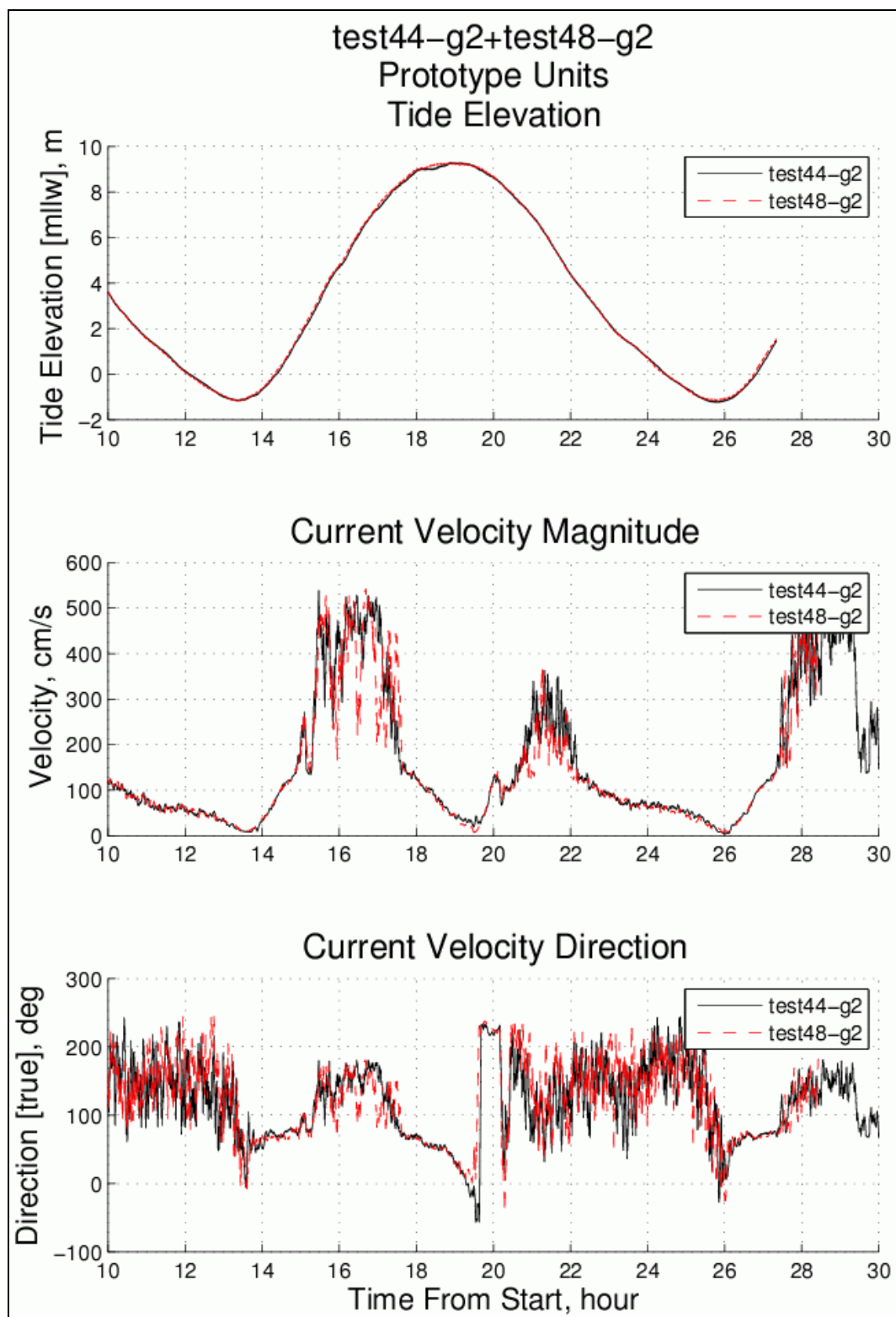


Figure A2. Consistency check for Test 48 at location Ref. ADV.

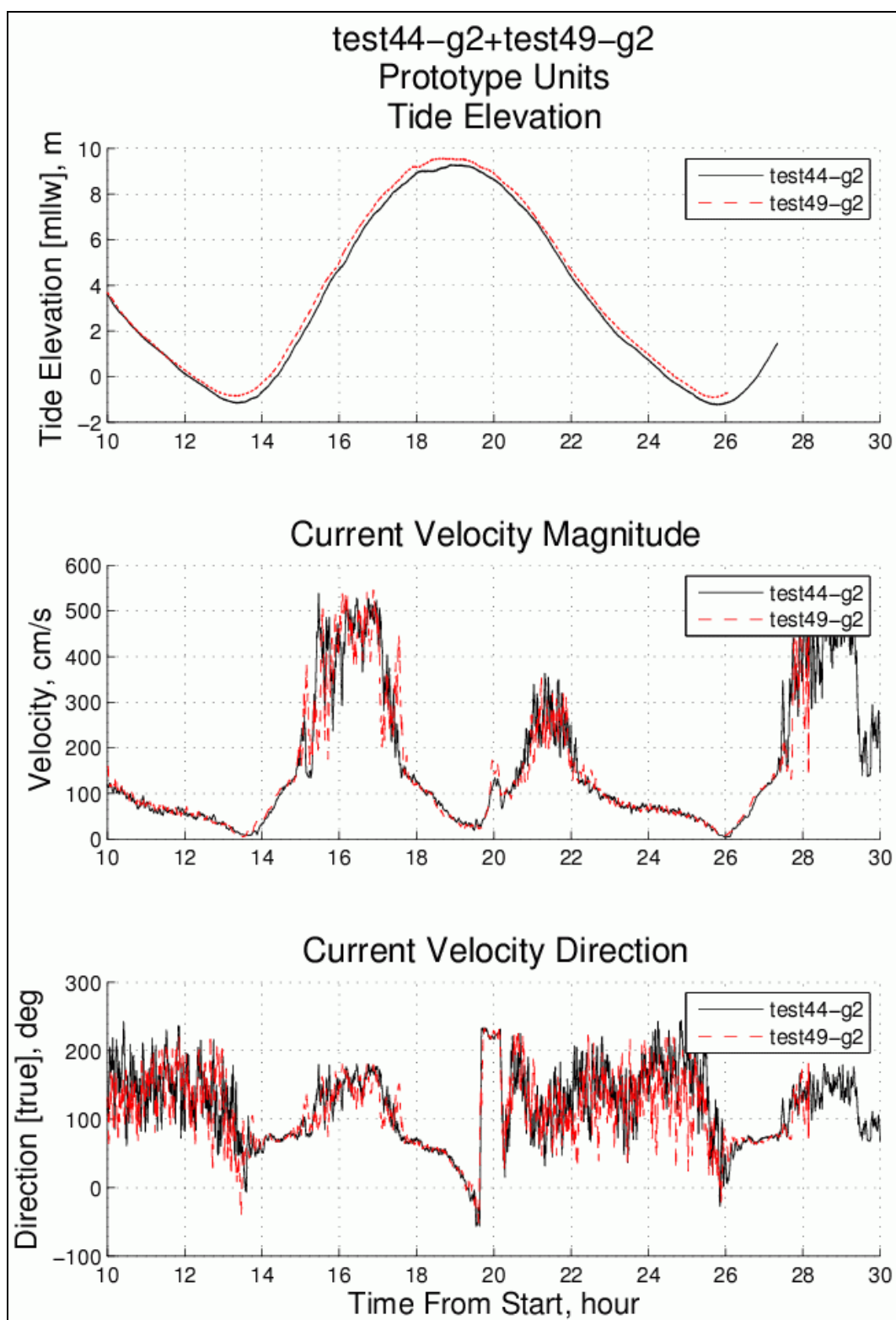


Figure A3. Consistency check for Test 49 at location Ref. ADV.

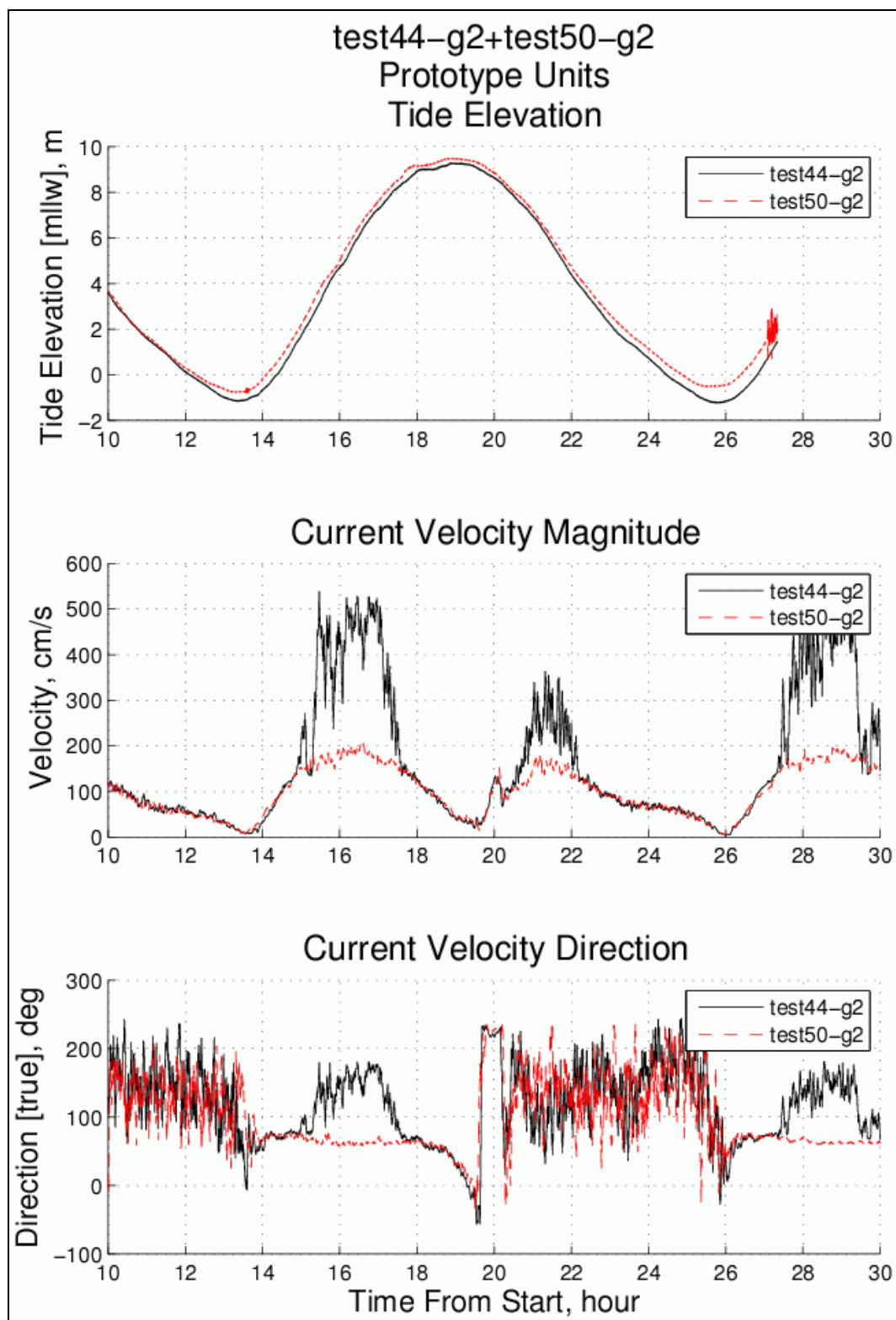


Figure A4. Consistency check for Test 50 at location Ref. ADV.

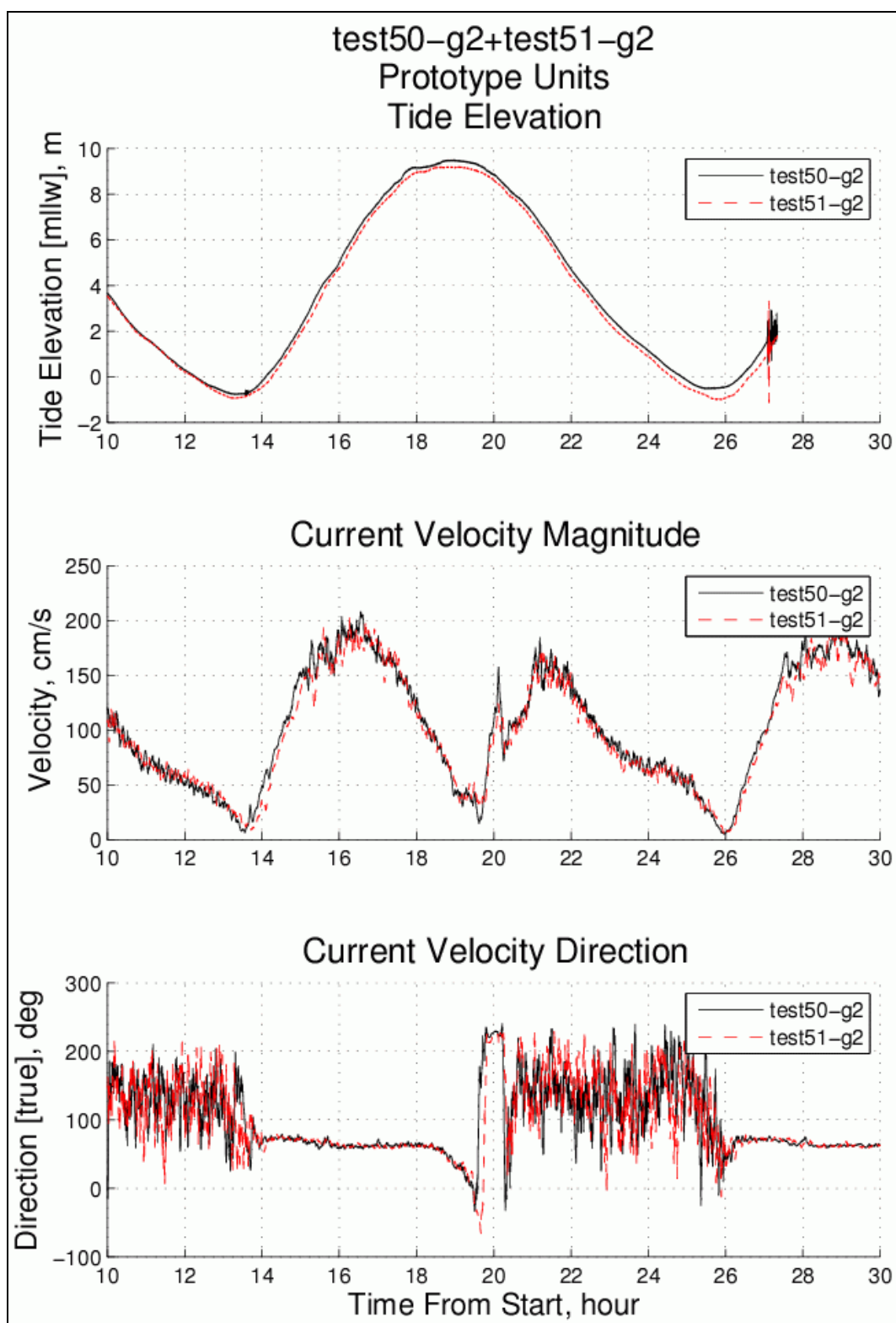


Figure A5. Consistency check for Test 51 at location Ref. ADV.

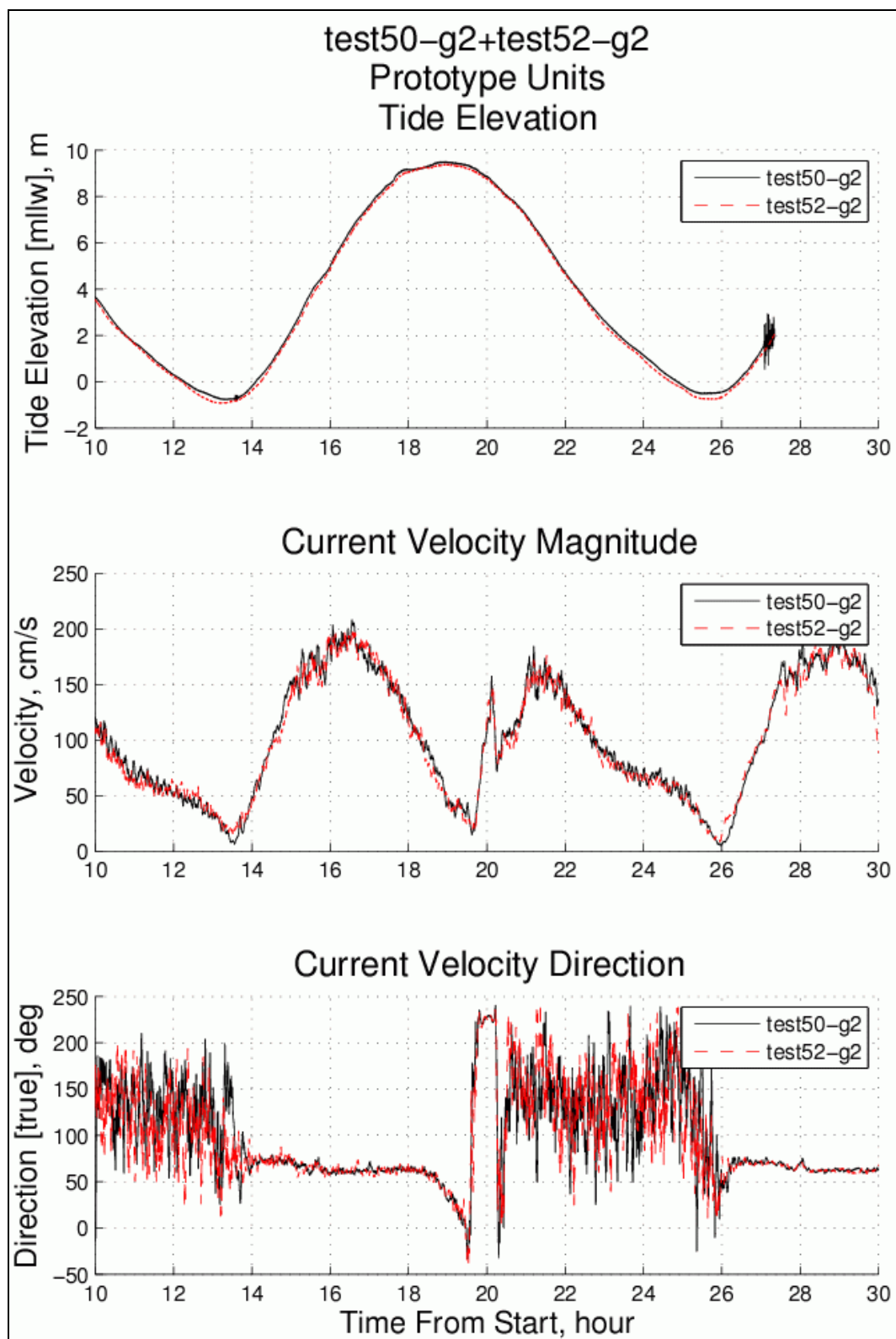


Figure A6. Consistency check for Test 52 at location Ref. ADV.

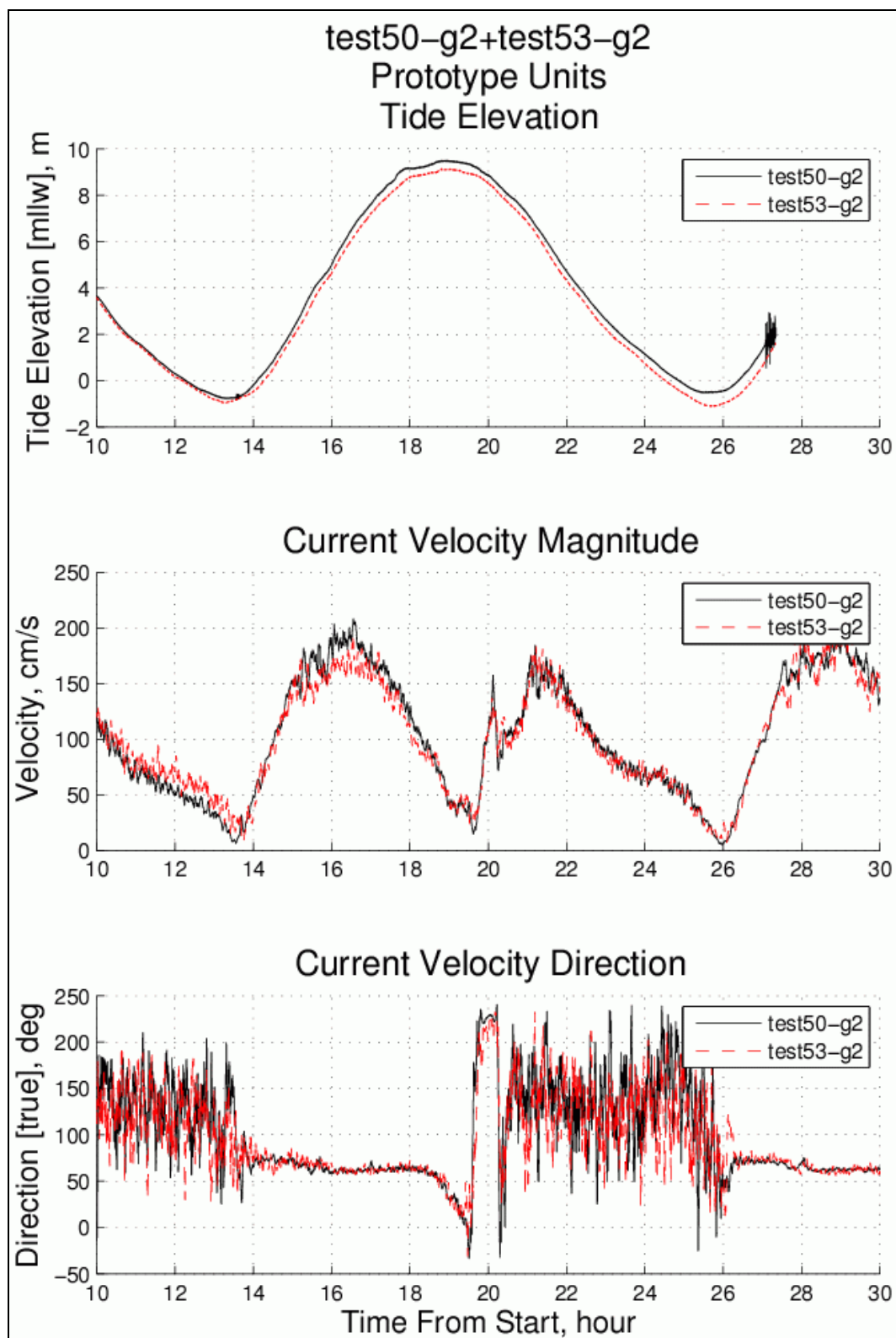


Figure A7. Consistency check for Test 53 at location Ref. ADV.

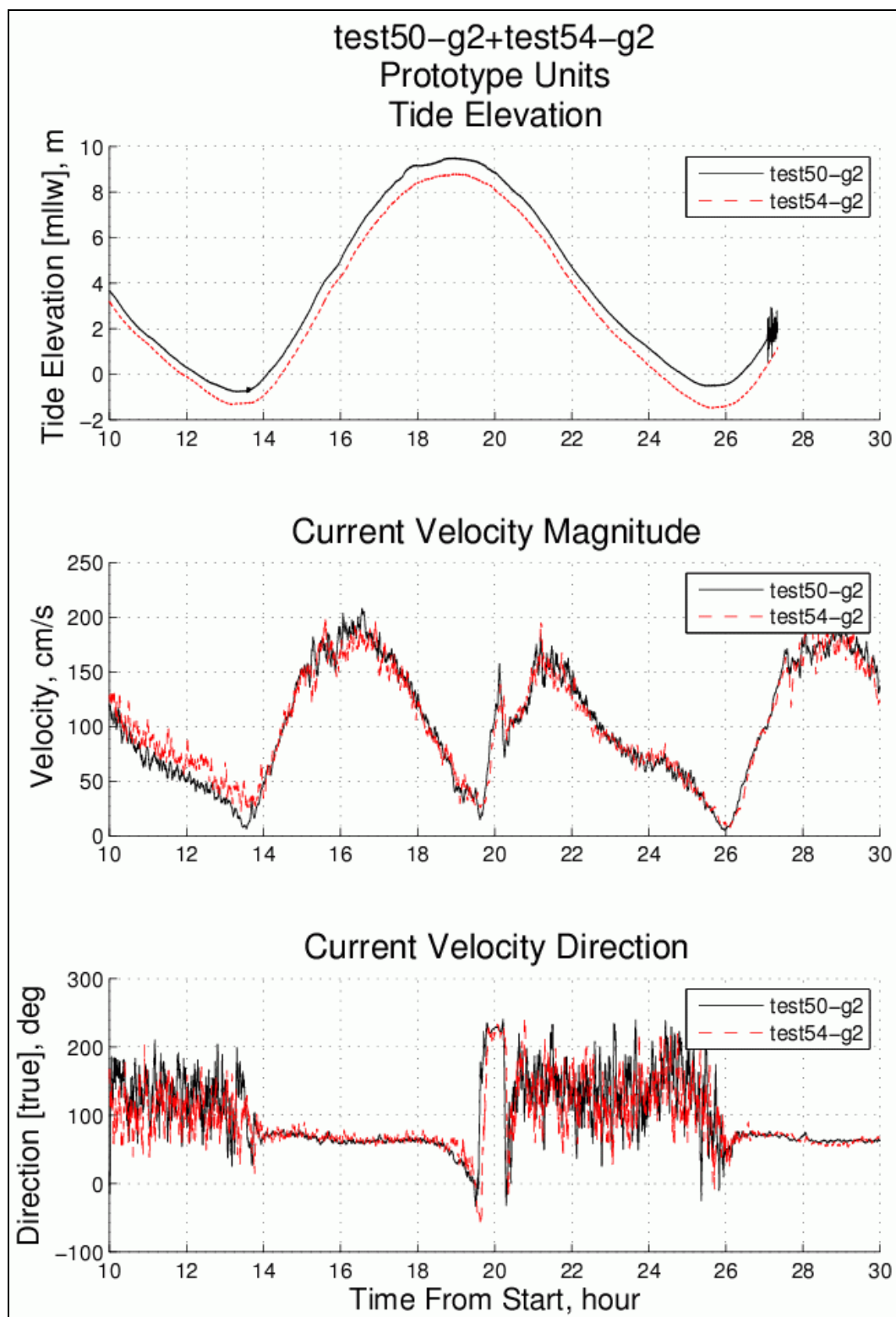


Figure A8. Consistency check for Test 54 at location Ref. ADV.

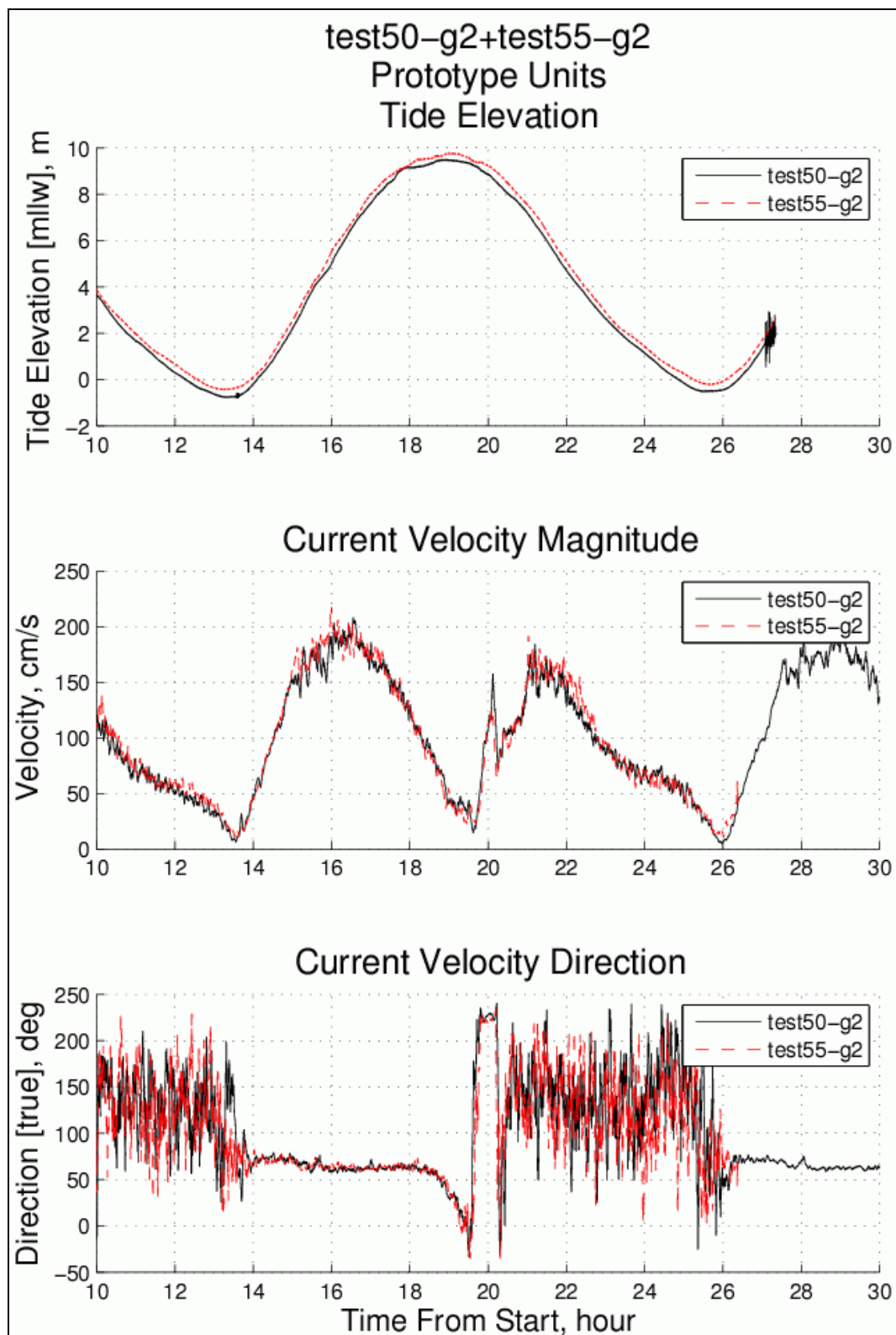


Figure A9. Consistency check for Test 55 at location Ref. ADV.

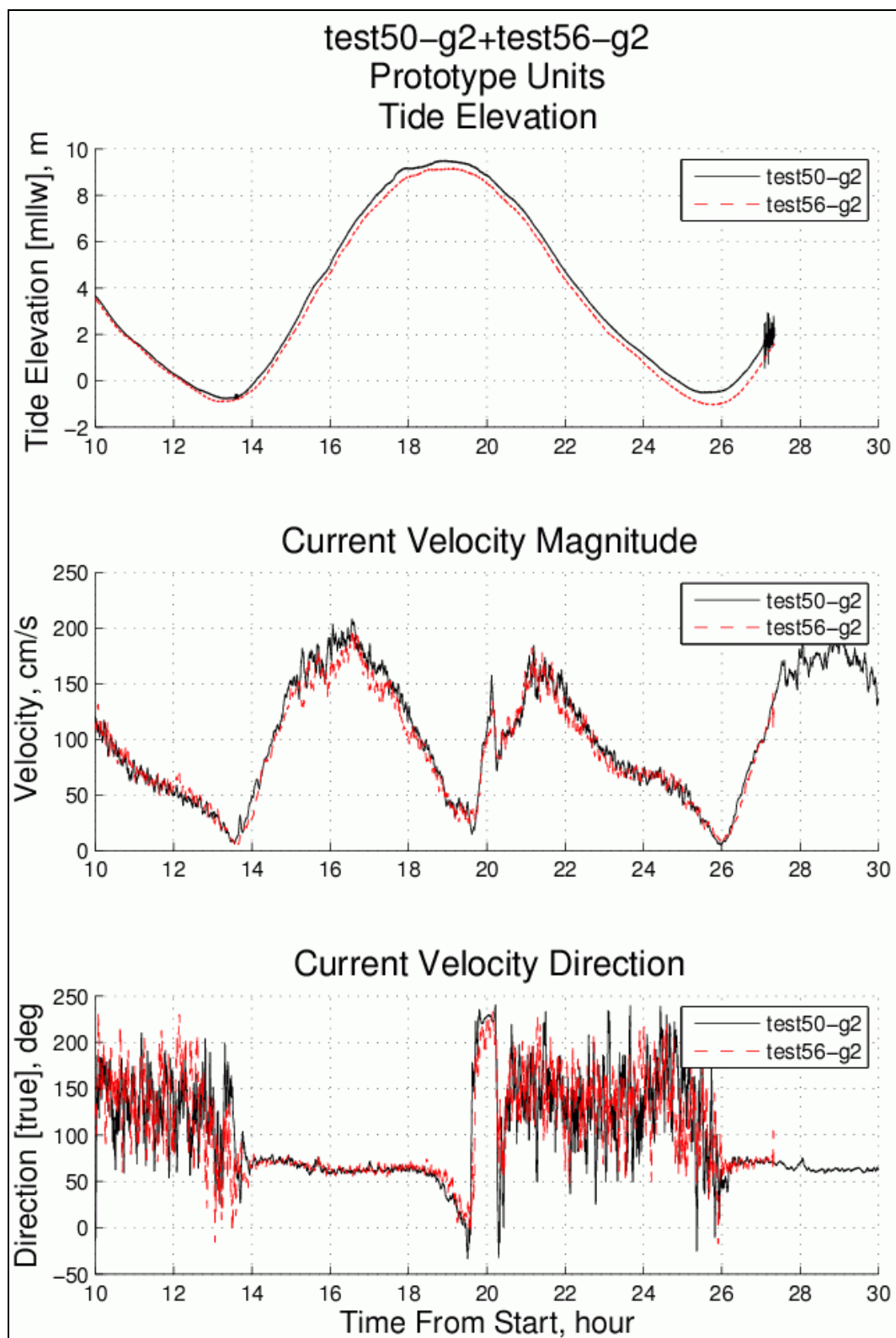


Figure A10. Consistency check for Test 56 at location Ref. ADV.

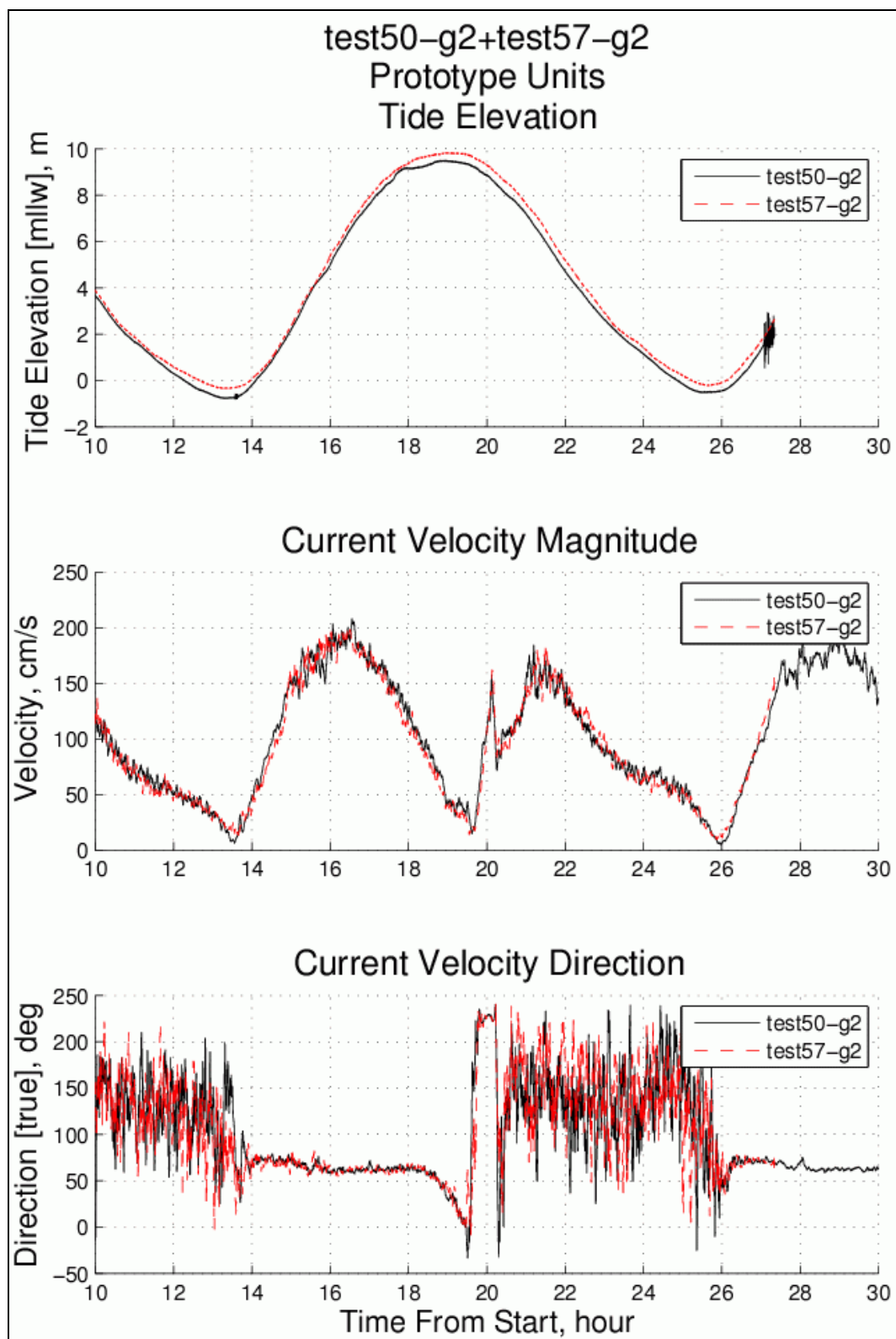


Figure A11. Consistency check for Test 57 at location Ref. ADV.

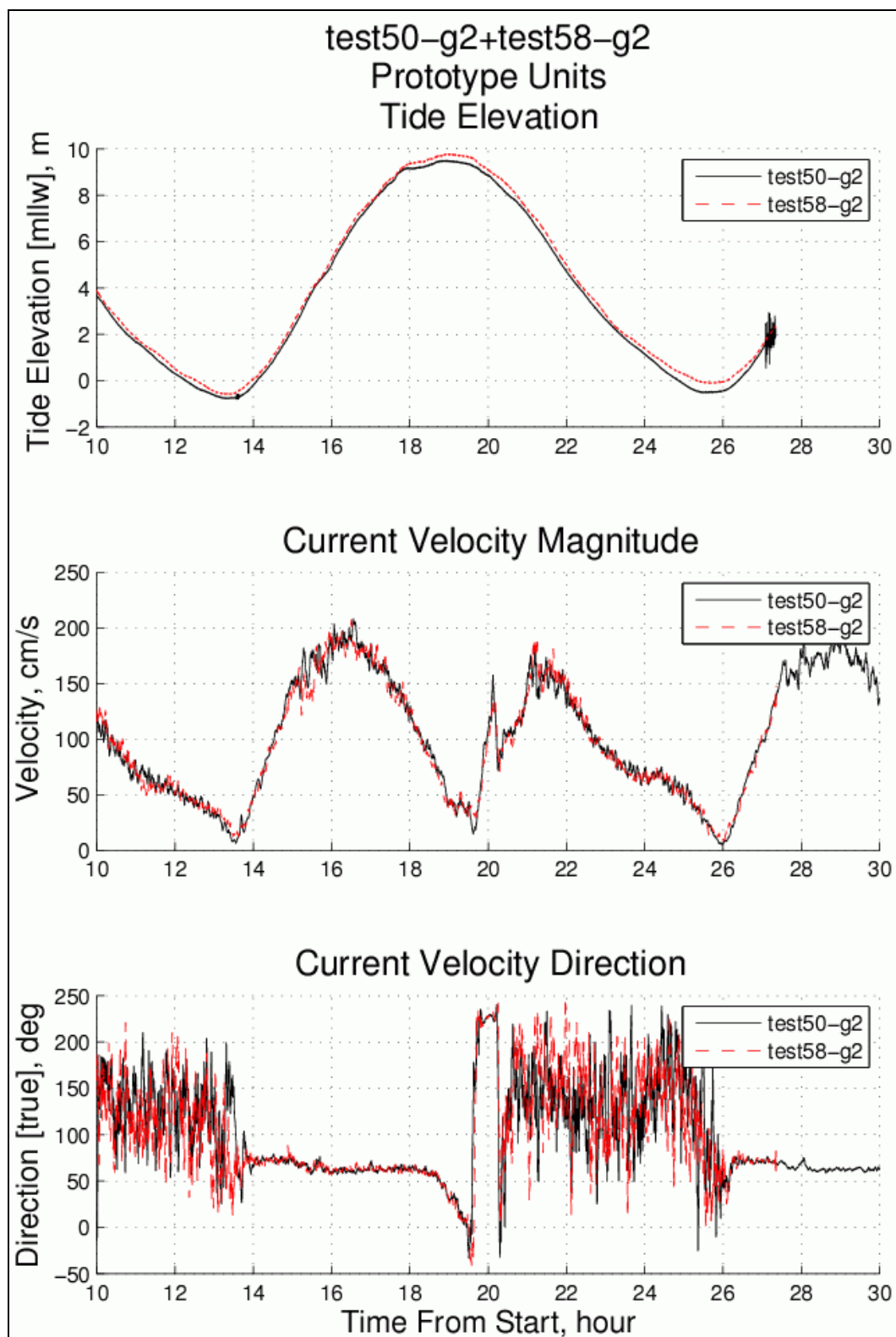


Figure A12. Consistency check for Test 58 at location Ref. ADV.

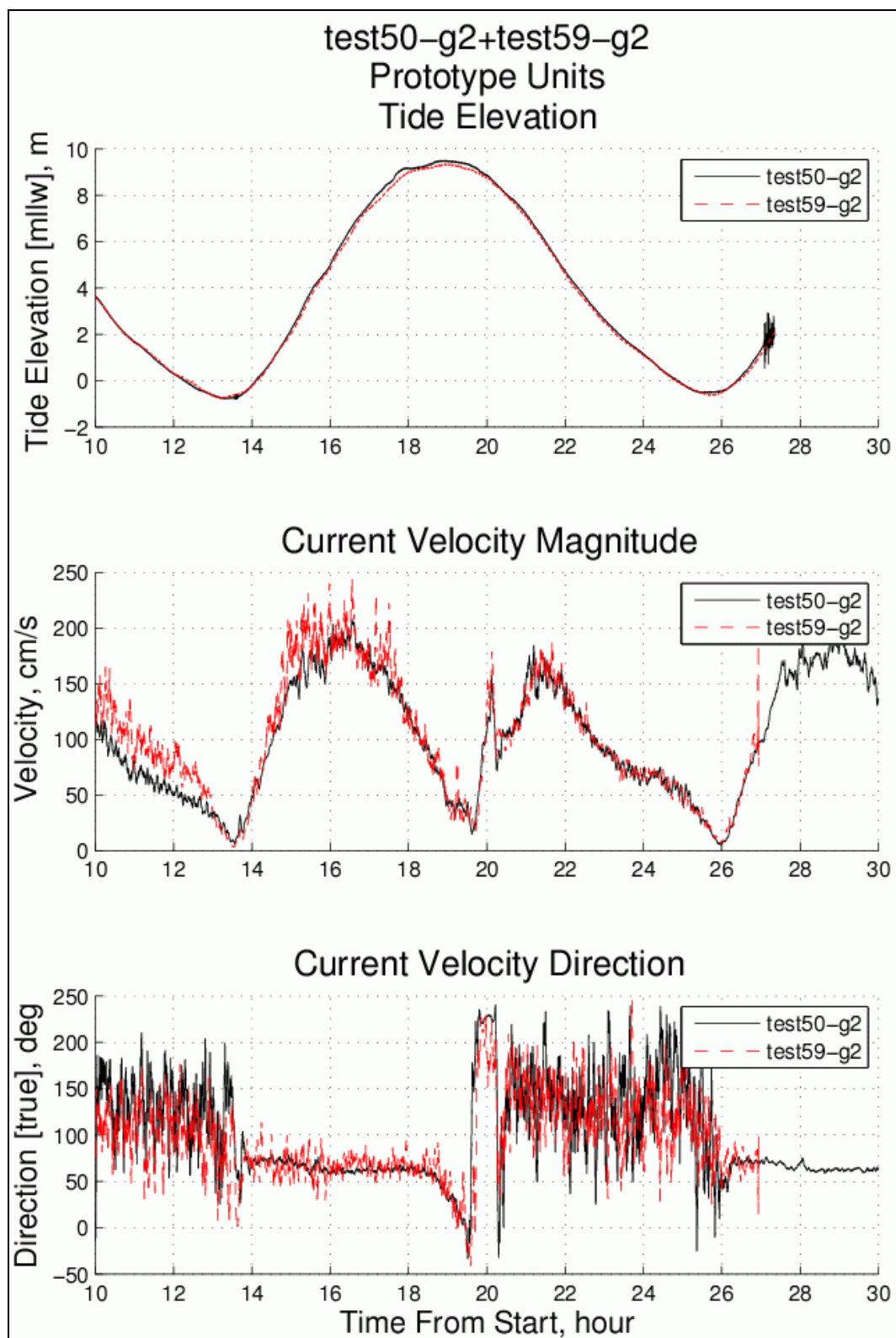


Figure A13. Consistency check for Test 59 at location Ref. ADV.

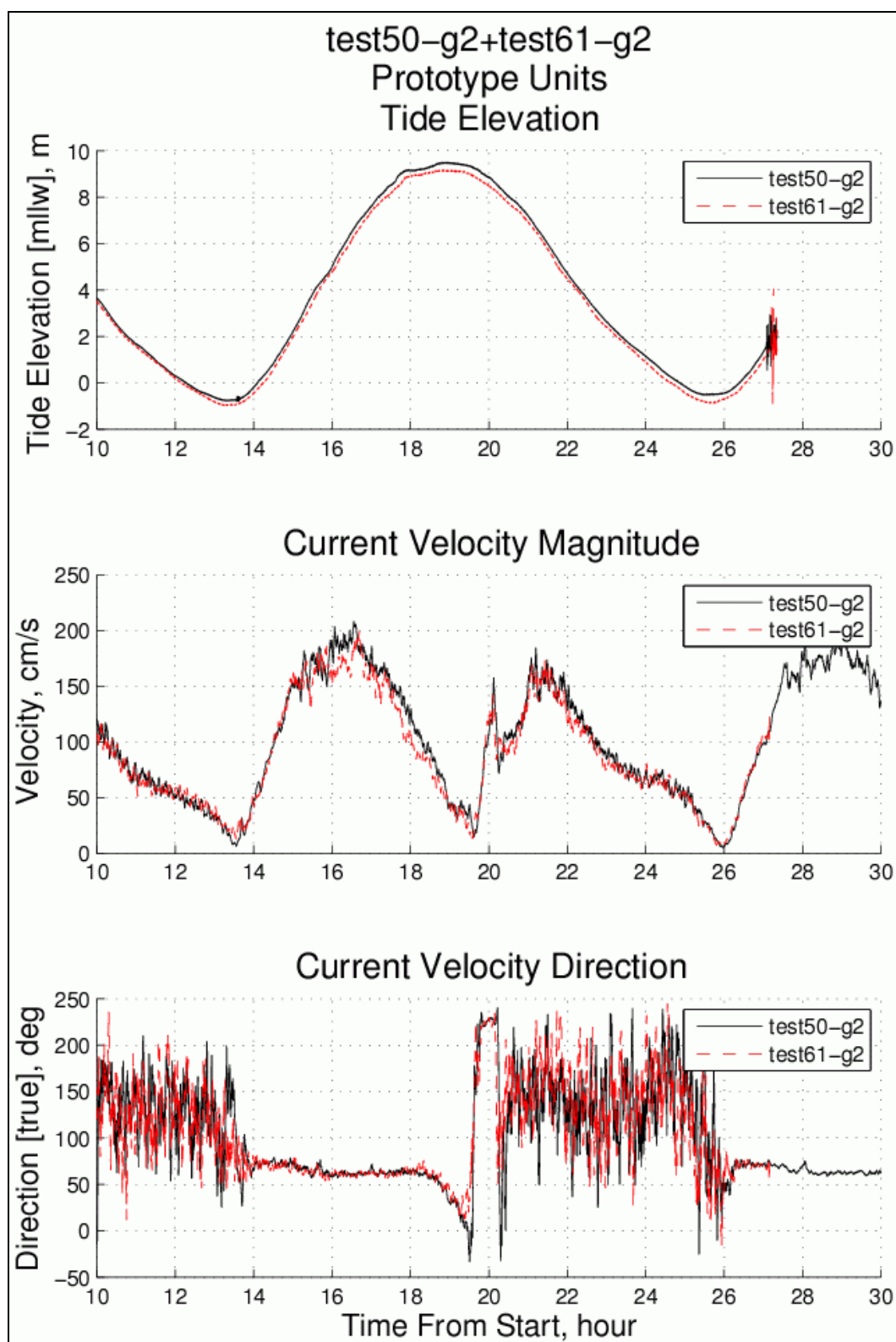


Figure A14. Consistency check for Test 61 at location Ref. ADV.

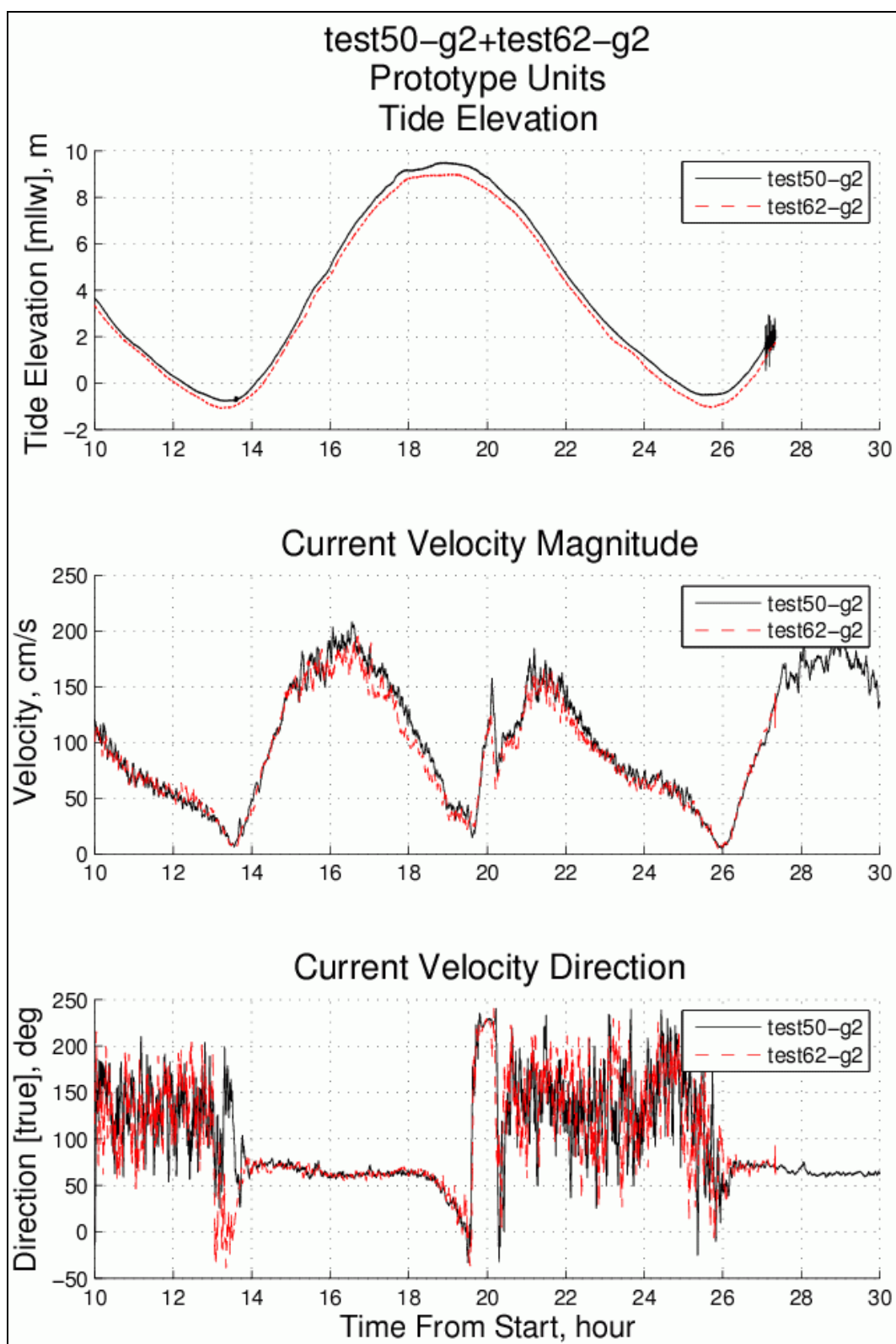


Figure A15. Consistency check for Test 62 at location Ref. ADV.

Appendix B: Velocity Plots for Port Expansion Phases

Existing Port Configuration

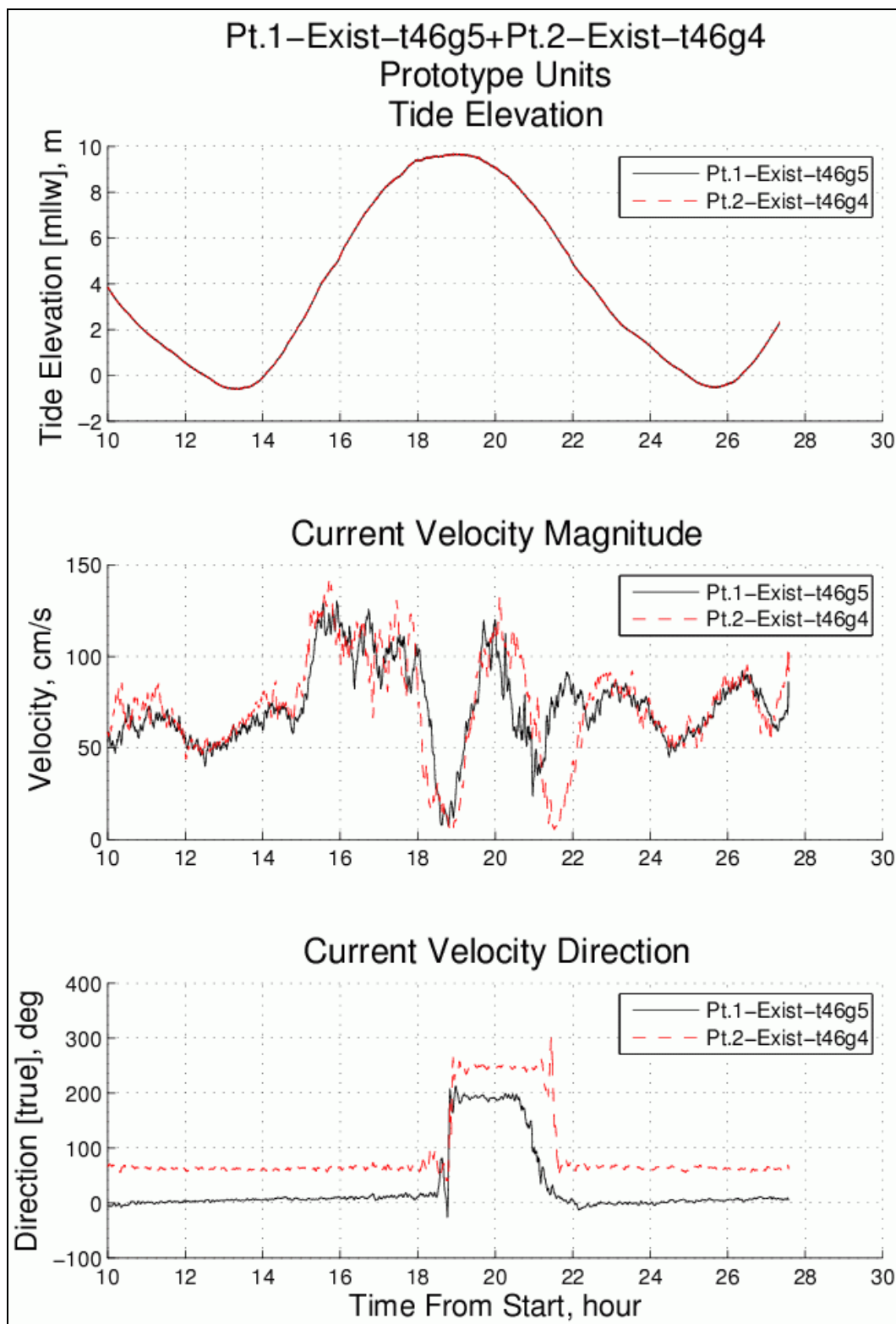


Figure B1. Velocity measurements at Pt. 1 and Pt. 2 (Existing configuration).

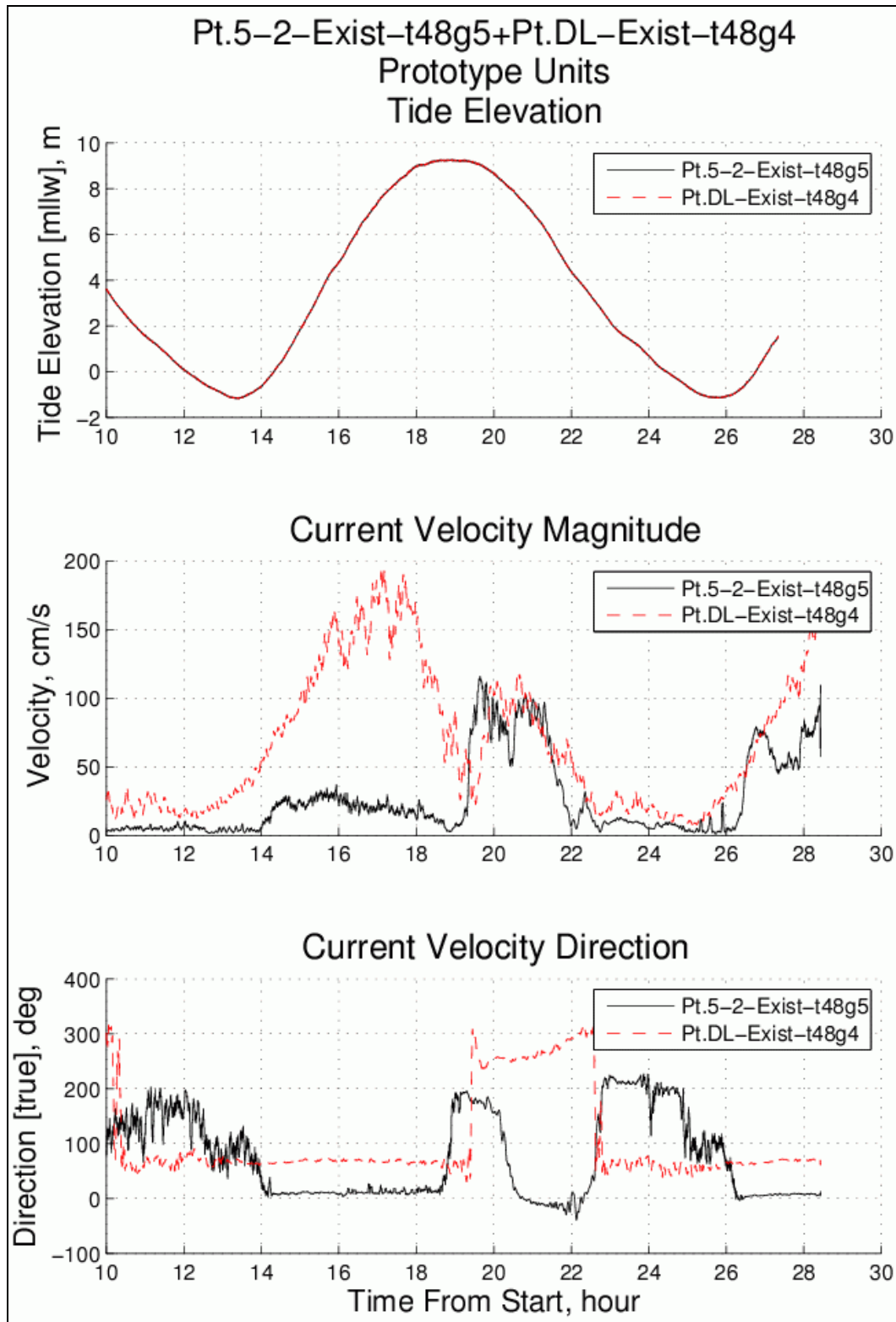


Figure B2. Velocity measurements at Pt. 5.2 and Pt. DL (Existing configuration).

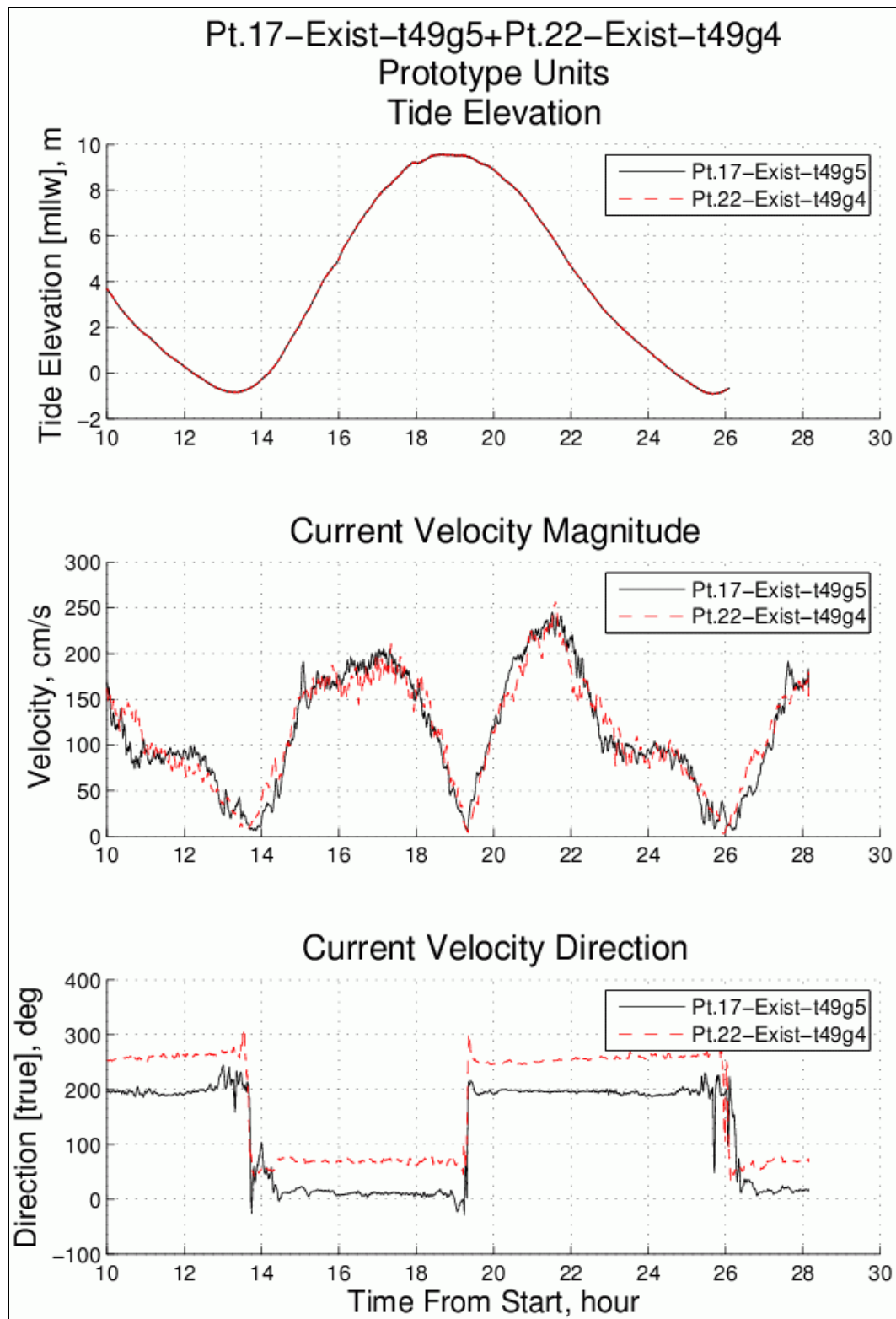


Figure B3. Velocity measurements at Pt. 17 and Pt. 22 (Existing configuration).

First Port Expansion Configuration

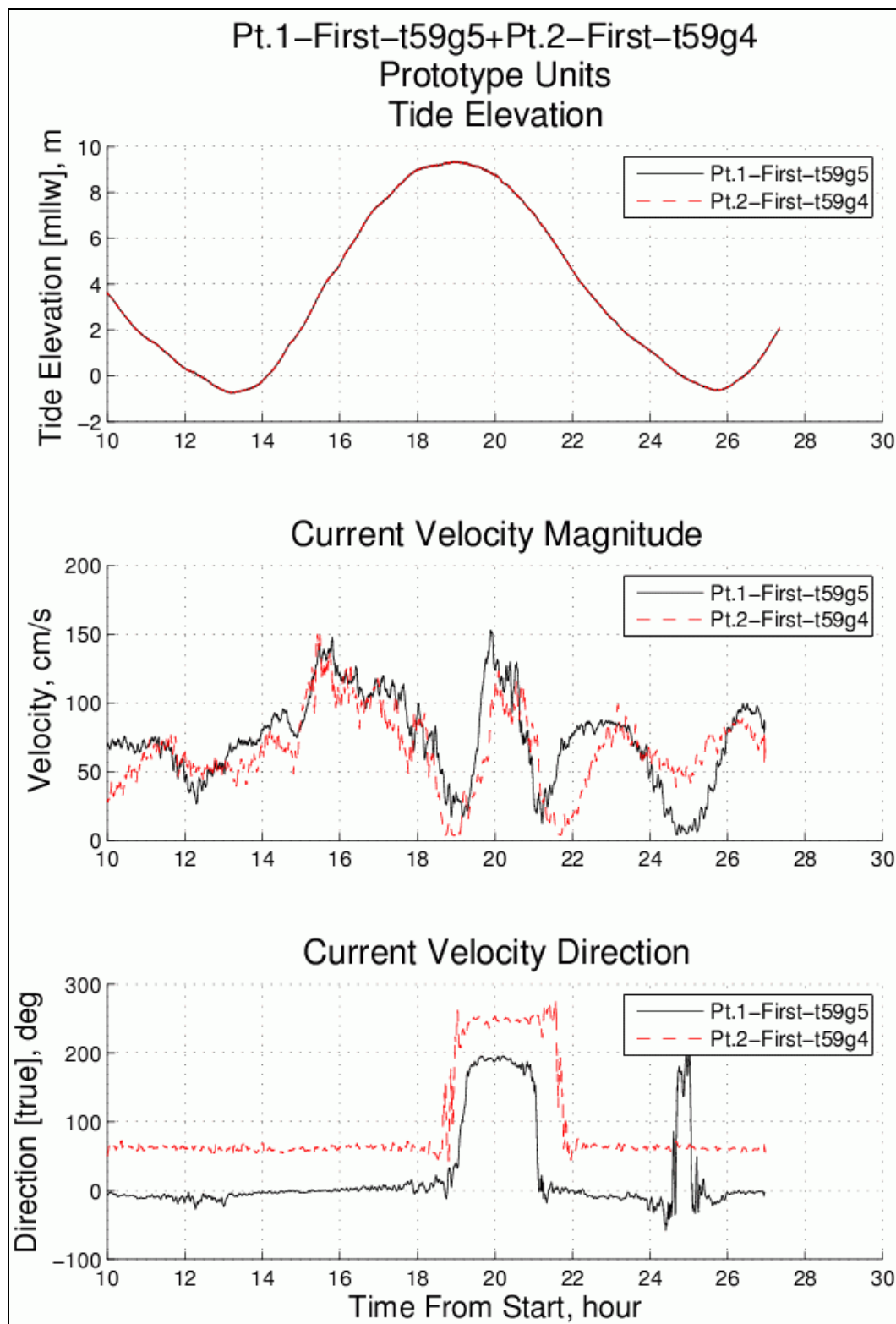


Figure B4. Velocity measurements at Pt. 1 and Pt. 2 (First Expansion configuration).

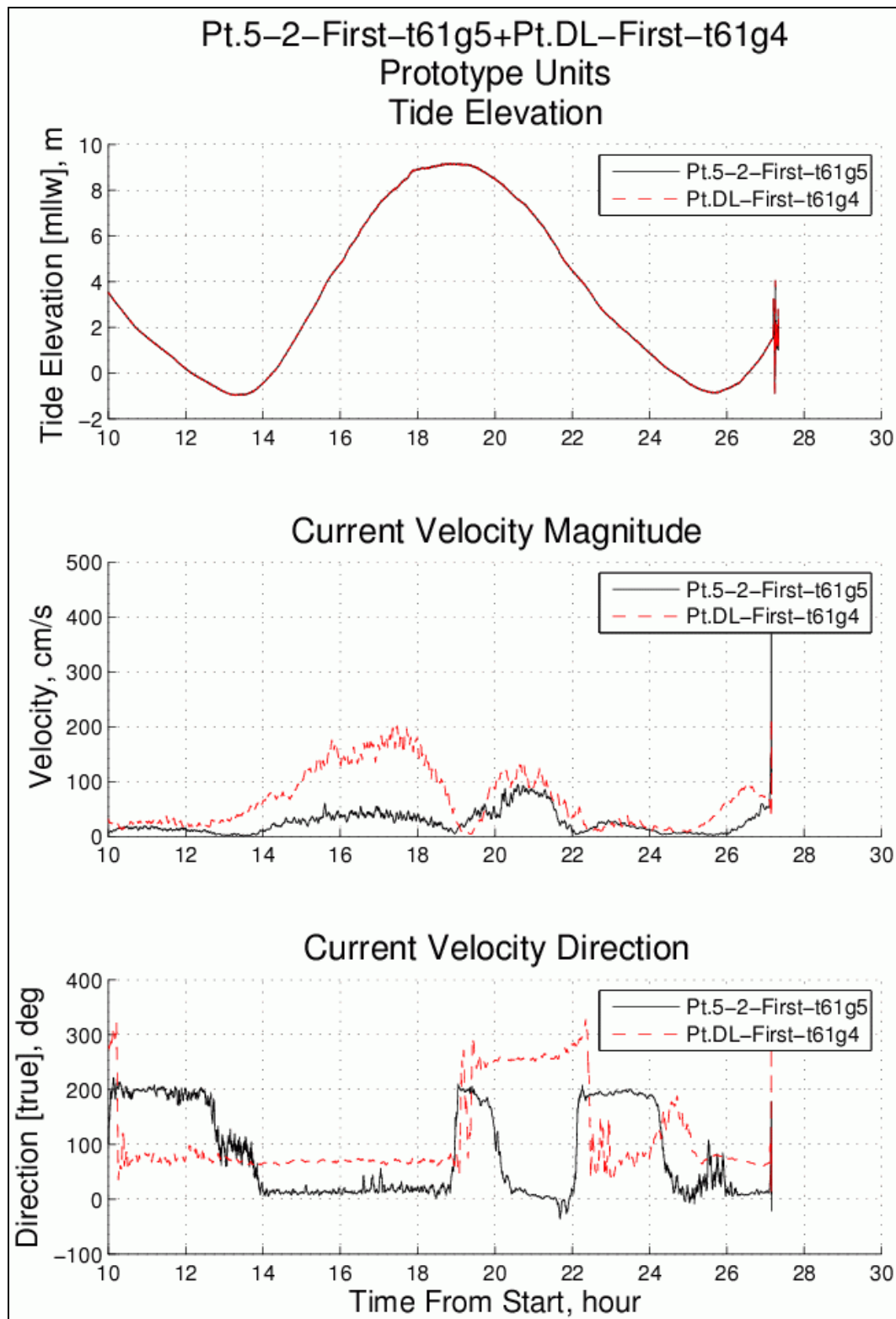


Figure B5. Velocity measurements at Pt. 5.2 and Pt. DL (First Expansion configuration).

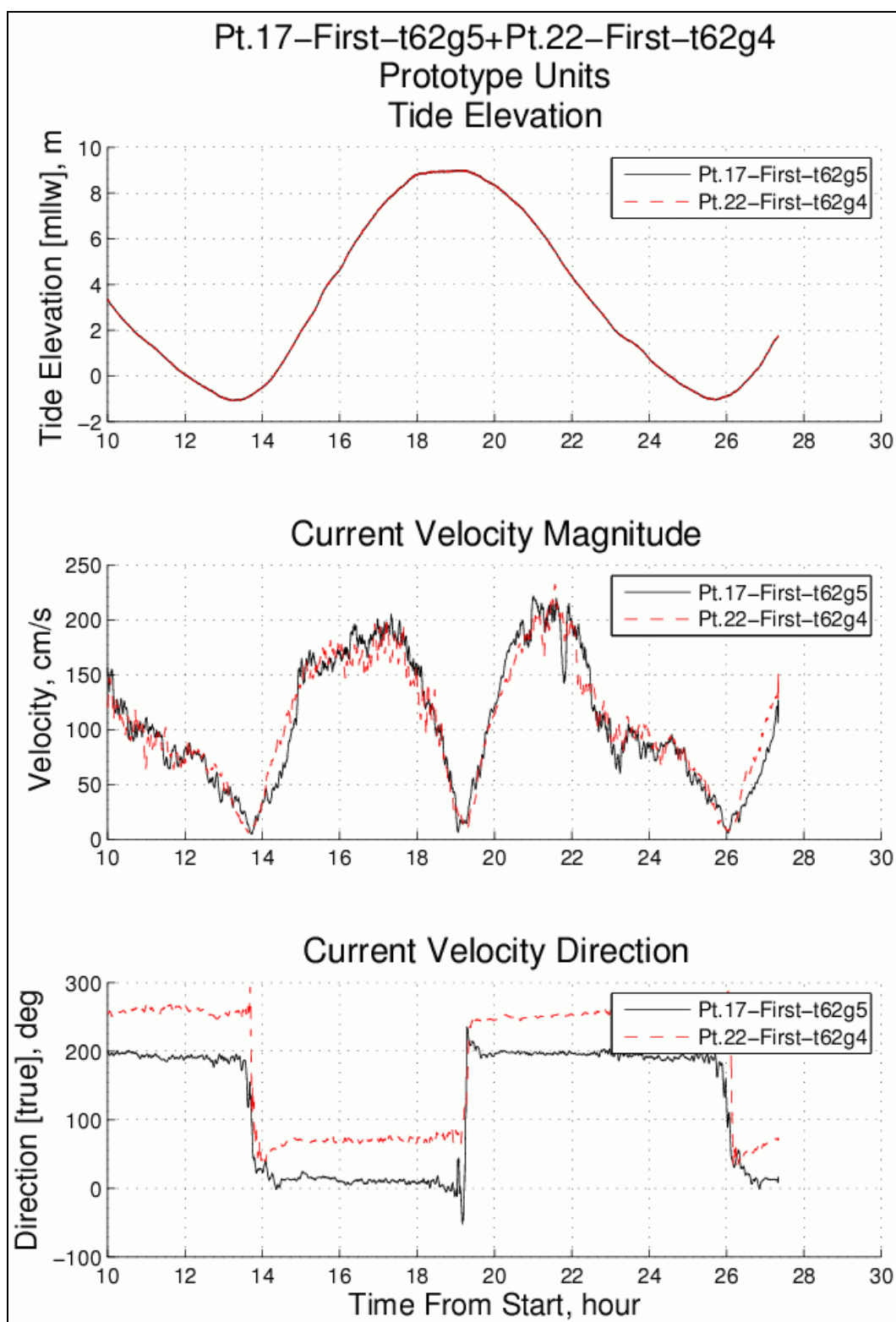


Figure B6. Velocity measurements at Pt. 17 and Pt. 22 (First Expansion configuration).

Second Port Expansion Configuration

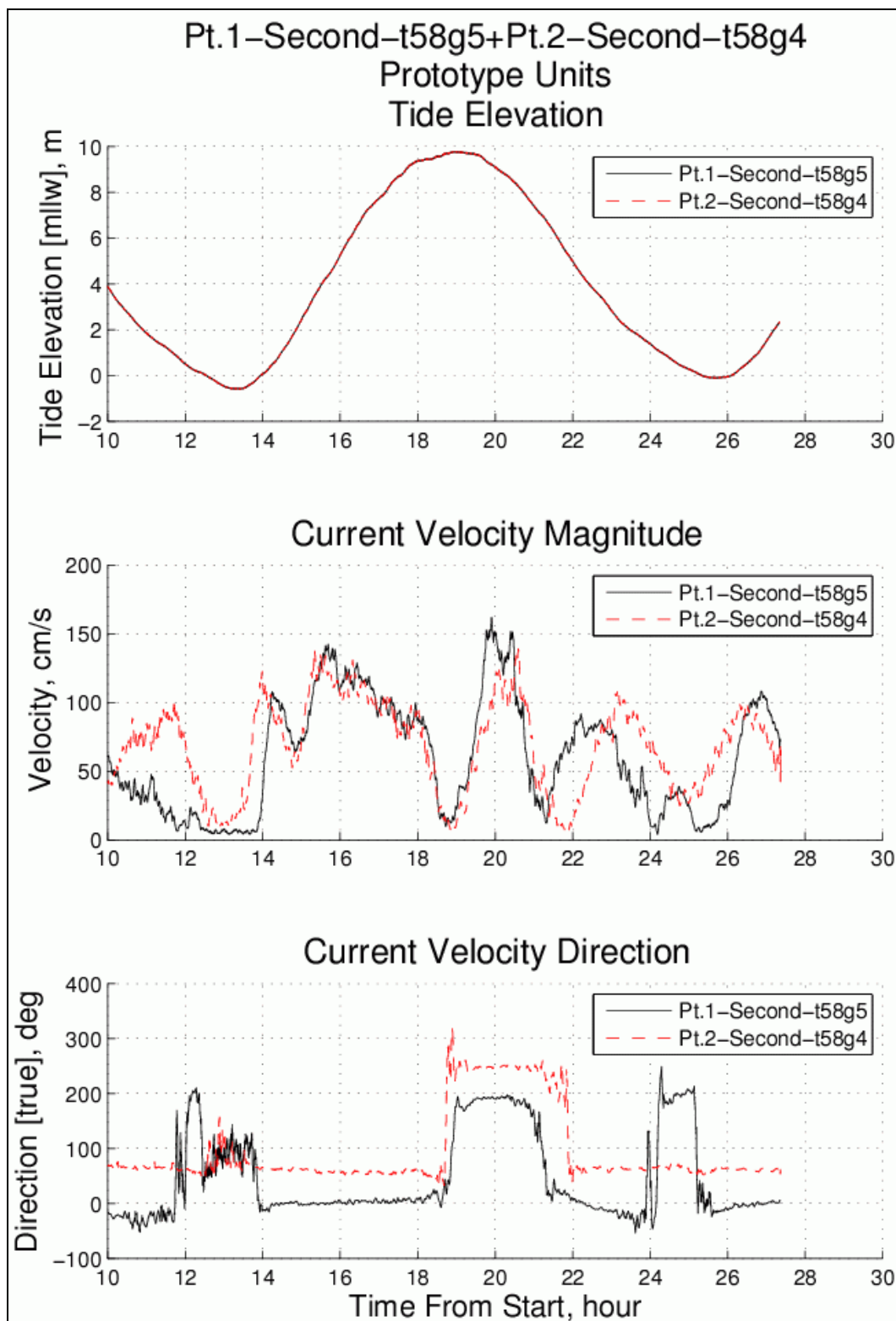


Figure B7. Velocity measurements at Pt. 1 and Pt. 2 (Second Expansion configuration).

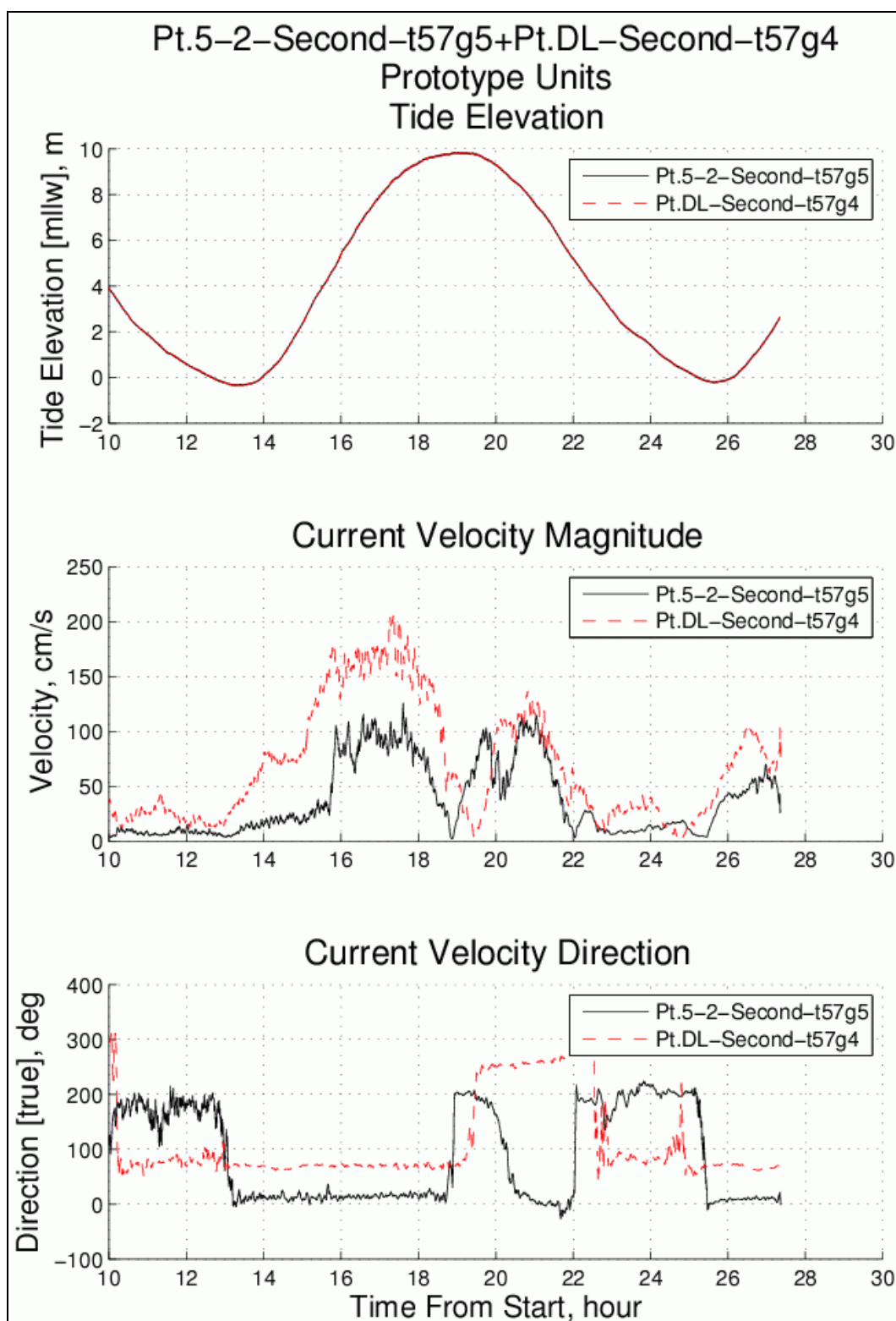


Figure B8. Velocity measurements at Pt. 5.2 and Pt. DL (Second Expansion configuration).

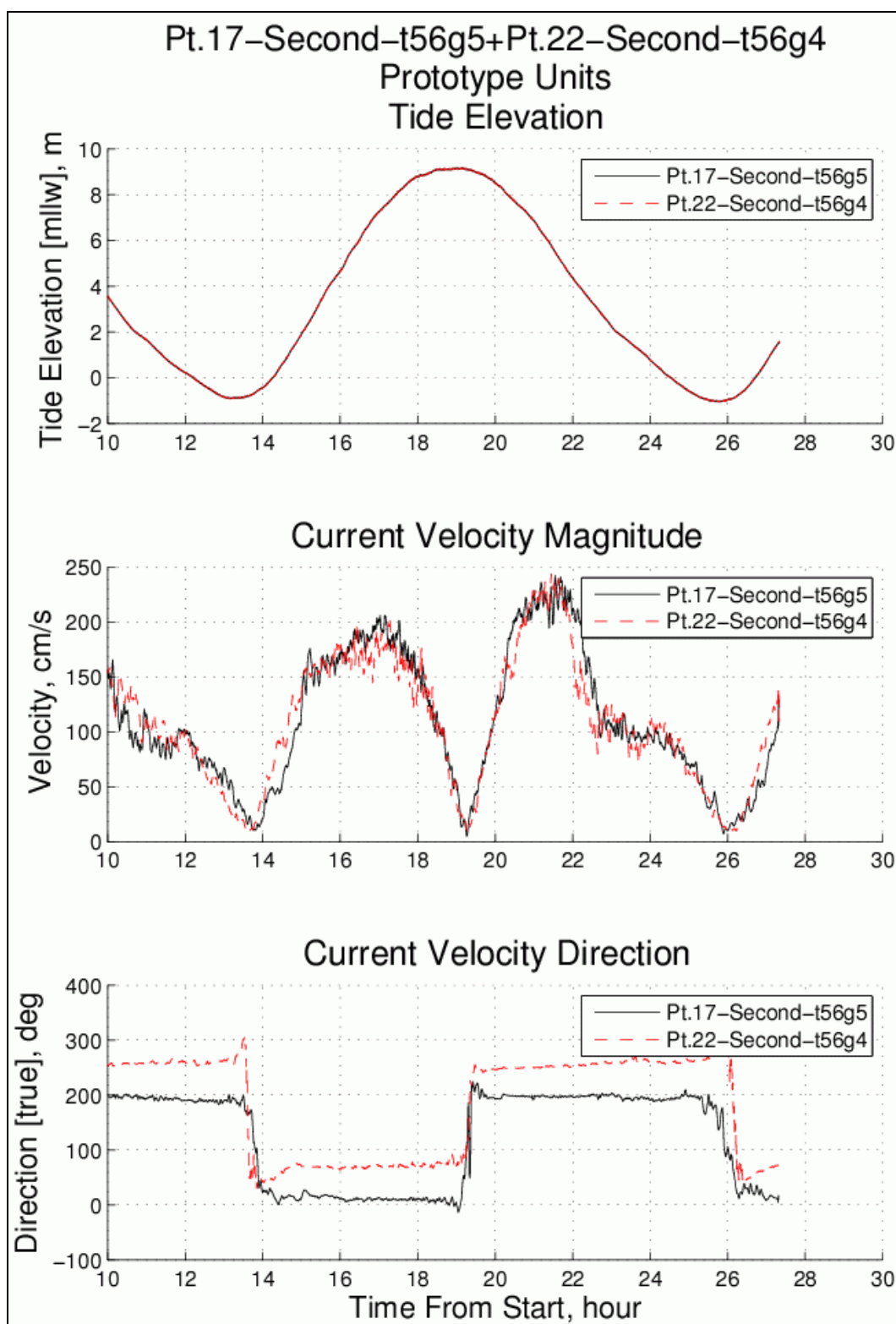


Figure B9. Velocity measurements at Pt. 17 and Pt. 22 (Second Expansion configuration).

Third Port Expansion Configuration

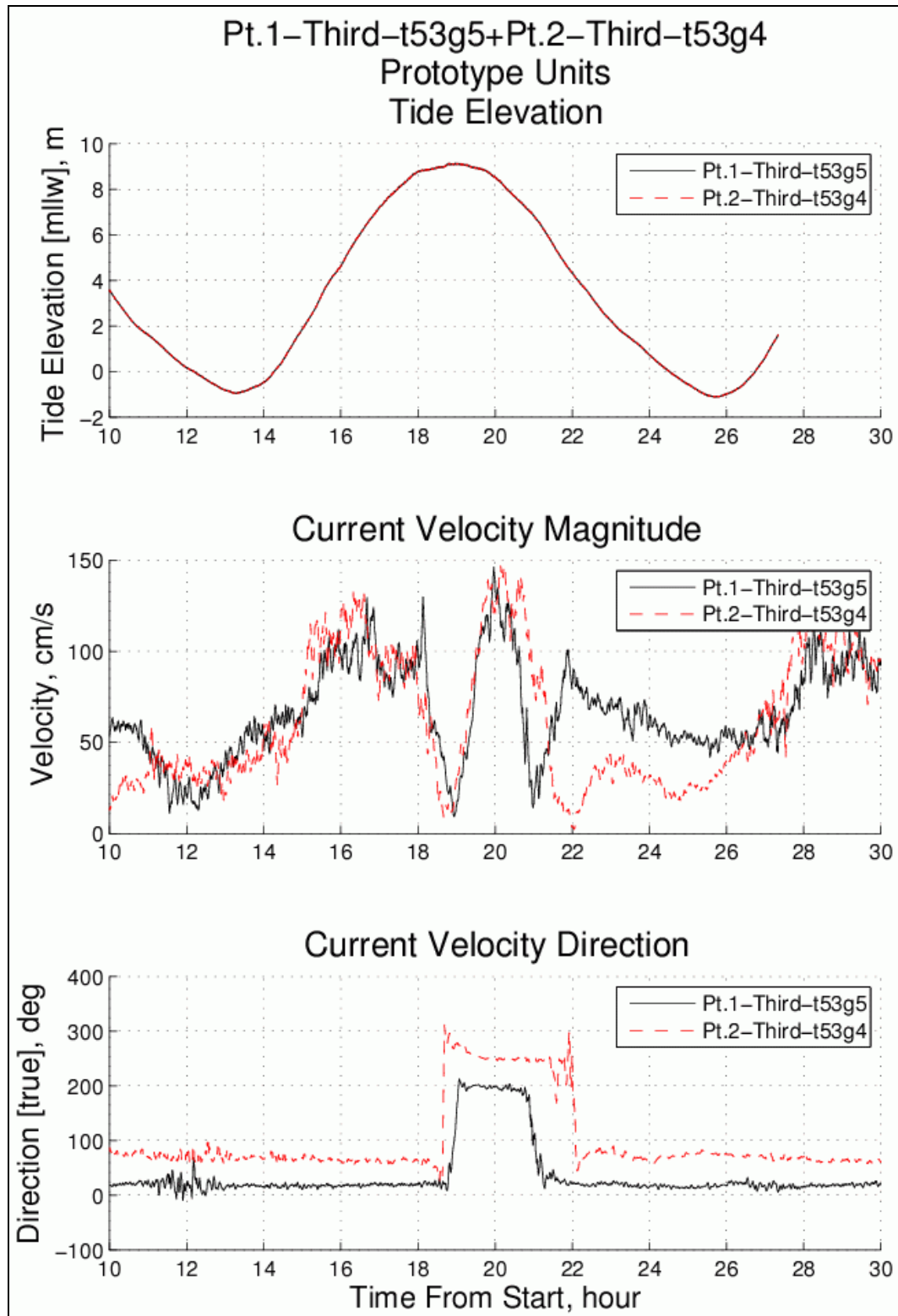


Figure B10. Velocity measurements at Pt. 1 and Pt. 2 (Third Expansion configuration).

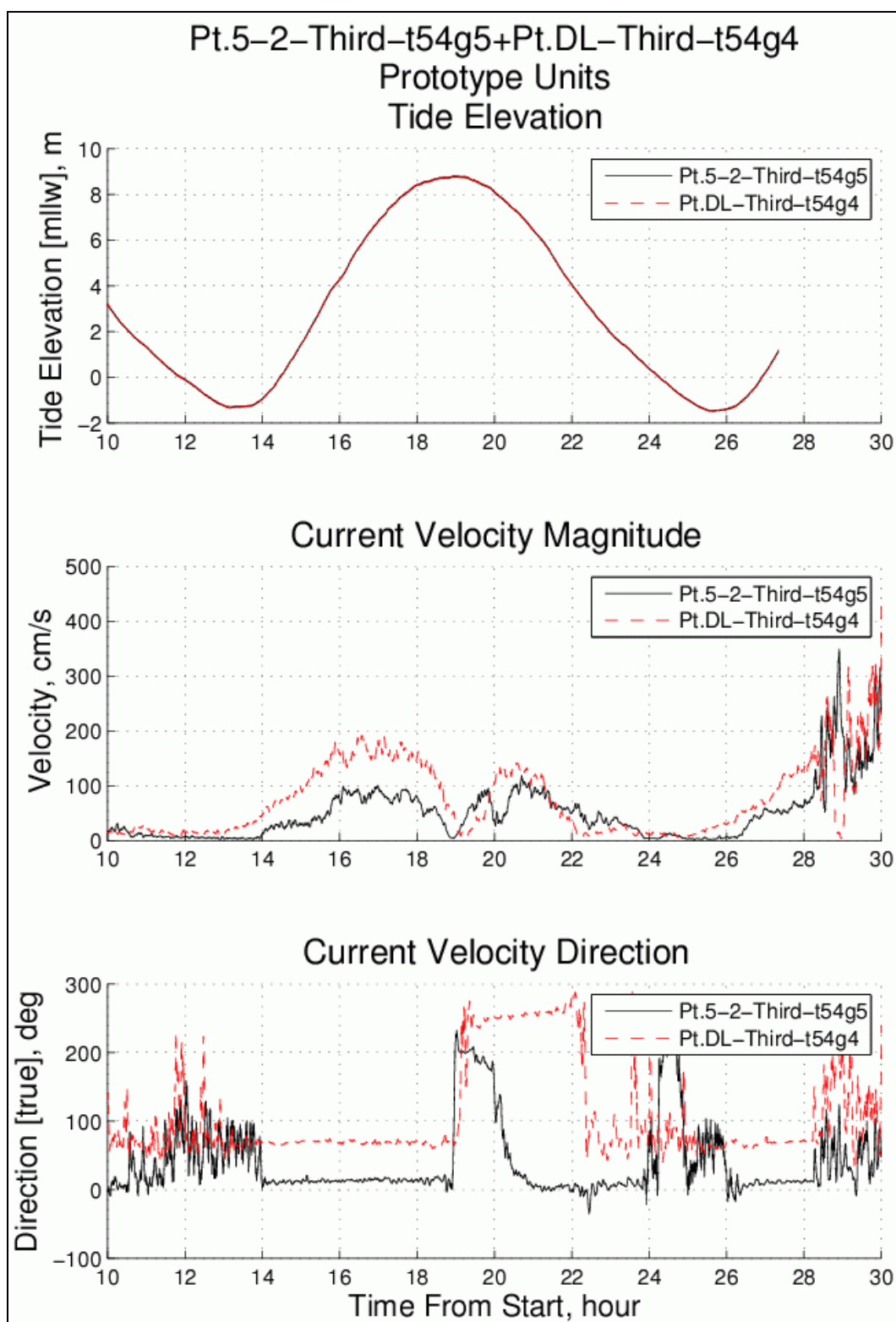


Figure B11. Velocity measurements at Pt. 5.2 and Pt. DL (Third Expansion configuration).

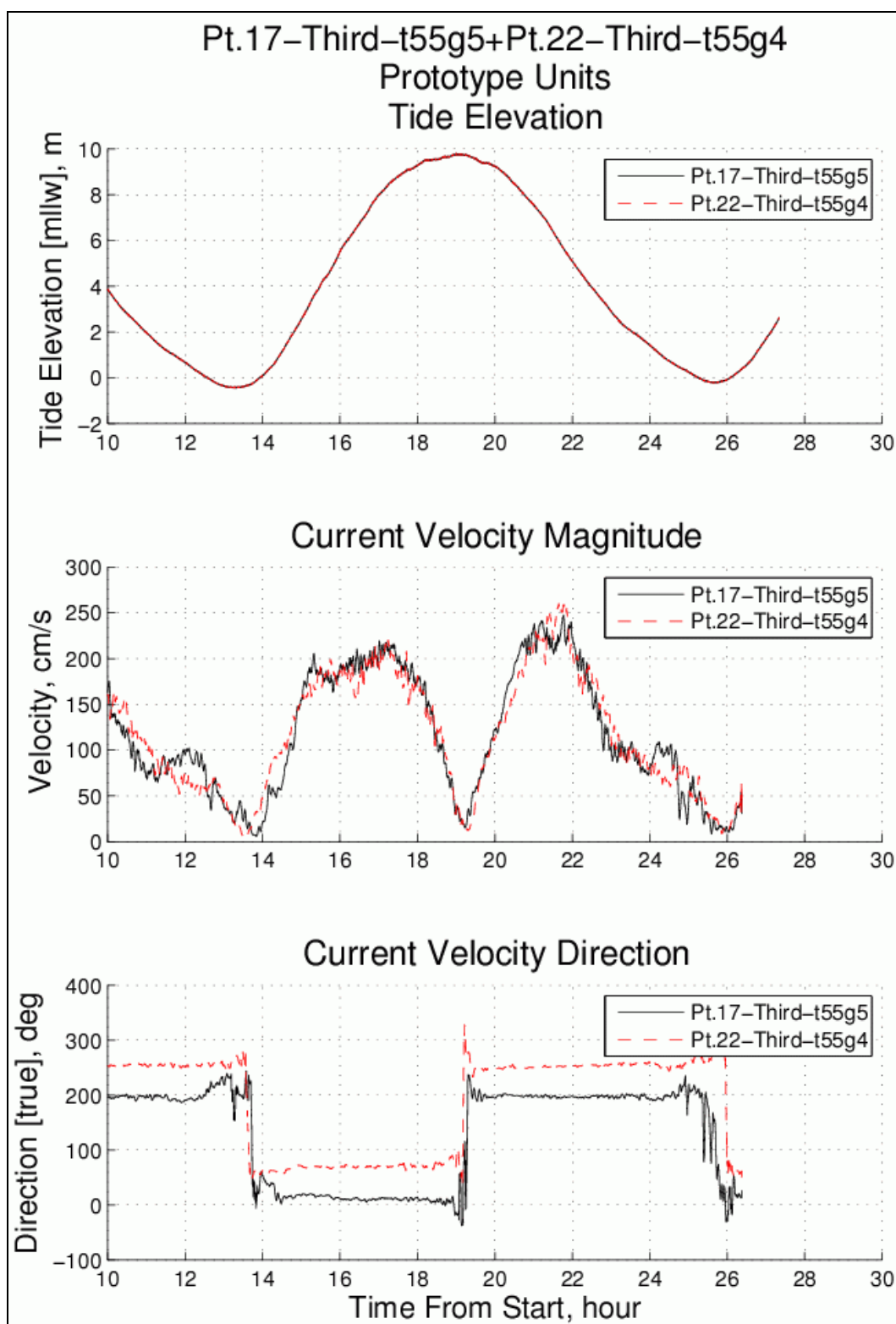


Figure B12. Velocity measurements at Pt. 17 and Pt. 22 (Third Expansion configuration).

Full Port Expansion Configuration

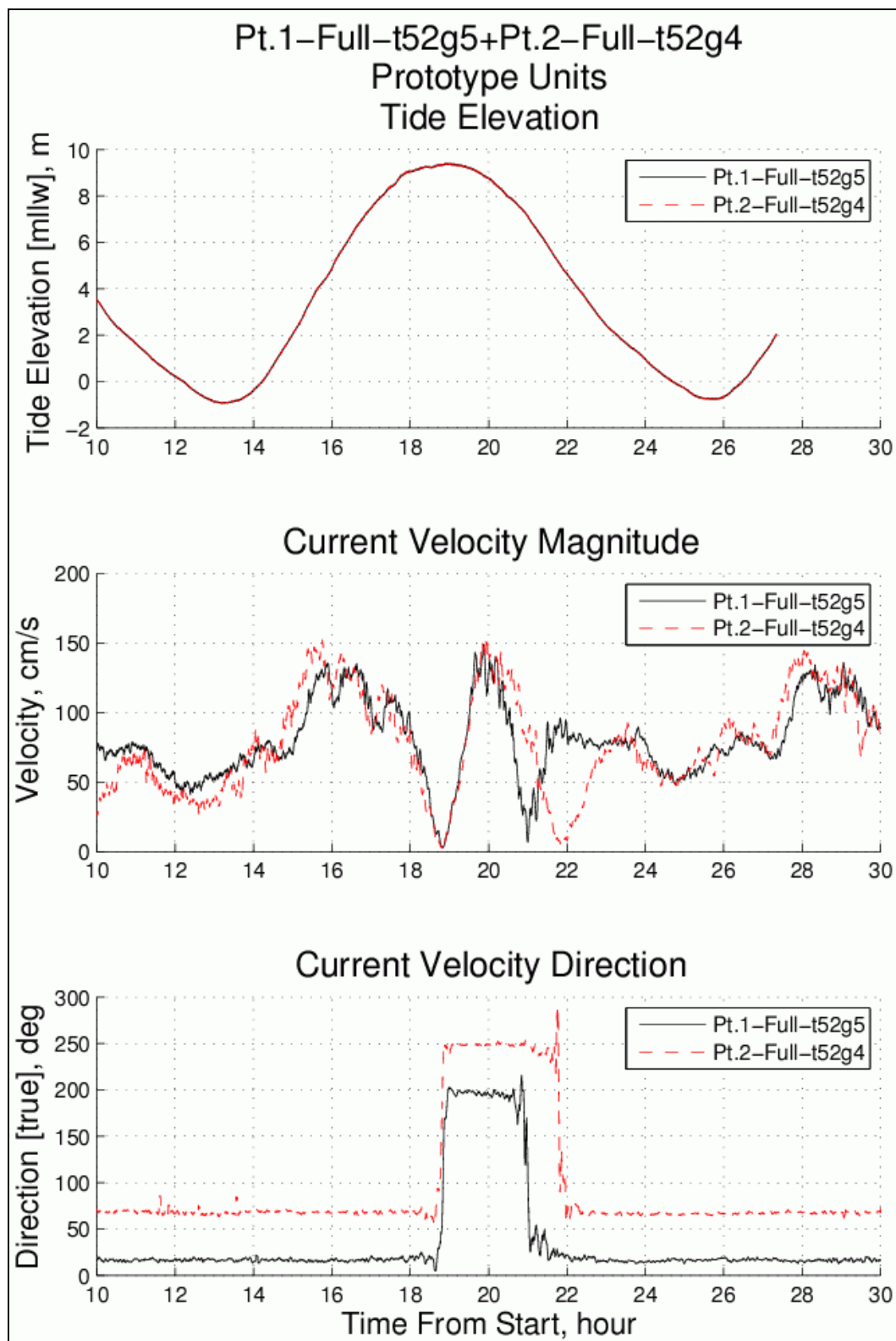


Figure B13. Velocity measurements at Pt. 1 and Pt. 2 (Full Expansion configuration).

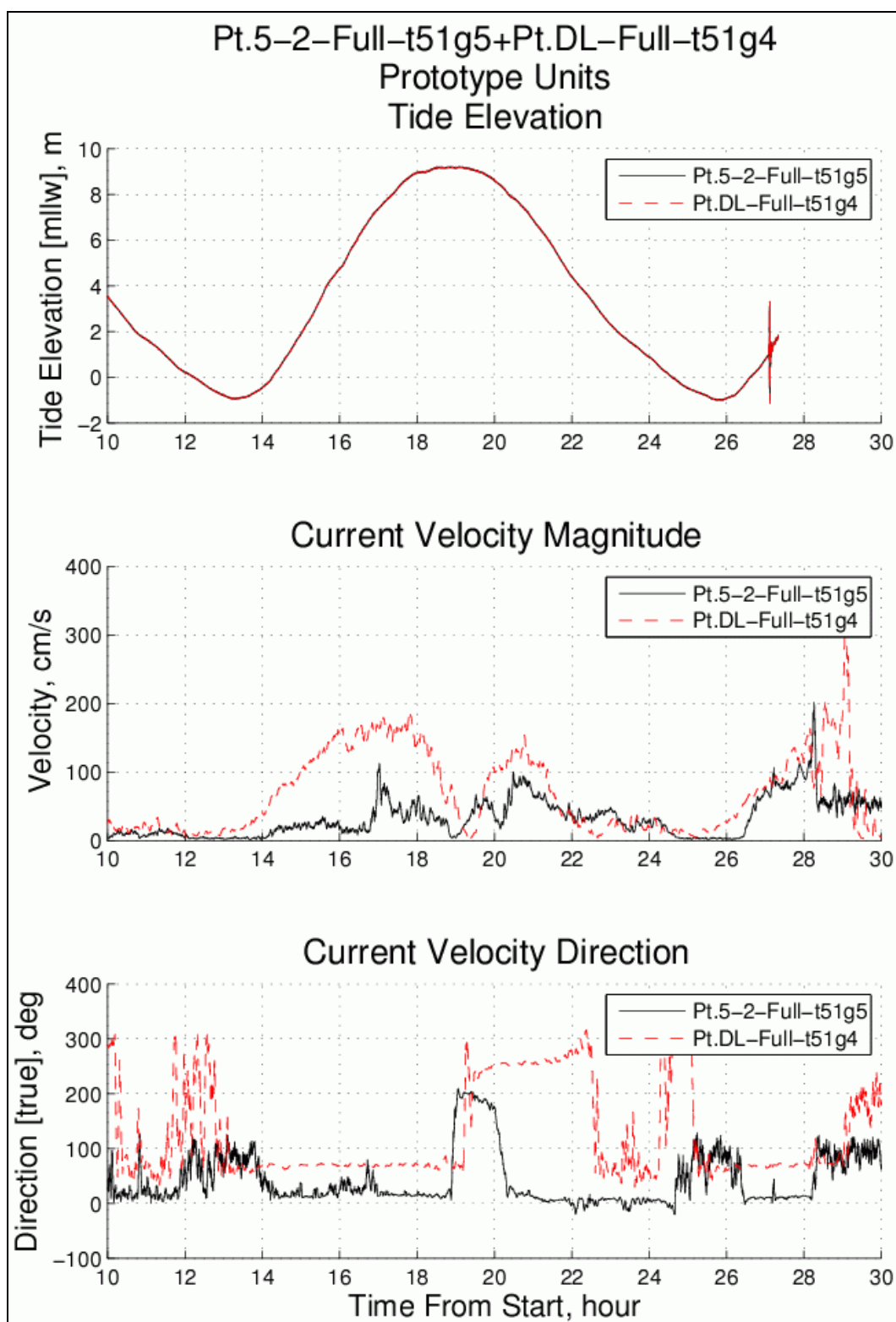


Figure B14. Velocity measurements at Pt. 5.2 and Pt. DL (Full Expansion configuration).

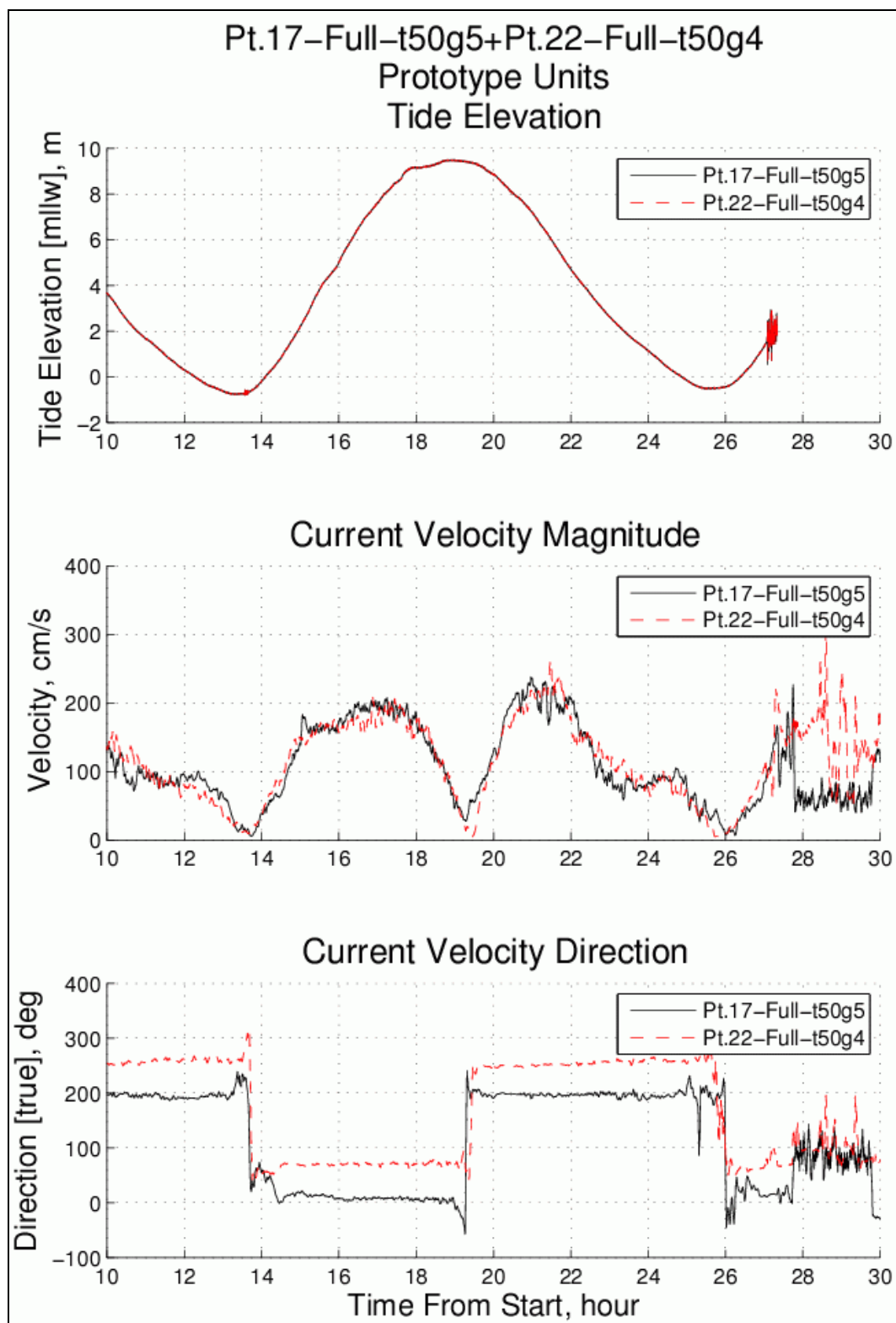


Figure B15. Velocity measurements at Pt. 17 and Pt. 22 (Full Expansion configuration).

Appendix C: Plots showing South Extension effect

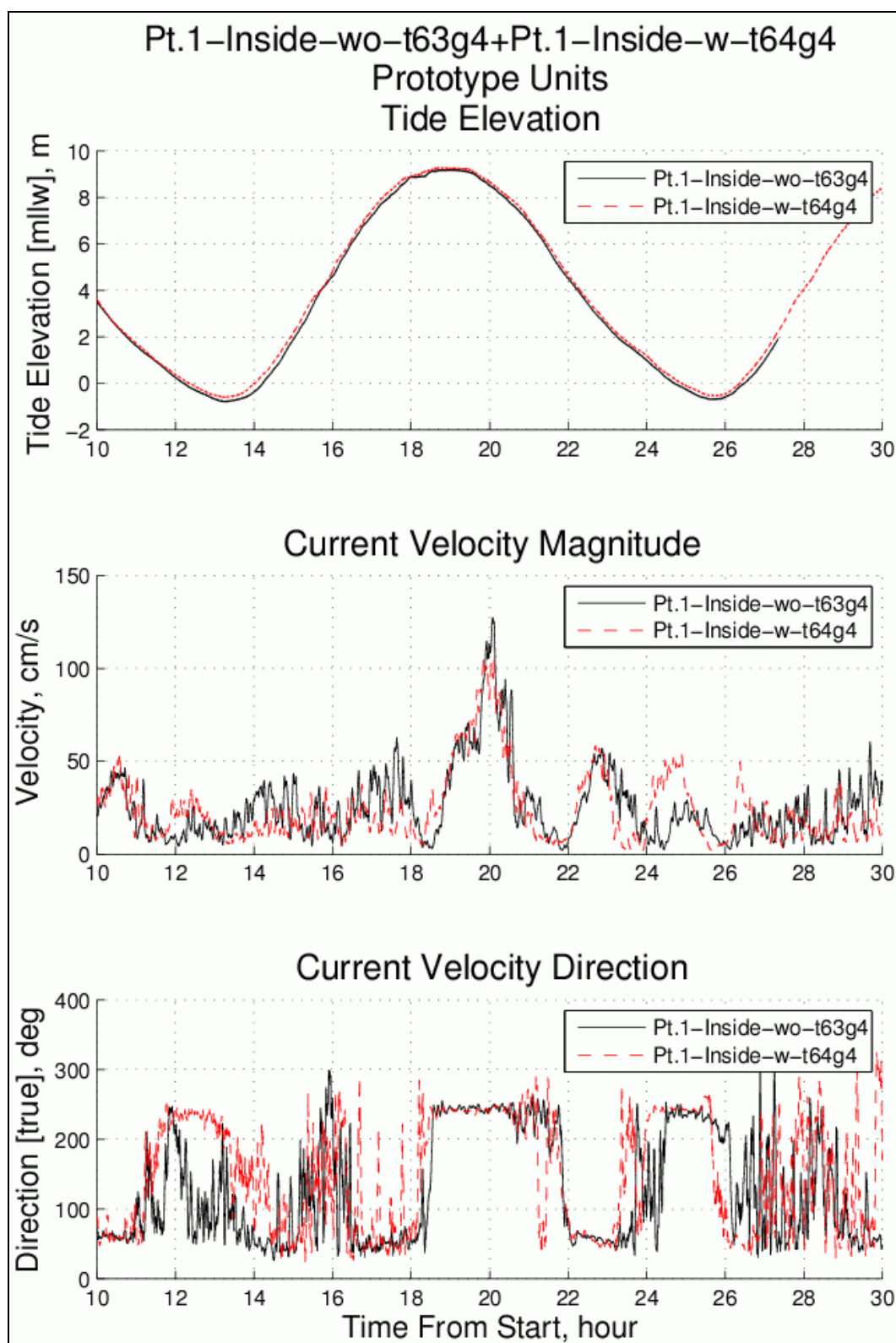


Figure C1. Effect of South Extension at measurement point 1.

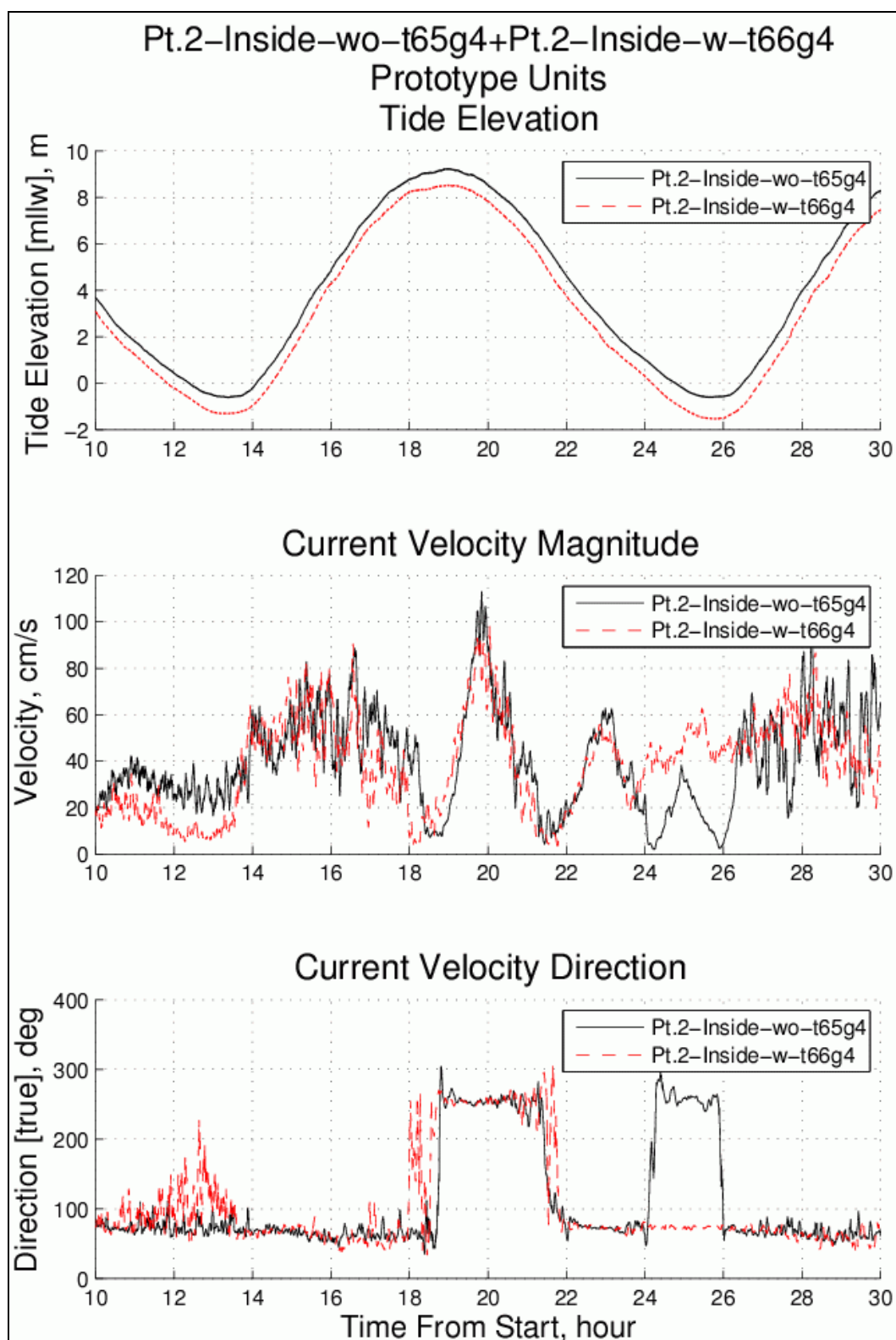


Figure C2. Effect of South Extension at measurement point 2.

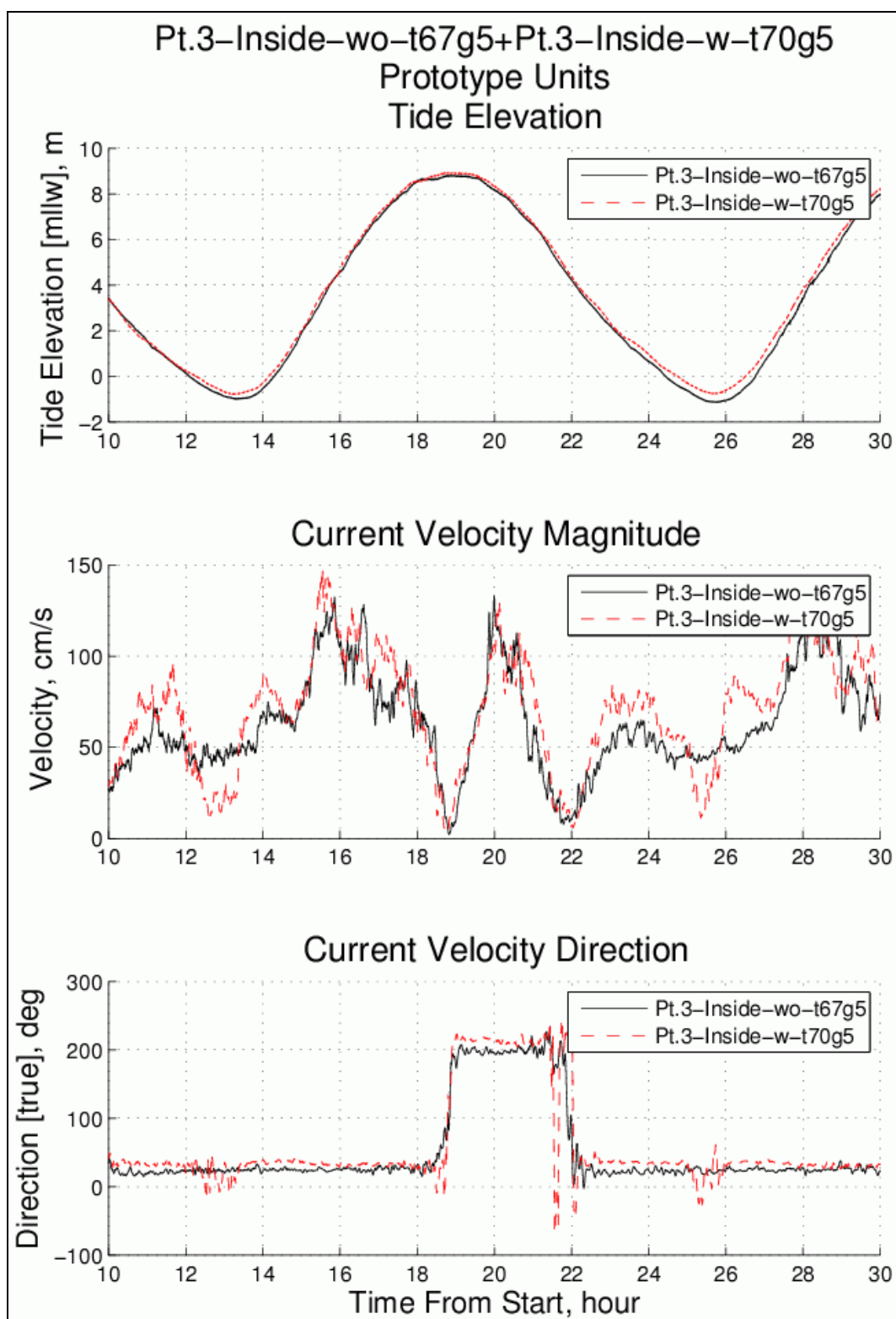


Figure C3. Effect of South Extension at measurement point 3.

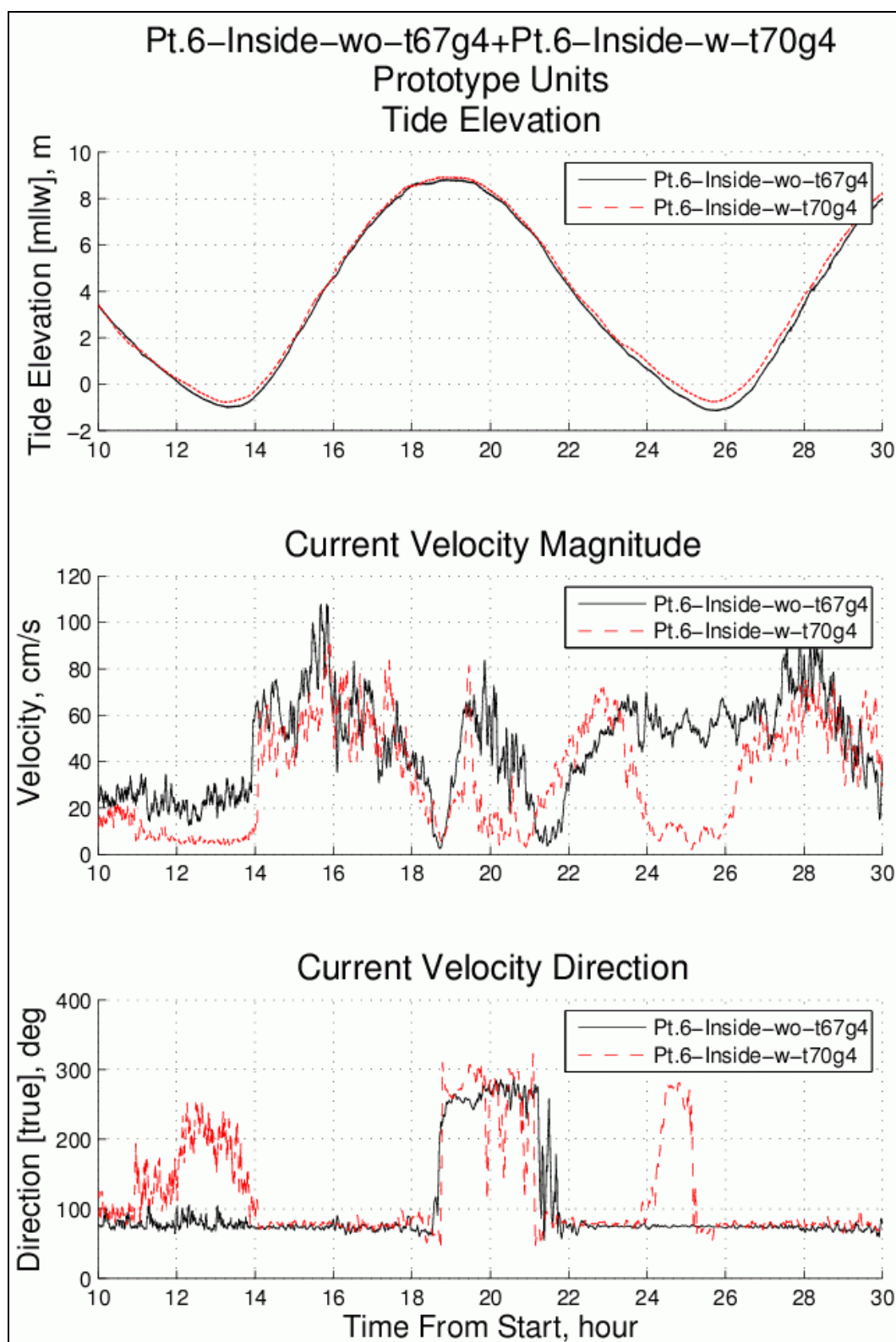


Figure C4. Effect of South Extension at measurement point 6.

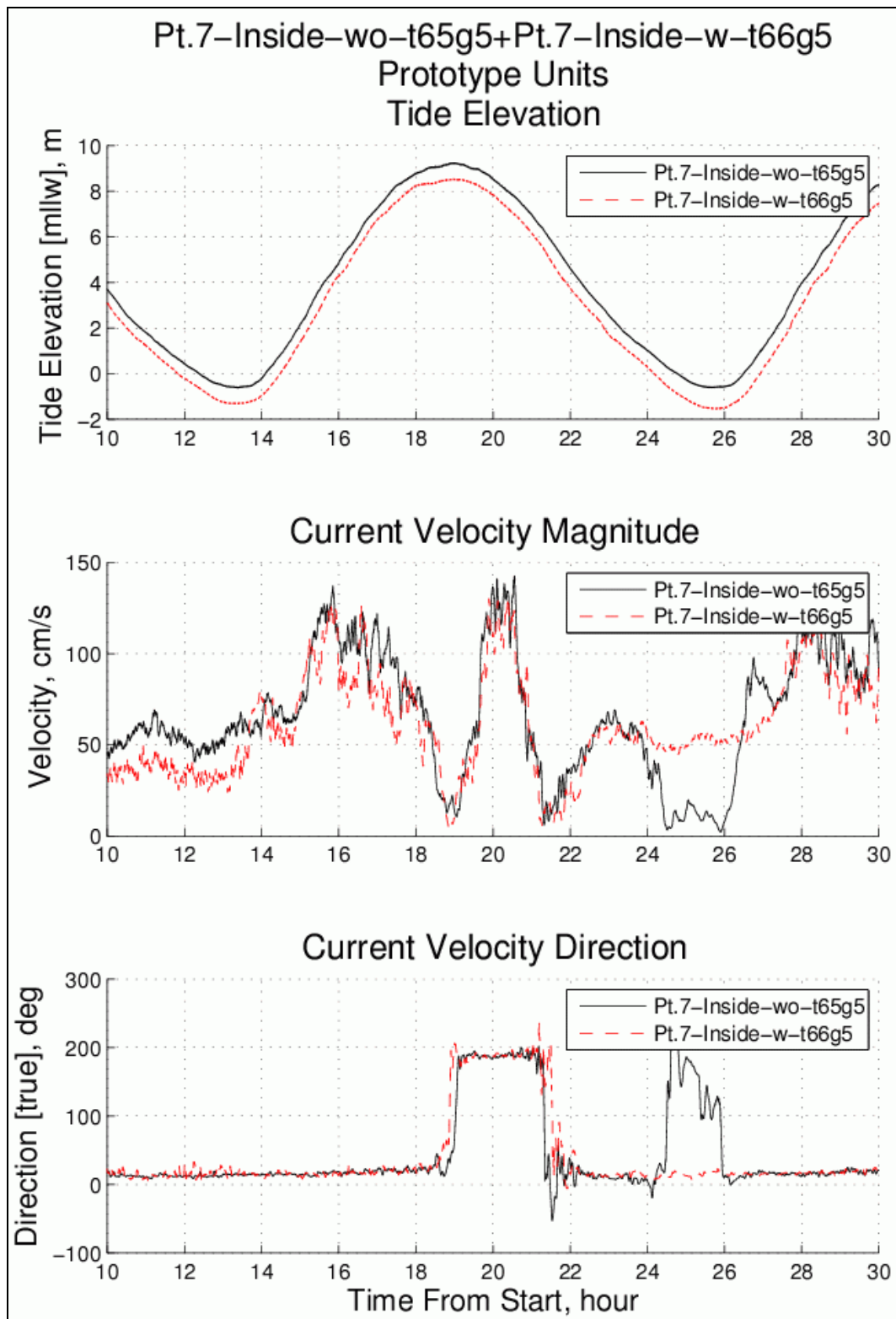


Figure C5. Effect of South Extension at measurement point 7.

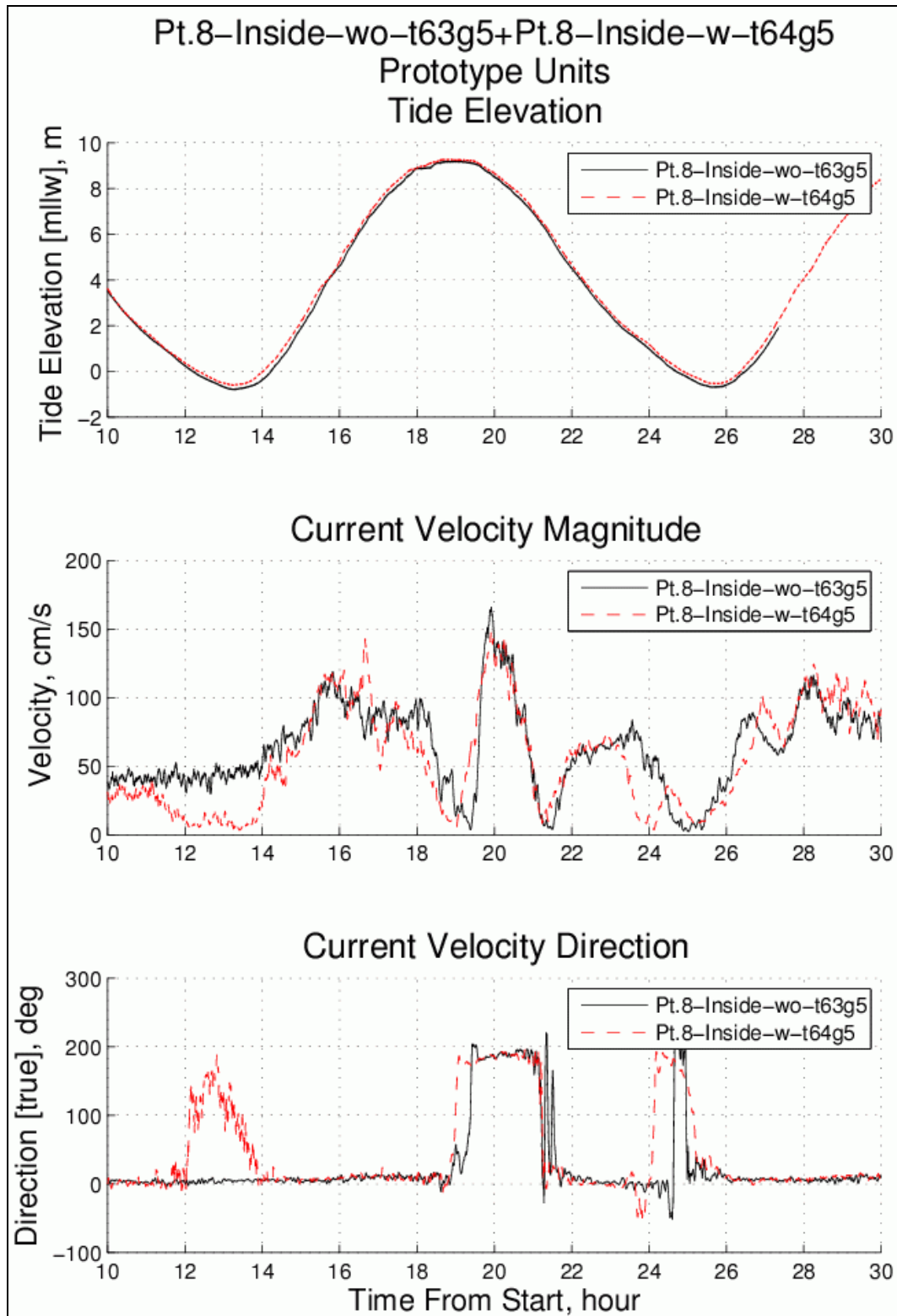


Figure C6. Effect of South Extension at measurement point 8.

| REPORT DOCUMENTATION PAGE | | | | Form Approved OMB No. 0704-0188 | |
|---|---------------------------------|----------------------------------|----------------------------|--|---|
| Public reporting burden for this collection of information is estimated to average 1 hour per response, including the time for reviewing instructions, searching existing data sources, gathering and maintaining the data needed, and completing and reviewing this collection of information. Send comments regarding this burden estimate or any other aspect of this collection of information, including suggestions for reducing this burden to Department of Defense, Washington Headquarters Services, Directorate for Information Operations and Reports (0704-0188), 1215 Jefferson Davis Highway, Suite 1204, Arlington, VA 22202-4302. Respondents should be aware that notwithstanding any other provision of law, no person shall be subject to any penalty for failing to comply with a collection of information if it does not display a currently valid OMB control number. PLEASE DO NOT RETURN YOUR FORM TO THE ABOVE ADDRESS. | | | | | |
| 1. REPORT DATE (DD-MM-YYYY) May 2010 | | 2. REPORT TYPE Final report | | 3. DATES COVERED (From - To) | |
| 4. TITLE AND SUBTITLE Physical Model of Knik Arm and the Port of Anchorage, Alaska | | | | 5a. CONTRACT NUMBER | |
| | | | | 5b. GRANT NUMBER | |
| | | | | 5c. PROGRAM ELEMENT NUMBER | |
| 6. AUTHOR(S) Steven A. Hughes, Julie A. Cohen, and Hugh F. Acuff | | | | 5d. PROJECT NUMBER | |
| | | | | 5e. TASK NUMBER | |
| | | | | 5f. WORK UNIT NUMBER | |
| 7. PERFORMING ORGANIZATION NAME(S) AND ADDRESS(ES) U.S. Army Engineer Research and Development Center Coastal and Hydraulics Laboratory 3909 Halls Ferry Road Vicksburg, MS 39180-6199 | | | | 8. PERFORMING ORGANIZATION REPORT NUMBER ERDC/CHL TR-10-3 | |
| 9. SPONSORING / MONITORING AGENCY NAME(S) AND ADDRESS(ES) U.S. Army Engineer District, Alaska Elmendorf Air Force Base, AK 99506-0898 | | | | 10. SPONSOR/MONITOR'S ACRONYM(S) | |
| | | | | 11. SPONSOR/MONITOR'S REPORT NUMBER(S) | |
| 12. DISTRIBUTION / AVAILABILITY STATEMENT Approved for public release; distribution is unlimited. | | | | | |
| 13. SUPPLEMENTARY NOTES | | | | | |
| 14. ABSTRACT A large physical model replicating approximately 19 miles of Cook Inlet was constructed at ERDC with a horizontal length scale of 800-to-1 and a vertical length scale of 200-to-1. The model included the Knik Arm, a portion of Eagle Bay, and a region south of Point Woronzof. The Port of Anchorage is located in the Knik Arm, and tidal flows at the Port generated by the +30-ft tide range are highly influenced by a large gyre that forms to the south of Cairn Point during ebb tide. The purpose of the physical model was to evaluate changes to tidal flows caused by a large, multi-phased Port expansion that might impact the Alaska District's navigation mission at the Port. Model validation consisted of reasonable reproduction of field-measured tidal velocities collected at three locations near the Port over the spring tide cycle. Velocity measurements over a tide cycle were acquired in the model at strategic locations near the Port berthing areas for each phase of the Port expansion. Comparisons between the different expansion phases quantified expected changes to the flow regime. Potential sedimentation problems were identified using both measurements and flow visualization techniques coupled with time-lapse video. | | | | | |
| 15. SUBJECT TERMS Cook inlet Knik Arm Port expansion Large gyres Port of Anchorage Distorted model Physical model Tidal flows | | | | | |
| 16. SECURITY CLASSIFICATION OF: | | | 17. LIMITATION OF ABSTRACT | 18. NUMBER OF PAGES 183 | 19a. NAME OF RESPONSIBLE PERSON: |
| a. REPORT UNCLASSIFIED | b. ABSTRACT UNCLASSIFIED | c. THIS PAGE UNCLASSIFIED | | | 19b. TELEPHONE NUMBER (include area code) |